DETECTION AND DEGRADATION OF ENDOCRINE DISRUPTORS USING ZnO NANOPARTICLES

Thesis

Submitted in partial fulfillment of the requirements

for the degree of

DOCTOR OF PHILOSOPHY

By

Kadam Vrushali Vinayak
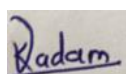
Reg. No. 165030CH16F03

DEPARTMENT OF CHEMICAL ENGINEERING

NATIONAL INSTITUTE OF TECHNOLOGY KARNATAKA,

SURATHKAL, MANGALORE – 575025

February, 2022

DECLARATION

I hereby declare that the Research Thesis entitled **"Detection and degradation of endocrine disruptors using ZnO nanoparticles"** which is being submitted to the **National Institute of Technology Karnataka, Surathkal** in partial fulfillment of the requirements for the award of the Degree of **Doctor of Philosophy** in the **Department of Chemical Engineering**, is a bonafide report of the research work carried out by me. The material contained in this **Research Thesis** has not been submitted to any University or Institution for the award of any degree.

Kadam Vrushali Vinayak
Registration number: 165030CH16F03
Department of Chemical Engineering

Place: NITK, Surathkal
Date: 24.02.2022

C E R T I F I C A T E

This is to certify that the Research Thesis entitled " **Detection and degradation of endocrine disruptors using ZnO nanoparticles**" submitted by **Kadam Vrushali Vinayak (Register Number: 165030CH16F03)** as the record of the research work carried by her, is *accepted as the Thesis submission* in partial fulfilment of the requiremnts for the award of **Doctor of Philosophy.**

Research Guide

Dr. Raj Mohan B.

Professor

Department of Chemical Engineering

NITK Surathkal

Research Co-Guide

Dr. P.E. JagadesshBabu

Associate Professor

Department of Chemical Engineering

NITK Surathkal

Chairman-DRPC

ACKNOWLEDGEMENT

ABSTRACT

Globally, the major concern is alarming levels of EDCs resulted due to rapid industrialization and urbanization. Industries produce these compounds for every aspect of our life, such as mobility, gadgets, health, agriculture and cosmetics. The inappropriate use or disposal of these products led to contamination of the water ecosystem and became a threat to human health. Thus, there is a constant need to develop detection methods for EDCs and further cleanup technology to eliminate those pollutants from the water ecosystem. In this aspect, ZnO nanoparticles were synthesized by chemical and biological approaches for the detection and degradation of EDCs, i.e., p-NP and BPA have been reported. For biological synthesis, a zinc metal tolerant endophytic fungus *C. geniculatus* was isolated from the medicinal plant *Nothapodytes foetida* and its ability to synthesize proteins that can aid in the synthesis of ZnO nanoparticles was evaluated. The discrete, polydisperse and quasi-spherical hexagonal wurtzite structured ZnO nanoparticles with an average size of 5.25 ± 1.43 nm were synthesized. The removal efficiency of 78.57 % and 85.18 % was obtained in the photocatalytic degradation of p-NP and BPA, respectively, under optimum reaction conditions. The experimental results with COD and TOC analysis exhibit 60 % and 50.9 % of the mineralization degree for p-NP (25 mg/L) and 63.6 % and 63.6 % for BPA (10 mg/L). The photocatalytic degradation of p-NP and BPA follows first-order reaction kinetics. Moreover, the degradation reaction of p-NP and BPA were found to be initiated and dominated by •OH and h^+ radicals. Subsequently, the intermediates and products of photocatalytic degradation of p-NP and BPA were identified through LC-MS analysis and the degradation pathway was proposed. Furthermore, the detection limit was found to be 17.9 μM and 0.35 μM for p-NP and BPA, respectively, using a fluorescence spectrophotometer. The hypothetical sensing mechanism for p-NP and BPA is ascribed to static and dynamic quenching, respectively. A yellow fluorescent, APTES@ZnO and β-CD@ZnO QDs were synthesized by co-precipitation method for detection of p-NP and BPA, respectively. The lower detection limit of functionalized QDs for p-NP and BPA was estimated to be 0.089 μM and 0.19 μM, respectively. Moreover, the hypothetical sensing mechanism in detection was ascribed to the partially inner filter effect of p-NP towards APTES@ZnO QDs, and the transfer of excited state electrons of the APTES@ZnO QDS to p-NP. In the case of BPA, the quenching mechanism was ascribed to electron transfer between β-CD-functionalized ZnO QDs and BPA due to inclusion complex formation.

Keywords: APTES@ZnO, BPA, β-CD@ZnO, *C. geniculatus*, fluorescence quenching, p-NP, photocatalyst, ZnO.

CONTENTS

LIST OF TABLES

LIST OF FIGURES

NOMENCLATURE

Symbol	Description
KeV	Kilo electron volt
kDa	Kilo Dalton
nm	Nanometer
cm	Centimeter
ºC	Degree Celsius
h	Hour
min	Minute
μg	Microgram
ml	Millilitre
mg	Milligram
L	Litre
g	Gram
w/w	Weight by weight
mM	Millimolar
μM	Micromolar
mol/L	Mole per litre
EC	Effective concentration
LC	Lethal concentration
MIP	Molecularly imprinted polymer
MOF	Metal-organic framework
In	Indium
Br	Bromine
Bi	Bismuth
V	Vanadium
Mo	Molybdenum
C	Carbon
N	Nitrogen
S	Sulfur
O	Oxygen
P	Phosphorus
W	Tungsten

CHAPTER 1

INTRODUCTION

Endocrine-disrupting chemicals (EDCs) are an exogenous substance or mixture that mimic, block, or interfere with the function(s) of the endocrine system and subsequently leads to adverse health effects (Bergman et al. 2013). These EDCs comprise numerous natural and synthetic organic compounds, primarily manmade compounds used as plasticizers (phthalates), plastics [bisphenol A (BPA)], industrial solvents/lubricants and their byproducts (polychlorinated and polybrominated biphenyls, dioxins), production of agricultural products [p-nitrophenol (p-NP)] and pharmaceutical agents (diethylstilbestrol) (Diamanti-Kandarakis et al. 2009). Moreover, these EDCs mainly consist of phenols and their derivatives included in the list of persistent priority pollutants by the United State environmental protection agency (USEPA) and the central pollution control board, India (CPCB), due to their toxicity and environmental concern (CPCB 2016; USEPA 2012). The persistent complex mixtures of EDCs in aquatic environments show spatial or temporal alarming levels due to the intentional or accidental release into their water ecosystem (Olujimi et al. 2010).

The 2,2-bis (4-hydroxyphenyl) propane, commonly known as BPA, was first synthesized by a Russian chemist, Dianin, in 1891 and then identified as an estrogenic substance by a British medical researcher Dodds in 1936 (Dodds and Lawson 1936). BPA is one of the most studied in vivo and in vitro EDC (Vandenberg et al. 2007; Esposito and Cimmino 2015). Epidemiological studies illustrate the association of BPA with diseases related to the pancreas, cardiovascular, thyroid (Moriyama et al. 2002), liver and immune systems (Rochester 2013). Due to their high endocrine disruptive activity and acute toxicity, the USEPA and United States Food and Drug Administration (US FDA) established 50 µg/kg/day as a safe reference dose for humans (USEPA 2012). Exposure even below this safe reference dose has exhibited cancer susceptibility in rodents (Seachrist et al. 2016) and humans (Shafei et al. 2018).

Bisphenol A is a key chemical compound used in the production of flame retardant products, electronic gadgets, powder paints and biomedical applications (Staples et al.
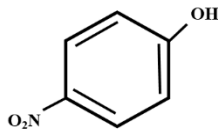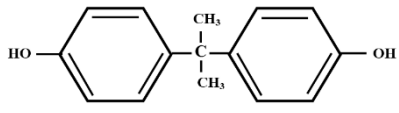
1998). Moreover, BPA is also found in common consumer goods such as thermal paper (57–79 $\mu g/cm^2$) (Kang et al. 2006), cosmetics (31 $\mu g/kg$), canned food (30-50$\mu g/kg$), pacifiers (0.28-0.36 μg/product) (Bakkar et al. 2014). Thus, the frequent and widespread use and disposal of BPA-based materials and leachates from the landfill made it ubiquitous. BPA is generally toxic to several species comprising mysids, daphnids, freshwater and saltwater fishes in the concentration range between 1.1 to 12.8 mg/L (Alexander et al. 1988). The LC_{50} and EC_{50} values of BPA ranging from 1.0 to 10.2 mg/L, which indicates that the compound is slight to moderately toxic towards fish and invertebrate species according to the current USEPA standards (Flint et al. 2012; Alexander et al. 1988; Environment Canada 2008).

p-Nitrophenol is usually considered as an EDC with estrogenic and anti-androgenic activities (Zhang et al. 2013b). The acute toxicity of p-NP leads to corneal opacity, chromosomal aberrations, drowsiness, eye irritation, headaches, nausea, cyanosis and methemoglobin formation. The chronic toxic effects of p-NP cause erythema, scaling, scabbing and cracking of the skin (NTP 1993; ATSDR 1992). The p-NP exhibits LC_{50} values ranging from 3.8 to 7.93 mg/L in static and flow-through conditions, indicating the toxic effect on fish and other organisms in the environment (Boehncke et al. 2000). p-NP is primarily used in the production of drugs (acetaminophen), pesticides, fungicides, herbicides, dyestuff and leather processing (ATSDR 1992). Extensive use and hydrolysis of p-NP based products have led to its release in subsurface water, resulting in groundwater pollution (Boehncke et al. 2000). Hence, the USEPA has provided an allowable limit of 0.43 μM for p-NP in drinking water (Wei et al. 2011).

The half-life values of BPA in water, soil, sediment and air are 38, 75, 340, and 0.2 days respectively (Corrales et al. 2015). In India, the highest concentration of BPA was observed in the Yamuna river (14,800 ng/L) (Lalwani et al. 2020). Similarly, the half-life values of p-NP in water, soil, air are 13.7, 10.2, 3.7 days, respectively (ATSDR 1992). Yoshida et al. (1983) developed a nonsteady-state equilibrium model which predicted the distribution of p-NP in water, soil, sediment and air as 94.6%, 0.95%, 4.44% and 0.0006%, respectively. Usually, these EDCs are hard to break and undergo slow metabolism or may convert into more toxic forms than the former. Thus, BPA and p-NP became persistent and have bioaccumulation ability that deteriorates human health and the environment (Environment Canada 2008; ATSDR 1992). Owing to the toxicity and distribution of BPA and p-NP, its effectual detection and elimination from the contaminated effluents before discharging to the environment is a foremost challenge.

Few studies have been reported that p-NP and BPA are biodegradable by micro-organisms (Arora et al. 2014; Chai et al. 2005; Eltoukhy et al. 2020). However, the recalcitrant nature of BPA ceases its utilization as an energy and carbon source in microbial metabolism. Moreover, biodegradation of BPA needs a co-substrate to undergo a co-metabolic degradation (Kamaraj et al. 2014b; Eio et al. 2014), making the treatment process complicated and expensive. p-NP contains $-NO_2$ group, which is readily unsusceptible for aerobic biodegradation (Spain 1995) thus became recalcitrant. The toxicity of p-NP and the lack of a catabolic system in the micro-organism needs enrichment of the microbial isolate tolerant to a higher concentration of p-NP (Sarkar et al. 2020), a crucial step in biodegradation that is time-consuming and cost-ineffective. However, these anthropogenic wastes imposed toxicity on micro-organism resulted in substrate inhibition at higher concentration hindering the effective degradation process (Goudar et al. 2000; Salehi et al. 2019). Table 1.1 summarizes the properties of two representative endocrine disruptors.

Table 1.1: Summary of the details of the representative endocrine disruptors

Properties	p-NP	BPA
IUPAC name	p-nitrophenol	4,4'-(propane-2,2-diyl)diphenol
Molecular formula	$C_6H_5NO_3$	$C_{15}H_{16}O_2$
Molar mass	139.110 g/mol	228.29 g/mol
pKa	7.08	9.6, 10.2
Appearance	Colorless to light yellow crystalline solid	White solid
Molecular structure		
UV-vis characteristic wavelength	317nm, 405nm	224nm, 276nm
Major uses	Production of acetaminophen, pesticides, fungicides, herbicides, dyestuff and leather processing	Production of polycarbonate plastic, epoxy resins, powder paints and electronic gadgets

Among several studies reported on the removal of EDCs from the environment, photocatalysis of EDCs using semiconductor-based nanoparticles is found to be one of the fast-growing research domains (Gmurek et al. 2017). Semiconductor photocatalyst such as cadmium sulfide (CdS), zinc sulfide (ZnS), ferric oxide (Fe_2O_3), titanium oxide (TiO_2), and zinc oxide (ZnO) nanoparticles can act as a sensitizer for light induced redox reactions due to their electronic structure (Hoffmann et al. 1995; Bhatkhande et al. 2002). Semiconductor-based photocatalysis has received enormous attention over the last few decades due to its potential to degrade organic and inorganic pollutants through heterogeneous photocatalysis (Mirzaei et al. 2016). Heterogeneous photocatalysis is found to be an effective treatment technique for the removal of phenolic compounds. These semiconductor photocatalysts utilize photon energy and convert it into chemical energy and offer great potential in wastewater treatment by eliminating the contaminant rather than transforming it into different phases (Ahmed et al. 2011). Among semiconductors, TiO_2 and ZnO are the most studied photocatalyst in the past decade and can detoxicate the water (Mondal and Sharma 2014). In recent years, ZnO has attracted considerable attention as a photocatalyst due to its high stability and photosensitivity and low cost than TiO_2 (Daneshvar et al. 2004). ZnO is a wide range, n-type of the semiconductor in groups II-VI, having a wurtzite structure with a direct bandgap of 3.37 eV and a large excitation binding energy of 60 meV, which possess excellent optical, electrical properties (Li and Wang 2010). ZnO is a biocompatible material and is recognized as SAFE (GRAS) by USFDA (Espitia et al. 2012). These ZnO nanoparticles have been used in various applications as chemical sensors, piezoelectric transducers, solar cells, photocatalyst, photovoltaics and photodiodes (Li et al. 2010b).

Over the years, certain advanced techniques have been employed in the detection of p-NP and BPA, such as electrochemical sensors (Tchieno et al. 2018; Zhou et al. 2019; Tajik et al. 2020), high-performance liquid chromatography (Elbarbry et al. 2006; Rodriguez et al. 2019) and immunoassay based analysis (Oubina et al. 1999; Zheng et al. 2011). The above-mentioned protocols provide a lower limit of detection (LOD) with good reproducibility. Still, these methods are time-consuming, involve complex operational conditions, and are expensive, limiting their practical applicability for routine detection of p-NP and BPA. Various fluorescent probes are also being used for the detection of BPA and p-NP viz. functionalized carbon dots (Liu et al. 2016; Han et al. 2019), functionalized metal nanoclusters (Wu et al. 2015; Yang et al. 2018), functionalized semiconductor quantum dots (QDs) (Kuang et al. 2010; Zhang et al. 2015a). Efforts have been taken using

metal nanoclusters such as gold (Au), copper (Cu), and silver (Ag) as fluorescent probes due to their less toxicity. However, the quantum yield of metal nanoclusters is low compared to semiconductor quantum dots such as cadmium selenide (CdSe), cadmium telluride (CdTe), ZnS and ZnO (Yang et al. 2020). These semiconductor QDs can be the right choice as fluorescent probes due to their unique optical properties. However, CdTe and CdSe QDs-based fluorescence sensors lead to heavy metal pollution resulting in fatal damage to the human body, limiting their practical applications (Gomes et al. 2011; Jamieson et al. 2007). Hence, there is a need to develop novel fluorescent probes that are non-toxic and simple.

Nanoparticles possess unique physical and chemical properties and these properties are dependent on the surrounding chemical environment and form the basis of pollutants sensing. Further, the selective and sensitive detection of pollutants can be achieved by grafting specific functional groups onto the surface of nanoparticles that systematically interact with the pollutants (Liu et al. 2011). Functional groups play a significant role in directing and controlling the reactions. Carbonyls (C=O), carboxylic acids (CO$_2$H), alcohols (-OH), esters (CO$_2$R), and amines (NH$_2$) are the most common functional groups used in chemistry (Kolev et al. 2011). Physical and chemical methods were used for the surface modification of nanoparticles. Physical modification can be carried out by adsorption of functional molecules on nanoparticles surfaces. In contrast, chemical modification occurs via the covalent bonding of functional molecules to the surface of the nanoparticles. Carboxylic acid, silanes and polymers such as β-cyclodextrin (β-CD), calixarene can be used as a coupling agent in the covalent grafting. Among these coupling agents, silane and β-CD are frequently used for surface modification of nanoparticles due to their several prominent properties (Ahangaran and Navarchian 2020).

β-CD is a water-soluble cyclic oligosaccharide having seven α-1, 4 linked D-glucopyranose units which form a toroidal hydrophobic cavity. Further, they can include numerous organic and inorganic guest molecules by non-covalent interactions such as hydrogen bonding, van der Waals forces, and hydrophobic interactions (Zhao and Chen 2007). The toroidal edges of β-CD consist of hydroxyl functional groups, facilitating hydrogen bond formation with other high electronegative elements (Del Valle 2004). Subsequently, each ZnO nucleus might be surrounded by many β-CD molecules, which abridge the aggregation. Moreover, the size distribution and reduced agglomeration state of the nanoparticles could be improved during the synthesis process.

Organosilanes are bifunctional molecules with the general formula X-(CH₂)n-SiRn(OR′)₃-n, where X represents the head group functionality, (CH₂)n a flexible spacer, and Si(OR)n the anchor groups by which (after hydrolysis of the alkoxy group) they can attach to free Si-OH surface groups. (3-Aminopropyl) triethoxysilane (APTES) is one of the amino silane commonly used for the functionalization of surfaces (Bruce and Sen 2005). Thus, based on its potential characteristics, β-CD and APTES can be used as a capping agent for ZnO in selective detection of p-NP and BPA.

Various solution-based methods such as hydrothermal, micro emulsion, coprecipitation and chemical bath deposition were used for the synthesis of ZnO nanoparticles. The coprecipitation method of nanoparticles synthesis offers several advantages such as easy scale-up and downstream process and abstains the use of harsh reaction conditions and is cheap compared to the above-mentioned chemical-based synthesis methods. Moreover, the coprecipitation method offers a synthesis of functionalized nanoparticles through a one-pot procedure. Furthermore, this functionalized nanoparticle controls the growth and surface defects with tuned physicochemical properties such as fluorescence, enabling its application in the field of sensors (Costenaro et al. 2013; Shaba et al. 2021).

Majorly, chemically synthesized semiconductor photocatalyst has been used in basic research and practical applications. Recently, researchers started exploring the biologically synthesized metal-oxides for photocatalytic applications. Nature has conceived various routes to synthesize inorganic nanomaterials, which have endowed with the recent development of a relatively new and eco-friendly alternative to the chemical synthesis of nanomaterials. Consequently, the necessity for developing biocompatible and ecological benign routes for nanoparticle synthesis led to the exploitation of various biological systems as a possible nano factory. In recent years, a plethora of work has been done for nanomaterial synthesis by means of several biological entities, including bacteria (Selvarajan and Mohanasrinivasan 2013), algae, fungi (Uddandarao and Balakrishnan 2016; Mohanpuria et al. 2008), plant extracts (Jayaseelan et al. 2012; Sharma et al. 2016) and virus. Fungal mediated synthesis of metallic nanoparticles has added practical advantages over the above-mentioned systems in terms of high metal tolerance, bioaccumulation capability (Sastry et al. 2003), fast growth rate, ease to culture and can be maintained in the laboratory at ambient conditions. The fungi's inherent ability of biomolecules secretion aids in nanoparticles synthesis and stability, further preventing

agglomeration (Jain et al. 2013). Moreover, biologically synthesized nanoparticles have gained research importance because of their biocompatibility and nontoxic nature.

Among the microbial diversity that encompasses an interesting group of fungal species, called endophytes, inhabit plant tissues entirely or partially of their life cycle, lacking harmful effects on their host and having a rich source of novel bioactive compounds. These bioactive compounds from endophytic fungi exhibit properties like antimicrobial, immunosuppressor, antioxidant, antitumor and antibiotic activities (Strobel 2003). The endophytic fungi form large biomass that can withstand agitation, produces structurally and functionally diversified biomolecules and are easily handled in downstream processes. Further, the employment of these endophytes for nanoparticle synthesis could be another great advantage as they are known for immediate uptake of metals and are capable of reducing metal salts for a rapid yield of nanoparticles under optimized conditions (Uddandarao and Balakrishnan 2016; Sharma et al. 2016). Various fungal species were used for ZnO nanoparticle synthesis, such as *Aspergillus sp.* (Jain et al. 2014), *A. aeneus* (Jain et al. 2013), *A. fumigatus* (Raliya and Tarafdar 2013), *A. alternata* (Sarkar et al. 2014), etc. Researchers have reported the employment of endophytic fungi in the synthesis of gold, silver (Mohanpuria et al. 2008; Sarkar et al. 2014) and ZnS nanoparticles (Uddandarao and Balakrishnan 2016). The interference of endophytes for nanoparticle synthesis is less explored and hence, the development of symbiosis between nanotechnology with other disciplines such as biotechnology and material chemistry to reformulate the novel nanomaterial with controlled size and shape is the need of the hour.

CHAPTER 2

LITERATURE REVIEW

2.1. Endophytic fungi

A mycologist, De Bary, coined the term endophyte in 1866, which describes the internal mycota of living plants. Endophytic fungi are defined as the organisms inhabiting interiors of plant organs for at least a part of their life cycle without causing apparent harm to the host (Petrini 1991). Endophytes maintain stable symbiosis as they produce a plethora of compounds with an added advantage for plant growth, sustainability and protection to an environmental condition (Wilson 1995; Strobel 2003; Yan et al. 2019). These are extensive secretors of novel bioactive molecules comprising quinones, phenols, flavonoids, steroids (Schulz et al. 2002; Yu et al. 2010), xanthans, terpenoids (De Souza et al. 2011) and alkaloids (Clay 1988). These active biomolecules have potential applications in the agriculture, medicine, food and cosmetic industry. *Taxomyces andreanae*, an endophytic fungal isolate from the Yew tree, was used to produce Taxol, the worlds' first billion-dollar anticancer drug used to treat human tissue-proliferating diseases (Stierle et al. 1993).

Endophytic fungi are widely distributed in the ecosystem and significantly contribute to microbial diversity. The endophytic fungi population varies with the host plant location and climatic conditions (Rana et al. 2020). A large number of fungal taxa can be recovered from the single host after surface sterilization of leaves (Hata et al. 2008), roots (Ananda et al. 2002), bark and stems (Verma et al. 2007).

Numerous researchers have reported the isolation of endophytes from *Nothapodytes Foetida*, a plant endemic to Western Ghats of India, one of the world's ten highly significant biodiversity hotspots (Myers et al. 2000; Musavi and Baalakrishnan 2013; Samaga and Rai 2014). The Western Ghats in India, starting from Gujrat through the states, Maharashtra, Karnataka, Kerala, Tamil Nadu and ending at Swamithoppe, near Kanyakumari, the southern tip of India, is a rich source of biodiversity. *N. Foetida* is a medicinal plant and a rich source of vital neoplastic alkaloids and other secondary metabolites having potential antimicrobial, antiviral and anticancer properties (Namdeo et al. 2008; Ramalingam et al. 2012; Velmurugan et al. 2014).

The common endophytic fungal species isolated from plant *N. Foetida* present in the Kudremukh region, Western Ghats belong to genera *Penicillium, Alternaria,*

Pestalotiopsis, Colletotrichum, Fusarium, Aspergillus, Curvularia, Neurospora, Gelasinospora and *Sordaria* (Raviraja 2005; Rehman et al. 2008; Musavi and Baalakrishnan 2013; Uddandrao and Balakrishnan 2016; Vijayanandan and Balakrishnan 2018). Endophytic fungi play a significant role in toxic metal remediation through metal accumulation and reduction (Bradley et al. 1982). This inherent metal detoxification ability can be considered as a fascinating fact for applying these fungi as a nano factory for nanomaterial synthesis (Shankar et al. 2003).

2.2. Biological synthesis of nanoparticles

Economics, biosafety and biogenic systems are considered as the current aspects of nanotechnology. Due to various implications such as non-toxic reducing agents and reactants, low energy consumption and non-hazardous by-products, biogenic nanoparticle synthesis has more prominence (Netala et al. 2016). Compared to other microorganisms, the employment of endophytic fungi for nanoparticle synthesis becomes potentially exciting due to the following reasons. (i) Easy isolation of endophytes, as other microorganisms, needs enrichment of culture. (ii) The secretion of large amounts of cellular enzymes, secondary metabolites and other cellular compounds that possess redox capacity which converts metal ions into nanoparticles.

Mukherjee et al. (2001) were the first to report the synthesis of gold nanoparticles using endophytic fungi *Verticillium sp.* isolated from the Taxus plant. The intracellular reduction of gold chloride to gold nanoparticles was observed through the cell wall and cytoplasmic membrane enzymes due to the metal stress/toxicity. Endophytes can synthesize nanoparticles either intracellularly (Mukherjee et al. 2001) or extracellularly (Shankar et al. 2003). Researchers have isolated numerous endophytic fungi from different host plants to synthesize nanoparticles of gold, silver, ZnS, copper oxide (CuO), etc., as represented in Table No. 2.1. As endophytes have been employed to synthesize various nanoparticles, ZnO nanoparticles are not explored to date.

Table 2.1 Synthesis of nanoparticles from endophytic fungi

Fungal species	Sources	Nanoparticles	SPR (nm)	Characteristic [Size(nm)]	References
Colletotrichum sp.	*Pelargonium graveolens*	Gold	540	12 (XRD); 9 (TEM)	Shankar et al. 2003
A. clavatus	*Azadirachta Indica*	Silver	-	10-25 (TEM)	Verma et al. 2010
Pestalotia sp.	*Syzygium cumini*	Silver	415	26 (NTA); 10-40 (TEM)	Raheman et al. 2011
Epicoccum nigrum	*Phellodendron amurense*	Silver	424	1-22 (TEM & DLS)	Qian et al. 2013
Guignardia Mangiferae	*Citrus Sp*	Silver	417	5-30 (HR-TEM);	Balakumaran et al. 2015
A. tamarii PFL2, A. niger PFR6 and P. ochrochloron PFR8	*Potentilla fulgens L.*	Silver	-	*A. tamarii* PFL2 3.5 ± 3.3 (TEM) followed by *P. ochrochloron* PFR8 7.7 ± 4.3 (TEM) and A. niger PFR6 8.7 ± 6 (TEM)	Devi and Joshi 2015

Epicoccum nigrum	*Helianthemum hirtum*	Silver	440-450	22.5 (HR-TEM)	Mohamed 2015
Aspergillus flavus	*Nothapodytes Foetida*	Zinc sulfate	320-340	18 (TEM); 58.9 (DLS)	Uddandarao and Balakrishnan 2016
Pestalotiopsis microspora	*Gymnema Sylvestre*	Silver	435	2.8 (DLS); 2-10 (TEM)	Netala et al. 2016
Penicillium sp	*Glycosmis mauritiana*	Silver	435	64 (SEM); 18 (XRD)	Govindappa et al. 2016
Alternaria sp.	*Raphanus sativus*	Silver	426	25 (XRD); 10-30 (TEM); 4-28 (AFM); 80 (DLS);	Singh et al. 2017
Cladosporium cladosporioides	*Sargassumwi ghtii*	Gold	540	30-60 (DLS); 60 (XRD)	Joshi et al. 2017
Aspergillus nidulans	*Nothapodytes foetida*	Cobalt oxide	315	10-30 (TEM); 123.8 (DLS); 41.97 (XRD)	Vijayanandan and Balakrishnan 2018
Fusarium solani	*Chonemorpha fragrans*	Gold	510-560	40-50 (DLS)	Clarance et al. 2020
Penicillium citrinum CGJ-C1)	*Tragia involucrata Lin.*	Silver	400	2-20 (HR-TEM)	Danagoudar et al. 2020
C. oxysporum	*C. wightii*	Gold	524	6.76 (XRD); 5-10 (TEM)	Munawer et al. 2020

Nowadays, ZnO is gaining importance in various fields such as UV absorber in textiles, biomedical, antimicrobial, biosensing, dye-sensitized solar cell, catalyst due to its non-toxic nature, high oxidation ability, production of reactive oxygen species, low cost and flexibility in fabrication/synthesis (Lee et al. 2016). However, there is a constant need to develop new synthesis methods to fulfill ZnO nanoparticles' overgrowing demand for the aforementioned applications. Various strategies for nanoparticle synthesis based on the "top-down" and "bottom-up" approaches are well documented (Lee et al. 2016, Kołodziejczak-radzimska and Jesionowski 2014). Moreover, the development of novel strategies that could be better than conventional methods, especially in terms of toxicity and cost, is a significant concern. Biological entities serve as a prominent source of inspiration due to their variety of complex structures and function in the field of material science. Few researchers have reported biosynthesis of ZnO nanoparticles using fungi isolated from soil, zinc mine, rotten fruits and vegetables, as given in Table No. 2.2.

Generally, not all microorganisms can convert precursor salt into nanoparticles due to the secretion of diverse enzymes or proteins or other metabolites. Hence, in this context, the isolation of organisms capable of synthesizing nanoparticles is the foremost challenge. The heavy metal toleration ability of microorganisms plays a significant role in the synthesis of metal and its oxide nanoparticles. Researchers reported the detoxification ability of endophytic fungi and further employed it in nanoparticle synthesis (Table 2.1). The synthesis of nanoparticles was explored through batch studies under optimum reaction conditions. After a typical incubation period, the fungal biomass is separated from the supernatant. Further, the obtained biomass and supernatant are tested for nanoparticle synthesis (Verma et al. 2010; Netala et al. 2016). The addition of precursor salt in the soluble form may get precipitated in the presence of supernatant/fungal biomass, leading to deposition at the bottom of the flask, or color change indicates the synthesis of nanoparticles (Singh et al. 2017). The extracellularly synthesized nanoparticles can be collected by simple centrifugation from the supernatant (Mohamed 2015). However, the intracellularly synthesized nanoparticles are released from the cell wall by either mechanical /chemical /thermal stress. These synthesized nanoparticles are collected and purified through the repetitive cycles of centrifugation/washing with distilled water (Messaoudi and Bendahou 2020) and used for different applications. Thus, nanoscience and endophytic fungi interface has provided a simple route for metal-based multifunctional nanoparticle synthesis with enormous applications.

Aspergillus spp. have been widely explored to synthesize ZnO nanoparticles, as shown in Table 2.2. The synthesized particles from this fungal strain are mostly spherical with varying size distribution. *Aspergillus aeneus* NJP02 synthesizes spherical ZnO nanoparticles with a size of 100-140 nm from TEM analysis. The UV-vis spectra at 375 nm confirmed the synthesis of ZnO nanoparticles (Jain et al. 2013). Oblate spherical and hexagonal ZnO nanoparticles with an average size of 3.8 nm were synthesized using *Aspergillus fumigatus* TFR 8 (Raliya and Tarafdar 2013). Thus, the size and properties of the synthesized ZnO nanoparticles are independent of the fungal species.

Table 2.2 Overview of biological synthesis of ZnO nanoparticles

Organism	Source	Precursor salt	Characteristic [size (nm)]	Application	Reference
A. fumigates TFR-8	Fungi(soil)	Zinc nitrate (0.1mM)	3.8(DLS); PDI 0.335	Phosphorous-Mobilizing Enzyme Secretion and Gum Contents in Cluster bean	Raliya and Tarafda 2013
A. terreus	Fungi (MTCC)	Zinc sulfate (1mM)	54.8-82.6(SEM)	Antifungal	Baskar et al. 2013
Alternaria alternate	Fungi (plant pathogen)	Zinc sulfate (1mM)	40-150(TEM & DLS)	-	Sarkar et al. 2014
A. aenes	Fungi (Zinc mine)	Zinc acetate (1mM)	80-120(TEM)	Photocatalytic degradation of methylene blue	Jain et al. 2014
A. fumigates JCF	Fungi (Vegetable waste)	Zinc sulfate (1mM)	50-60(SEM)	Antimicrobial	Rajan et al. 2016
C. albicans	Fungi	Zinc oxide(1mM)	25(XRD); 15-25(SEM);20(TEM)	synthesis of steroidal pyrazolines	Shamsuzzaman et al 2017

2.3 Biosynthesized ZnO as a photocatalyst

Fujishima and Honda (1972) first reported splitting of water in the presence of UV irradiation (Fujishima and Honda 1972) and after this pioneering work, research in the field of semiconductor photocatalysis for the pollutant degradation has been expanded extensively (Ahmed et al., 2018; Gautam et al. 2020). Generally, photocatalytic degradation is the elimination/removal of environmental pollutants by light-induced redox reactions. The photocatalytic performance of a material is dependentm on the light absorption property, charge separation and transportation on the catalyst surface. The exposure of catalyst surface with photon energy equal to or more than the bandgap energy leads to the transition of electrons from the valence band to the conduction band, leaving behind the holes in the valence band. These formed electrons and holes further generate active radical species leads to oxidation and reduction reaction, thus eliminating the pollutants in an aqueous solution (Sarvanan et al. 2021).

Majorly, chemical-mediated synthesized semiconductor photocatalyst has been used in basic research and practical applications. Recently, researchers started exploring the biologically synthesized metal-oxides for photocatalysis of dyes. The photocatalytic activity of biologically synthesized ZnO nanoparticles was evaluated extensively by using MB as a model pollutant. Further, the researchers have reported the removal of MB, methyl orange (MO), malachite green (MG), rhodamine B (RhB) and reactive yellow (RY), as shown in Table 2.3. Mostly, plant extract-mediated ZnO nanoparticles have been explored for the degradation of dyes. There are very few studies available on ZnO nanoparticles synthesized from fungi, yeast, bacteria and algae. However, researchers have used a higher dosage of nanocatalyst to treat the lower concentration of pollutants. Further, detailed investigation on process parameters such as catalyst loading, pH, and initial pollutant concentration that affected contaminants removal efficiency was not extensively explored.

Singh et al. (2010) first reported biogenic ZnO as a photocatalyst for methylene blue (MB) degradation. They have used *Actinobacter sp.* for ZnO nanoparticle synthesis. The synthesized ZnO nanoparticles were calcinated at 400°C and utilized for the degradation experiment. Almost complete degradation of MB was observed within 30 min under UV irradiation. Protein-capped ZnO nanoparticles synthesized using *Aspergillus sp.* exhibit higher photocatalytic activity than bare nanoparticles for MB degradation (Jain et al. 2014). As surface proteins provide binding sites to accept electron or charge transfer from ZnO nanoparticles, it reduces electron-hole recombination and subsequently increases the degradation rate.

The synthesis and application of ZnO nanoparticles from microbial sources is a less extensively studied approach than plant extract mediated synthesis. Thus, mycosynthesized photocatalyst's utilization to remove contaminants from water directs an exciting research area for environmental clean-up technology.

Table 2.3 Photocatalytic degradation of organic pollutant using biosynthesized ZnO nanoparticles

Biological entity	Light source	Pollutant	Spiked concentration	Catalyst loading	pH	Reaction Time	Efficiency	Reaction Kinetics	Reference
Fungi									
Cordyceps militaris	UV	MB	10ppm	0.25 mg/ml	-	180 min	97%	First-order	Li et al. 2019
Aspergillus sp.	UV	MB	10 μM	10 mg/mL	-	30 min	89.68%	pseudo-first-order	Jain et al. 2014
Bacteria									
Serratia nematodiphila	UV	MO	5ppm	100mg/100ml	-	80 mins	90%	-	Jain et al. 2020
Algae									
Chlorella microalgae	UV	Dibenzothiophene	10 ppm	0.01g	7	180 min	97%	-	Khalafi et al. 2019
Plant extract									
Dolichos Lablab L. Leaf extract	visible and near-UV	MB	5ppm	1g/L	11	210 min	80%	First-order	Kahsay et al. 2019
		RhB	5ppm	1g/L	9	210 min	95%		
		Orange II	5ppm	1g/L	5	210 min	66%		
G. mangostana Fruit pericarp	Solar	MG	10ppm	50mg/50ml	-	180 min	99%	First-order	Aminuzzaman et al. 2018

Coriandrum sativum leaf extract	Solar	RY186	10ppm	20mg/50ml	-	160 min	94%	First-order	Singh et al. 2019
Artocarpus Heterophyllus Leaf extract	UV	Rose Bengal	20ppm	60mg/250ml	8	60 min	85%	L-H	Vidya et al. 2016
Lauris Nobilis Leaf extract	UV	Remazol Red	50mg/l	0.5 g/l	-	45 min	98%	-	Chemingui et al. 2019
Jujube fruit extract	UV	MB	100ppm	15mg/15ml	-	300 min	92%	Pseudo-First-order	Golmohammadi et al. 2020
	Solar	Eriochrome black-T	100ppm	15mg/15ml	-	300 min	86%		
Abutilon indicum Leaf extract	Solar	Acid Black	13mM	0.005g/5ml	-	100 min	100%	-	Khan et al. 2018
L. speciose Leaf extract	Solar	MO	1mg/100ml	0.1mg/10ml	-	100 min	93.5%	-	Saraswathi et al. 2017
Broccoli Leaf extract	UV	MB	5×10^{-5} M	20mg/25ml	-	180 min	74%	Pseudo-first-order	Osuntokun et al. 2019
		Phenol red	5×10^{-5} M		-	180 min	71%		
*Prunus cerasifera Ehrh.*Fruit extract	Solar	Methyl red		15mg/10ml	-	50 min	82.65%	First-order	Jaffri et al. 2018
		Bromophenol blue		15mg/10ml	-	50 min	96.77%		

Trianthema portulacastrum Extract	Solar	Synozol navy blue K-BF dye	10ppm	1.0 g/L	-	150 min	91%	-	Khan et al. 2019
corriandrum sativum leaf extract	UV	Anthracene	25μg/l	1000 μg/l	7	240 min	96%	Pseudo-first-order	Hassan et al. 2015

2.4 Photocatalytic degradation of organic pollutant

The reaction parameters such as pH, catalyst loading and pollutant concentration affect the efficiency of the photocatalysis process.

2.4.1 pH of the reaction mixture

The efficiency of photocatalytic degradation can be enhanced by altering the pH of the reaction mixture. This is because pH influences the adsorption of pollutants on the ZnO nanoparticles surface, which is a crucial step in photocatalytic degradation (Wang et al. 2010; Bechambi et al. 2015). Table 2.4 represents the effect of pH on photocatalytic degradation of organic pollutants. The point of zero charge (pzc) of ZnO is around 8 (Ravichandran et al. 2007; Palominos et al. 2009). Due to the amphoteric nature of ZnO, its surface remains positively charged in an acidic medium (pH < 8) and negatively charged in an alkaline medium (pH > 8).

The change in pH affects the formation of the hydroxyl radicals by the reaction between hydroxide ions and positive holes. The positive holes are the predominant oxidation species at low pH, whereas, at neutral or high pH levels, hydroxyl radicals act as the major species (Palominos et al. 2009). Hydroxyl radicals are easily generated in alkaline pH by oxidizing more hydroxyl ions available on the ZnO surface resulted in an increase in the efficiency of the process (Tao et al. 2012). Similar results have been shown in the degradation of tetracycline using ZnO nanoparticles (Palominos et al. 2009). However, it should be noted that in alkaline pH, there is Coulombic repulsion between the negatively charged surface of photocatalyst and the hydroxide anions. This would prevent the generation of hydroxyl radicals and thus decrease the photodegradation. Hence, it is essential to optimize the pH of the reaction medium to attain the highest photocatalytic degradation.

Table 2.4 Effect of pH on photocatalytic degradation of pollutants

Pollutant	Catalyst	Light source	pH Range	Optimum	Reference
BPA	Lanthanum-ZnO	UV	2, 8, 11	8	Selvam et al., 2013
17α-ethinylestradio	CuO	Visible	7, 8, 10	7	Mukherjee et al. 2017

Pollutant	Catalyst	Light source		Reference
nonylphenol and 2,4-dinitrophenol	e-hexacyanocobaltates	Solar	2-11	7	Rani et al. 2020
Catechol	ZnO	UV	3-11	3	Bazrafshan et al. 2019
2–chlorophenol	Ag-TiO$_2$	UV	4.11, 7.05 ,10.5	10.5	Onkani t al. 2020

2.4.2 Catalyst loading

The photocatalytic reaction rate increases with the catalyst loading, but after the particular loading of the catalyst, the reaction rate decreases and becomes independent of catalyst loading (Rajmanickam and Shanthi 2012; Pham et al. 2020). Table 2.5 displays the effect of catalyst loading on photocatalytic degradation of organic pollutants. The catalyst amount has both positive and negative impacts on the photodegradation rate. The enhancement of the degradation rate with an increase in catalyst loading has been attributed to (i) an increase in the number of pollutant molecules adsorbed, with the increase in the amount of catalyst loading. Catalyst addition increases the active sites for pollutant adsorption on the photocatalyst surface as well as the free hydroxyl radical (.OH) generation (Bechambi et al. 2016) (ii) increase in the density of particles in the area of illumination (Lee et al. 2016).

A higher amount of catalyst may not be helpful as it may lead to aggregation as well as reduced irradiation field due to an increase in light scattering (Neppolian et al. 2002). Furthermore, the degradation rate may decrease due to the loss in surface area available for light-harvesting affected by agglomeration (particle-particle interactions) at high solid concentrations. Thus, to avoid the excess catalyst and increase photons absorption capacity, optimum catalyst loading is necessary.

Table 2.5 Effect of catalyst loading on pollutant degradation

Pollutant	Catalyst	Light source	Catalyst loading range (g/L)	Optimum (g/L)	Reference
2,6-dimethylphenol	CuO-clinoptilolite	Visible	0.1-0.4	0.25	Soori et al. 2018

nonylphenol ethoxylate	g-C$_3$N$_4$/BiVO$_4$	Visible	0.1-1	0.5	Dong et al. 2020
dibutyl phthalate	Fe$_2$O$_3$	Solar	0-0.04	0.03	Liu et al. 2018
BPA	g-C$_3$N$_4$/ZnO	UV	0.2-0.8	0.8	Garg et al. 2020
Cephalexin	ZnO	Solar	0.02-0.08	0.02	He et al. 2019
2–chlorophenol	Ag-ZnS	UV	0.005, 0.0075, 0.001125	0.005	Onkani t al. 2020
BPA	Cu/BiVO$_4$ /g-C$_3$N$_4$ p	Solar	0.2-0.6	0.4	Lee et al. 2020
p-NP	silver	Solar	0.125-1	0.5	Samuel et al. 2019

2.4.3 Pollutant concentration

Initial pollutant concentration is a significant parameter in photocatalytic degradation. Table 2.6 shows the effect of initial pollutant concentration on photocatalytic degradation of organic pollutants. It was observed that the increase in concentration leads to a decrease in degradation efficiency (Pham et al. 2020). This may result from an increase in the initial concentration, leading to a decrease in the path length of the photons entering the solution due to the impermeability of the pollutant (Neppolian et al. 2002). Further, the increase in initial pollutant concentration leads to decreased production of reactive radical species as the active sites of the catalyst are covered by pollutant molecules and, in turn, affect the catalytic efficiency. Hence, the initial concentration of pollutants needs to optimize to attain the highest degradation efficiency.

Table 2.6 Effect of initial pollutant concentration on photocatalytic degradation of organic pollutants

Pollutant	Catalyst	Light source	Pollutant concentration range (mg/L)	Optimum	Reference
BPA	Cerium-ZnO	Solar	10-30	10	Kamraja et al., 2014

BPA	g-C$_3$N$_4$/MoS$_2$-PANI	Visible	20-60	20	Ahamad et al. 2020
p-NP	TiO$_2$/CS	Visible	30-50	30	Afzal et al. 2019
2–chlorophenol	Ag-ZnO	UV	8,20,50	8	Onkani t al. 2020
BPA	g-C$_3$N$_4$/ZnO	UV	10-40	30	Garg et al. 2020
p-NP	Silver	Solar	5-40	35	Samuel et al. 2019

2.4.4 Degree of mineralization

The degradation of pollutants leads to the conversion of organic carbon into gaseous CO_2. During the photocatalysis process extent of mineralization attained is generally assessed by total organic carbon (TOC) and chemical oxygen demand (COD) (Aljuboury et al. 2017). Generally, the mineralization of organic pollutants during the photocatalysis process is evidenced by a decrease in TOC and COD with an increase in irradiation time. The COD is widely used as an effective technique to measure the organic strength of wastewater by analyzing the total quantity of oxygen required for the oxidation of organic matter to CO_2 and water (Sakhtivel et al. 2003).

A small decrease in TOC or COD values may be due to the decomposition of pollutant molecules to lower molecular weight compounds and a sharp decrease corresponds to oxidation of most stable compounds, which indicates the complete mineralization of intermediates (Bechambi et al. 2015). Therefore, TOC and COD must be carried out to check the degree of mineralization of pollutants.

2.4.5 Scavenging experiment

Generally, superoxide (O_2^-) are the most reactive oxygenated species involved in the photocatalytic degradation of organic pollutants (Stylidi et al. 2004). However, recent findings revealed that some photocatalytic degradation reactions are favored mainly by hydroxyl radicals (•OH) and hole (h^+) rather than superoxide radicals (Huang et al. 2018). Table 2.7 represents the active species involved in the photocatalytic degradation of various

organic pollutants. Yan et al. (2010) reported that the utilization of the same photocatalyst for different pollutants might result in different photocatalytic performances depending on the generation of active species. Thus, when exposed to light, the photocatalyst generates radicals that will favor the degradation process. Therefore, it is necessary to find out the active radicals species involved in photocatalytic degradation.

Table 2.7 Active species involved in the photocatalytic degradation of organic pollutants

Pollutant	Catalyst	Light source	Scavenger	Active species	Reference
RhB	$ZnIn_2S_4$	Visible light	benzoquinone	O_2^-	Liu et al. 2017b
Carbamazepine	$CuWO_4$-TiO_2	Visible light	Isopropyl alcohol	$\cdot OH$	Anucha et al. 2021
Methylene blue	TiO_2	UV light	Terephtalic acid	h^+	Hou et al. 2018
Tetracycline	Ag_2O/AgBr–CeO_2	Visible light	benzoquinone	O_2^-	Su et al. 2021
Methylene blue	ZnO	UV light	benzoic acid	$^\bullet OH$	Alsheri et al. 2019
Acetaminophen	Ag_2S-ZnO@rGO	Visible light	EDTA–2Na	h^+	Khavr et al. 2019
Atrazine	Cu-ZnO/g-C_3N_4	Visible light	Potasiium iodide	h^+	Truc et al. 2019
methyl orange					Chen et al. 2017
Congo red	ZnO	UV light	benzoquinone	O_2^-	
Direct black					

2.4.6 Identification of intermediates, degradation products and the degradation pathway

Radical species react nonselectively with organic compounds leads to the generation of various by-products in a broad range of concentrations. Moreover, the formation of by-products during and at the end of the degradation process was found to be

inevitable (Di Paol et al. 2003; Lin et al. 2020b). Consequently, assessment of by-products is the crucial factor to optimize and maximize the treatment process. In the degradation studies, the analytical evaluation depends on the disappearance of initial pollutant concentration by UV analysis combined with TOC and COD analysis (Sakhtivel et al. 2003, Neppolian et al. 2002). However, the data from the above analysis techniques are not sufficient to treat real waters or commercial organic pollutant formulations due to the presence of other sources of ions and organic compounds. Moreover, such a treatment process leads to the generation of toxic compounds at low concentrations. Therefore, there is a substantial need to determine the specific compounds produced during photocatalytic degradation. Identification of intermediates and degradation products is crucial for the large-scale application of the photocatalysis process. Further, it can be used to evaluate the kinetics of formation and decomposition of the by-products (Ding et al. 2016; Rani and Shanker 2018; Lin et al. 2020a).

Several analytical techniques such as high-performance liquid chromatography (HPLC) (Paola et al. 2003), gas chromatography-mass spectroscopy (GC-MS) (Ding et al. 2016; Rajmanickam and Shanthi 2012) and liquid chromatography-mass spectroscopy (LC-MS) (Eltoukhy et al. 2020) were used for the determination of degradation pathway. Herrmann et al. (1999) reported the advantages of LC-MS techniques over the GC-MS and HPLC to determine intermediate products. Moreover, the presence of atmospheric pressure ionization (API), LC-MS interfaces, such as atmospheric-pressure chemical ionization (APCI) and electrospray (ES), which provide structural information and sensitivity, overcome the limitations of other interfacing LC-MS devices. This allows the identification of highly polar, less volatile and thermally labile compounds, as well as direct analysis of the water samples, avoiding the possibility of polar by-products escaping or modifying their relative concentration due to the extraction procedures applied. Therefore in this study, the identification of intermediates and products produced during photocatalysis was carried out using LC-MS analysis.

2.5 Detection of organic pollutants
2.5.1 Fluorescence mechanism of ZnO

The fluorescence of ZnO nanoparticles generally contains the exciton-related ultraviolet emission and the defect-related visible emission. Further, the visible emission depends on the synthesis routes, surface defects, size, shape, deep levels and vacancies. Zinc vacancies, zinc interstitials, oxygen vacancies, oxygen antisite and oxygen

interstitials resulted in the origin of violet, blue, orange, green and yellow emissions of ZnO nanoparticles (Raji and Gopchandran 2017; Galdámez-Martinez et al. 2020). Table 2.8 represents the various fluorescent mechanisms of ZnO nanoparticles. Guell et al. (2019), reported ZnO nanowires synthesized by vapor transport method exhibits green, yellow and red emission bands at around 520, 590 and 720 nm, respectively. The transition of electrons from extended zinc interstitials states below the zinc interstitials to the valance band resulted in blue emissions (Zheng et al. 2010). However, zinc and oxygen vacancies lead to the green emission band (Leung et al. 2013), while oxygen and zinc interstitial leads to the yellow and orange emission bands (Raji and Gopchandran 2017).

Table 2.8 Overview of fluorescence mechanism of ZnO nanoparticles

Sr. No.	Material	Size (nm)	Excitation (nm)	Emission (nm)	Fluorescent mechanism	Reference
1.	ZnO	-	390	440	zinc interstitials	Zeng et al. 2010
2.	ZnO	7.4	365	530	Surface defects	Cheng et al. 2021
3.	ZnO	250	380	500	Zinc vacancy	Fabbri et al. 2014
4.	Zno	9	350	425	Surface defects	Zhao et al. 2012
5.	ZnO	5	365	565	Interstitial oxygen	Zhao et al. 2014
6.	ZnO nanorods	100-150	380	500	Oxygen vacancy	Acgour et al. 2019

Alteration in fluorescence intensity of QDs due to fluorescence resonance energy transfer (FRET) (Tang et al. 2008), electron transfer (ET) (Singh et al. 2014), or other interactions (Cao et al. 2014) occurring on the quantum dots surface may be responsible for the sensing mechanism of the system. Further, the primary inner filter effect (IFE) can occur effectively only when the absorption spectrum of an analyte completely overlaps with an excitation spectrum of a fluorophore, and secondary IFE occurs when an absorption spectrum of an analyte overlaps with the emission spectrum of a fluorophore (Khan et al.

2018). Fluorescence quenching is a process in which the fluorescence intensity of a compound can be decreased by the molecular interaction, including energy transfer, molecular rearrangements and ground or excited state complex formation. The static quenching resulted due to the formation of the ground state non-fluorescent complex between the fluorophore and quencher. Whereas dynamic quenching resulted due to the collision of excited state fluorophore and a ground-state quencher. So, the difference between static and dynamic quenching is the sequence of excitation and complex formation, while the physical bases of the two quenching mechanisms are the same. Thus, molecular contact between the fluorophore and quencher is a prerequisite for static and dynamic quenching (Lakowicz 2006, Gaviria-Arroyave et al. 2020). The process involving the formation of an excited-state complex known as dynamic quenching is described by the Stern-Volmer equation (1), and the quenching leading to a ground-state complex formation between an analyte and fluorophore is referred to as static quenching and it is described by Lineweaver-Burk equation (2) (West 2017; Mao et al. 2017),

$$\frac{F_0}{F} = K_{SV}[Q] + 1 \tag{1}$$

$$\frac{1}{(F_0 - F)} = \frac{1}{F_0} + \frac{K_{LB}}{F_0[Q]} \tag{2}$$

where Ksv is Stern-Volmer constant, K_{LB} is Lineweaver-Burk constant, and Q is quencher concentration. F_0 and F represent the fluorescence intensities of functionalized ZnO QDs in the absence and presence of analyte, respectively

2.5.2 Fluorescence mediated detection of organic pollutants

The "on-site" detection of organic pollutants is one of the promising areas in water treatment. The ultralow concentration of pollutants and their separation from the aqueous phase are significant challenges in detecting organic pollutants. Furthermore, the reproducibility and exact quantification of contaminants are critical points in detecting pollutants (Moliner-Martínez et al. 2015). Therefore, developing a relatively simple, rapid and pretreatment-free analytical method with a lower detection limit is necessary. Fluorescence-based sensors offer rapid and real-time detection of organic pollutants using various nanostructures (Cialla-May et al. 2020). Table 2.9 represents the fluorescence-mediated detection of various contaminants. Nanomaterials exhibit excellent physicochemical properties, high surface-to-volume ratio and unique optoelectronic properties, enabling them to manufacture economically viable and portable fluorescent devices.

Table 2.9 Fluorescence mediated detection of organic pollutants

Analyte	Fluorophore	Linear range	Sensitivity (LOD)	Detection mechanism	References
2,4,6-Trichlorophenol	MIP-ZnO QDs	0–160 µmol/L	0.083 µmol/L	Dynamic quenching	Lin et al. 2018
Picric acid	Nitrogen-doped carbon dots	0.5–30 µmol/L	0.041 µmol/L	FRET	Wang et al. 2018
o-nitrophenol			0.05 µM	Electron transfer amd inclusion complex formation	
m-nitrophenol			0.3 µM		
p-nitrophenol	β-CD-CdTe QDs		0.05 µM		Zhang et al. 2015a
		20-100 µM			
Ornidazole	Graphene QD-SMIP	0.75 - 30 µM	0.24 µM	photo-induced electron transfer	Mehrzad-Samarin et al. 2019
BPA	Manganese doped ZnS QDs-MIP	10-700 ng/ml	8.036 ng/ml	Electron transfer	Zhang et al. 2015b
Tetracycline	Europium-doped CdTe QDs	0–80 µM	2.2 nM	Electron transfer	Han et al. 2020
Phosphate	MOF with ZnO QDs	0.5–12 µM	53 nM	Electron transfer	Zhao et al. 2014

Thioacetamide	ZnO QDs	200–1000 μM	2.14 nM	Electron transfer	Saha and Negi 2018
2,4,6-trinitrotoluene	L-cystene-capped CdTe QDs	10 nM–8 μM	3.3 nM	Electron transfer	Qian et al. 2016
Dopamine	ZnO-associated carbon dots	180 nM to 15 μM	1.06 nM	Electron transfer	Jana et al. 2019
Dopamine	Carbon quantum dots	0.2 mM - 100 mM	0.2 mM	Electron transfer	Bharathi et al. 2018
Chlorine	ZnO QDs	0.05–0.7 μM	0.041 μM	Electron transfer	Singh and Mehta 2016
Dimethoate	MIP-coated ZnO QDs	0.02–3.2 mg/L	0.006 mg/L	Dynamic quenching	Vahid 2017
Amoxicillin	MIP-CdTe QDs	0.20–50.0 μg/L	0.14 μg/L	Dynamic quenching	Chullasat et al. 2018

2.6 Scope and objectives of the study

Majorly, chemical-mediated synthesized semiconductor photocatalyst has been used in basic research and practical applications. Based on a detailed literature survey, there is a constant need to synthesize biocompatible, less toxic and environmentally benign material for the application in water clean-up technology. The biosynthesized ZnO nanoparticles can be considered as an efficient photocatalyst for the degradation of endocrine disruptors by avoiding electron-hole recombination due to the presence of protein capping on nanoparticles surfaces. The fluorescence property of ZnO nanoparticles can be explored for the detection of p-NP and BPA.

The following are the specific objectives:

1. To isolate, identify, and screen zinc metal tolerant endophytic fungi from a medicinal plant, *Nothapodytes foetida.*

2. To optimize the synthesis of ZnO nanoparticles by an endophytic fungal species.

3. To study the structural, morphological, and optical characteristics of the nanoparticles.

4. To analyze the various reaction parameters such as the effect of catalyst concentration, initial concentration, pH on degradation of p-NP and BPA, and their reaction kinetics.

5. To study the photocatalytic mechanism involved in the degradation of p-NP and BPA and their cytotoxicity study.

6. To study the detection characteristic of BPA and p-NP by biologically and chemically synthesized ZnO nanoparticles.

2.7 Organization of the thesis

The research study is presented and explained in five chapters.

Chapter 1 introduces the scenario of the endocrine disruptor, BPA and 4-NP in terms of its toxicity, stability and distribution in the ecosystem. A detailed explanation was given for the utility of the nanocatalyst for effective wastewater treatment.

Chapter 2 gives an extensive literature review related to the synthesis of nanoparticles, their properties and potential applications. Further, the studies on the detection and degradation of BPA and 4-NP were discussed. It also outlines the main objectives of the current work and concludes with the scope of the work. Based on the detailed literature review, the scope and objectives of the present work are outlined.

Chapter 3 describes the detailed methodology used in this research work to accomplish the stated objectives.

Chapter 4 is a compilation of the outcomes of the research methodologies for the synthesis of nanoparticles by biological and chemical method, its characterization, undertaking synthesis mechanism, and application of nanoparticles for the detection and degradation of BPA and p-NP with the support of relevant literature.

Chapter 5 provides a summary of the entire investigation and direction for future research work.

CHAPTER 3

RESEARCH METHODOLOGY

The current chapter deals with the materials used, the description of the experimental methodologies and the analytical procedures adopted to attain the stated objectives.

3.1 Biological synthesis of ZnO

3.1.1 Isolation and identification of zinc metal tolerant endophytes

Healthy leaves of the medicinal plant *Nothapodytes foetida* were collected from Agumbe forest, Western Ghats, Dakshin Kannada, India (Fig. 3.1 a and b). The leaves were collected using a sterile scalpel and stored in a sterile bag. Isolation of endophytes was carried out with a slight modification of procedure, as demonstrated (Musavi and Balakrishnan 2013). Briefly, collected leaves were washed under running tap water to remove the dust particles. Then, the leaves were surface sterilized successively with 75 % ethanol (Changshu Hong sheng Fine Chemical Co. Ltd., China; ≥ 99% Purity) for 1 min, 2.5 % sodium hypochlorite (Loba Chemie Pt. Ltd., India) for 10 min, and again with 75 % ethanol for 1 min.

Further, the surface-sterilized leaf segments were kept on a potato dextrose agar (PDA) plate (HiMedia, India) supplemented with chloramphenicol (Sigma-Aldrich, USA). And incubated at 28 ± 1 °C under dark conditions and monitored periodically for endophytic fungal growth. The periodic sub-culturing of the fungal isolate was performed at a regular interval of 3 weeks to replenish the nutrients. Further, each fungal isolate was selected and purified by repetitive subculturing and subjected to a metal tolerance study.
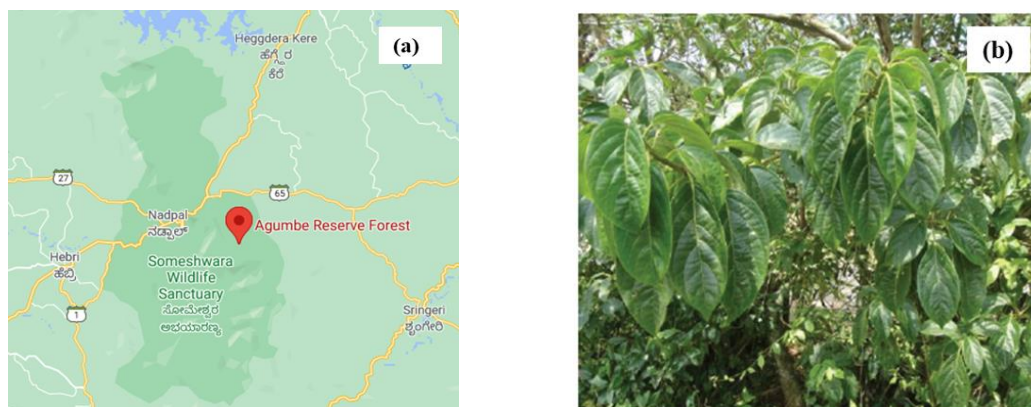
Fig. 3.1 (a) Sampling site location and (b) leaves of *Nothapodytes foetida*

Tolerance index (TI) study was carried out with each pure endophytic fungal isolates (FI) (4 days old) on a PDA plate (two replicates) supplemented with 2 mM zinc acetate (Sigma-Aldrich, USA; ≥ 99% Purity) incubated at 28 °C for 5 days along with control (without added metal salt). TI was calculated by measuring the colony diameter (in millimeters) of the FI exposed to metal salt divided by the colony diameter of FI in the control plate (Valix and Loon 2006). The greater TI value displays a high level of resistance.

Primary identification of endophytic fungal isolate showing the highest TI was accomplished based on colony characteristics and further sent to Agharkar research institute, Pune, India, for 16s rDNA-based molecular identification. The obtained 16s rDNA ITS sequence was subjected to a basic local alignment search tool-nucleotide (BLAST-n) algorithm to obtain the closest phylogenetic match with the GenBank database by using the BLASTn algorithm (http://blast.ncbi.nlm.nih.gov/Blast.cgi) on the national center for biotechnology information (NCBI) site. Further, the obtained sequence was saved in fast adaptive shrinkage threshold algorithm (FASTA) format and aligned by multiple sequence alignment using ClustalW and a molecular evolutionary genetic analysis (MEGA) file was constructed. Finally, the obtained MEGA file was used to construct a phylogenetic tree based on the neighbour-joining bootstrap method using MEGA-X software.

A maximum tolerance concentration (MTC) assay was also performed to determine the zinc metal tolerance profile of the fungal isolate. 5 mm disks from the 4-day old culture of FI were inoculated into PDA (two replicates) supplemented with increasing concentration of zinc acetate (0.5 mM to 15 mM). In parallel, fungal culture without zinc acetate was used as a control. The inoculated plates were incubated at $28 \pm 1 \,^\circ C$ in the dark for 8 days. The radial growth was evaluated by measuring the colony diameter. The initial diameter of the inoculated portion was subtracted from the growth diameter. The maximum concentration of zinc acetate, which allowed the growth of fungal isolate, was considered as MTC.

3.1.2 Selection of broth media

The isolated fungus was grown in various broths such as nutrient broth (NB), sabouraud dextrose broth (SDB), potato dextrose broth (PDB), and malt glucose yeast extract peptone broth (MGYP) to identify the appropriate growth media (three replicates). All the growth media were purchased from HiMedia, Mumbai, India. The fungal spores

from 4 days old culture were inoculated into 100 mL of respective media in 250 mL Erlenmeyer flasks and incubated at 28 ± 1 °C for 96 h on a rotary shaker (150 rpm) under dark conditions.

The growth characteristics of the fungal isolate were studied in terms of dry biomass weight (g/L) and protein concentration (mg/mL) (three replicates). Lowry Protein Assay (Lowry et al. 1951) was performed to estimate the amount of protein present in different media by keeping bovine serum albumin (BSA) (Sigma-Aldrich, USA) as a standard protein and expressed in terms of mg/mL. Standard curve was prepared with the BSA concentration in the range of 0, 0.05, 0.1, 0.15, 0.2, 0.25, 0.3, 0.4, 0.5, 0.6, 0.7, 0.8, 0.9 and 1 mg/mL (Fig. 3.2). Solution A was prepared by adding 2 % (*w/v*) sodium carbonate (Sigma-Aldrich, USA; ≥ 99.5% Purity) in 0.1 N sodium hydroxide (NaOH) (Loba Chemie Pt. Ltd., India; ≥ 98%) and solution B was prepared by adding 0.5 % (*w/v*) copper sulfate (Sigma-Aldrich, USA; ≥ 99% Purity) in 1 % sodium potassium tartarate (Sigma-Aldrich, USA; ≥ 99%). Lowry solution was prepared by adding 23 mL of solution A and 2 mL of solution B. For Lowry assay, 0.1 mL of the test sample was diluted to 1 mL using ultrapure water and 5 mL of Lowry solution was added and incubated in a boiling water bath for 10 min. Further, a solution was cooled at room temperature and 0.5 mL of Folin reagent (Sigma-Aldrich, USA) was added to this and kept for 30 min in the dark at room temperature. The total protein present in the sample was analyzed by measuring the absorbance (at 660 nm) of the end product of the Folin reaction against the BSA standard curve.
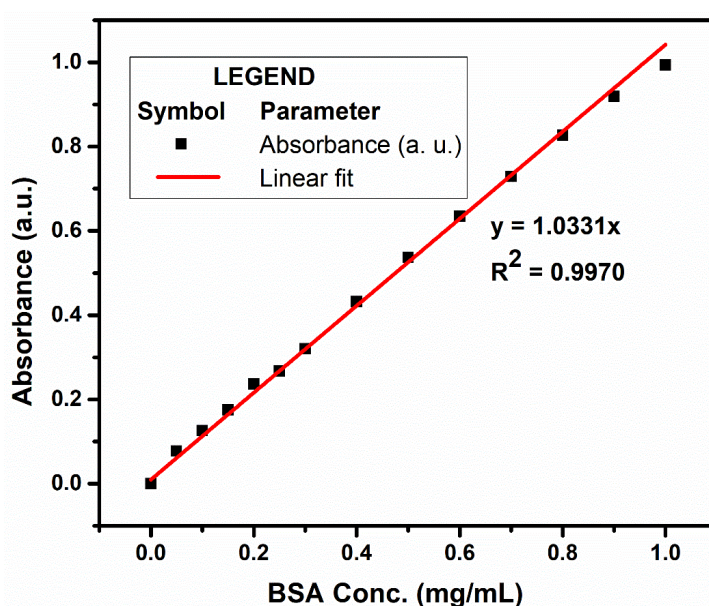
Fig. 3.2 Calibration curve for BSA protein

3.1.3 Growth analysis of *C. geniculatus* in MGYP media

The fungal spores from 4 days old culture were inoculated into 100 mL of MGYP media in a 250 mL Erlenmeyer flask and incubated at 28 ± 1 °C for 96 h on a rotary shaker under dark conditions for their growth and development. The growth of fungal isolate was observed by measuring fresh weight and dry weight at every 24 h intervals. For each experimental data, three replicates were taken for concordance.

3.1.4. Optimization of physicochemical parameters for the biosynthesis of ZnO nanoparticle

Fungal isolate was inoculated in 100 mL of optimized media in 250 mL of Erlenmeyer flask and maintained at 28 ± 1 °C for 72 h in an incubator shaker (150 rpm) (Lead instruments, India). Further, the fungal biomass was collected by centrifugation and media components were removed by repeated washing with sterile ultrapure water. Approximately 10 g of fungal biomass was transferred to 100 mL of sterile ultrapure water and subsequently incubated under the above-mentioned conditions for 72 h. The mycelial free filtrate was obtained by separating fungal mycelial biomass by centrifugation. Further, it was brought in contact with precursor salt to synthesize ZnO nanoparticles and kept at 28 ± 1 °C for 72 h in an incubator shaker. The experimental flask (flask b) along with a set of positive (flask a) and negative controls (flask c) in three replicates were used to judge the nanoparticle synthesis. The positive control contains precursor salt with protein-free filtrate and the negative control contains filtrate without precursor salt.

The different reaction parameters, such as precursor salt and its concentration, pH and incubation time, were identified as factors affecting the formation of ZnO nanoparticles. The one-factor design method was used to optimize reaction conditions to synthesize ZnO nanoparticles. To perform a one-factor design, one independent variable was varied at a time (OVAT) and the remaining variables were kept constant. The effect of various precursor salts viz. zinc acetate dihydrate ($Zn(CH_3CO_2).2H_2O$), zinc sulfate heptahydrate ($ZnSO_4.7H_2O$) (Sigma-Aldrich, USA; ≥ 99%) and zinc nitrate hexahydrate ($ZnNO_3)_2.6H_2O$ (Sigma-Aldrich, USA; ≥ 99%) on the synthesis of ZnO nanoparticles was studied. The effect of varying concentrations (1 mM, 10 mM, 20 mM, 30 mM, 40 mM, and 50 mM) of selected precursor salt on ZnO nanoparticle formation was studied. The duration of the reaction was maintained at 72 h. Further, the effect of incubation time (0 h, 24 h, 48 h, and 72 h) on ZnO nanoparticle formation was examined by keeping the reaction mixture

at the above-optimized precursor salt and its concentration. The formation of ZnO nanoparticles at different reaction pH was studied by maintaining the reaction pH at 6, 7, 8, 9, 10, 11, and 12. The pH of the reaction mixture was adjusted using 0.1 N hydrochloric acid (HCl) (Loba Chemie Pvt. Ltd., India; 35% Purity) or 0.1 N NaOH.

3.1.5. Purification of proteins and sodium dodecyl sulfate-polyacrylamide gel electrophoresis (SDS-PAGE) analysis

Extracellular proteins present in the aqueous mycelial free filtrate were purified by ammonium sulfate precipitation. The ammonium sulfate (Merck, Germany) was added gradually to the filtrate at a final concentration of 80 % (*w/v*) and stirred overnight at 4 °C (Green and Hughes 1955). The subsequent protein precipitate was obtained by 20 min centrifugation (Kubota Corporation, Japan) at 13,300×g (4 °C). The resulting protein pellet was resuspended in an ample volume of 50 mM phosphate buffer (pH 7.2) (Loba Chemie, India) and subsequently dialyzed using a 12 kDa cut-off dialysis bag (Sigma-Aldrich, USA). The dialysis bag was stirred slowly at 4 °C and the buffer was changed 3 times over a 24 h period. The dialyzed portion was examined by SDS-PAGE (Laemmli, 1970).

6 % stacking gel was prepared using 30:0.8 % acrylamide and bisacrylamide, 1 M Tris-HCl (pH 6.8), 20 % SDS (Merck, Germany), 10 % ammonium persulfate (APS) and TEMED. 12 % separating gel was prepared by using 30:0.8 % acrylamide and bisacrylamide, 1 M Tris-HCl (pH 8.8), 20 % SDS, 10 % APS and TEMED. 25 % glycine, 20 % SDS, 5 % β-mercaptoethanol, 0.1 % bromophenol blue was used for the preparation of 3× sample loading dye. All the chemicals were obtained from Sigma-Aldrich, USA.

The proteins acting as capping agents on the surface of ZnO nanoparticles were identified by treating the sample with 1 % SDS for 10 min and subsequently centrifuged for 10 min at 8500×g to obtain the supernatant containing detached proteins. Nanoparticles untreated with 1 % SDS were used as a control. Further, samples were denatured in 3X Laemmli's dye and heated for 5 min and centrifuged for 1 min at 8500×g (4 °C). The pre-stained molecular weight marker (HiMedia, India) was run on 12 % SDS-polyacrylamide gel along with the samples using the Bio-Rad Mini-Protean gel system (Bio-Rad, USA) at a constant voltage of 70 kV for 2.5 h. Further, the gel was stained with Coomassie brilliant blue dye (Thermo Fisher Scientific, US) and examined for the appearance of protein bands.

3.2 Chemical synthesis of ZnO
3.2.1 Preparation of β-CD@ZnO QDs

Zinc acetate dihydrate, 109.7 mg, was dissolved in 25 mL of ethanol to obtain 0.02 M of zinc precursor solution and 59.99 mg NaOH was dissolved in 5 mL of ethanol to obtain 0.3 M of NaOH solution separately under ultrasonication for 1 h. The obtained NaOH solution was further added dropwise to zinc acetate precursor solution under the vigorous stirring condition for 1 h at room temperature to obtain ZnO suspension. The suspension thus obtained from the mixture was centrifuged at 13300×g at 4 °C for 20 min. Further, an obtained white precipitate (ZnO) was washed thoroughly by ethanol to remove the unreacted compounds. The precipitate was resuspended in 20 mL of ethanol and agitated to attain uniform dispersion. For functionalization with β-CD (Sigma-Aldrich, USA; ≥ 97%), 0.05 mmol of β-CD in 10 mL of ethanol was added to 20 mL of dispersed ZnO solution. Subsequently, 0.5 mL of ultrapure water was swiftly added to initiate the functionalization reaction. The reaction mixture was stirred for 2 h at room temperature, and the contents were subjected to centrifugation. The precipitate obtained after centrifugation was repeatedly washed with ethanol and water to remove the unreacted components. Lastly, the β-CD-functionalized ZnO QDs were redispersed in ultrapure water for further analysis.

3.2.2 Preparation of APTES@ZnO QDs

ZnO QDs were synthesized by adding 0.02 M of zinc acetate to 25 mL of ethanol and 0.3 M of KOH (Loba Chemie Pt. Ltd., India; ≥ 98% Purity) in 5 mL of ethanol separately under ultra-sonication for 60 min. Further, KOH was added dropwise to zinc acetate solution under vigorous stirring for 60 min at room temperature. After centrifugation at $13300 \times g$ (4°C) for 15 min, the obtained white precipitate was dispersed in 20 mL of ethanol under ultra-sonication. Further, 0.5 g of APTES (Sigma-Aldrich, USA; ≥ 99% Purity) in 5 ml of ethanol was added dropwise to the 20 mL ZnO QDs solution under vigorous stirring. Subsequently, 0.2 mL of deionized water was quickly added to the system under stirring. The reaction mixture was kept under constant stirring at room temperature for 60 min. The precipitate was obtained by centrifugation at $13300 \times g$ (4°C) for 15 min, which was further washed with ethanol three times to remove unreacted components. Finally, the white precipitate of APTES@ZnO QDs obtained was redispersed in 30 mL of deionized water under ultra-sonication and agitation for further studies.

3.3. Characterization of ZnO nanoparticles

The synthesis of ZnO nanoparticles was observed by measuring the absorbance spectra between 200-800 nm on the UV-vis spectrophotometer (Thermo Scientific Genesys 10S, USA). The effective mass approximation equation was used to calculate the size of synthesized nanoparticles which exhibits the relationship between the radius of nanocrystals (R) and their bandgap (E) as given below in Eq. (3),

$$E = E_g + \frac{h^2\pi^2}{2R^2}\left(\frac{1}{m_e} + \frac{1}{m_h}\right) - \left(\frac{1.8e^2}{\mathcal{E}R}\right) \qquad (3)$$

where E_g is the bandgap of the bulk material (3.3 eV), h is the reduced Planck's constant, m_e and m_h are effective masses of the electrons and holes, respectively, and is given by; $m_e = 0.26m_o$ and $m_h = 0.59m_o$. Where m_o is the free electron mass, e is the charge of the electron, $\mathcal{E}$ is the semiconductor dielectric constant (Prabhu et al. 2013; Aboulaich et al. 2012). A derivative of absorbance was used to estimate band gap energy (Darroudi et al. 2014).

The phase and purity of synthesized ZnO nanoparticles were checked using x-ray diffraction (XRD) spectroscopy (Rigaku MiniFlex 600, Japan) with CuKα radiation (λ= 1.54060 Å). The lattice parameter geometry equations 4, 5, 6, and 7 (Cullity and Stock 2001) were used for the evaluation of lattice parameters (a,c), d spacing, and unit cell volume (V) of ZnO nanoparticles.

$$\frac{1}{d^2} = \frac{4}{3}\left(\frac{h^2+k^2+hk}{a^2}\right) + \frac{l^2}{c^2} \qquad (4)$$

$$a = \frac{\lambda}{\sqrt{3}sin\theta_{100}} \qquad (5)$$

$$c = \frac{\lambda}{sin\theta_{002}} \qquad (6)$$

$$V = \frac{\sqrt{3}a^2c}{2} \qquad (7)$$

where h, k, and l are Miller indices.

The surface topography of ZnO nanoparticles was revealed using a field emission-scanning electron microscopy (FE-SEM) (Carl Zeiss Sigma) instrument operated at 5 kV. The purity and elemental analysis of the ZnO nanoparticles were analyzed using energy dispersive x-ray analysis (EDX) (Oxford instrument) combined with FESEM. A dynamic light scattering study was performed to evaluate the zeta potential (Nano ZS 90, Malvern, UK), and their optical properties were analyzed using a Horiba Fluromax-4 spectrofluorometer. The morphological analysis, such as size and shape, was carried out by the high-resolution transmission electron microscopy (HRTEM) (JEOL/JEM 21000, USA).

Moreover, the interpretations from the XRD data were correlated using the selected area electron diffraction (SAED) pattern.

The presence of functional group and capping on ZnO nanomaterial were determined by Fourier transform infrared spectroscopy (FTIR) (Thermo Nicolet Avatar 370). The spectroscopic studies were carried out under KBr mode at ratio 1:100 and scanned (range $400 - 4000$ cm^{-1}) with 4 cm^{-1} resolution.

3.4 pH$_{pzc}$ determination

The pH at which the net charge of the particle surface is zero called as pH$_{pzc}$. It mainly influences the interaction between the catalyst and pollutant. The pH drift method was used to determine the pH$_{pzc}$ by adding 50 mg of catalyst to 50 mL of pH-adjusted solution and shaken for 48 h. The pH of 0.01 M NaCl (Loba Chemie Pt. Ltd., India) solution was adjusted between 2 and 12 using 0.1 M HCl or 0.1 M NaOH. The final pH was measured and plotted against the initial pH. The pH at which the pH-initial and pH-final intersects was taken as the pzc.

3.5 Stock solution preparation

(a) BPA: 10 mg of BPA (Sigma-Aldrich, USA; ≥ 99% Purity) granules were dissolved in 100 mL of distilled water to make a 100 ppm stock solution of BPA (100 mg/L). The volumetric flask containing BPA granules in distilled water is mixed with a magnetic stirrer and kept at a constant temperature (30 °C) for 24 h.

(b) p-NP: 100 ppm stock solution was prepared by dissolving 10 mg of p-NP (Sigma-Aldrich, USA; ≥ 99% Purity) in 100 mL distilled water in a volumetric flask.

These stock solutions were stored at 5 °C upon complete dissolution of BPA and p-NP. When necessary, the stock solutions were further diluted with distilled water to give final concentrations such as 10 mg/L.

3.6 Calibration curve of BPA and p-NP

A calibration curve was prepared for different concentrations of BPA and p-NP using absorbance value at their characteristic wavelength as described in Chapter 1, Table 1.1. Standard solutions of the p-NP and BPA in the range of 10 to 100 ppm with increments of 10 ppm were prepared by taking 10 to 100 mL of p-NP and BPA stock solution in increments of 10 mL in a 100 mL standard flask and making it up to the mark with distilled water. The standard solutions of the p-NP and BPA were transferred to a quartz cuvette and

the absorbance was recorded against distilled water as blank at their respective characteristic wavelengths using a UV-vis spectrophotometer. The values of absorbance and concentrations for p-NP and BPA in standard solutions are presented in Table 3.1. Figure 3.3 a and 3.3 b represent the calibration graph for p-NP and BPA, respectively. Linear equations for calibration are also shown in Figure 3.3 a and b.

Table 3.1: Calibration table for p-NP and BPA

Concentration of p-NP (mg/L)	Absorbance	Concentration of BPA (mg/L)	Absorbance
10	0.013	10	0.161
20	0.036	20	0.297
30	0.05333	30	0.45
40	0.06867	40	0.6
50	0.087	50	0.736
60	0.105	60	0.884
70	0.12267	70	1.042
80	0.14067	80	1.179
90	0.15333	90	1.321
100	0.171	100	1.469
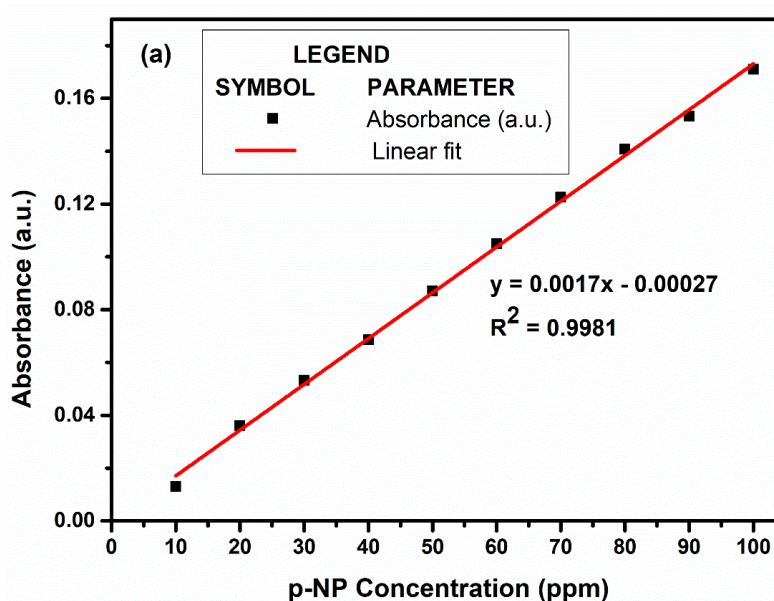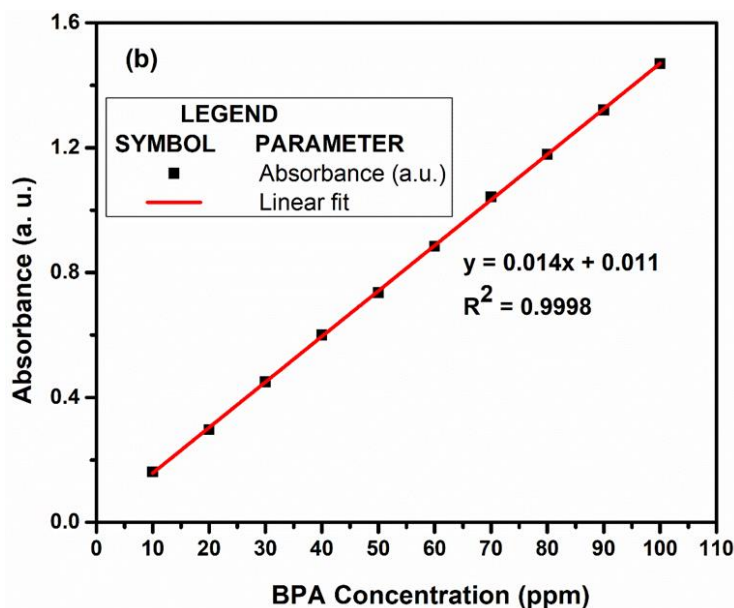
Fig. 3.3 Calibration curve for (a) p-NP and (b) BPA

3.7 Degradation study

The reactor (1L volume) consists of a double-walled quartz immersion well for mercury-vapor lamp and inlet and outlet tubes for cooling. The schematic representation of the photoreactor is shown in Fig. 3.4. For the degradation study, a known concentration of EDCs (4-NP and BPA) with a known amount of bionanocatalyst was introduced in the reactor and the pH of the reaction mixture was maintained at a particular value. The reaction mixture was stirred in the dark for 30 min to attain the adsorption-desorption equilibrium. Further, this reaction mixture was subjected to UV irradiation (365 nm) produced by a high-pressure mercury vapor lamp. After a regular time interval, the sample was withdrawn and subjected to catalyst removal by centrifugation. The obtained supernatant was subjected to UV-vis analysis to assess the extent of degradation. The absorbance values were converted to the concentration using the linear equation obtained from the calibration curve. The degradation percentage was calculated using the following equation (8),

$$\text{Degradation \%} = \frac{(C_0 - C)}{C_0} \times 100 \tag{8}$$

where C_0 and C are the initial and final concentrations of EDCs, respectively.
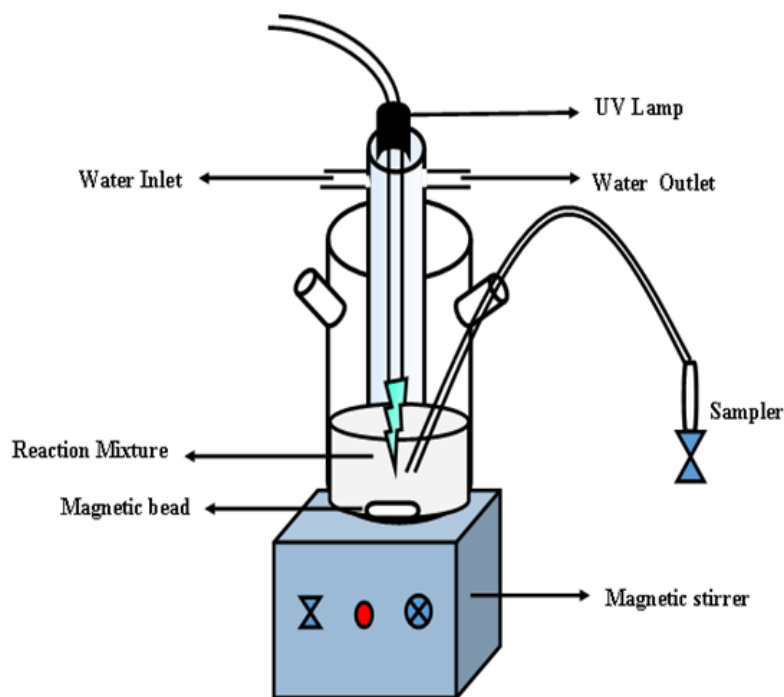
Fig. 3.4 Schematic of a photocatalytic reactor for p-NP/BPA degradation

The influence of reaction parameters such as catalyst loading, initial pollutant concentration and pH on degradation efficiency of p-NP and BPA was evaluated by the OVAT method. For p-NP degradation experiment, the variables used for OVAT method were pH (5, 7, 9, 11), catalyst loading (0.05, 0.1, 0.2 g/L) and p-NP concentration (25, 50, 75, 100 mg/L). The variables used for OVAT method for achieving higher BPA degradation efficiency were catalyst loading (0.1. 0.15, 0.2 g/L), pH (5, 7, 9, 11) and BPA concentration (5, 10, 15, 20 mg/L). The experiments were performed in triplicates to determine the effect of selected variables on BPA and p-NP degradation efficiency.

3.7.1 Reaction kinetics

The pseudo-first-order rate expression is given by equation (9)

$$r = -\frac{dC}{dt} = k_1 C \tag{9}$$

where r, C, and k_1 are the reaction rate, concentration of a pollutant (mg/L) at time t (min), and the pseudo-first-order rate constant (min^{-1}), respectively. Integration of equation (9) resulted in equation 10,

$$ln\ C_0/C = k_1 t \tag{10}$$

42

A modified Langmuir–Hinshelwood (L-H) model is commonly used to study the relationship between initial pollutant concentration and k_1 (Li et al. 2008; Ahmed et al. 2011). Previously, authors have used this approach in the photocatalytic degradation of pollutants using ZnO (Rajamanickam and Shanthi 2012; Shafaei et al. 2010; Pare et al. 2008). The modified L-H equation is given by equation (11),

$$r = -\frac{dC}{dt} = \frac{K_r K C_0}{1 + K C_0} \tag{11}$$

where, C_0 is initial concentration (mg/L), K_r is an apparent rate constant (mg/L/min) and K is adsorption constant (mg/L)$^{-1}$. Values of K_r and K in the L-H model, are affected by initial pollutant concentration, catalyst loading, and physical properties of reactants. Thus, a general mathematical equation used to describe the kinetics will be challenging and alter reaction order in a different stage of the reaction. Substantial deviation from the real kinetics could be unavoidable by describing the whole reaction process with a fixed model (Qingshan et al. 2012; Gmurek et al. 2017). The experimental data were fit to zero order, first order, pseudo-first-order and second-order kinetic model equations based on the results. And the factors affecting the kinetic model were explored. From the equation 9 and 11, the k_1 constant can be written as given by equation 12,

$$\frac{1}{k_1} = \frac{1}{K_r K} + \frac{C_0}{K_r} \tag{12}$$

The equations representing the zero-order (Din et al. 2019) and second-order (Qingshan et al. 2012) reaction kinetics are given below by equation 13 and 14,

$$C_0 - C = k_0 t \tag{13}$$

$$\frac{1}{C} - \frac{1}{C_0} = k_2 t \tag{14}$$

where, k_0, and k_2 are zero (mg L^{-1} min^{-1}) and second-order rate constants (L mg^{-1} min^{-1}), respectively.

3.7.2 Characterization of photocatalytic degradation

The photocatalytic degradation of p-NP and BPA was characterized using UV-vis, TOC, COD and LC-MS analysis. After photocatalytic degradation of p-NP and BPA, the degree of mineralization was evaluated by a TOC analyzer (TOC-V$_{CSN}$, Shimadzu, Japan). TOC analysis in terms of non-purgeable organic carbon (NPOC) was carried out by removing the total inorganic carbon by purging the acidified sample with carbon-free zero air prior to measurement. The sample was injected onto a platinum catalyst at 680 °C, where organic carbon was oxidized into carbon dioxide in an oxygen-rich atmosphere. The

concentration of carbon dioxide generated was measured with a non-dispersive infrared (NDIR) detector. The zero air transports the CO_2 through a moisture trap to remove water vapor from the gas stream before reaching the detector. Potassium hydrogen phthalate was used as a standard for TOC analysis. The percentage removal of TOC was calculated by equation (15),

$$\text{\% TOC removal} = \frac{TOC_0 - TOc}{TOC_0} * 100 \qquad (15)$$

where TOC_0 and TOC are the initial and final TOC of the BPA at a given reaction time.

The carbon-based matter in industrial discharge was characterized by COD, a collective measure of the organic material which is mineralized to end-products. The COD determines the amount of oxygen required for the chemical oxidation of organic matter using a strong chemical oxidant, such as potassium dichromate ($K_2Cr_2O_7$) (Sigma-Aldrich, USA; $\geq 99\%$ Purity), under reflux conditions. COD analysis was carried out using 0.25 N $K_2Cr_2O_7$, digested sulphuric acid (Loba Chemie Pt. Ltd., India; $\geq 98\%$ Purity), 0.1 N ferrous ammonium sulfate (FAS) (Sigma-Aldrich, USA; $\geq 99\%$ Purity) and ferroin indicator (RANKEM™, Avantor, US). A sample was refluxed with a known amount of $K_2Cr_2O_7$ in sulphuric acid medium and the excess of dichromate was titrated against FAS. The amount of $K_2Cr_2O_7$ consumed is proportional to the oxygen required to oxidize the oxidizable organic matter. Briefly, 0.04 g mercury sulfate (Loba Chemie Pt. Ltd., India; $\geq 98\%$ Purity) was added to 1 mL of $K_2Cr_2O_7$, 2 ml sample and 3 mL of digested sulphuric acid. 2-3 glass beads were added and mixed thoroughly. The sample was digested for 2 h in a COD digester maintained at 150 ˚C. Blank was prepared in the same manner using ultrapure water instead of sample. The following equation (16) was used to calculate COD (mg/L),

$$COD = \frac{(mL\ of\ FAS\ for\ Blank - mL\ of\ FAS\ for\ sample) * normality\ of\ FAS * 8000}{mL\ sample} \qquad (16)$$

The following equation (17) gives the percentage removal of COD,

$$\text{\% COD removal} = \frac{COD_0 - COD}{COD_0} * 100 \qquad (17)$$

where COD_0 and COD are the initial and final COD of the BPA for a given reaction time.

The intermediate compounds formed during the BPA and p-NP degradation were analyzed using a liquid chromatography-mass spectrometry (LC-MS-2020, Shimadzu, Japan) with electrospray ionization (ESI) interface and ion trap mass analyzer. Chromatographic separation of the intermediates formed at different time intervals was carried out using a C-18 reverse phase column operated at 30 ˚C with a 20 µL of injection

volume. The mobile phase composition was methanol/water (60/40, *v/v*) with 0.1 % trifluoroacetic acid (Sigma-Aldrich, USA) with a 1 mL/min flow rate.

3.7.3 Catalyst reuse study

The loss of degradation ability of catalyst after its first usage and their reuse feasibility was tested by repeating the experiment with the same catalyst. After an experiment with a fresh catalyst, the nanoparticles were reused thrice for the degradation experiments. Thus, the nanoparticles were used for 4 cycles. After the first batch of degradation experimentation (180 min of UV irradiation), the catalyst particles were removed from the mixture through centrifugation. The sediment – catalyst was washed several times with distilled water, followed by drying at 70 ˚C. The dried catalyst (ZnO NPs) were subjected to the next batch of p-NP/BPA degradation experiments to check its photocatalytic performance. The above procedure was repeated for 3 subsequent cycles under the same experimental conditions.

3.7.4 Radical scavenging experiment

To identify the reactive oxidative species and further demonstrate the degradation mechanism, scavenging agents such as benzoquinone (BQ) (Loba Chemie Pvt. Ltd., India; ≥98% Purity), isopropyl alcohol (IPA) (Loba Chemie Pvt. Ltd., India; ≥ 99.5% Purity) and ethylenediaminetetraacetic acid disodium salt (EDTA-Na_2) (Molychem, India; ≥ 99.5% Purity) were added to scavenge superoxide species ($\bullet O^{-2}$), hydroxyl radicals ($\bullet OH$) and holes (h^+) respectively. The experiments were conducted as described in section 3.7 in the presence of scavengers at a concentration of 1 mM.

3.7.5 In vitro cytotoxicity study

The cytotoxicity study of BPA and p-NP before and after photocatalytic degradation was carried out as per ISO 10993:5 by MTT assay (3-(4,5-dimethylthiazol-2-yl)-2,5-diphenyltetrazolium) at CoE-biological laboratory, The South India textile research association (SITRA). The MTT assay was carried out to determine the viable cells with functional mitochondria. L929 mouse fibroblast cell lines were obtained from the national centre for cell science (NCCS) Pune. These cells were cultured in minimum essential medium (MEM) supplemented with fetal bovine serum at 37 ^{0}C with 5% CO_2 for 24 h. Viable cells reduce the tetrazolium into a purple formazan precipitate that accrues inside

the cells and in the culture medium and absorbance was recorded at 570 nm to determine the cell viability. Cell images were recorded using an inverted phase-contrast microscope.

3.8 Fluorescence mediated sensing studies

The sensing of BPA and 4-NP was carried out using fluorescence measurement. The sensing property of biologically synthesized nanoparticles was compared with chemically synthesized nanoparticles. A fixed amount of ZnO QDs were added to a varying concentration of BPA and p-NP. 100 μL of functionalized ZnO QDs were added to each 300 μL of analyte solution. The reaction mixtures were further diluted and mixed thoroughly and transferred into fluorescence spectroscopy cuvettes and fluorescence measurements were recorded. The fluorescence measurements of functionalized QDs in the reaction mixtures were carried out at an excitation wavelength, and the emission spectra were also recorded. The fluorescence quenching efficiency of QDs for different analyte concentrations is represented by (F_0-F).

The effect of reaction parameters such as different buffer solutions, pH and time on EDCs detection for a constant dosage of QDs was evaluated by measuring the fluorescence emission intensities of functionalized ZnO QDs. Buffer solutions, such as acetate buffer (pH 5.6, 0.1 M), ultrapure water (pH 6.9), tris buffer (pH 7.4, 0.1 M), phosphate buffer (pH 7.4, 0.1 M) and phosphate buffer saline (pH 7.4, 1 X) were chosen for this study. Phosphate buffer saline was prepared by using 10 mM disodium monohydrogen phosphate (Na_2HPO_4), 1.8 mM potassium dihydrogen phosphate (KH_2PO_4), 2.7 mM potassium chloride (KCl) in ultrapure water. Phosphate buffer was prepared by using 75.4 mM disodium monohydrogen phosphate heptahydrate ($Na_2HPO_4 \bullet 7H_2O$), 24.6 mM sodium dihydrogen phosphate monohydrate ($NaH_2PO_4 \bullet H_2O$) in ultrapure water. Acetate buffer was prepared by using 94.1 mM sodium acetate and 5.9 mM acetic acid in ultrapure water. Tris buffer was prepared by adding a 0.1 M tris base in ultrapure water. All the chemicals were procured from Loba Chemie Pt. Ltd., India. All the reagents are of analytical grade, and ultrapure water obtained from ultrapure water purification system (LoboStar™ Siemens) was used for solution preparation. The influence of pH on the detection of EDCs was evaluated by varying the reaction mixture's pH from 1 to 12. Further, the specificity of the functionalized ZnO QDs towards EDCs detection was evaluated by analyzing its structural analogs. The limit of detection (LOD) for BPA and p-NP was calculated by equation (18),

$$LOD = \frac{3\sigma}{slope} \tag{18}$$

where σ is the standard deviation of blank measurements (n = 10). The slope was obtained by plotting (F_0-F) *vs.* analyte concentration.

The quenching mechanism usually follows either static or dynamic interaction between the analyte (BPA and p-NP) and fluorophore.

CHAPTER 4

RESULTS AND DISCUSSIONS

The outcomes of the research methodologies for the synthesis of nanoparticles by biological and chemical method, its characterization, undertaking synthesis mechanism, and application of nanoparticles for the detection and degradation of BPA and p-NP are presented in this section with the support of relevant literature. Initially, the results related to the isolation and identification of endophytic fungi, media optimization, growth characteristic and optimization of ZnO nanoparticles synthesis are described. Moreover, optical, structural and morphological properties of nanoparticles and their stability studies are reported. Further, the degradation studies of BPA and p-NP are discussed based on the maximum degradation efficiency by optimizing reaction parameters, degree of mineralization, cytotoxicity, degradation pathway by radical scavenging experiment and LC-MS analysis. Moreover, a detailed description of the detection of BPA and p-NP using fluorescence spectroscopy is given. Lastly, the LOD for sensing of BPA and p-NP by biologically and chemically synthesized nanoparticles is reported.

4.1 Biological synthesis of ZnO nanoparticles

4.1.1 Isolation and identification of zinc acetate tolerant endophytic fungi

The population of endophytic fungi is mainly affected by the climatic condition and location of the host plant (Fisher et al. 1994). The common endophytic species isolated from the Kudremukh region, western Ghats plants were *Curvularia clavata, C. lunata, C. pallescens* and *Fusarium oxysporum* (Raviraja 2005; Musavi and Baalakrishnan 2013). In the present study, a total of 6 fungal isolates (FI) viz. FI 01, FI 02, FI 03, FI 04, FI 05 and FI 06 were isolated as shown in Fig. 4.1 from the healthy leaves of *Nothapodytes foetida* based on discrete morphological characteristics as represented in Table 4.1.
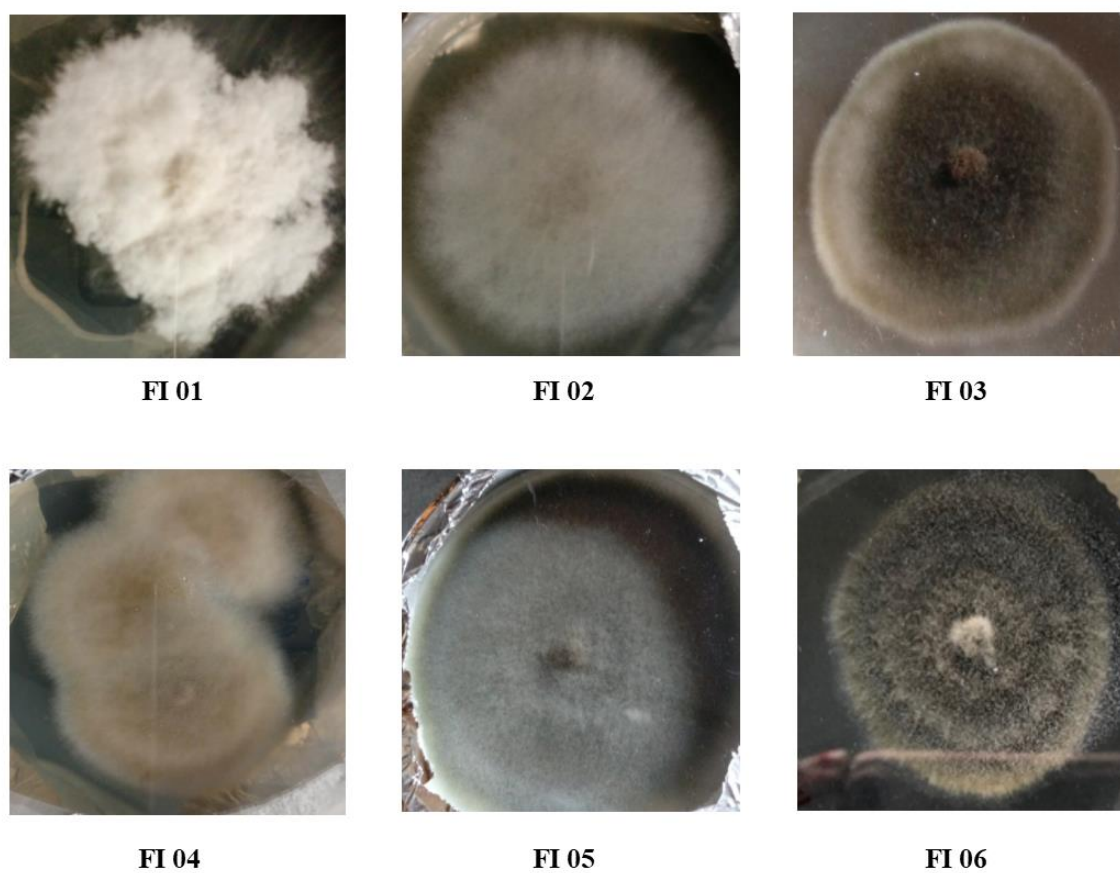
Fig. 4.1 Endophytic fungal isolates from healthy leaves of medicinal plant *Nothapodytes foetida*

Table 4.1 Morphology of fungal isolates (on PDA plate) isolated from *Nothapodytes foetida* leaves

Fungal Isolate	Morphology	Texture
FI 01	White conidia with pink pigment, white reverse	Granular
FI 02	Pale white conidia with yellow reverse	Cottony
FI 03	Green conidia with the white periphery, yellowish-green reverse	Cottony
FI 04	Yellow - white conidia with yellow reverse	Cottony
FI 05	Light green conidia with dark green reverse	Velvety
FI 06	White to green radially sulcate growth with and pale white center with patterned light green and dark green reverse	Velvety

The growth of each fungal isolate on the PDA plate was observed periodically by measuring its colony diameter in millimeters (mm), as shown in Fig. 4.2. All the fungal isolates showed an increase in colony diameter with an increase in incubation period from 0 h to 120 h. However, isolate FI 05 and FI 06 indicated a comparable increased level of growth, while isolate FI 03 showed moderate growth over the same incubation period. Isolate FI 01, FI 02 and FI 04 showed significant growth on the PDA plate. Further, FI 05 and FI 06 isolates were subjected to growth studies in terms of biomass dry weight and protein concentration.
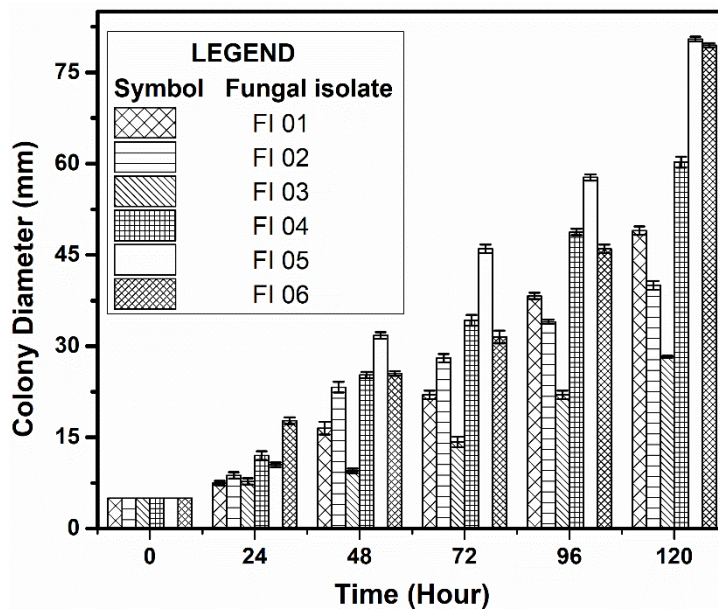
Fig. 4.2 Growth of endophytic fungal isolates on the PDA plate

4.1.1.1 Selection of broth media

The media components play a vital role in the growth of fungi and their sporulation. The yield of fungi can be directly enhanced by culturing them into appropriate growth media containing specific carbon, nitrogen and energy sources. FI 06 exhibited a maximum dry biomass weight of 18.9 ± 1.23 g/L in MGYP followed by 17.3 ± 0.57 g/L in PDB after 96 h at $28 \pm 1' =$ °C at 150 rpm. Further, the biomass grown on SDB showed a dry weight of 13.83 ± 1.72 g/L as compared to that, NB displayed less biomass dry weight under the same incubation condition. However, FI 05 exhibited a decreased biomass dry weight in MGYP, PDB and SDB media compared to FI 06 (Fig. 4.3a).
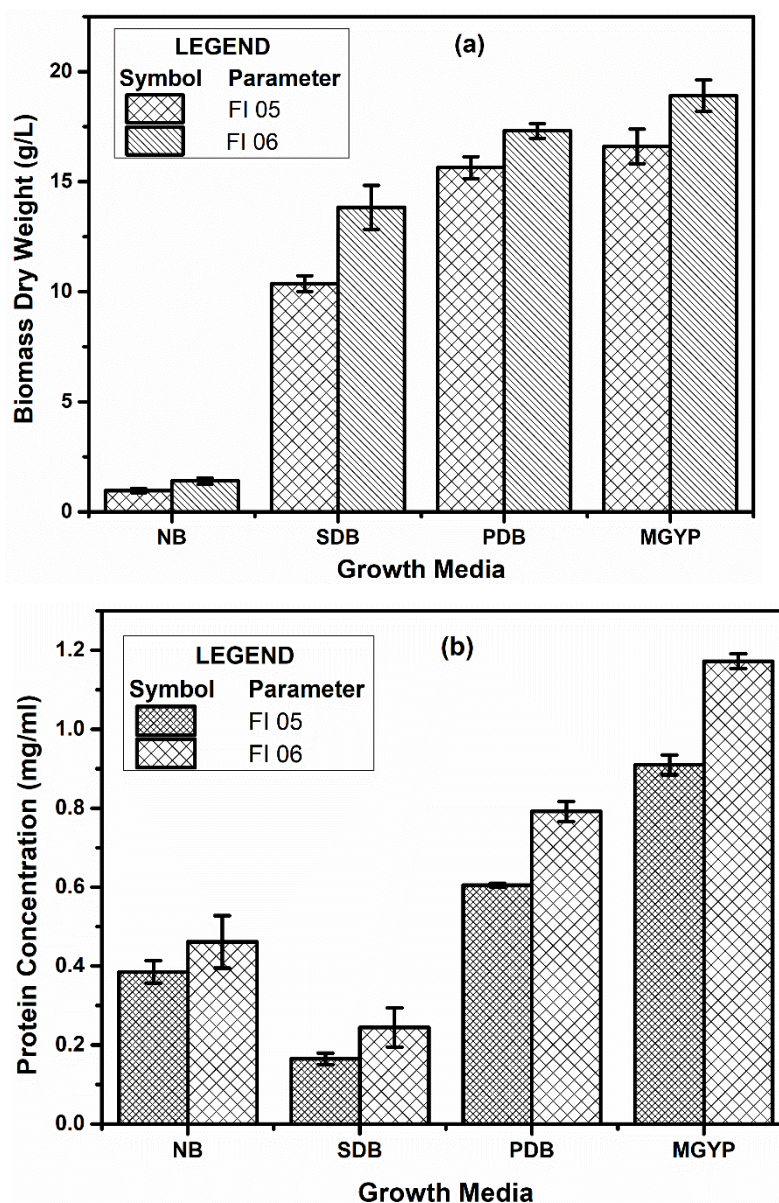
Fig. 4.3 Influence of different media on (a) biomass dry weight and (b) protein concentration

Among the four growth media, FI 06 displays a higher protein concentration of 1.17 ± 0.018 mg/mL after 96 h in MGYP media than FI 05. This is followed by PDB > NB > SDB (Fig. 4.3 b). The components of MGYP, such as malt extract and yeast extract, play a unique role in the growth and metabolism of fungus, while peptone being the source of nitrogen, supports the luxuriant growth of the fungus and glucose acts as a source of carbohydrate. FI 06 can readily uptake the components of MGYP compared to other growth media, resulting in the highest biomass and protein yield. Consequently, the MGYP

medium was found to be most suitable for the growth of the tested fungus and used as a growth medium for further study.

The TI of the individual fungal isolate was calculated as described in section 3.1.1. 50 % of FI showed a significant tolerance level to the zinc acetate with varying degrees of magnitude. FI 06 exhibited a higher level of zinc acetate tolerance with a TI of 0.74 compared to other FI, as shown in Fig. 4.4 (a). Owing to its higher TI, FI 06 was further subjected to its MTC assay; an almost 50 % reduction in colony diameter was observed for a 3 mM concentration of zinc acetate. There was a remarkable decrease in colony diameter with an increase in zinc acetate concentration, for which 9 mM was the highest MTC value of FI 06 (Fig. 4.4 b). Due to its high TI, FI 06 was subjected to molecular identification and further employed for nanoparticle synthesis.
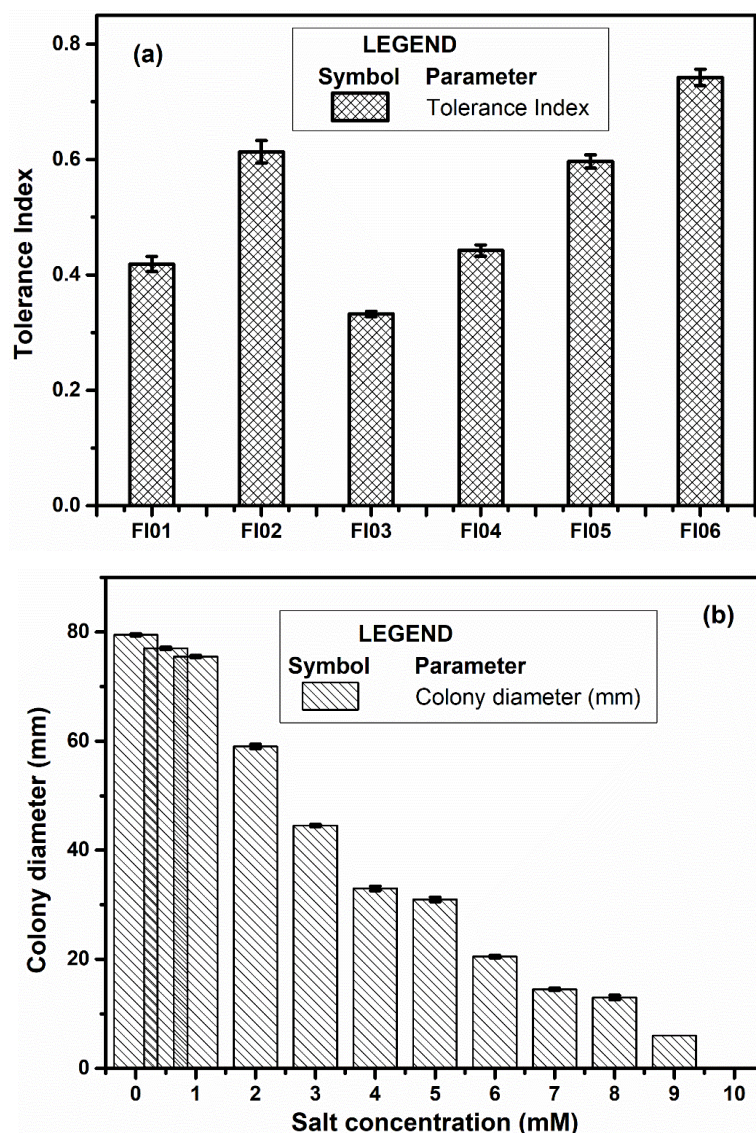
Fig. 4.4 Zinc acetate tolerance potential of endophytic fungal isolates (a) TI study, (b) MTC assay of FI exhibiting high TI

Morphological identification of FI was carried by colony characteristic examination. FI06 is opaque and smooth with white to green color, raised filamentous fungus with filiform margin, as shown in Fig. 4.5 (a,b). Molecular identification of FI 06 was carried out by 16s rDNA ITS sequencing. The results of BLASTn exemplified that the isolate FI 06 was highly homologous to species from phylum Ascomycota and class Ascomycetes. The ITS region of rDNA showed 100 % similarity to *C. geniculatus* as shown in the phylogenetic tree constructed by Mega X software and sequence analyzed with NCBI accession number KF946042 (Fig. 4.6).
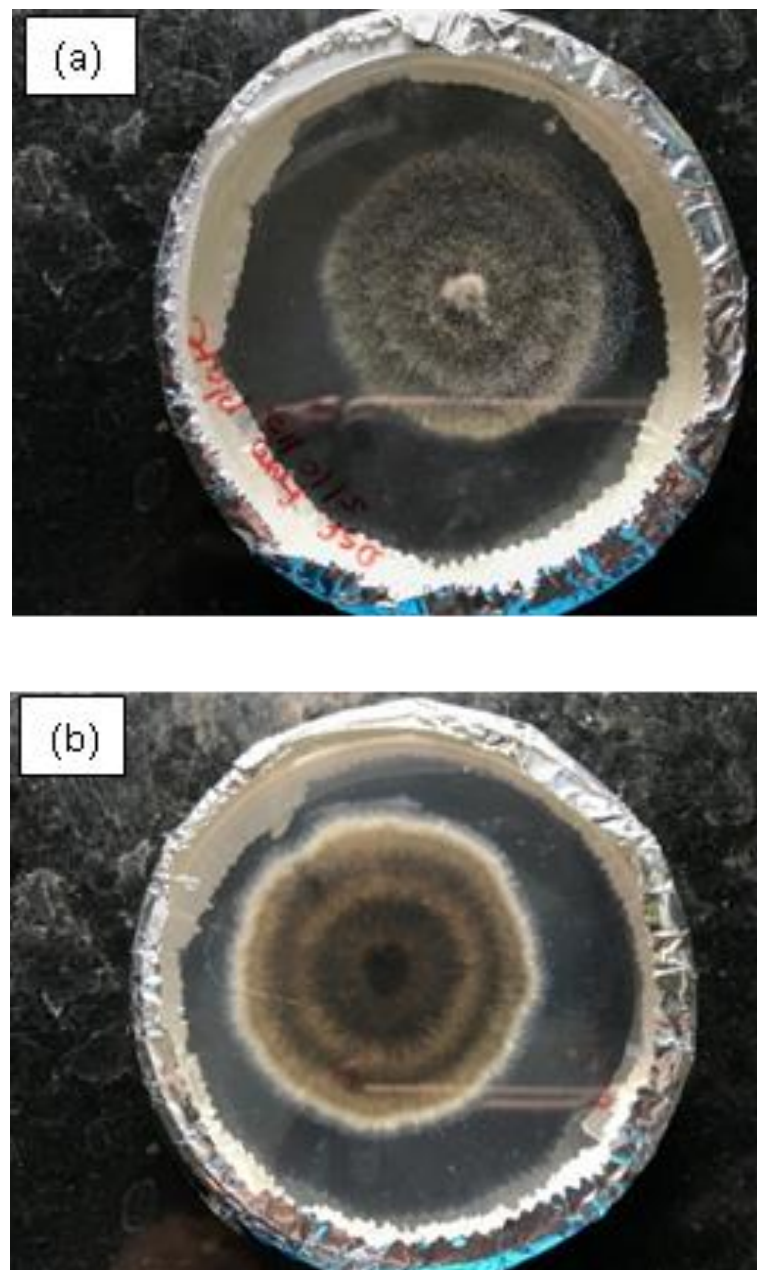
Fig. 4.5 Growth of *C. geniculatus* on PDA plate (a) Front side and (b) Backside

The rDNA ITS sequence of the *C. geniculatus:*

```
GTGATATAGAGTCTTGATGGAGTGCCGTCCTCTTTTGCTGATTGCAAGCGCAAA
AATGTGCTGCGCTGCGAAACCAGTAGGCCGGCTGCCAATCGTTTTAAGGCGAGT
CTTTGGACAAAACCAAAGACAAAAAACGCCCAACACCAAGCAAAGCTTGAGGG
TACAAATGACGCTCGAACAGGCATGCCCTTTGGAATACCAAAGGGCGCAATGTG
CGTTCAAAGATTCGATGATTCACTGAATTCTGCAATTCACACTACGTATCGCATTT
CGCTGCGTTCTTCATCGATGCCAGAACCAAGAGATCCGTTGTTGAAAGTTGTAA
ATGATTTACATTTGTTGTACTGACGCTGATTGCAACTGCATAAAAAGGTTTATC
ATGTGGTCCTGGAGGCGGGCGAACCCGCCCAGGAAACAACAAGTGCGCAAAAG
ACAAGGGTAATAAAATACTCCAGCCTTGCCGCCTGTTGGCGGTGCAGCCTTCAT
ATGTTTATTGTGTAATGATCCCTCCGCAGGTTCACCTACGGAGACCTTGTTACGA
TTTT
```
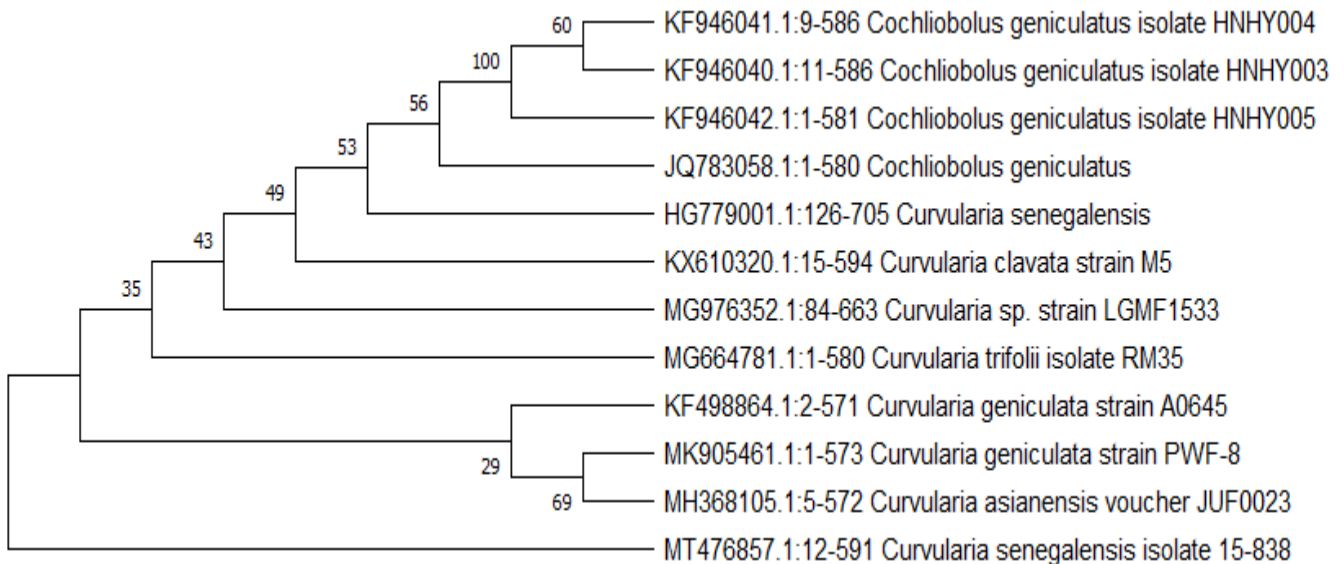

Fig. 4.6 Phylogenetic analysis of fungal isolate based on a neighbour-joining bootstrap method using Mega X software

4.1.1.2 Growth analysis of *C. geniculatus* in MGYP media

The growth of *C. geniculatus* was studied in terms of biomass dry weight (g/L) over the periodic incubation time (Fig. 4.7). Generally, the growth pattern of fungus was divided into (i) hyphae initiation phase, or lag phase, (ii) rapid growth of mycelia or log phase, (iii) stationary phase and (iv) declining phase (Vrabl et al. 2019). *C. geniculatus* showed a lag phase up to 24 h, where fungal cells adapt to growth conditions. Cell division is very slow in this growth phase, and the synthesis of biomolecules such as RNA, enzymes, and proteins occurs. The initial lag phase was followed by the log phase from 24-72 h. In this

phase, cell division accelerates into an exponential phase until one or more nutrients becomes limiting with oxygen depletion (Prosser 1995). After 72 h, fungal cells entered the stationary phase where there was no distinct change in the biomass concentration observed and continued until 144 h. Finally, after 144 h, cell lysis resulted in the decreased biomass concentration and entered into a decline phase (Fig. 4.7).
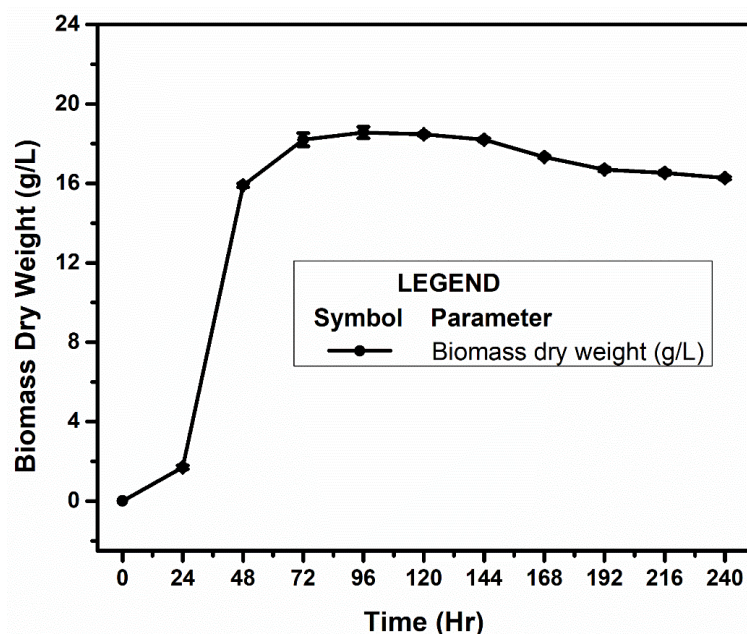
Fig. 4.7 Growth analysis of *C. geniculatus* in MGYP media

4.1.2 Optimization of physicochemical parameters for the biosynthesis of ZnO nanoparticles

The potential usage of ZnO nanoparticles for various applications depends on their physicochemical and morphological characteristics. Thus, there is a need to control the composition, morphology and size of nanoparticles. Therefore, in the present investigation effect of pH, reaction time, precursor salt and its concentration on the formation of ZnO nanoparticles were studied.

4.1.2.1 Effect of precursor salts

The FESEM coupled EDX analysis was carried out to study the impact of various precursor salts on the structural, morphological and compositional characteristics of synthesized nanoparticles (Fig. 4.8). Zinc acetate dihydrate (1mM) as a precursor salt leads to a strong intensity peak of Zn at 1.1 KeV and oxygen peak at 0.6 KeV in EDX spectrum as shown in Fig. 4.8 (a), signifying the existence of oxygen as it is an oxide form of zinc (Jain et al. 2014; Kundu et al. 2014). In the case of zinc sulfate heptahydrate (1 mM) as a

precursor salt, the EDX spectrum shown in Fig. 4.8 (b) manifests the peak of zinc, sulfur and oxygen at 1.1, 0.6 and 2.4 KeV, respectively. The presence of sulfur in the EDX spectrum of zinc sulfate heptahydrate as a precursor salt confirms the synthesized nanoparticles contain impurity in the form of sulfur, which may lead to the formation of ZnO and ZnS nanoparticles (Hitkari et al. 2017).

Zinc nitrate hexahydrate $(ZnNO_3)_2.6H_2O$ as a precursor salt exhibited a high-intensity peak of zinc at 1.1 KeV and oxygen at 0.6 KeV, as depicted in Fig 4.8 (c). The EDX spectrum displayed a peak of oxygen and zinc confirms the presence of zinc in its oxide form (Nagajyothi et al. 2014). As represented in Fig. 4.8 (a,b and c), the EDX spectrum contains a signal for carbon as a carbon grid is used for sample preparation.
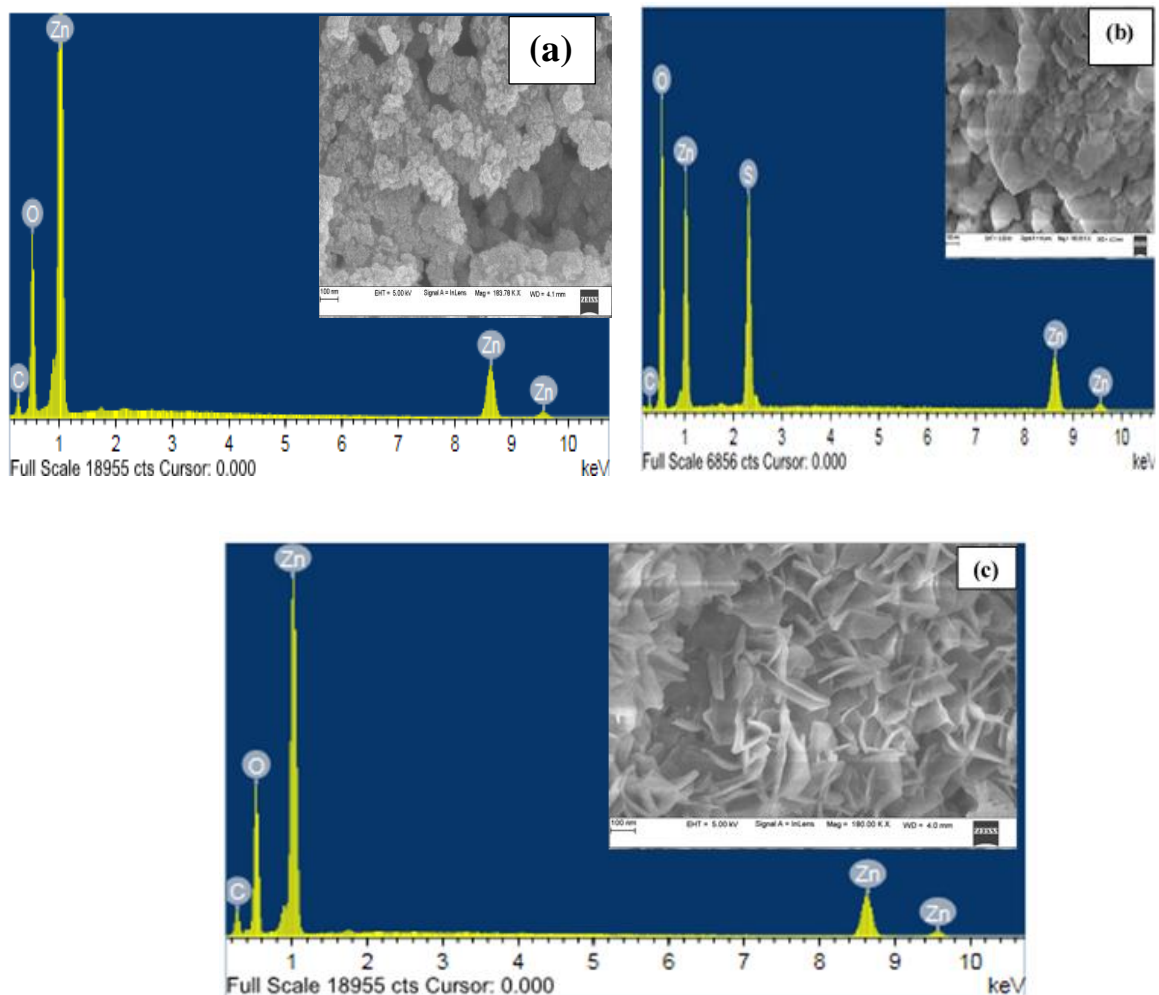
Fig. 4.8 FESEM-EDX spectra recorded to study the effect of various precursor salts (a) zinc acetate dihydrate (b) zinc sulfate heptahydrate and (c) zinc nitrate hexahydrate on ZnO nanoparticles formation

FESEM coupled EDX micrograph of zinc acetate dihydrate exhibits the formation of ZnO nanoparticles and zinc nitrate hexahydrate leads to the synthesis of ZnO nanosheets. However, zinc sulfate heptahydrate as a precursor salt leads to the formation of ZnS and ZnO nanoparticles. Further, the phase and purity of synthesized ZnO nanoparticles and ZnO nanosheets were confirmed by XRD analysis. As shown in Fig. 4.9 (a), the XRD pattern of ZnO nanoparticles exhibit peaks at $2\theta = 31.64, 34.11, 36.11, 47.42, 56.44, 62.69, 67.66, 76.82$ attributed to the (100), (002), (101), (102), (110), (103), (112) and (202) planes of hexagonal ZnO nanoparticles respectively which was indexed with ICSD No. 67849. Furthermore, an absence of diffraction peaks associated with any other phase or impurity in XRD analysis confirmed the purity of biosynthesized ZnO nanoparticles (Selvarajan and Mohanasrinivasan 2013; Kundu et al. 2014).
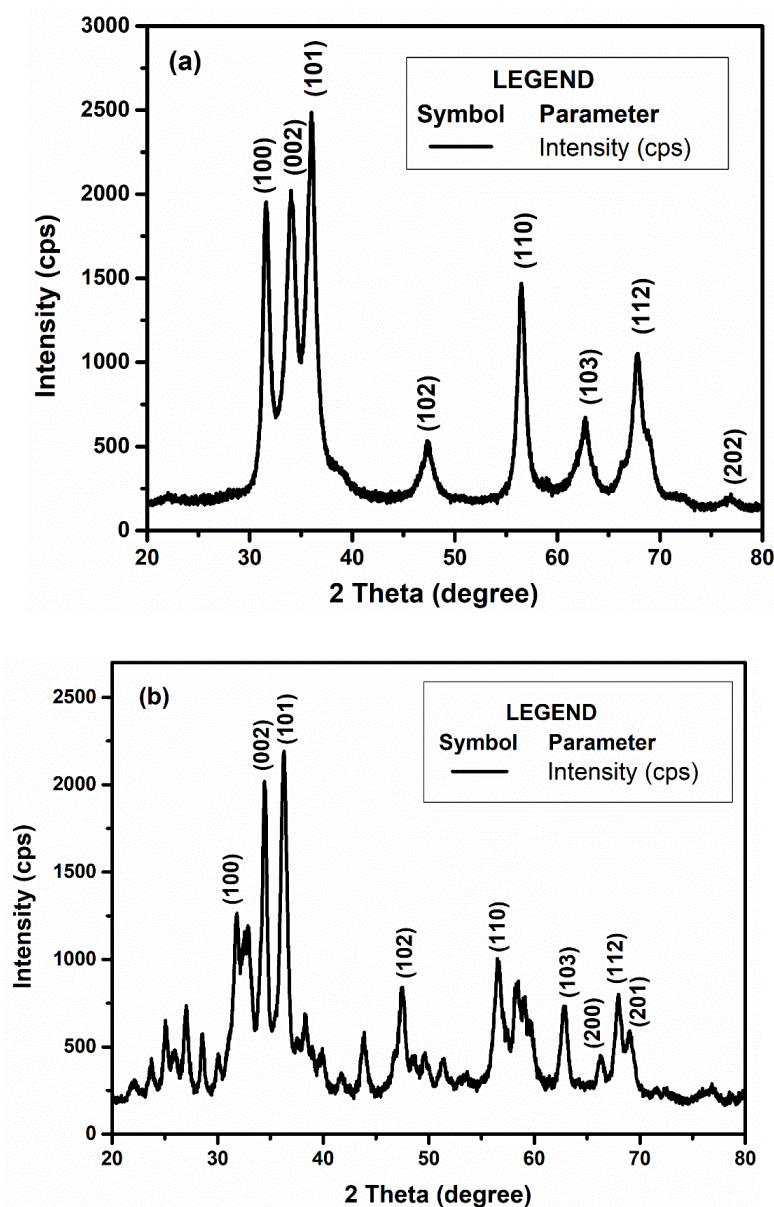
Fig. 4.9 X-ray diffraction pattern of (a) ZnO nanoparticles using zinc acetate dihydrate as precursor salt (b) ZnO nanosheets using zinc nitrate hexahydrate as precursor salt

As shown in Fig. 4.9 (b), the XRD pattern displays peaks at 2θ = 31.80, 34.42, 36.34, 47.44, 56.45, 62.80, 66.13, 67.92 and 68.97 attributed to the (100), (002), (101), (102), (110), (103), (112) and (202) planes of hexagonal ZnO nanoparticles respectively which was indexed with ICSD No. 00-036-1451. However, zinc nitrate hexahydrate as a precursor salt resulted in the presence of the other diffraction peaks associated with any other impurity (Fig. 4.9 b). Based on the FESEM-EDX and XRD analysis, zinc acetate dihydrate was used as a precursor salt for the synthesis of ZnO nanoparticles.

The calculated lattice parameters and unit cell volume (UCV) values shown in Table 4.2, are in agreement with previous findings and confirmed hexagonal (wurtzite structure) phase of ZnO nanoparticles (Jayaseelan et al. 2012; Morkoc and Ozgur 2009). The obtained c/a ratio (Table 4.2) is close to the ideal value of a hexagonal cell, i.e., 1.633. The lattice ionicity and stability may lead to deviance from the ideal hexagonal phase (Morkoc and Ozgur 2009). Diffraction peak line broadening in XRD referred to the nanometer range of biosynthesized ZnO nanoparticles (Selvarajan and Mohanasrinivasan 2013).

Table 4.2 Lattice parameters of biosynthesized ZnO nanoparticles

Material	2θ (deg.)	Hkl	d-spacing (Å)	Lattice parameter (Å)	UCV (Å^3)
ZnO	31.63	100	2.82492	a = 3.263	48.43
	34.11	002	2.62598	c = 5.253	
	36.11	101	2.4853	c/a = 1.6099	

4.1.2.2 Effect of precursor salt concentration

Fig. 4.10 displays UV-vis spectra of ZnO nanoparticles synthesized from the mycelial free filtrate of *C. geniculatus* with various concentrations of zinc acetate dihydrate (1 mM, 10 mM, 20 mM, 30 mM, 40 mM and 50 mM). After incubating mycelial free filtrate with precursor salt, the solution changes color from yellowish-green to white owing to excitation of surface plasmon resonance (SPR) vibrations (Kundu et al. 2014) which is indicative of ZnO nanoparticle formation (Jayaseelan et al. 2012; Pudukudy and Yaakob 2015).
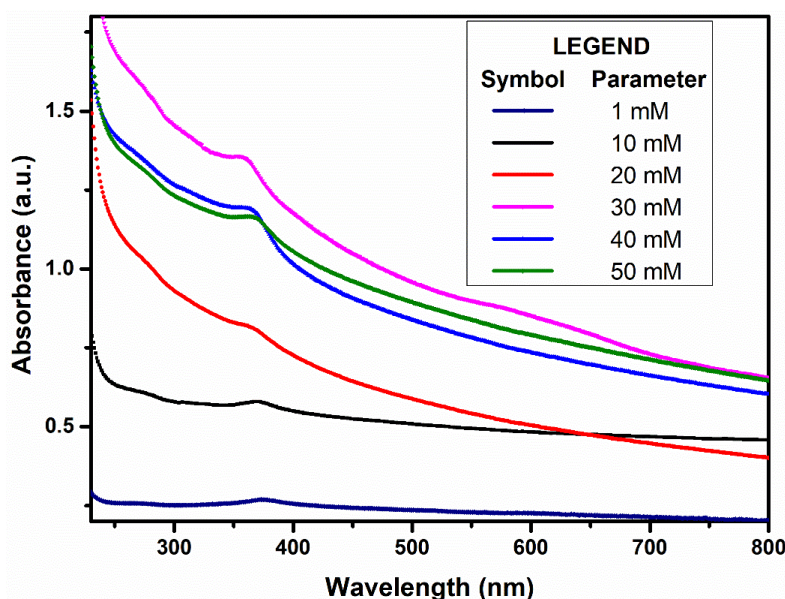
Fig. 4.10 Effect of precursor salt concentration on the biosynthesis of ZnO nanoparticles

As the precursor salt concentration increases from 1 to 30 mM, the SPR shifts to a lower wavelength, i.e., blue shift. The blue shift in SPR represents a reduction in particle size. Surface plasmon absorbance increases with an increase in precursor salt concentration. As depicted in Fig. 4.10, maximum synthesis takes place at 30 mM. However, a further increase in the precursor salt concentration from 30 mM to 50 mM leads to a shift towards longer wavelengths, i.e., redshift. The shift towards a longer wavelength indicates the rapid reduction of zinc acetate dihydrate into ZnO nanoparticles with increased particle size. Thus, 30 mM is found to be the optimum precursor salt concentration for ZnO biosynthesis.

4.1.2.3 Effect of reaction time

An increase in particle size leads to shifting of UV-vis peak towards a longer wavelength (redshift), dominated by the SPR of metal nanoparticles (Birla et al. 2013). The influence of reaction time on ZnO nanoparticle synthesis was studied by obtaining UV-vis spectra at a regular time interval of 24 h, as shown in Fig. 4.11. The spectroscopic signature peak of ZnO nanoparticles was observed with an increase in reaction time from 0 to 24 h. An increase in reaction time from 24 h to 72 h leads to shifting SPR to a longer wavelength due to increased particle size. The reaction time of 24 h showed maximum production of ZnO nanoparticles under optimized reaction conditions with 30 mM of zinc acetate dihydrate.
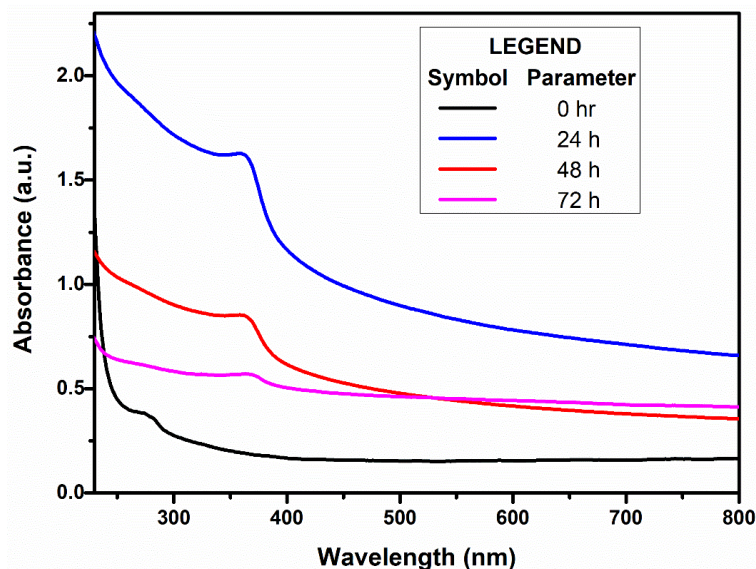
Fig. 4.11 Effect of reaction time on the biosynthesis of ZnO nanoparticles

4.1.2.4 Effect of pH

The pH of mycelial free filtrate has a profound effect on the charges of biomolecules, which affects the reducing and capping ability and, consequently, the growth of nanoparticles (Khalil et al. 2017). The mycelial free filtrate of *C. geniculatus* maintained at pH 6 resulted in the absence of a spectroscopic signature peak dominated by SPR for ZnO nanoparticles, confirming that ZnO nanoparticle synthesis does not occur at acidic pH. Thus, the high concentration of H^+ ions and low concentration of OH^- ions in the mycelial free filtrate halt the synthesis of ZnO nanostructures (Alias et al. 2010). However, at pH 7, there is less ZnO nanoparticle formation than alkaline pH as an equivalent of H^+ and OH^- ions are present in the mycelial free filtrate (Fig. 4.12).
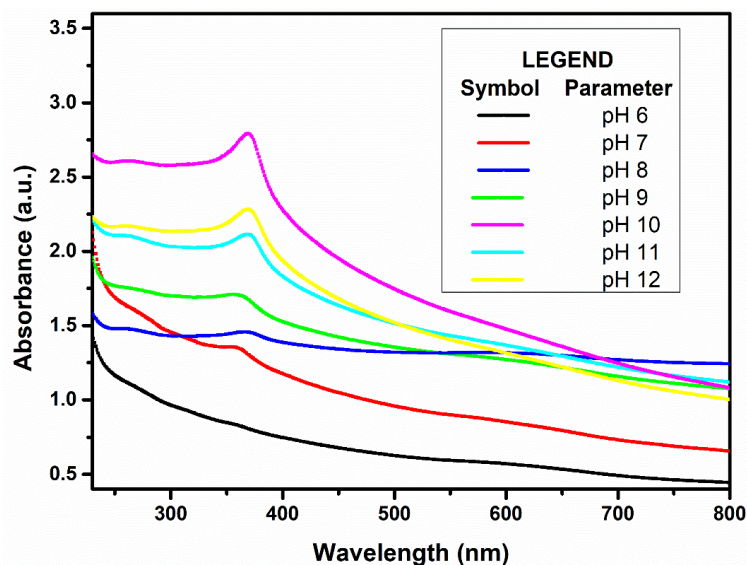
Fig. 4.12 Effect of pH on the biosynthesis of ZnO nanoparticles

60

As depicted in Fig. 4.12, pH increases from basic to alkaline (i.e., from 7 to 12), the corresponding spectroscopic signature peak starts to appear following the peak sharpening, suggesting the formation of ZnO nanoparticles. At pH 10, ZnO exhibits a peak with a relatively high absorbance and sharpness compared to the other pH owing to the intrinsic bandgap, related to the transition of electrons from the valence band to the conduction band (Kundu et al. 2014). A sharp peak confirms the narrow range distribution of the nanoparticles (Darroudi et al. 2014). At pH 11 and 12, i.e., under strong alkaline conditions, OH^- ions dominate in the solution, which forms a complex with Zn^{2+} cations and resulted in $Zn[OH]^{2-}_4$ and $Zn(OH)_2$, which could restrain the formation of ZnO nanoparticles and subsequently decrease in SPR absorbance (Mohhamadi et al. 2018).

4.1.3   Optical, structural and morphological characterization of ZnO

The synthesis of ZnO nanoparticles was confirmed using UV-vis spectrum based on the SPR exhibited by a spectroscopic signature peak at 369 nm (Fig. 4.13), according to the reports by (Jayaseelan et al. 2012; Pudukudy and Yaakob 2015). Furthermore, the blue shift was observed for biogenic ZnO nanoparticles compared to its bulk counterpart, indicating nano-size particles with a narrow range distribution (Darroudi et al. 2014).
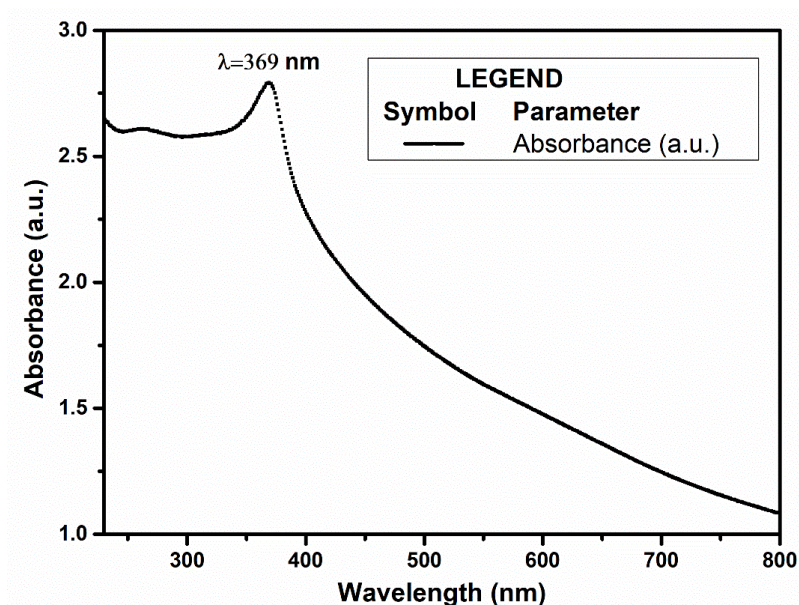
Fig. 4.13 UV-vis spectrum of biogenic ZnO nanoparticles

Additionally, a derivative of absorbance with respect to photon energy was used to estimate the bandgap of ZnO nanoparticles and found to be 3.26 eV (Fig. 4.14) as the electron transitions occur from the valence band (VB) to the conduction band (CB) ($O_{2p} \rightarrow Zn_{3d}$) (Darroudi et al. 2014). Moreover, the obtained band gap is lesser than bulk ZnO nanoparticles (3.7 eV), thus indicating quantum confinement effects and intrinsic crystal defects (Pudukudy and Yaakob 2015).
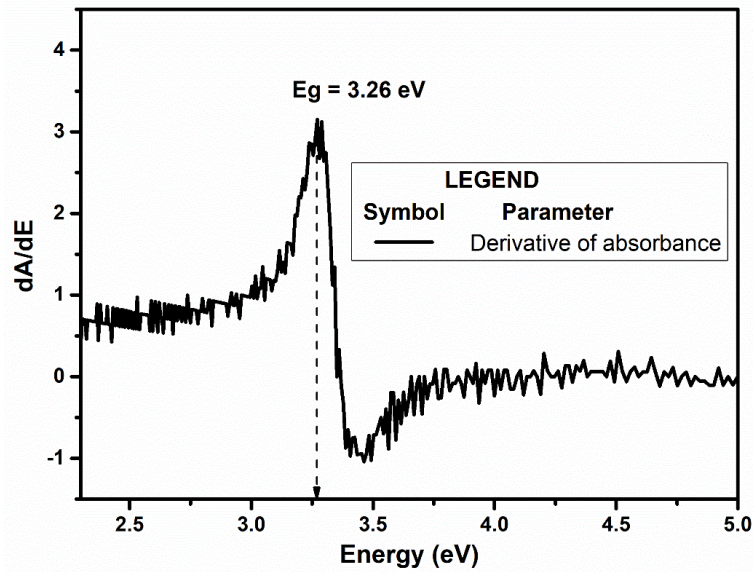
Fig. 4.14 A derivative of absorbance for ZnO bandgap estimation
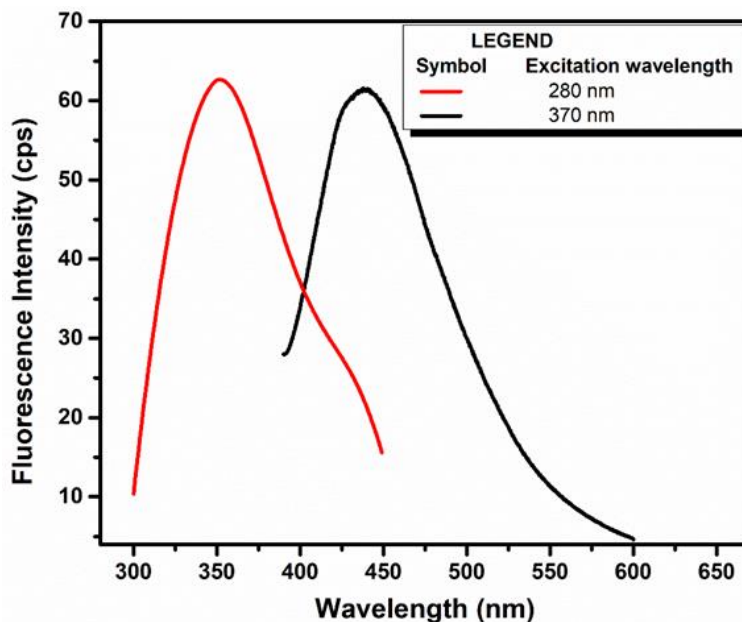
Fig. 4.15 Fluorescence spectra of ZnO nanoparticles excited at 280 nm and 370 nm

The occurrence of capping protein on the ZnO nanoparticles surface was evaluated by recording the fluorescence spectra at an excitation wavelength of 280 nm and 370 nm, respectively (Fig. 4.15). A distinctive emission peak was observed at 350 nm confirms the existence of tyrosine moieties in capping protein (excitation wavelength, 280 nm) (Jain et al. 2014; Sarkar et al. 2014). Moreover, a characteristic emission peak was observed at 440 nm due to the blue emission of ZnO. The intrinsic defects such as oxygen and zinc interstitials are attributed to the blue emission band of biogenic ZnO nanoparticles (Liqiang et al. 2006).

Further, the existence of possible biomolecules in the filtrate of *C. geniculatus,* which confer stability and mediate the ZnO nanoparticle synthesis, was confirmed by FTIR spectra. Fig. 4.16 (a) displayed FTIR spectrum of mycelial free filtrate of *C. geniculatus* attributed vibration bands at 1657.17 cm^{-1} (amide I) resemble the carbonyl group and 1592.47 cm^{-1} (amide II) assigned to N-H group of the proteins (Gole et al. 2001) and their conforming stretching band vibrations were visible at 3281.50 cm^{-1} and 2939.93 cm^{-1}, respectively. The results from UV-vis (Fig. 4.13) and fluorescence data (4.15) support the presence of proteins in the filtrate. The bands observed at 1397.62 cm^{-1} can be attributed to symmetric stretching vibrations of the carboxyl group present in amino acid residues of the protein, and 1089.90 cm^{-1} may be ascribed to C-O stretching vibrations (Sarkar et al. 2014).
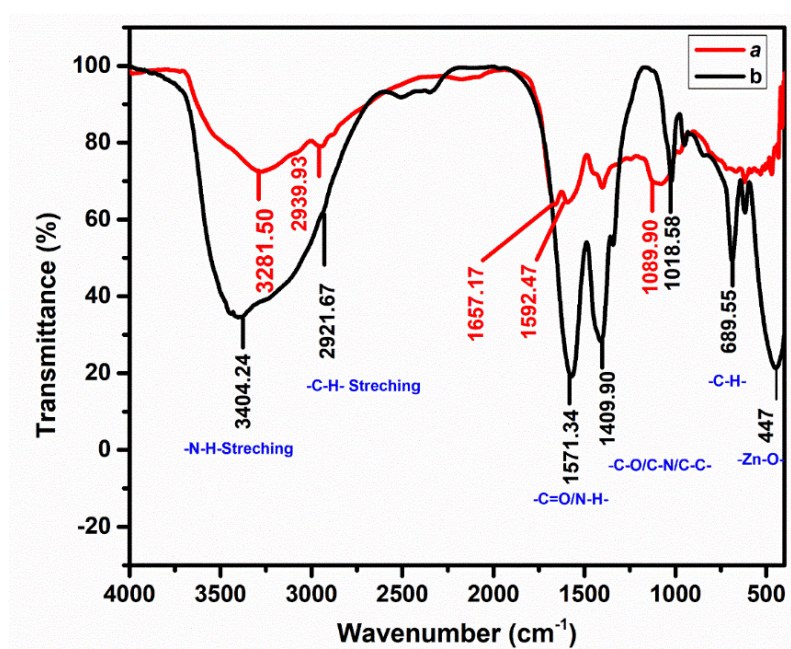
Fig. 4.16 FTIR spectra of (a) mycelial free filtrate of *C. geniculatus* and (b) biosynthesized ZnO nanoparticles

Alteration in FTIR absorption bands and shifts in band positions at 3281.50-3404.24, 2939.93-2921.67, 1592.47-1571.34 and 1089.90-1018.58 (Fig. 4.16) supported a predominant role of amide I, amide II, aromatic and aliphatic amines in ZnO nanoparticles synthesis and can lead to their possible stabilization.

The nanoparticle-protein interactions may arise due to the presence of free amino, phosphate, or carboxyl group or electrostatic attraction. Consequently, stabilization of ZnO nanoparticles by surface-coated protein is possible. The vibration bands between 400 and 600 cm^{-1} were assigned to Zn-O (metal-oxygen) (Kundu et al. 2014) and subsequently vibration band at 447 cm^{-1} was attributed to ZnO nanoparticles. The overall observations confirmed that the presence of extracellular metabolites (proteins) in the filtrate was found to form a coating on the ZnO nanoparticles surface. However, these proteins in the filtrate prevented nanoparticles from agglomerating and subsequently offered stabilization by forming a coating on the surface of the nanoparticles.

The XRD pattern (Fig. 4.17) exhibits peaks at 2θ = 31.43, 34.03, 35.86, 47.11, 56.17, 62.37, 65.97, 67.45, 68.59, 76.44 attributed to the (100), (002), (101), (102), (110), (103), (200), (112), (201) and (202) planes of hexagonal ZnO nanoparticles respectively which was indexed with JCPDS file No. 01-089-1397.
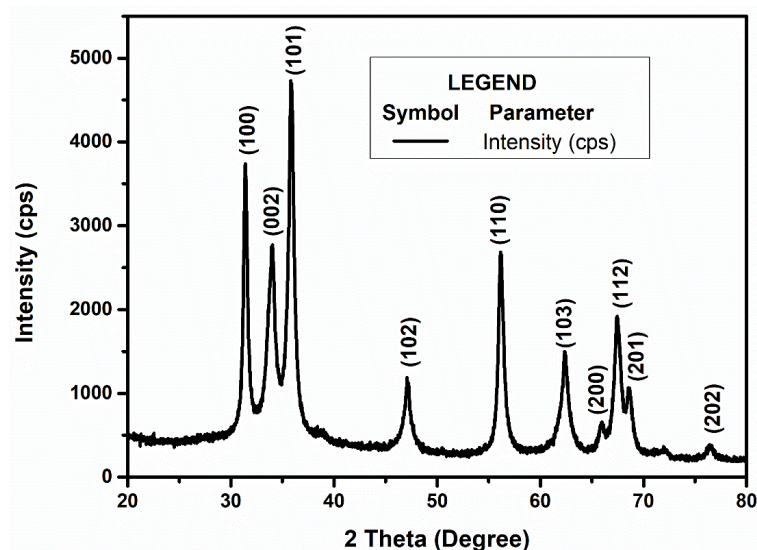
Fig. 4.17 X-ray Diffraction pattern of biosynthesized ZnO

An absence of diffraction peaks associated with any other phase or impurity in XRD analysis confirmed the purity of biosynthesized ZnO nanoparticles (Selvarajan et al. 2013;

Kundu et al. 2014) which was further demonstrated by EDX analysis (Fig. 4.18). The EDX spectrum manifested strong peak intensity of Zn at 1.1 KeV, and an oxygen peak at 0.6 KeV signified the existence of oxygen as it is an oxide form of zinc (Jain et al. 2014; Kundu et al. 2014). EDX spectrum contains a signal for carbon as a carbon grid is used for sample preparation. The calculated lattice parameters and unit cell volume (UCV) values, as shown in Table 4.3, are in agreement with previous findings and confirmed hexagonal (wurtzite structure) phase of biogenic ZnO nanoparticles (Jayaseelan et al. 2012; Morkoc and Ozgur. 2009).
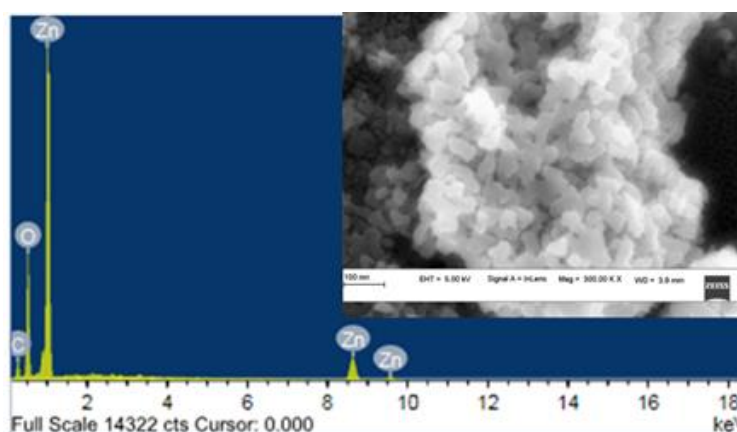
Fig. 4.18 EDX spectrum recorded in spot profile mode from one of the densely populated ZnO nanoparticles area. FESEM micrograph is shown as an inset at a 100 nm scale bar

Table 4.3 Lattice parameters of biosynthesized ZnO nanoparticles under optimum condition

Material	2θ (deg.)	hkl	d-spacing (Å)	Lattice parameter (Å)	UCV (Å^3)
ZnO	31.43	100	2.844	a = 3.285799	49.28034
	34.02	002	2.6348	c = 5.270612	
	36.86	101	2.501	c/a= 1.604058	

The obtained c/a ratio (Table 4.3) is close to the ideal value of a hexagonal cell, i.e., 1.633. The lattice ionicity and stability may lead to deviance from the ideal hexagonal phase (Morkoc and Ozgur 2009). The fluorescence spectroscopy results depicted in Fig. 4.15 revealed the presence of point defects such as zinc antisites and oxygen vacancies that play a role in the deviation of lattice parameters from ideal values and also increases the lattice constants (Morkoc and Ozgur 2009). Diffraction peak line broadening in XRD referred to

the nanometer range of biosynthesized ZnO nanoparticles (Selvarajan and Mohanasrinivasan 2013).

The biogenic ZnO nanoparticles were found to be discrete, polydisperse, and quasi-spherical with 2 nm - 9 nm with an average size of 5.25 ± 1.43 nm with a polydispersity index of 0.27 (Fig. 4.19 (a, b, c, d, and e)). A cysteine group at numerous positions in proteins directs quasi-spherical-shaped nanoparticles (Makhal et al. 2012). The distinct lattice fringes observed in the HRTEM analysis further confirms the high crystallinity of biogenic ZnO nanoparticles. Lattice fringes with a value of 0.28 nm correspond to the 100 crystal plane, as shown in Fig. 4.19 (c). The SAED pattern represented in Fig. 4.19 (d) can be well indexed with (100), (002), (101), (102), (110), (103), (200), (112), (201) and (202) reflection lines of a hexagonal phase of biogenic ZnO, which is in accordance with XRD results.

66
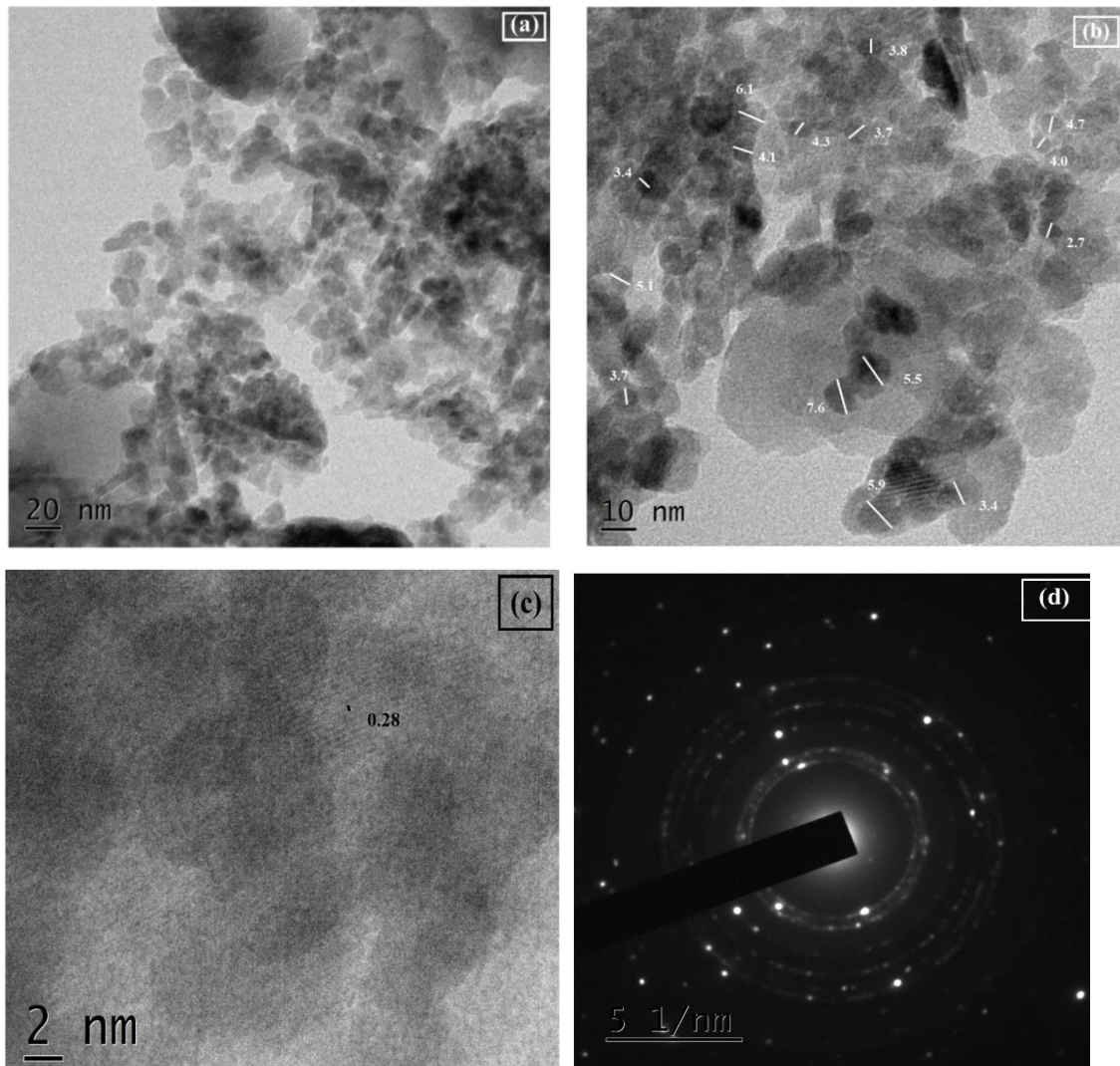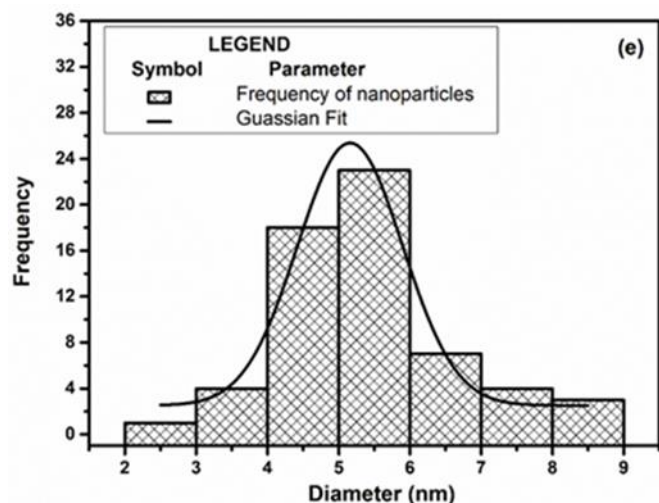
Fig. 4.19 HRTEM micrograph of biosynthesized ZnO nanoparticles at a scale bar of (a) 20 nm, (b) 10 nm, (c) 1 nm, (d) SAED pattern, and (e) particle size histogram with the Gaussian fit

4.1.4 Role of extracellular proteins in the synthesis of ZnO nanoparticles

The ZnO nanoparticle synthesis may occur due to: (i) chemical conversion of zinc acetate dihydrate by the secreted extracellular proteins or carbohydrates in the mycelial filtrate; and or (ii) enzyme-mediated biological transformation. The reaction mixture in the flask (b) displayed a time-dependent color change from yellowish-green to white with intensity increased during the incubation period, as shown in Fig. 4.20. White coalescents start to appear in the flask (b) owing to the excitation of surface plasmon resonance (SPR) vibrations (Kundu et al. 2014), indicating the initiation of the transformation of ZnO. Whereas flask (a) and (c) were observed to maintain their original color, suggesting that proteins play a vital role in ZnO nanoparticle synthesis (Fig. 4.20).
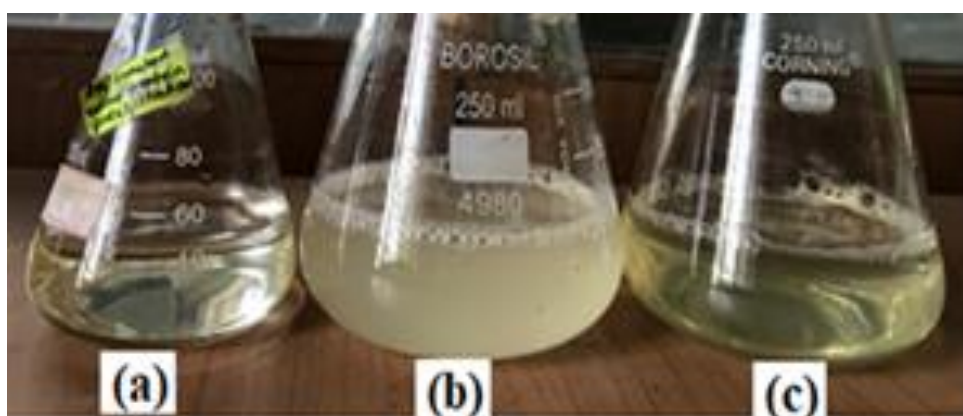
Fig. 4.20 Erlenmeyer flask containing the filtrate of *C. geniculatus* (a) precursor salt (zinc acetate) with protein-free filtrate (b) precursor salt and (c) without precursor salt

Further, the role and nature of proteins in the synthesis of ZnO nanoparticles were determined by recording the UV-vis spectra, as shown in Fig. 4.21. The absence of signature peak associated with proteins or nanoparticles in UV-vis spectra of positive control (pink line), i.e., precursor salt with protein-free filtrate, confirms that proteins are a prerequisite for nanoparticle synthesis. UV-vis spectroscopy analysis of flask (c) containing negative control (blue line), i.e., mycelial free filtrate without precursor salt exhibits a signature peak at 280 nm (Fig. 4.21) due to $\pi \rightarrow \pi$ transitions arising from tyrosine and tryptophan moieties of proteins (Sastry et al. 2003; Kundu et al. 2014; Gole et al. 2001). Further, the concentration of proteins present in the filtrate was estimated by Lowry assay and found to be 0.375 ($\pm$ 0.0014) mg/mL. These proteins present in the filtrate of *C. geniculatus* may form a coat on ZnO nanoparticles and aids in stabilization (Jain et al. 2011), which was further confirmed by the fluorescence spectroscopy and FTIR analysis.

Heat denaturation of proteins was carried out to understand the nature of the proteins present in the mycelial free filtrate. Denatured (black line) and native (red line) proteins with precursor salt show a characteristic absorption peak at 360 nm, which revealed that the native form of protein is not essential for nanoparticle synthesis (Fig. 4.21). However, the synthesis of nanoparticles is a nonenzymatic process as the enzyme activity depends on the native form of the enzyme, which changes during heat denaturation (Daniel et al. 2008).
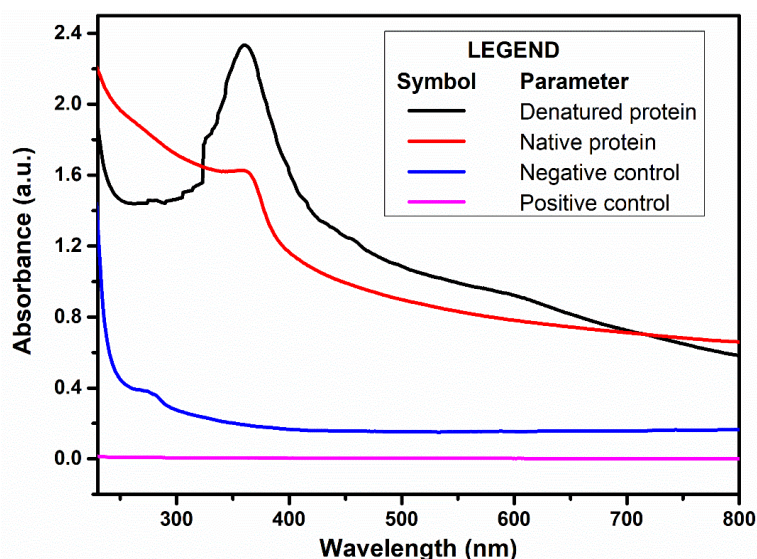
Fig. 4.21 Role and nature of extracellular proteins in the synthesis of ZnO nanoparticles

Denatured proteins showed an increased rate of ZnO nanoparticle formation as compared to the native proteins (Fig. 4.21). Heat denaturation leads to hydrogen bond

breaking resulted in the destruction of the hydrophobic core, which increases the interaction between Zn metal ion and amino acid residues (Xie et al. 2007; Maliszewska et al. 2014). Previous studies demonstrated, the interaction between amino acids and metal ions is responsible for nanoparticle synthesis (Jain et al. 2013; Xie et al. 2007). However, it can be concluded that the reduction of metal ions resulted from the amino acid residues rather than the enzymatic process. Further, the phase and purity of synthesized ZnO nanoparticles from denatured protein were confirmed by XRD, FESEM-EDX analysis. The XRD pattern depicts peaks at $2\theta = 31.72, 34.17, 36.09, 47.42, 56.55, 62.59, 68.00$ attributed to the (100), (002), (101), (102), (110), (103), and (112) planes of hexagonal phase of ZnO nanoparticles (Fig. 4.22) respectively which was well indexed with ICSD No. 0650726.
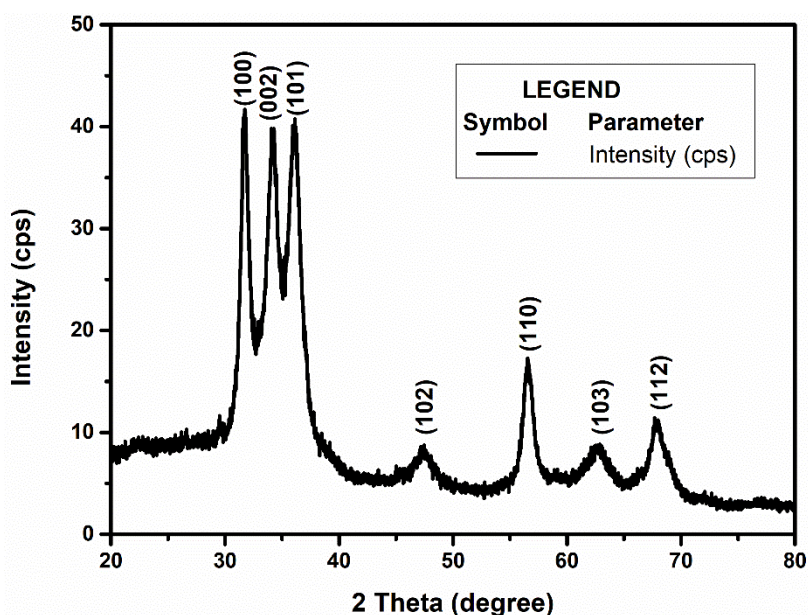
Fig. 4.22 X-ray diffraction pattern of ZnO nanoparticles synthesized from denatured proteins

Lattice parameters and unit cell volume of synthesized nanoparticles from denatured proteins are represented in Table 4.4, which confirms the hexagonal wurtzite structure of ZnO nanoparticles.

Table 4.4 Lattice parameters of ZnO nanoparticles synthesized from denatured proteins

Material	2θ (deg.)	hkl	d-spacing (Å)	Lattice parameter (Å)	UCV (Å^3)
ZnO	31.72	100	2.818535	a = 3.2546	48.18
	34.17	002	2.621788	c = 5.2528	
	36.09	101	2.486314	c/a = 1.613	

EDX spectrum recorded in spot profile mode from one of the densely populated ZnO nanoparticles area manifests a strong peak at 1.1, 8.6, and 9.6 keV corresponds to Zn Lα, Zn K α, and Zn Kβ, respectively. The presence of a peak at 0.5 keV ascribed to O kα confirms the oxide form of Zn metal (Fig. 4.23). The absence of any other peak related to any other metal ensures the purity of synthesized ZnO nanoparticles. The morphology of synthesized ZnO nanoparticles is found to be quasi-spherical. The appearance of the quasi-spherical shape of synthesized biogenic nanomaterial is in accordance with the previous reports, which hypothesized that the quasi-spherical shape of nanoparticles arises due to the presence of a cysteine group at numerous positions in proteins (Makhal et al. 2012).
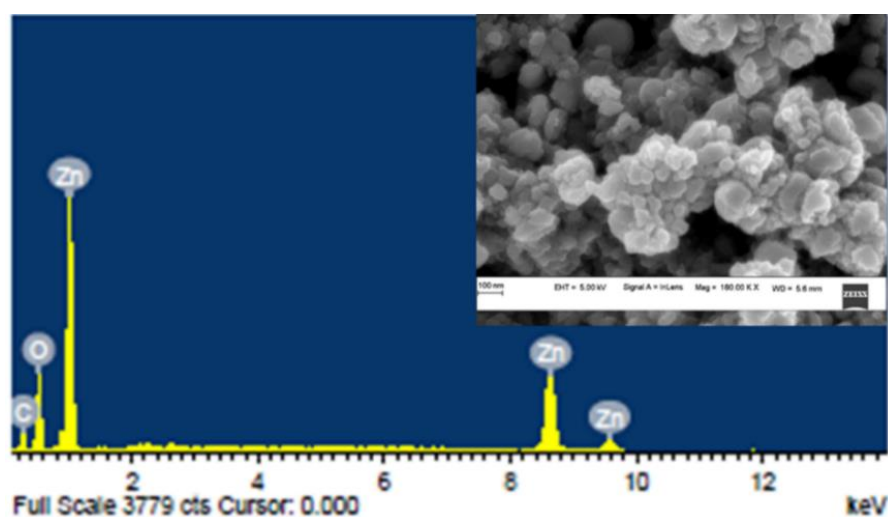
Fig. 4.23 FESEM-EDX spectrum of ZnO nanoparticles synthesized from denatured proteins

The FTIR spectrum of ZnO nanoparticles synthesized from denatured proteins was recorded to understand the role of denatured proteins in the reduction and subsequent

stabilization of ZnO nanoparticles (Fig. 4.24). As depicted in Table 4.5, amide I, amide II, aromatic, and aliphatic amines from denatured proteins are involved in the possible reduction and stabilization of ZnO nanoparticles.
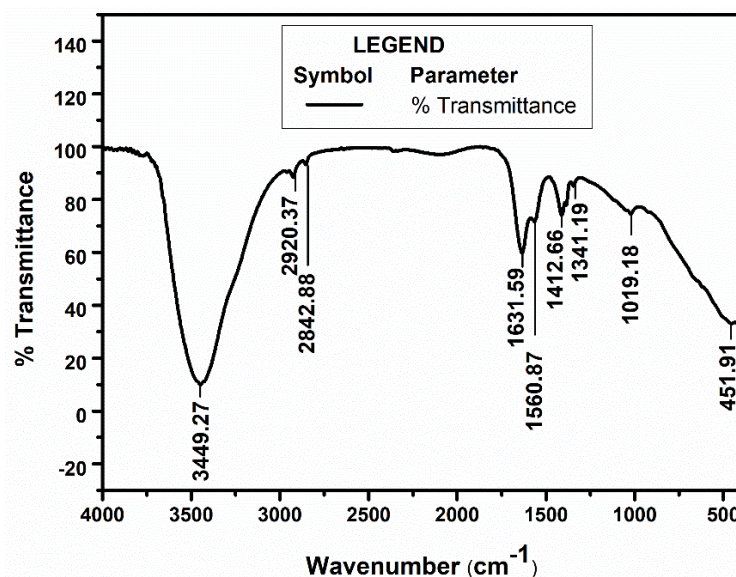
Fig. 4.24 FTIR spectrum of ZnO nanoparticles synthesized from denatured proteins

Table 4.5 Constituents of denatured proteins involved in the reduction and stabilization of ZnO nanoparticles

Wavenumber (cm^{-1})	Functional Group
3449.27	Intermolecular hydrogen bonds arising from NH_2 and OH groups in protein molecules
2920.37, 2842.88	Symmetric and asymmetric stretching vibration of sp3 hybridized CH_2 groups, respectively
1631.59, 1560.87	Amide I and II bands of proteins
1412.66	Carboxyl group
1341.19, 1019.18	C–N stretching vibrations of aromatic and aliphatic amines, respectively
451.91	Zn-O

4.1.5 Analysis of fungal proteins in synthesis and capping of ZnO nanoparticles

The protein profiles were analyzed by SDS-PAGE followed by Coomassie brilliant blue staining (Fig. 4.25) to determine the role of extracellularly secreted proteins by *C. geniculatus* in the synthesis and capping of ZnO nanoparticles. The protein profile in Lane

2 distinctly indicated the existence of numerous bands of molecular weight from 97 kDa to 36 kDa (Fig. 4.25). These proteins may be accountable for the synthesis/stabilization of nanoparticles. Similar findings were also reported in the literature where the vital role of extracellularly secreted proteins in synthesis and stabilization of synthesized nanoparticles were discussed (Sastry et al. 2003; Kundu et al. 2014).

The SDS-treated ZnO nanoparticles resulted in the detachment of fungal proteins from the surface of nanoparticles and subsequently analyzed by SDS-PAGE exhibited the presence of bands at 52 and 58 kDa (lane 4), which were absent in the SDS untreated sample (Lane 3). These resultant protein bands are similar to the protein band present in *C. geniculatus* filtrate (Lane 2). Consequently, 58 and 52 kDa proteins act as capping material in ZnO nanoparticle synthesis and impart stability to the biogenic nanomaterial. Further, existing biogenic capping eliminates the capping/ coating of nanoparticles, which is essential in various applications.
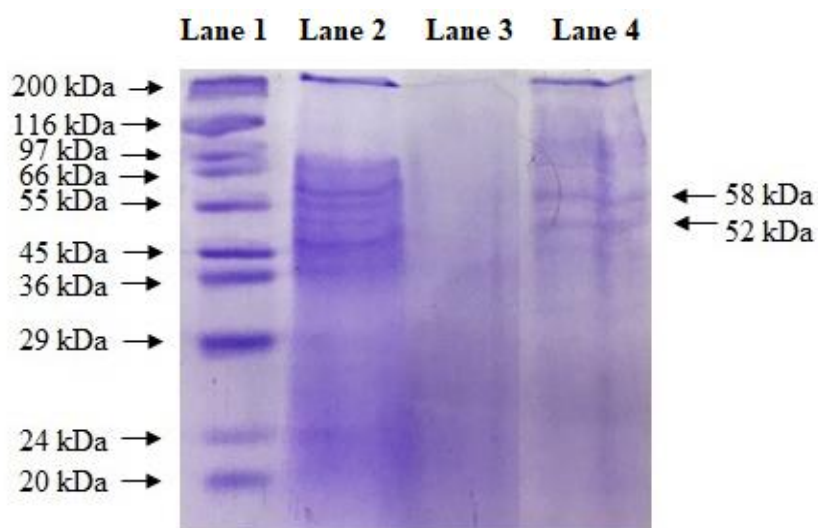
.**Fig. 4.25** SDS-PAGE analysis exhibiting proteins as capping agents on the ZnO nanoparticles surface

Lane 1 is 14.2 kDa-200.0 kDa prestained molecular weight markers; Lane 2, a profile of dialyzed fraction of extracellular proteins secreted by *C. geniculatus*; Lane 3, SDS untreated nanoparticles indicated an absence of protein band and Lane 4, SDS treated nanoparticles stated the presence of 2 bands of 58 kDa and 52 kDa proteins.

4.1.6 A mechanism for the biosynthesis of nanoparticles

The schematic illustration of the plausible mechanism for *C. geniculatus* mediated synthesis of biogenic ZnO nanoparticles is postulated (Fig. 4.26). The synthesis of biogenic ZnO nanoparticles was carried out in two steps: (i) the first step involves transforming zinc

acetate into ZnO and subsequently, (ii) protein capping on the ZnO nanoparticles surface. The UV-vis spectroscopy, fluorescence spectroscopy, FTIR, and SDS-PAGE analysis revealed the possibility of proteins as capping material in ZnO nanoparticle synthesis. Protein with a molecular weight in the range of 97 kDa - 36 kDa involved reducing zinc acetate into ZnO nanoparticles. Consequently, proteins with a molecular weight of 58 kDa and 52 kDa form a coat around the synthesized ZnO nanoparticles. FTIR spectroscopy results in this study confirmed the presence of amide I, amide II, and carboxyl groups (as shown in Fig. 4.16); subsequently, these groups from the above-mentioned proteins are involved in protein-nanoparticle interaction and halt the aggregation and provide stability.

C Fungal extracellular protein (Mol. wt. range 97-36 kDa)
⊕ Zinc ion
O Acetate ion
✳ Water molecules
● ZnO nanoparticles
✺ 58 kDa and 52 kDa capped ZnO nanoparticles
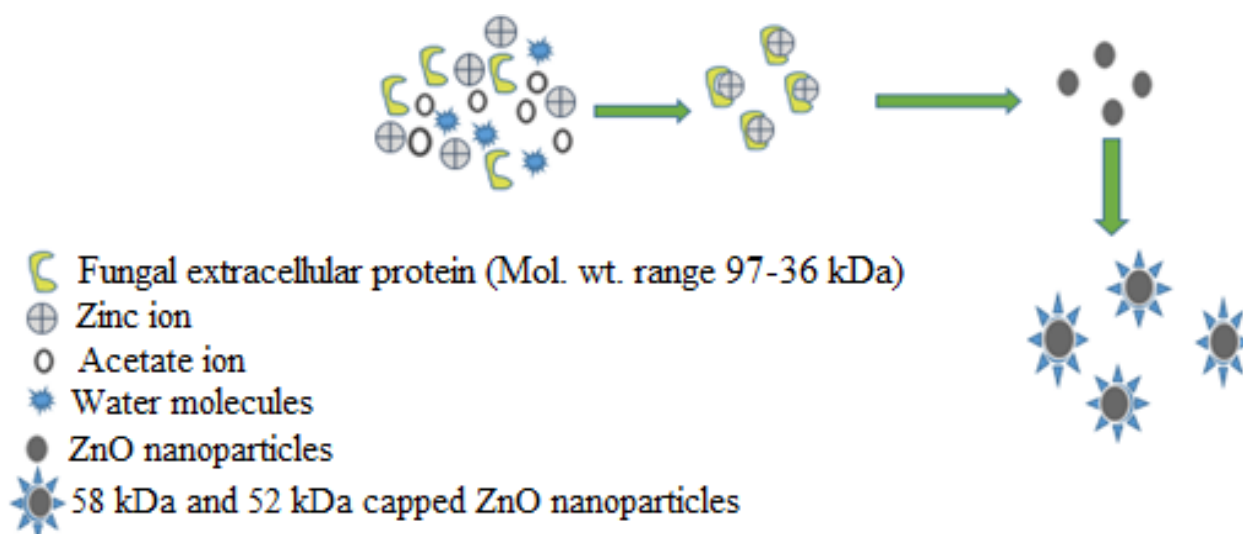
Fig. 4.26 Hypothesized mechanism showing the synthesis of biogenic ZnO nanoparticles

4.2 Optimization of parameters affecting photocatalytic performance of biosynthesized ZnO

The efficacy of biosynthesized ZnO nanoparticles for the degradation of p-NP and BPA under UV light was studied. BPA and p-NP solution in the absence of catalyst were found to be stable under UV irradiation of 180 min and 480 min, respectively (Fig. 4.27). Under the dark conditions, initially, a slight decrease in BPA and p-NP concentration was noticed and then remained unchanged in the presence of a catalyst. The Adsorption of pollutant molecules on the catalyst surface leads to an initial reduction in its concentration (Rajamanickam and Shanthi 2012). In the presence of the catalyst, p-NP displays 48 % degradation within 480 min (Fig. 4.27 a) and BPA displays 44.4 % of degradation under 180 min of UV irradiation, as shown in Fig. 4.27 b. The decreased concentrations of p-NP and BPA may be due to the degradation under UV irradiation, further confirmed by LC-

MS, TOC and COD analysis. Moreover, the reaction parameters such as catalyst loading, pH of the reaction mixture and pollutant concentration were optimized to attain the higher removal efficiency.
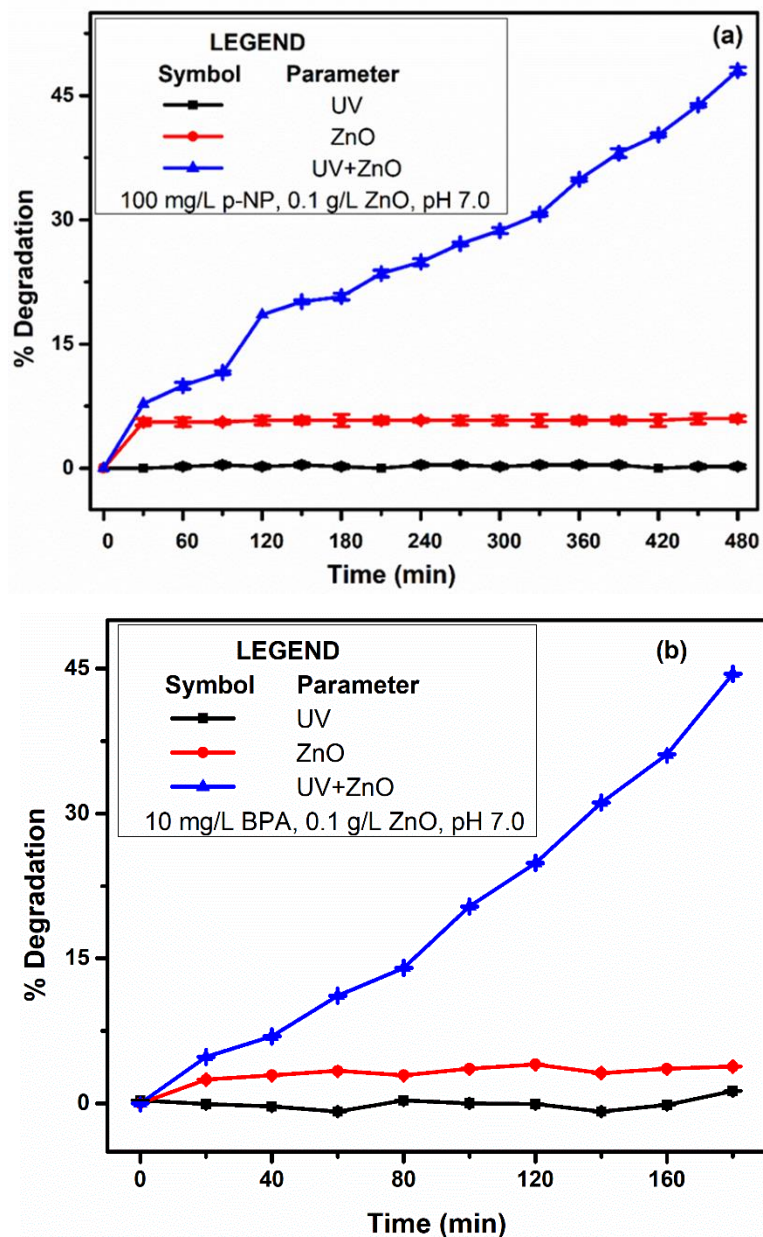
Fig. 4.27 Photocatalytic performance of ZnO for (a) p-NP and (b) BPA

4.2.1 Reaction pH

The reaction mixture's pH has a profound impact on both, surface charges of the catalyst and the structure and ionization degree of pollutants (Bechambi et al. 2015). The number of active sites on the catalyst surface depends on the concentration of H^+ and OH^- in solution, resulting in an alteration of adsorption property and photocatalyst degradation

ability (Wang et al. 2010). In this study, the influence of pH on ZnO's photocatalytic performance was evaluated by varying the pH from 5.0 to 11.0.
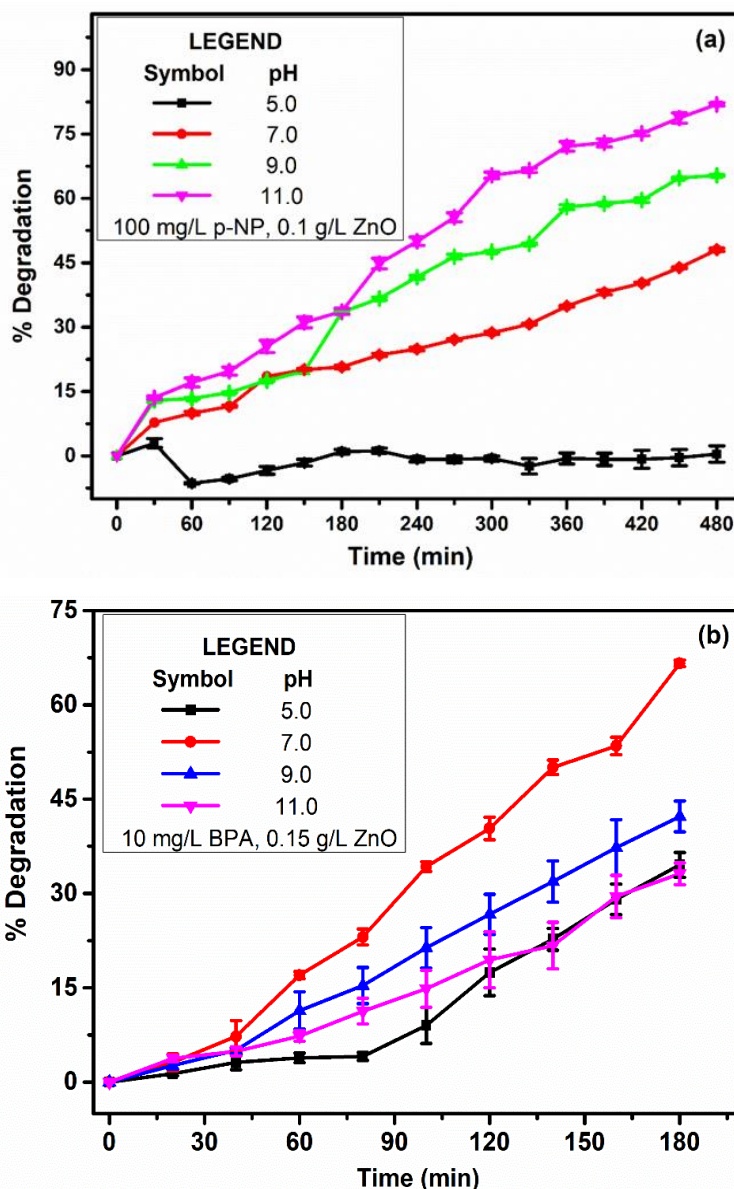
Fig. 4.28 Influence of pH on (a) p-NP degradation (b) BPA degradation

From Fig. 4.28, it is noted that an increase in pH from 5.0 to 7.0 increases the BPA degradation efficiency from 34.5 % to 66.6 %. Further, an increase in pH from 7.0 to 11.0 resulted in reduced degradation efficiency from 66.6 % to 33.14 %. However, it is observed that p-NP degradation efficiency increased with an increase in initial pH from 5 to 11.0. The perceived trends can be allied with the electrostatic interaction amongst BPA, p-NP and catalyst surface, which is explained based on a pH at the point of zero charge (pH$_{pzc}$). pH$_{pzc}$ of ZnO was measured by the pH drift method and is found to be 7.9 (Fig. 4.29). Thus,

the surface of ZnO is positively charged below the pHpzc and negatively charged above the pHpzc.
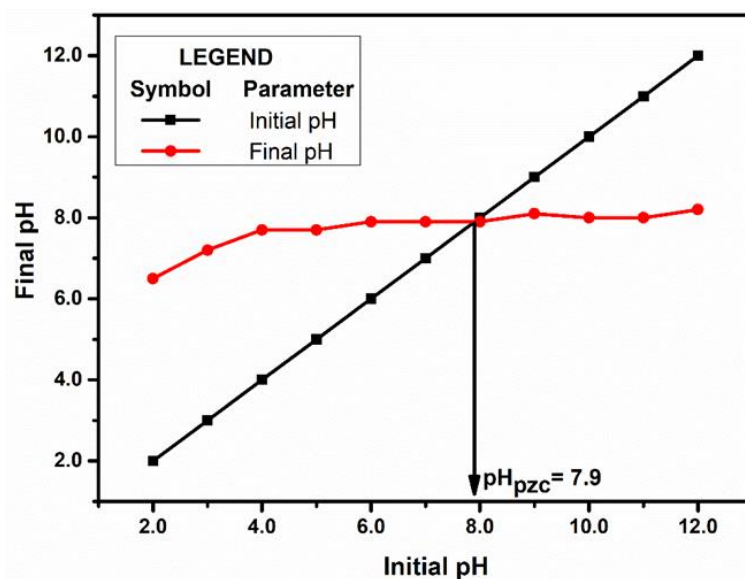
Fig. 4.29 pH$_{pzc}$ of ZnO nanoparticles

p-NP has a pKa value of 7.08, which shows that pH < pKa, p-NP exists in molecular form, whereas pH > pKa indicates that it exists in its dissociated form as a negative phenolate ion (Zhang and Xiong 2015). Under alkaline conditions, electrostatic repulsion leads to decreased interaction between p-NP and electron-hole of ZnO. However, this effect may result in the increased production of •OH on the surface of ZnO with increased concentration of OH$^-$ in solutions, resulted in the increased mass transfer efficiency of •OH. Consequently, increased degradation efficiency under alkaline conditions (Tao et al. 2012).

BPA has a pKa value of 9.6 and 10.2, which indicates that the BPA exists in a nonionic form below pH 9.6 and above this pH exists in ionic form as BPA$^-$ and BPA^{2-} (Daskalaki et al. 2011). BPA exists in the nonionic form at neutral pH, favors the adsorption on the catalyst surface, and leads to higher degradation (Lee et al. 2016; Rani and Shanker 2018). However, the addition of the 0.1 N HCl solution to adjust the reaction mixture's pH at 5.0 leads to the formation of chlorate ions, thereby hindering the interaction between ZnO nanoparticles and BPA molecules, resulting in decreased degradation efficiency (Rani et al. 2018).

4.2.2 Catalyst loading

The catalyst loading is one of the crucible parameters in photocatalytic degradation. The excess usage of catalysts can be avoided by optimizing their concentration to attain higher photocatalytic degradation efficiency (Lee et al. 2016). The degradation experiment was carried out using different catalyst loading of 0.05 to 0.2 g/L. As shown in Fig. 4.30 (a), the p-NP degradation efficiency increases with an increase in catalyst loading from 0.05 to 0.1 g/L and then decreases marginally with a further increase in catalyst concentration. Also, an increase in catalyst dosage from 0.1 to 0.15 g/L increases the degradation efficiency of BPA from 44.5 % to 66.6 % (Fig. 4.30 b).
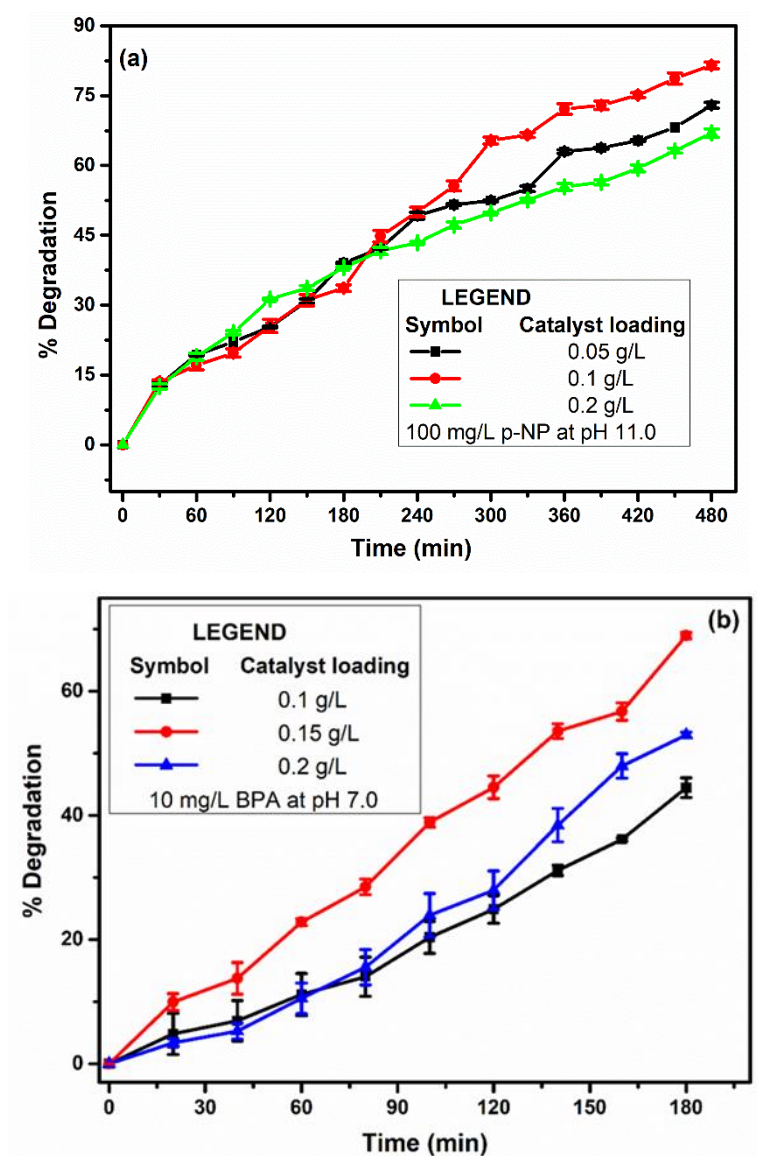
Fig. 4.30 Influence of catalyst loading on (a) p-NP and (b) BPA degradation

The number of active sites increases with an increase in catalyst loading, facilitating more absorption of photons on the catalyst surface, leading to better degradation (Pham et al. 2020). Whereas, if the catalyst loading is higher than the optimal value, the particle starts agglomerating, resulting in a decrease in specific surface area and photon energy absorption, with reduced degradation efficiency (Neppolian et al. 2002). Moreover, excess catalyst particles lead to light scattering and photon energy that reduces photocatalytic activity (Bechambi et al. 2016).

4.2.3 Initial pollutant concentration

The degradation efficiency of 85.18 % was achieved in 180 min for 5 mg/L of BPA. Further, increasing BPA concentration from 10 to 20 mg/L, the degradation efficiency significantly decreased from 66.6 % to 18.58 %, as shown in Fig. 4.31 b.
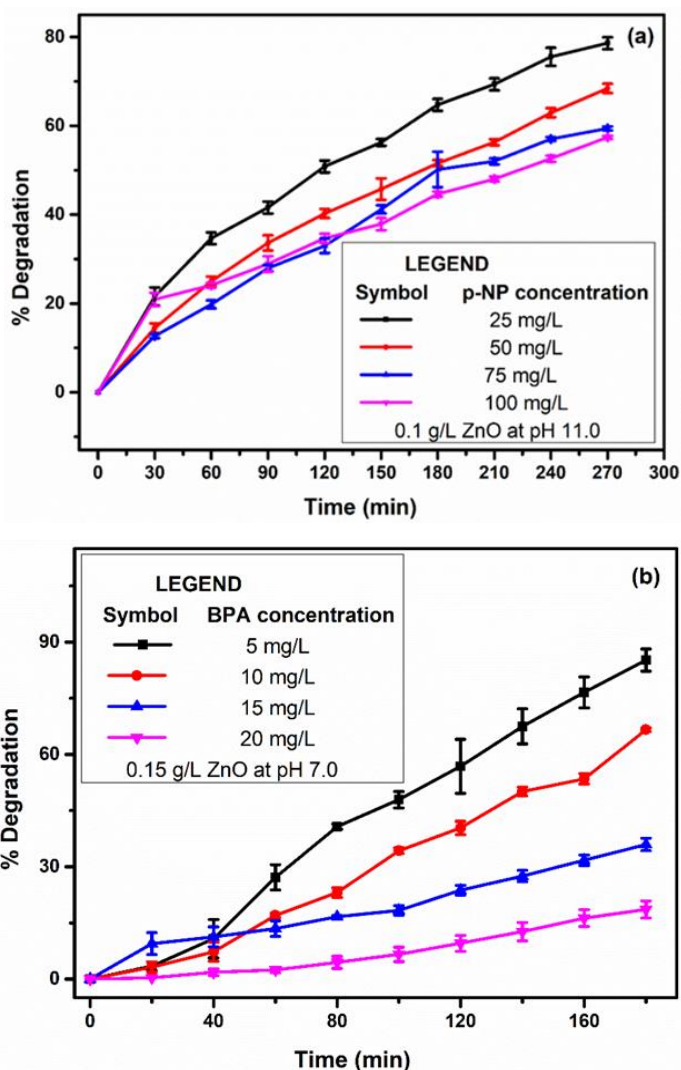
Fig. 4.31 Influence of initial pollutant concentration on (a) p-NP degradation and BPA degradation

The p-NP degradation efficiency decreases with an increase in initial pollutant concentration from 25 mg/L to 100 mg/L (Fig. 4.31 a). At a constant catalyst loading, an increase in pollutant concentration decreases the path length of the photons into the solution and at low pollutant concentration reverse effect is observed; thus, at the lower pollutant concentration number of photon absorption by a catalyst is high (Neppolian et al. 2002; Rajamanickam and Shanthi 2012). The detrimental effect on higher concentrations can be explicated as follows: (i) at higher concentrations, a surplus of BPA and p-NP molecules present on the catalyst surface behave as blinding elements from the light and available active sites get saturated, resulting in decreased degradation efficiency (Kumar et al. 2019). (ii) Increasing the BPA and p-NP concentration also leads to the generation of more intermediates that may compete with BPA and p-NP molecules in interacting with the catalyst along with the light blinding effect (Pham et al. 2020).

4.2.4 Reaction kinetics

The kinetic parameters of p-NP and BPA degradation for initial pollutant concentrations were tabulated in Table 4.6 and 4.7, respectively. In the case of p-NP, the correlation coefficient (R^2) from the first-order kinetic model is higher than the others (zero and second-order), as shown in Table 4.6.
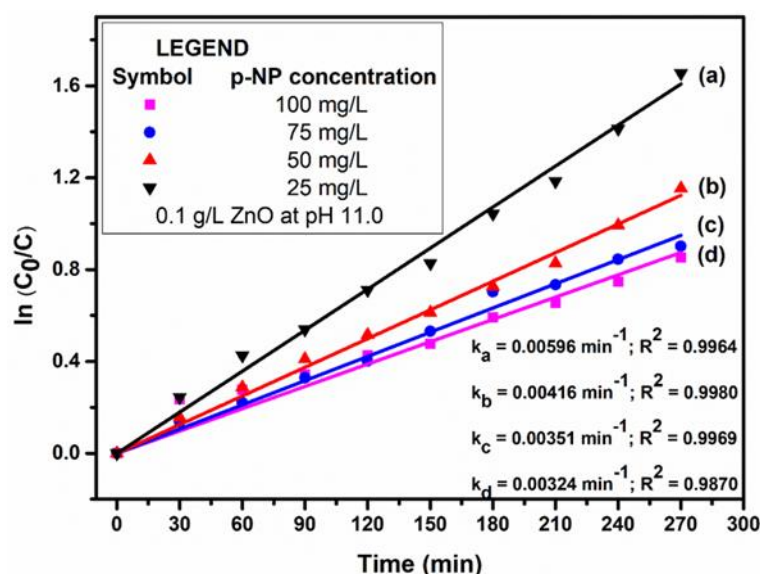
Fig. 4.32 First-order linear plot of ln (C_0/C) Vs. Irradiation time

As the initial concentration of p-NP was increased, the rate of degradation decreased. The rate constant (k) decreases with an increase in p-nitrophenol concentration from 25 mg/L to 100 mg/L, as shown in Fig. 4.32. Therefore, as the initial pollutant

concentration increases, the catalyst surface needed for the degradation also increases. As the catalyst loading is constant, the number of primary radicals formed on the catalyst surface is constant and, in turn, decreases in pollutant degradation with an increase in pollutant concentration.

From Table 4.7, it can be observed that BPA concentration at 15 mg/L follows first-order reaction kinetics. In contrast, BPA concentrations at 5, 10 and 20 mg/L follow zero-order kinetics due to the reactant saturation, electron transfer and light supply (Chiu et al. 2019). Olis (2018) reported that if the reaction rate is truly zero-order, then the initial rate, $k_o = k_1 C_0$ = constant. The initial experimental rate was calculated from the product of k_1 and C_0 to obtain k_0, as given in Table 4.7. The reaction rate is not truly zero-order for BPA at a concentration of 5 and 10 mg/L; the actual reaction kinetic is disguised by zero-order. However, at 20 mg/L of BPA concentration, $k_o = k_1 C_0$ indicates that the reaction is truly zero-order.

Table 4.6 Reaction kinetic parameters of p-NP

p-NP (mg/L)	Zero-order k_0 (mg L^{-1} min^{-1})	R^2	First-order k_1 (min^{-1})	R^2	Second-order k_2 (L mg^{-1} min^{-1})	R^2	k_0 $k_1 C_0$
25	0.08588	0.9700	0.0059	0.9974	4.5E-4	0.9268	1.475
50	0.1395	0.9828	0.00416	0.9980	1.3E-4	0.9471	0.208
75	0.1850	0.9859	0.00351	0.9969	7.0E-4	0.9779	0.263
100	0.2330	0.9656	0.00324	0.9870	4.6E-5	0.9765	0.324

Table 4.7 Reaction kinetic parameters of BPA

BPA (mg/L)	Zero-order k_0 (mg L^{-1} min^{-1})	R^2	First-order k_1 (min^{-1})	R^2	Second-order k_2 (L mg^{-1} min^{-1})	R^2	k_0 $k_1 C_0$
5	0.0210	0.9954	0.0119	0.8496	0.00552	0.7877	0.0595
10	0.0322	0.9903	0.00489	0.9593	0.0008	0.8867	0.0489
15	0.03049	0.9888	0.00236	0.9908	0.00018	0.9868	0.0354
20	0.01751	0.9531	0.0009	0.9458	0.00005	0.9390	0.018

4.2.5 Scavenging experiment

It is well known that oxidative radical species such as h^+, $\cdot OH$ and $\cdot O_2{}^-$ are mainly involved in the photocatalytic degradation of pollutants (Liu et al. 2017b). Moreover, the degradation efficiency of the photocatalytic reaction was decreased by eliminating the oxidative species by adding various radical scavengers (Zhu et al. 2017). Thus, the oxidation reactions were repressed differently by the addition of various scavengers, demonstrating the role of different reactive oxidative species in the photocatalytic degradation of pollutants. As shown in Fig. 4.33, the p-NP and BPA degradation decreased slightly upon the addition of BQ, indicating $\cdot O_2{}^-$ are not active radical species involved in photocatalytic degradation. However, the addition of IPA and EDTA-Na$_2$ have detrimental effects on p-NP and BPA degradation. The presence of IPA and EDTA-Na$_2$ leads to decreased photocatalytic degradation efficiency of p-NP to 37.74 % and 47.02 %, respectively. BPA exhibits reduced photocatalytic degradation efficiency to 36.45 % and 30.13 % in the presence of IPA and EDTA-Na$_2$, respectively. The degradation efficiency of p-NP decreased more profoundly in the presence of IPA, indicating $\cdot OH$ is the most active species involved in degradation compared to h^+. In contrast, in the case of BPA, a substantial decrease in degradation efficiency was observed in the presence of EDTA-Na$_2$, indicating h^+ is the most active species involved in degradation compared to $\cdot OH$. Thus, the decreased degradation efficiency in the presence of scavengers indicating $\cdot OH$ and h^+ are active radicle species involved in the degradation of p-NP and BPA.
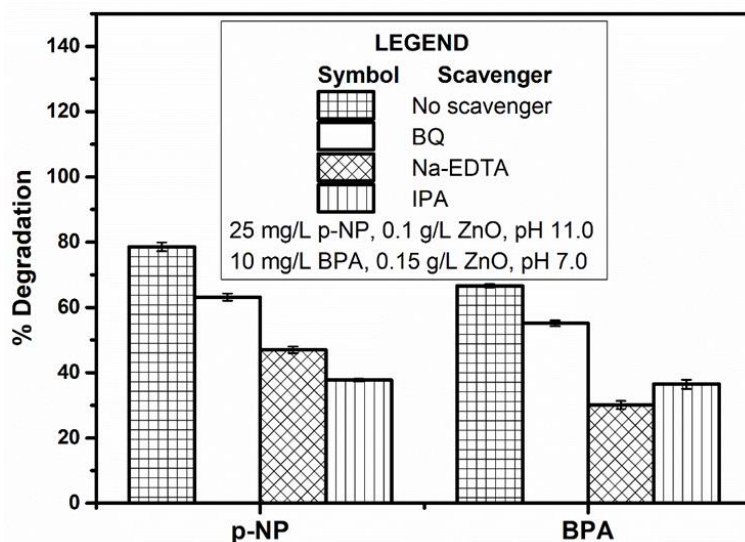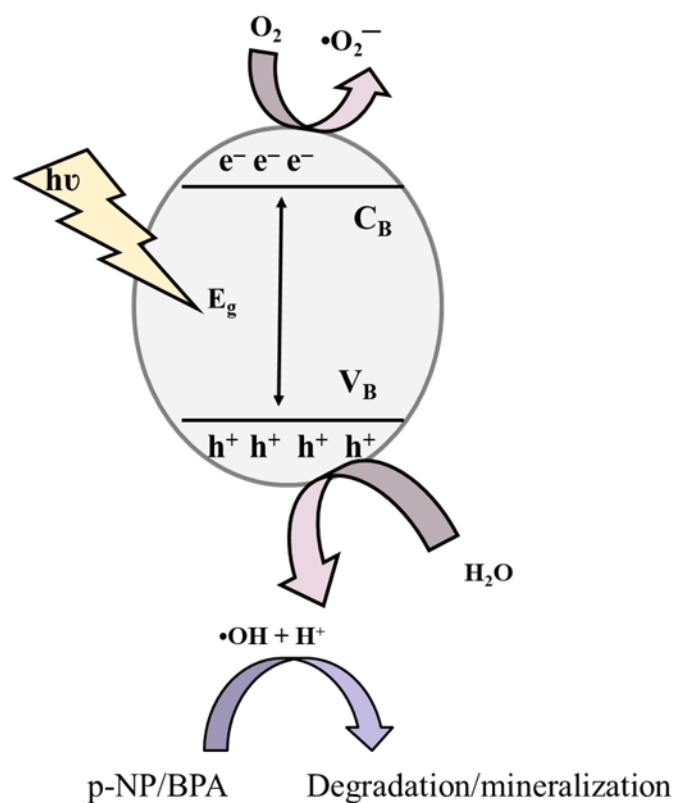
Fig. 4.33 (a) Influence of scavengers on p-NP and BPA degradation and (b) schematic representation of photocatalytic degradation mechanism.

From Fig. 4.33, the possible route for photocatalytic degradation of p-NP and BPA is represented in Fig. 4.33 (b) and could be proposed as follows:

Irradiation of photons with energy greater than or equivalent to a bandgap of ZnO leads to the movement of valence band (VB) electrons (e^-) to the conduction band (CB), resulted in the same number of positive h^+ in the valence band (Lee et al. 2016) and is given by equation 19,

$$ZnO + h\upsilon \rightarrow ZnO\ (e_{CB}^- + h_{VB}^+) \tag{19}$$

Thus, generated e^- and h^+ transfer to the particles' surface to either recombine or be involved in interfacial redox reactions (Rajamanickam and Shanthi 2012). Further, generated holes react with adsorbed water molecules or hydroxyl groups resulted in the production of •OH that react with p-NP/BPA as given by equation (20),

$$H_2O + h_{VB}^+ \rightarrow •OH + H^+ \tag{20}$$

Moreover, holes lead to direct oxidation of p-NP and BPA to the degradation products (Ding et al. 2016) and is given by equation 21,

$$p\text{-NP/BPA} + h^+ \rightarrow \text{Degradation products} \qquad (21)$$
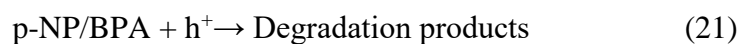
When e^- in conduction band reacts with O_2 leads to the formation of $\bullet O_2^-$ and is given by equation (22),

$$e_{CB}^- + O_2 \rightarrow \bullet O_2^- \qquad (22)$$

These superoxide species ($\bullet O_2^-$) are highly unstable and reactive. When BQ is added to the system, it will scavenge $\bullet O_2^-$ species and leads to slightly decreased degradation efficiency, revealed that $\bullet O_2^-$ are not active species in p-NP/BPA degradation. However, these $\bullet O_2^-$ radicals lead to the formation of $\bullet OH$ radicles (Di Paola et al. 2003) and it is governed by the following equation 23, 24 and 25,

$$\bullet O_2^- + H_2O \rightarrow OH^- + \bullet HO_2 \qquad (23)$$

$$\bullet HO_2 + \bullet HO_2 \rightarrow H_2O_2 + O_2 \qquad (24)$$

$$H_2O_2 + \bullet O_2^- \rightarrow \bullet O_2^- + OH^- + O_2 \qquad (25)$$
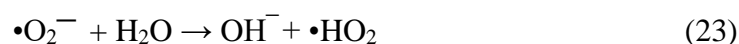
4.2.6 Catalyst reuse study

The regeneration of the catalyst is a crucial factor in scale-up studies for the effective removal of the pollutant. As shown in Fig. 4.34, the photocatalyst showed a p-NP and BPA degradation efficiency of 78.5 % and 66.6 %, respectively, during the first cycle. During the second and third cycles, the catalyst showed a reduction in the p-NP efficiency to 75.1 % and 72.3 %, respectively. At the same time, BPA exhibits reduced degradation efficiency to 63.2 % and 59.8 % during the second and third cycles, respectively. Further, when the catalyst was subjected to the subsequent cycle leads to a decrease in degradation efficiency of p-NP to 67.7 % and BPA to 54.21 %. It was observed that the second and third cycles showed a slight reduction in degradation efficiency of p-NP and BPA upto ~5 %. Thus, the degradation efficiency was not significantly decreased for a third consecutive cycle of catalyst reuse. However, at the end of the fourth cycle, the degradation efficiency was reduced to ~7 % for p-NP and ~9 % for BPA. Hence, photocatalyst can be reused for three subsequent cycles without much compromise in its degradation efficiency. The decreased degradation may be due to the loss of functional groups/active sites during the multiple regenerations and reuse processes.
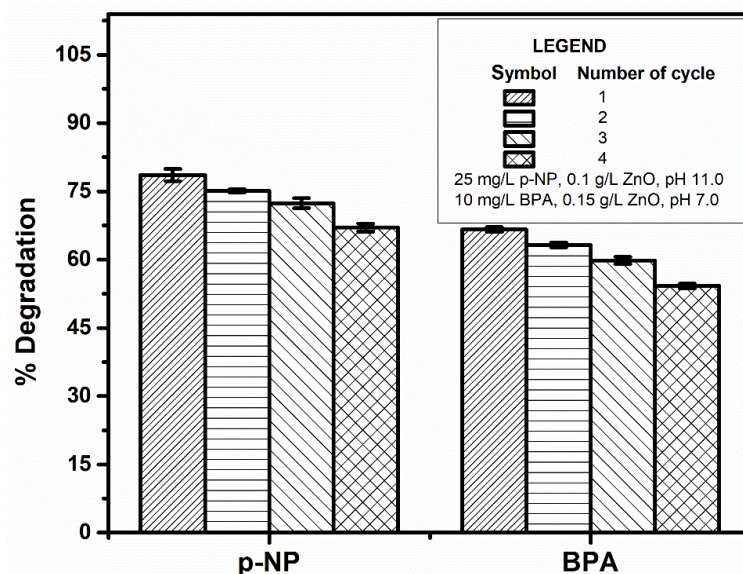
Fig. 4.34 Reuse study of catalyst

4.2.7 Characterization of degradation

The conversion of an organic substance into water and CO_2 is called mineralization. Various intermediates will be produced during the photocatalytic degradation of pollutants, which may be toxic or nontoxic. Therefore, mineralization should be ensured before discharging the pre-treated water into the ecosystem. The extent of mineralization of p-NP and BPA degradation was studied by TOC and COD analysis. As depicted in Fig. 4.35a, the significant TOC removal was not observed for photocatalysis of p-NP solution at the end of 120 min due to the generation of intermediates. However, as the irradiation time increased, significant TOC removal was observed after 120 min of p-NP degradation. An increase in irradiation time resulted in an increase in TOC and COD removal after photocatalytic degradation of p-NP (Fig. 4.35a) and BPA (Fig. 4.35b). The p-NP solution obtained after 300 min of irradiation shows 60% of COD removal and 50.97% of TOC removal. BPA solution after 220 min of photocatalysis exhibits 65.9% and 63.6% of TOC and COD removal, respectively.
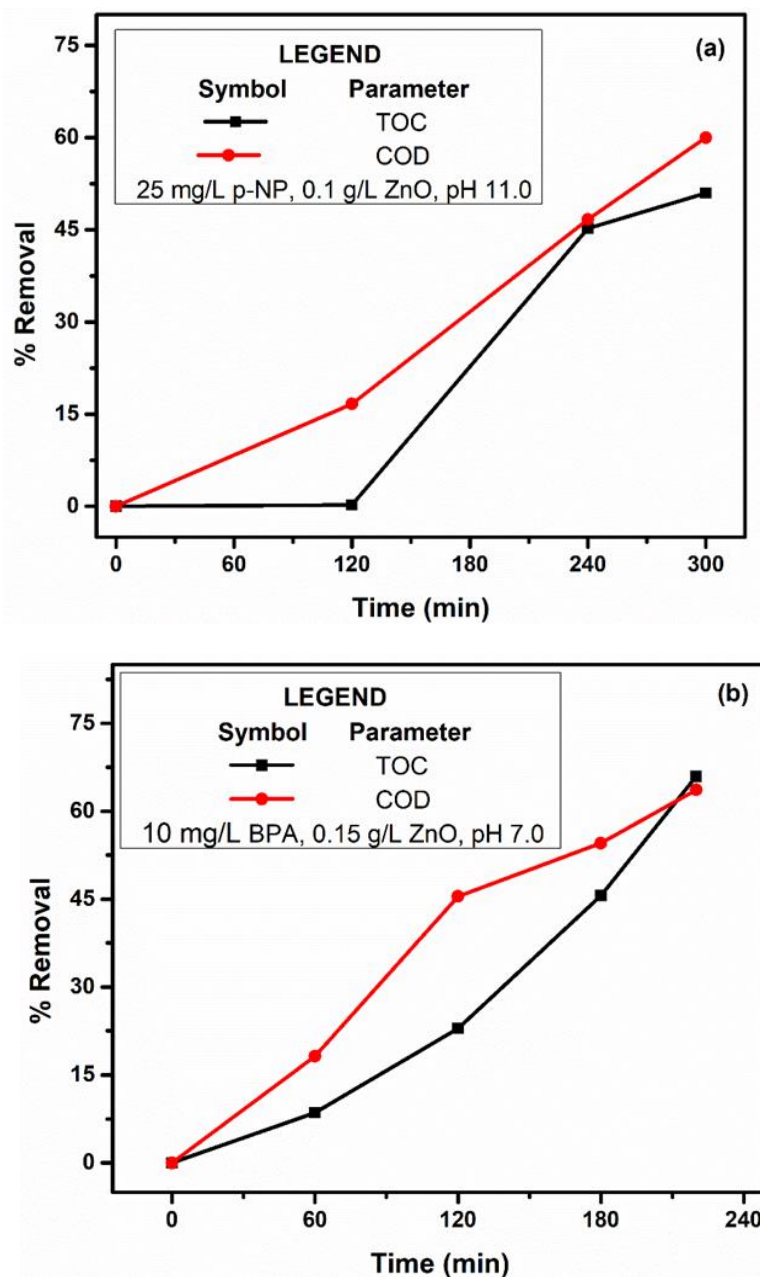
Fig. 4.35 Degree of mineralization (a) p-NP and (b) BPA

As shown in Fig. 4.36 (i), the degradation in p-NP was observed by a reduction in absorbance value at a characteristic wavelength over the period of 0 - 300 min using UV-vis analysis. Moreover, LC-MS analysis presented in Fig. 4.360 (ii), displays the reduction in peak intensity at a retention time of 6.3 min over 300 min of UV irradiation, confirms the degradation of p-NP. Based on LC-MS analysis and the mass to charge ratio obtained from mass spectra, the intermediate compounds were identified (Fig. 4.36 iii) and the possible degradation pathway of p-NP was proposed (Fig. 4.38 a).

Initially, p-NP showed a distinct peak at 6.3 min elution time with m/z = 139 (Fig. 4.36 iii). As discussed earlier, a radical scavenging experiment describes •OH radicals are

the most active species involved in photocatalytic degradation. Thus, the formation of p-nitrocatechol (Fig. 4.36 iii b) might be explained by the electrophilic attack of •OH radical on the ortho position of p-NP. Attack of the electrophilic radical •OH occurred at the ring positions activated by the presence of the two substituents. The phenolic –OH group was electron-donating for the electrophilic aromatic substitution, while the –NO$_2$ group was electron-withdrawing. The electron-donating substituents increased the electron density at the ortho and para positions, while the electron-withdrawing substituents were strongly deactivating and meta directing. When both the substituents (-OH and –NO$_2$) were present, the electrophilic attack would occur preferentially in ortho and para positions with respect to the –OH group (Rajmanickam and Shanthi 2012). In the case of p-nitrophenol, only p-nitrocatechol could be obtained.

Simultaneously, if •OH attacked the carbon carrying a nitro group, phenol radicals and/or its derivatives, such as hydroquinone (quinol), catechol and quinones (Fig. 4.36 iii c), would be generated and the radical addition-elimination releases nitrate ions. Furthermore, reactions of the primary intermediates mentioned above with •OH led to benzene ring cleavage and the formation of oxygenated aliphatic compounds such as propionic acid (Fig. 4.36 iii d). Finally, these aliphatic by-products would be mineralized to CO_2 and H_2O (Ramacharyulu et al. 2013).
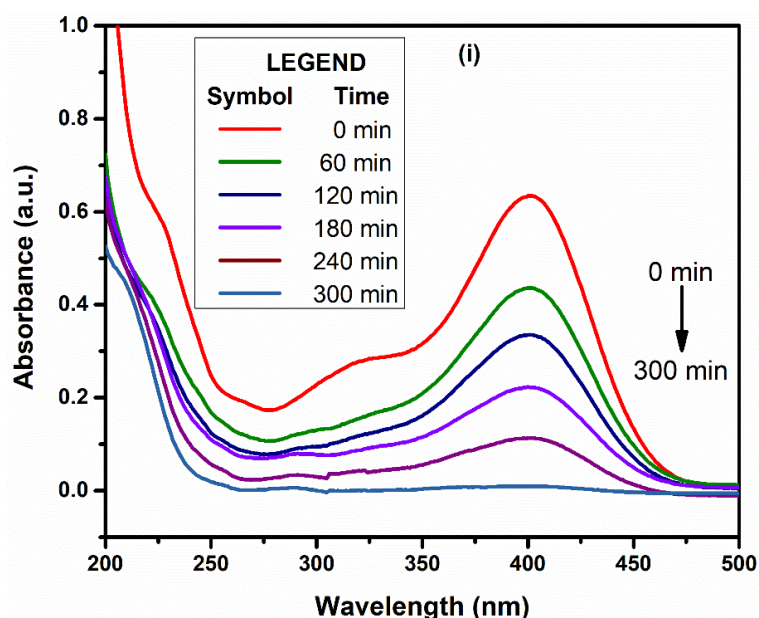
(ii)
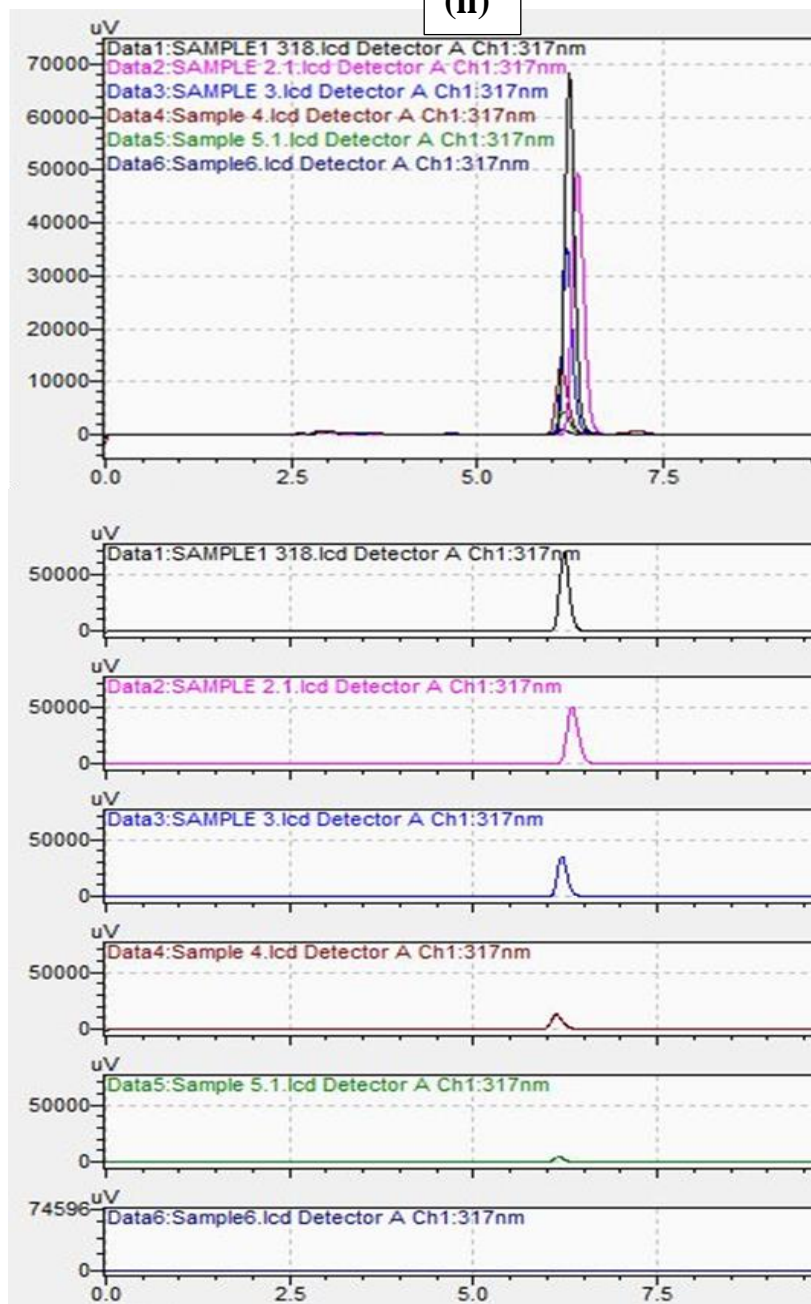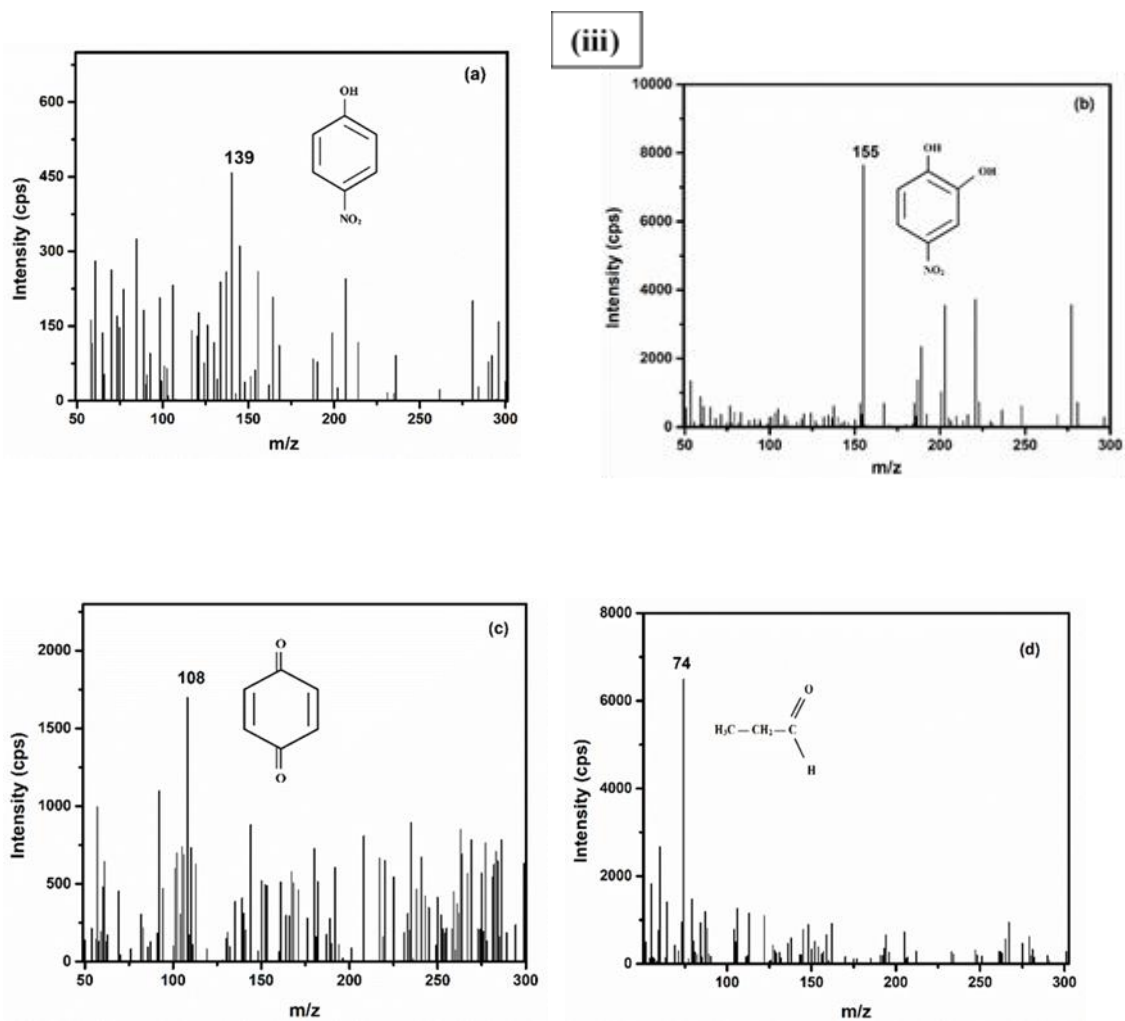
Fig 4.36 (i) UV-vis spectra (ii) LC of p-NP at 0 min, 40 min, 80 min, 120, 160 and 220 min, respectively and (iii) MS chromatograph of intermediate compounds (a) p-NP, (b) p-nitrocatechol, (c) 1, 4-benzoquinone and (d) propionic acid

BPA degradation was analyzed by a reduction in the absorbance at a typical wavelength of 276 nm over the irradiation time of 0 min – 220 min (Fig. 4.37 i). As the degradation proceeds, the peak intensity at a retention time of 10.57 min gradually decreases with UV irradiation time upto 220 min (Fig. 4.37 ii). The mass spectrum exhibit multiple peaks at different m/z, indicating the formation of various intermediates in the reaction mixture (Fig. 4.37 iii).
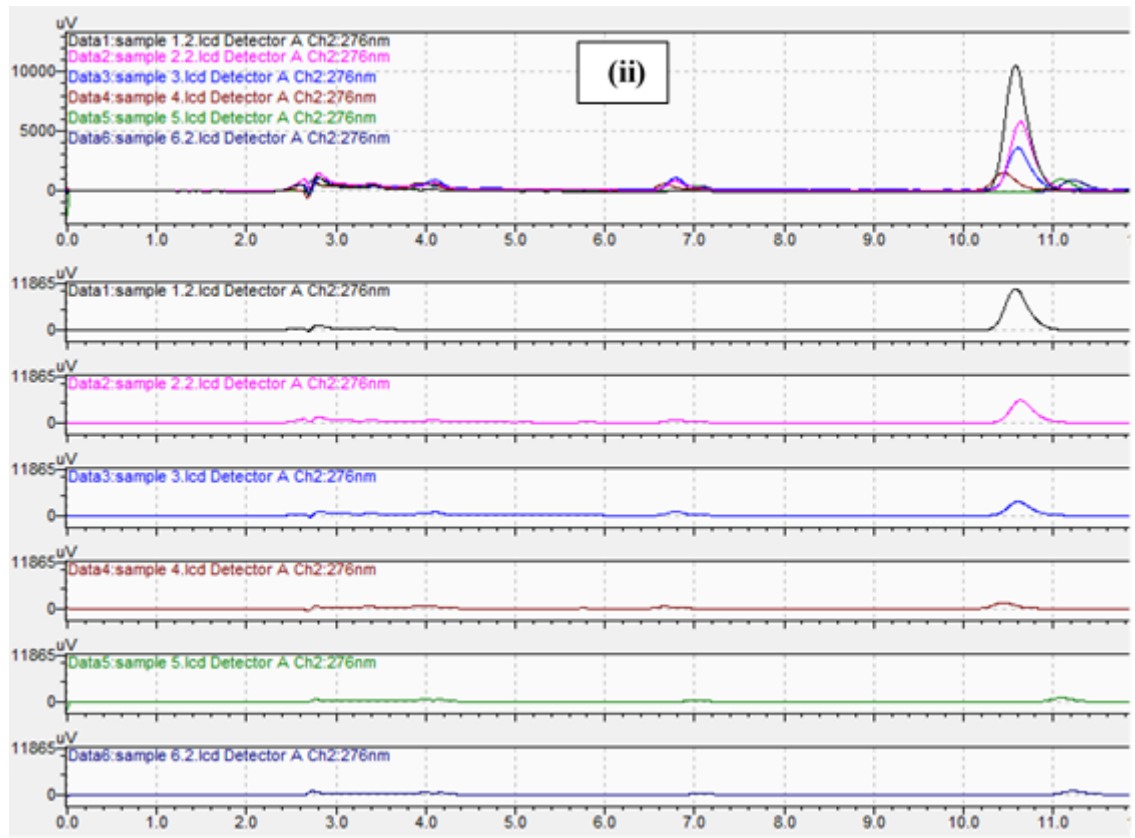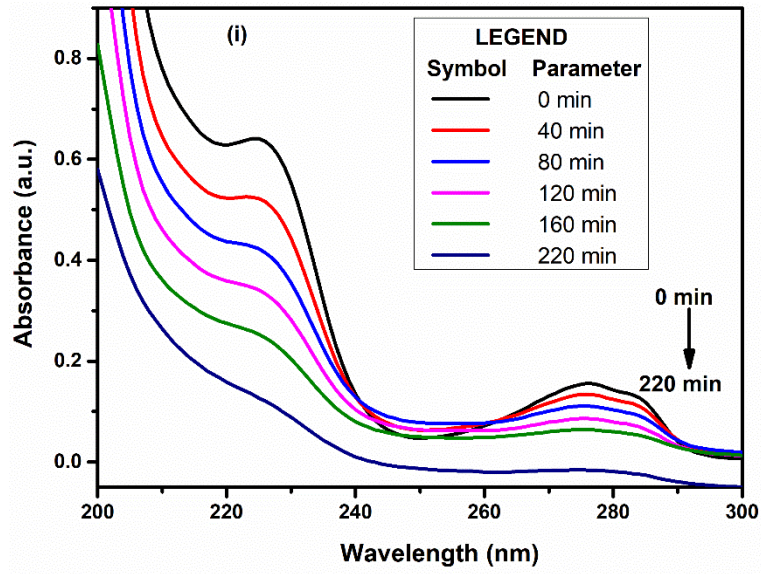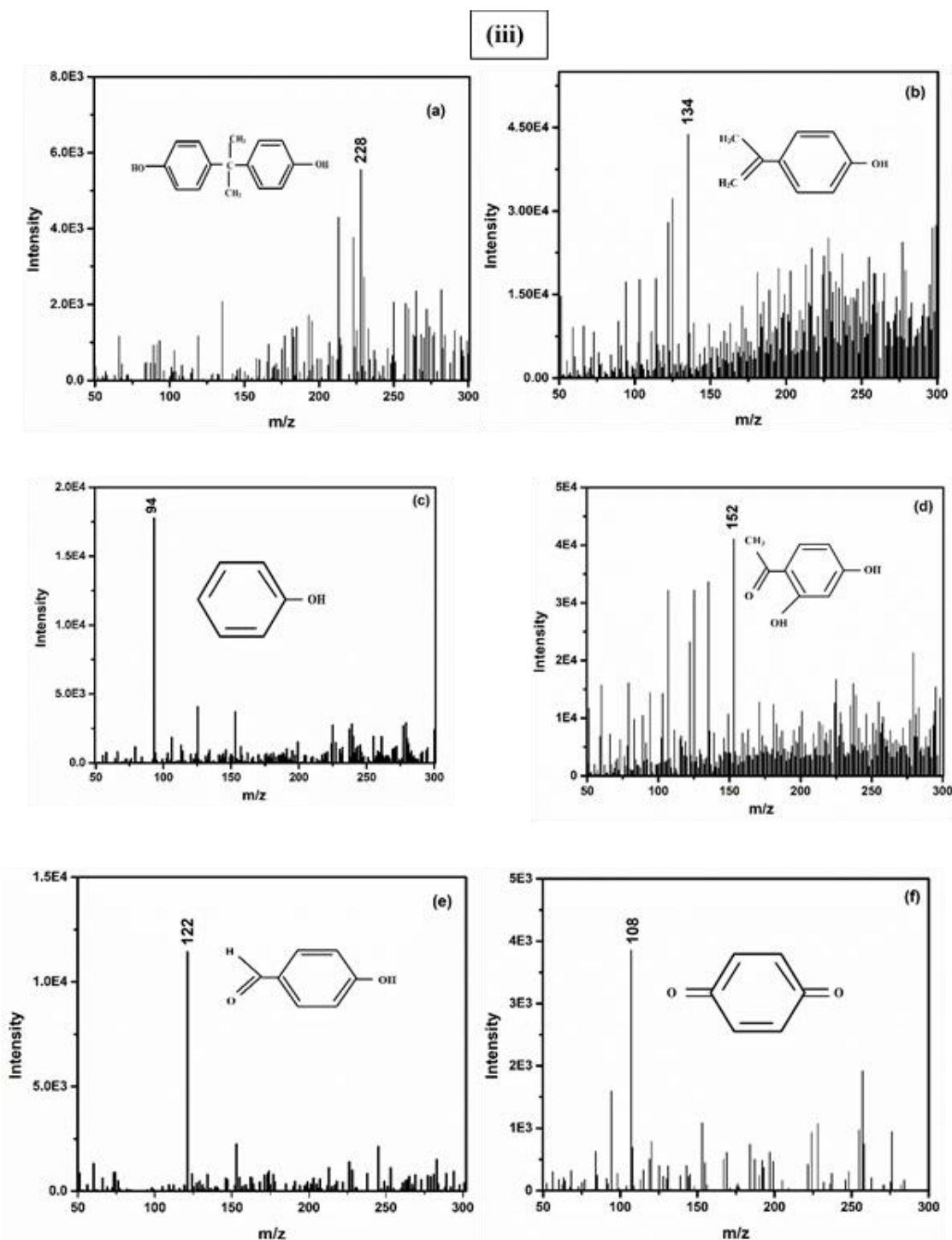
Fig. 4.37 (i) UV-vis spectra (ii) LC of BPA at 0 min, 40 min, 80 min, 120, 160 and 220 min, respectively and (iii) MS chromatograph of intermediate compounds (a) 2,2-bis (4-hydroxyphenyl) propane, (b) 4-isopropenyl phenol, (c) phenol, (d) 2,4 dihydroxyacetophenone, (e) 4-hydroxybenzenaldehyde and (f) 1,4-benzoquinone

As represented in LC-MS analysis, a compound at a retention time of 10.57 min is BPA with corresponding m/z = 228 (Fig. 4.37 (iii) a). As per the radical scavenging experiment, •OH and h^+ are the active radical species involved in the BPA degradation. These active radicals attack different carbon atoms of BPA molecules and generate various intermediates (Wang et al. 2010; Ding et al. 2016). The resulting intermediate compounds in the BPA degradation are presented in Fig. 4.37 (iii) b, c, d, e and f. Initially, BPA gets oxidized into different primary intermediates, as shown in Fig. 4.38 b. Further, these prominent intermediates undergo degradation into simple/smaller secondary and tertiary intermediate compounds with the help of active radical species produced by photocatalyst under UV irradiation. As time progresses, the secondary/tertiary intermediates also get degraded to a much simpler form, as shown in Fig. 4.37 (iii) and Fig. 4.38 b. The reaction mechanism of this degradation process is illustrated in the following section.

The existence of two electron-donating hydroxyl groups upsurges electron density on each benzene ring, making the C-C bond connecting two benzene rings more susceptible (Han et al. 2015). Further resulted in the photocleavage of phenyl groups by the active radicals and formation of 4-isopropenyl phenol (m/z = 134) (Fig. 4.37 iii b) and phenol (m/z = 94) (Fig. 4.37 iii c) as represented in Fig. 4.38 b (Route I). Wang et al. (2010), Ding et al. (2016) and Bechambi et al. (2016) also reported 4-isopropenyl phenol and phenol as primary intermediates obtained in the BPA degradation by the cleavage of a C-C bond. Subsequently, the formed 4-isopropenyl phenol undergoes hydroxylation to convert into 2,4 dihydroxyacetophenone observed at m/z = 152 (Fig. 4.37 iii d) (Xie et al. 2018). Further, the phenolic hydroxyl groups in the benzene ring of 2,4 dihydroxyacetophenone were readily oxidized by •OH radicals to form 4-hydroxybenzenaldehyde (Fig. 5.11 iii e) (m/z = 122) (Yang et al. 2016). BPA gets oxidized to 1,4-benzoquinone (Fig. 4.37 iii f) (m/z = 108) by h^+ radicals through ring-opening as shown in Fig. 4.38 b (Route II) (Ding et al. 2016). Moreover, the phenol formed in the route I gradually oxidized to 1,4-benzoquinone, as represented in Fig. 4.38 b (Han et al. 2015). 1,4-Benzoquinone was commonly considered as a significant intermediate during the ring-opening of aromatic compounds and their mineralization into CO_2 and water (Ding et al. 2016).

(a)

p-NP; m/z=139 → (•OH) → p–nitrocatecol; m/z=155 → 1, 4 benzoquinone; m/z=108 → Propionic acid; m/z = 74 → $CO_2 + H_2O$

(b)

2,2-bis (4-hydroxyphenyl) propane; m/z = 228

Route I •OH, h$^+$ **Route II** h$^+$

4-isopropenyl phenol; m/z = 134 + **Phenol; m/z = 94**

2,4 dihydroxyacetophenone;

m/z = 152

1,4-benzoquinone; m/z = 108

4-hydroxybenzenaldehyde;

m/z = 122

Ring opening

Low molecular weight organic compound + CO$_2$ + H$_2$O
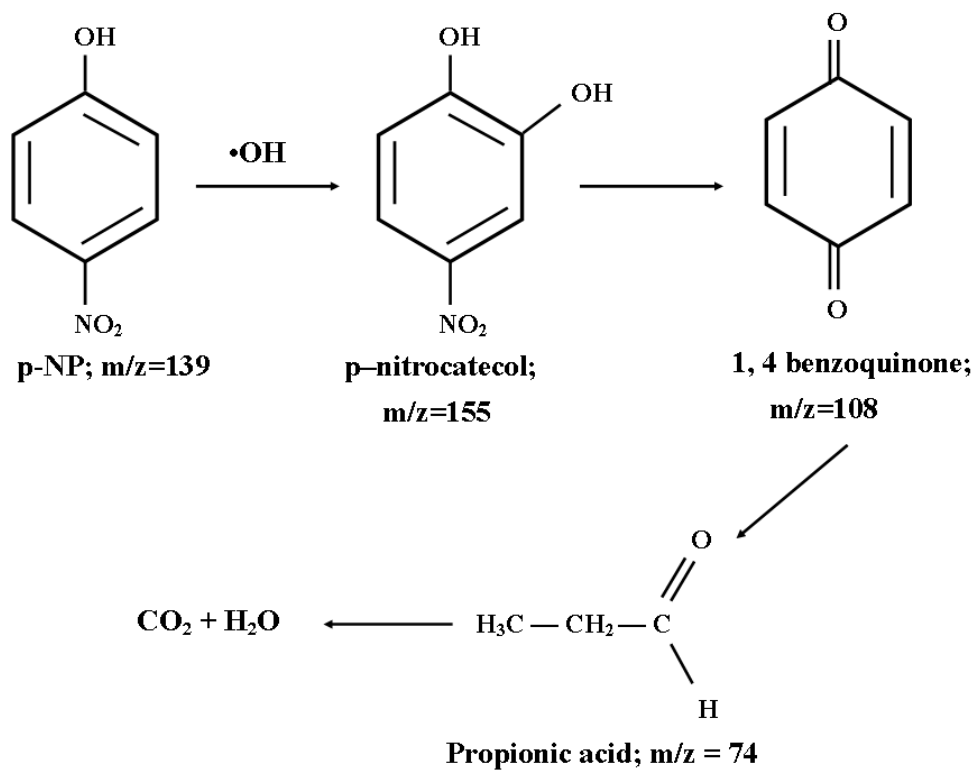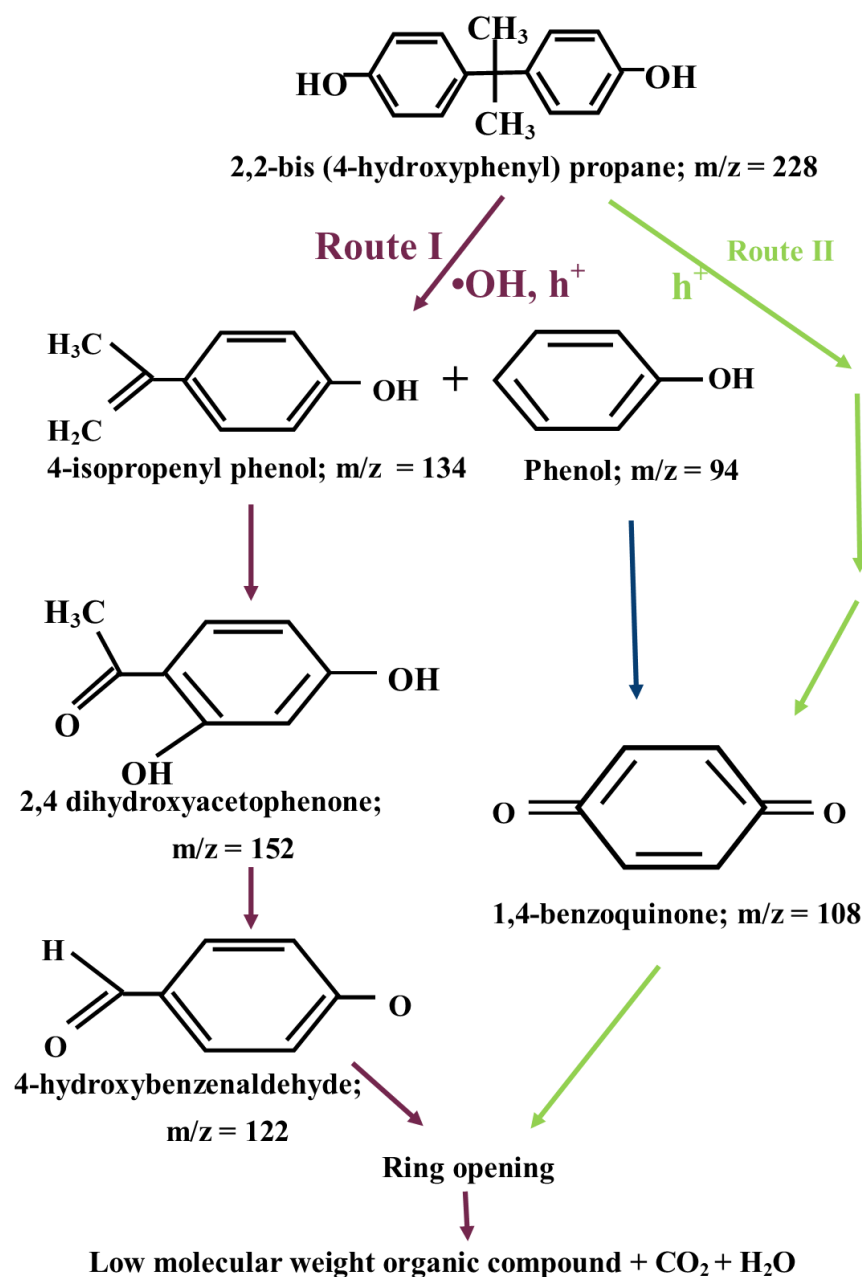
Fig. 4.38 Schematic representation of the degradation pathway of (a) p-NP and (b) BPA

4.2.8 Cytotoxicity study

Fig. 4.39 shows the phase-contrast microscopic images of cells treated with p-NP and BPA samples before and after photocatalysis compared with the control. The control exhibits 100 % cell viability and 0 % cytotoxicity (Fig. 4.39 a). Cells exposed with 25 mg/L of p-NP (Fig. 4.39 b) shows cell viability of 42.2 % compared to that of the control revealing the potent cytotoxicity (59.8 %) and the cells exposed with 10 mg/L of BPA (before photocatalysis) exhibit reduction in the cell viability upto 55.8 % with 44.2 % of

93

cytotoxicity (Fig. 4.39 d). However, cells exposed with p-NP and BPA samples after photocatalysis display cell viability of 90.4 % (Fig. 4.39 c) and 96.1 % (Fig. 4.39 e), respectively, compared to control, indicating slight cytotoxicity of 9.6 % and 3.9 %, respectively. Thus, the cytotoxicity of p-NP and BPA was considerably decreased after the photocatalytic degradation. These results are in agreement with the results from UV-via and LC-MS analysis (Fig. 4.36 i, ii and 4.37 i, ii), where the initial peak intensity of p-NP and BPA (before photocatalysis) was drastically decreased (almost disappeared) at 300 min and 220 min (after photocatalysis), respectively.
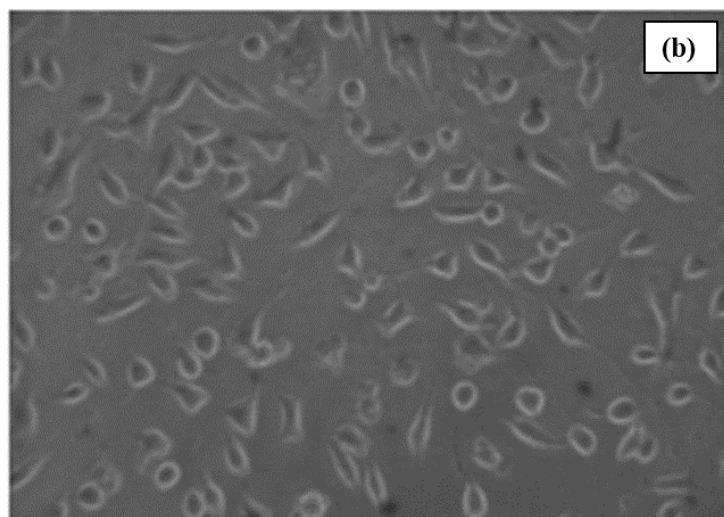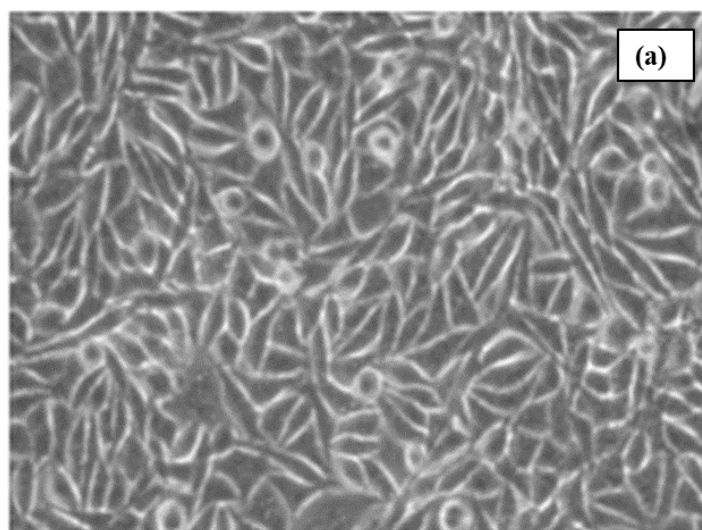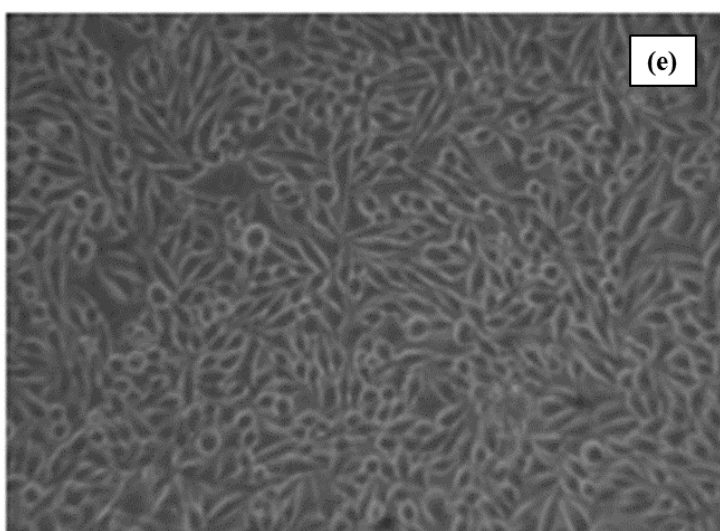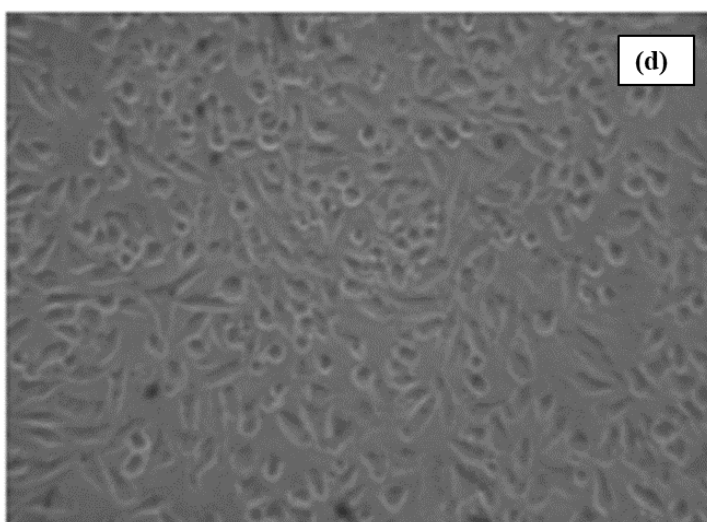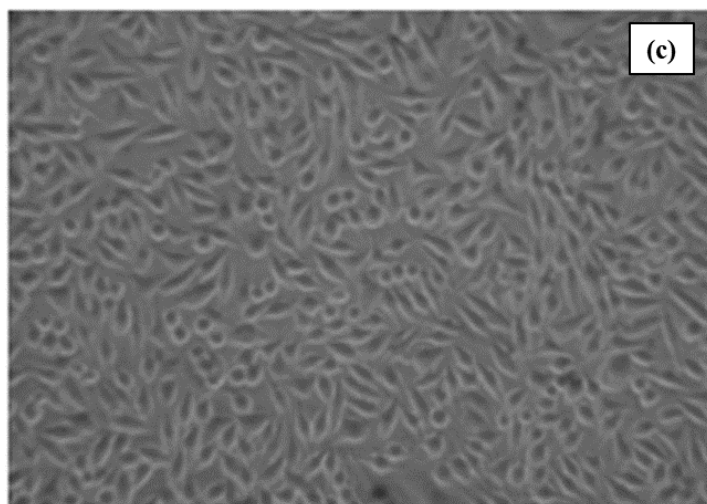
Fig. 4.39 Cytotoxicity study (a) control (b) p-NP before photocatalysis (c) p-NP after photocatalysis (d) BPA before photocatalysis and (e) BPA after photocatalysis

4.3 Biosynthesized ZnO for detection of p-NP and BPA

4.3.1 Fluorescence quenching of ZnO

ZnO nanoparticles displayed a fluorescence emission spectrum at 440 nm (Fig. 4.15) in the absence of p-NP and BPA. However, the addition of BPA and p-NP leads to fluorescence quenching of ZnO with the shift in emission wavelength. The Addition of BPA leads to a blue shift (Fig. 4.40b) of emission wavelength, whereas p-NP leads to the redshift in emission wavelength (Fig. 4.40a). As presented in Fig. 4.40a and Fig. 4.40b, the fluorescence intensity of ZnO was decreased to 92.8 % and 67.1 % in the presence 750 μM of p-NP and 400 μM of BPA, respectively, indicating the fluorescence quenching of ZnO.
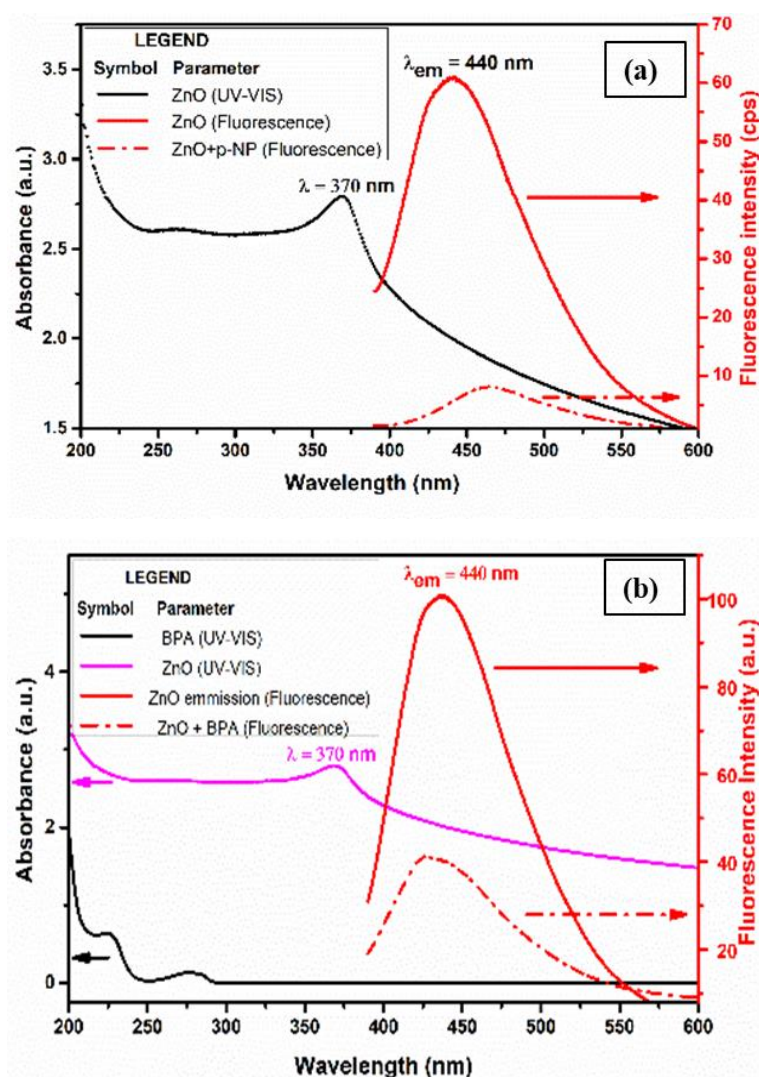
Fig. 4.40 UV-vis spectrum of ZnO and fluorescence spectra of ZnO
in presence of (a) p-NP and (b) BPA

The fluorescence intensity of ZnO nanoparticles decreased with an increase in p-NP concentration from 150 μM – 750 μM (Fig. 4.41a). Further, the fluorescence quenching efficiency (F_0-F) exhibits linearity with the increased concentration of p-NP with a correlation coefficient of 0.9947 (Fig. 4.41b) and the LOD was found to be 17.9 μM.
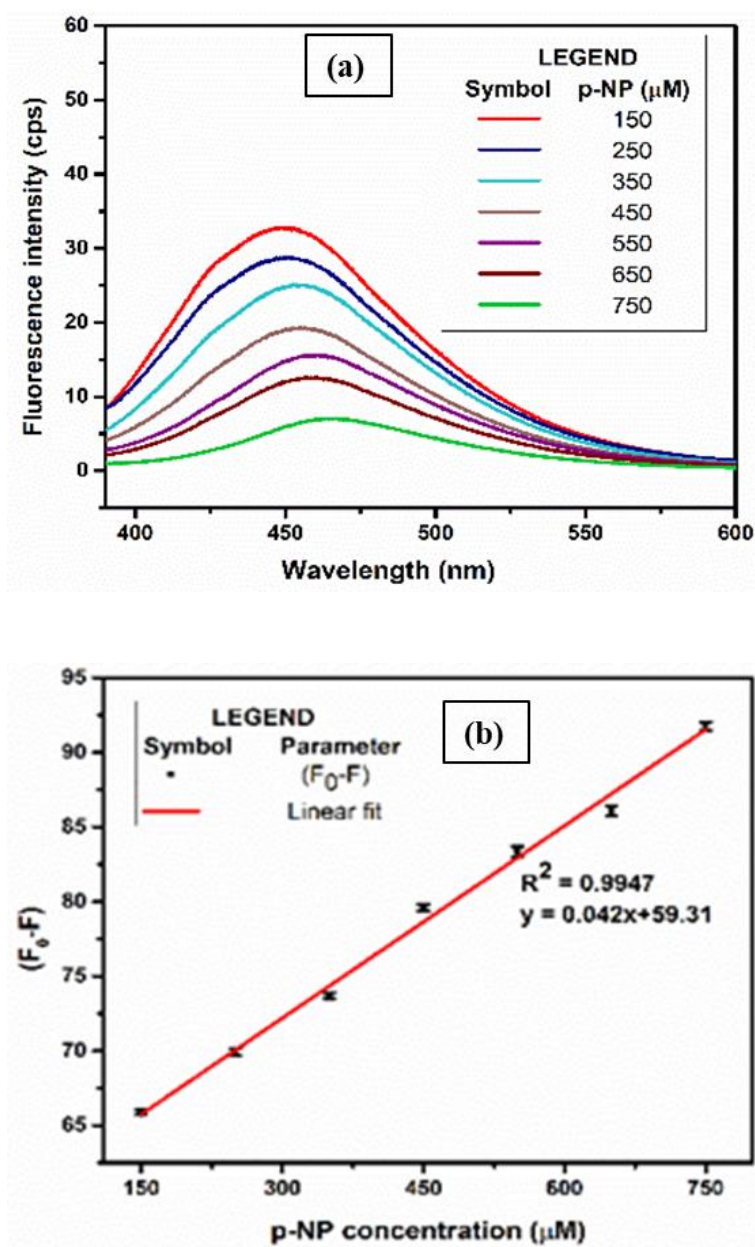
Fig. 4.41 (a) Effect of p-NP concentration on fluorescence emission spectra of ZnO and (b) fluorescence quenching efficiency of ZnO with different concentrations of p-NP

As represented in Fig. 4.42, the fluorescence intensity of biosynthesized ZnO nanoparticles was reduced gradually with increasing concentration of BPA from 10 μM –

400 µM. Moreover, the fluorescence quenching efficiency displays linearity with the increased concentration of BPA with a correlation coefficient of 0.9847 (Fig. 4.42 b). Furter, the LOD for BPA was found to be 0.35 µM.
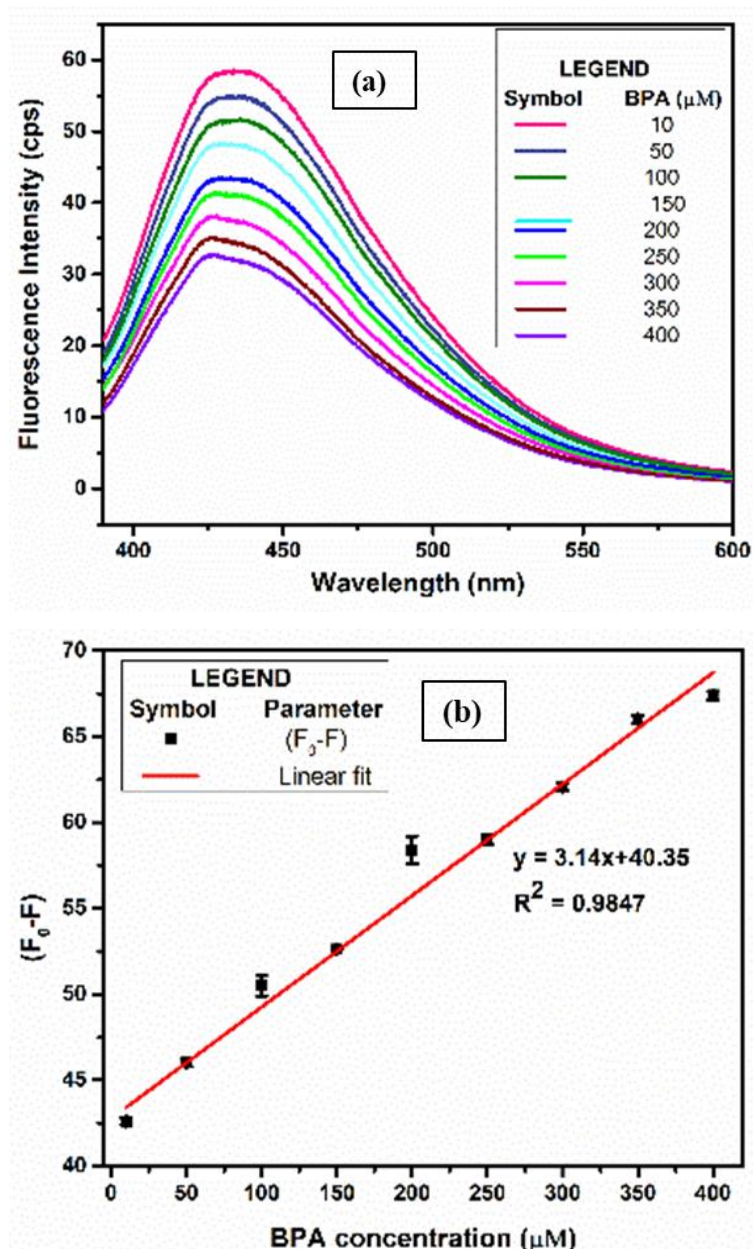
Fig. 4.42 (a) Effect of BPA concentration on fluorescence emission spectra of ZnO and (b) fluorescence quenching efficiency of ZnO with different concentrations of BPA

4.3.2 Plausible Sensing mechanism

Wang et al. (2021), have reported fluorescence-based detection of p-NP using nitrogen, silicon co-doped carbon dots. Further, they observed the complete spectral overlap between the excitation spectrum of a fluorophore and the absorption of p-NP,

indicating IFE as an undertaking mechanism. As represented in Fig. 4.43a; The fluorescence emission spectrum of biosynthesized ZnO slightly overlaps with the UV-vis spectrum of p-NP, indicating partial secondary IFE. Further, the Lineweaver-Burk plot and Stern-Volmer plot were used to describe the p-NP sensing mechanism. The Stern-Volmer plot shows nonlinearity with p-NP concentration (Fig. 4.43c), nullifies the possibility of dynamic quenching. However, $1/(F_0-F)$ Vs. p-NP concentration exhibits linearity with a correlation coefficient of 0.9834 is an indication of stating quenching (Fig. 4.43b). Thus, the addition of p-NP to ZnO solution leads to the formation of ground-state complex, resulted in quenching of fluorescence (Lakowicz 2006), forms the basis of p-NP detection.
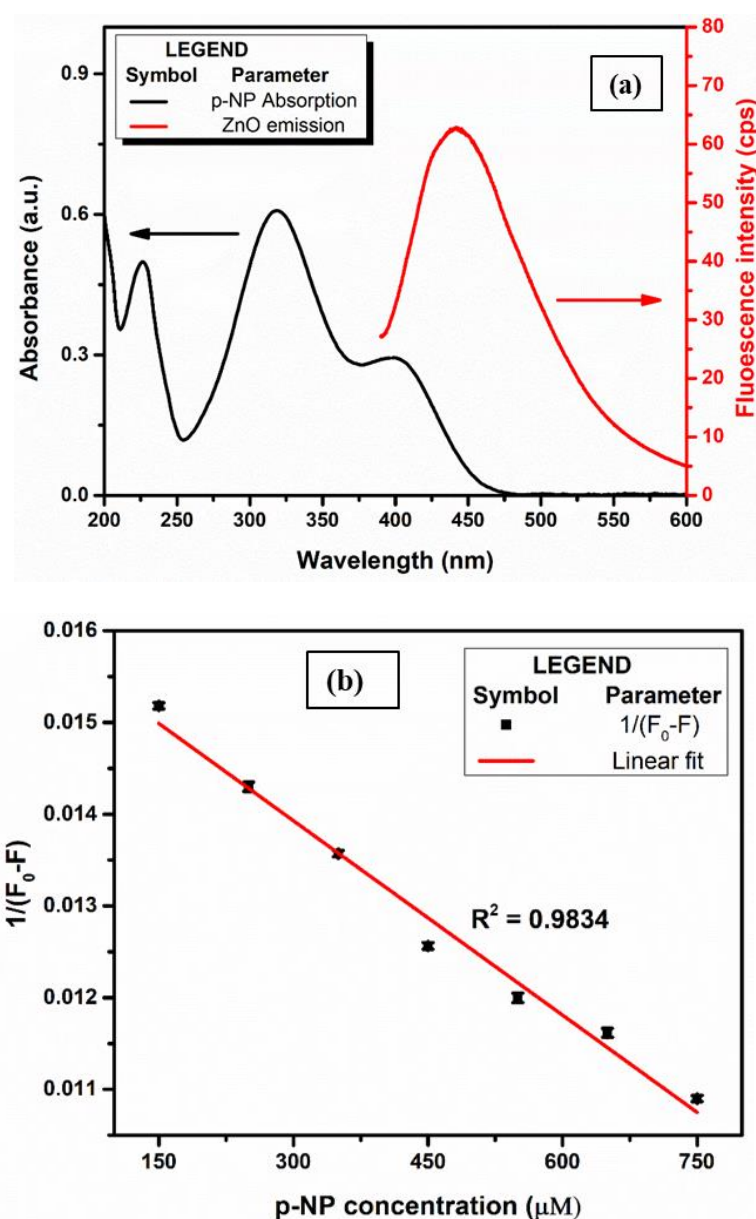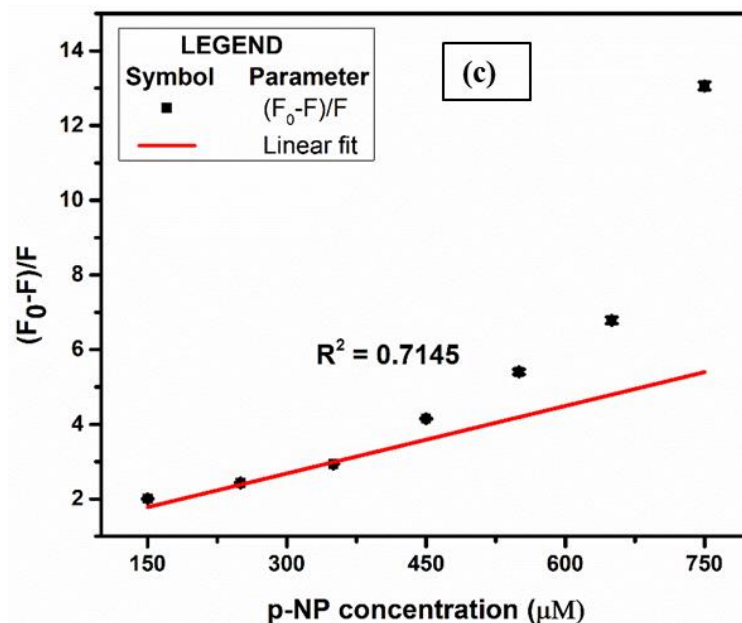
Fig. 4.43 Sensing mechanism of p-NP (a) UV-vis spectrum of p-NP and fluorescence spectrum of ZnO (b) Lineweaver-Burk plot and (c) Stern-Volmer plot

BPA exhibits a spectroscopic signature peak at 224 nm and 276 nm (Table 1.1). ZnO nanoparticles displayed a UV – Vis peak at 370 nm and fluorescence emission peak at 440 nm upon excitation with 370 nm. Thus, excluding the possibility of primary and secondary IFE (Khan et al. 2018). The Lineweaver-Burk plot displays nonlinearity with BPA concentration nullifies the possibility of static quenching (Fig. 4.44a). However, the linear relationship was observed for $(F_0-F)/F$ Vs. BPA concentration is an indication of complex formation between the excited state of ZnO nanoparticles and the ground state of BPA molecules (Gaviria-Arroyave et al. 2020).

100
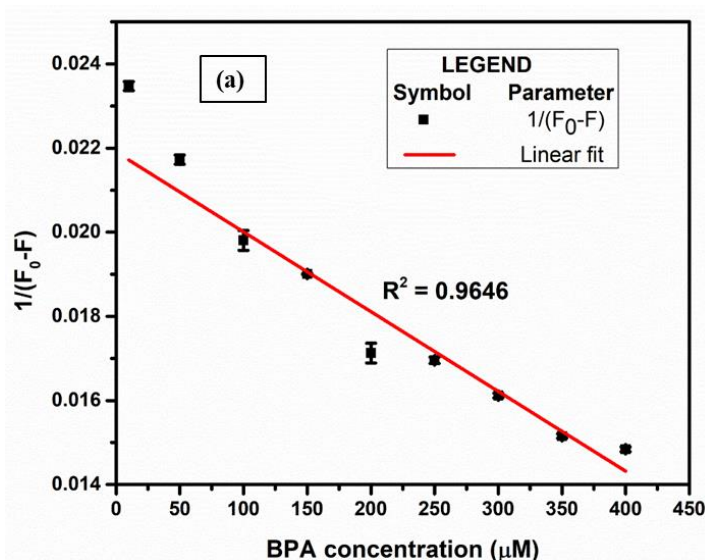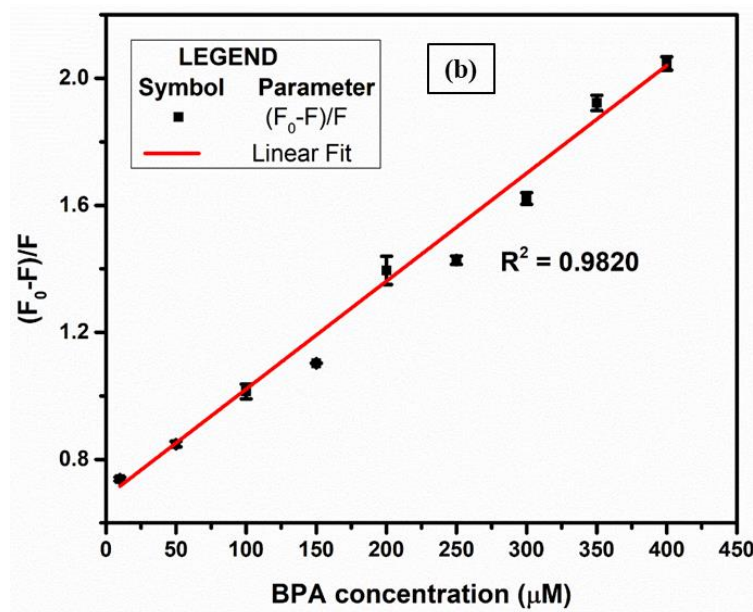
Fig. 4.44 Sensing mechanism of BPA (a) Lineweaver-Burk plot and (c) Stern-Volmer plot

4.4 Chemical synthesis and functionalization of ZnO for detection of p-NP
4.4.1 Synthesis and characterization of bare and functionalized ZnO QDs

UV-vis spectrum of ZnO and APTES@ZnO exhibited a characteristic absorption shoulder at 348 nm and 335 nm, respectively (Fig. 4.45a). However, a blue shift is observed in APTES@ZnO nanoparticles compared to bare ZnO nanoparticles, as bare ZnO are unstable in water, leading to the growth and aggregation of bare ZnO QDs (Zou et al. 2020). TEM micrograph of functionalized QDs (Fig. 4.45b) exhibits spherical particles with narrow size distribution. As shown in Fig. 4.45(b and c), particle size histogram obtained from TEM analysis displayed particles in the range of 2-6 nm with an average size of 3.7 ± 0.51 nm with a polydispersity index of 0.13. The peak at absorbance value of 335 nm for APTES@ZnO corresponds to a size of 3.4 nm based on an effective mass approximation equation (3), which is in agreement with TEM size. Thus, from UV-vis and TEM analysis, the synthesized APTES@ZnO particles were found to have a size less than 10 nm confirming the quantum dot regime.
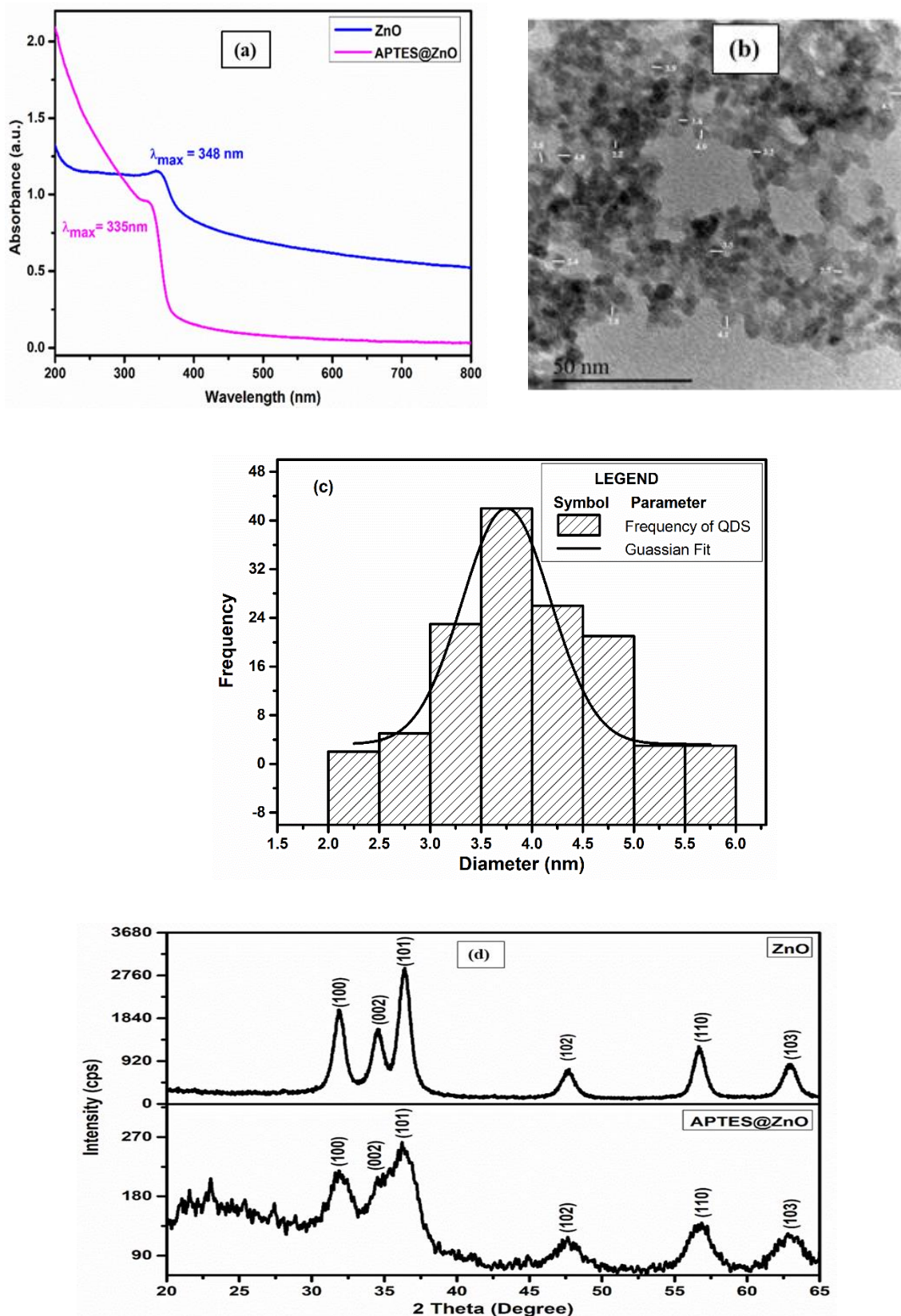
Fig. 4.45 Bare and APTES@ZnO QDs characteristics (a) UV-vis analysis (b) TEM micrograph at 50 nm scale bar (c) Particle size distribution histogram with the Gaussian fit and (d) X-ray diffraction pattern

The characteristic diffraction pattern of bare and functionalized ZnO QDs is represented in Fig. 4.45d. The presence of a diffraction peak at 2θ = 31.90, 34.53, 36.38, 47.64, 56.71, and 62.94 corresponds to (100), (002), (101), (102), (110), and (103) diffraction planes, respectively indicate the obtained diffraction pattern fits well with the hexagonal wurtzite structure of ZnO with JCPDS card no. 36-1451. Further, the functionalized ZnO displays a diffraction peak at 2θ = 31.88, 34.57, 36.23, 47.65, 56.83 and 62.81 corresponding to (100), (002), (101), (102), (110) and (103) diffraction planes, respectively. The diffraction peaks get broadened and coincide with the crystalline phase of the ZnO after functionalization with APTES. The broadening of the diffraction peak of APTES@ZnO compared to bare ZnO displays a small size of nanoparticles after APTES functionalization (Aboulaich et al. 2012). The diffraction peak corresponding to aminopropyl siloxane is observed between 2θ values of 20 to 30, which confirms the capping of ZnO with APTES (Fig. 4.45d) (Zou et al. 2020).
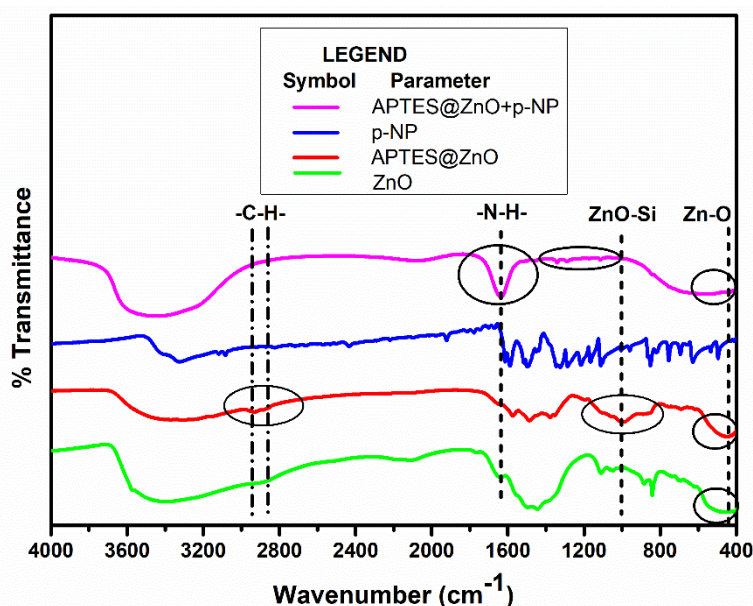
Fig. 4.46 FTIR spectra of ZnO, APTES@ZnO, p-NP and APTES@ZnO+p-NP

FTIR spectra of ZnO and APTES@ZnO are shown in Fig. 4.46. The characteristic Zn–O bond stretching vibration for APTES@ZnO is shifted to a higher wavenumber at 449.65 cm^{-1} compared to bare ZnO (444.38 cm^{-1}), which can be explained by the formation of the Zn-O-Si bond that appeared at 999.62 cm^{-1} (Raevskaya et al. 2014). The presence of Zn-O-H groups on the surface of ZnO is replaced by Zn–O–Si(O–), whereas the higher electronegativity of –Si(O–)$_2$ compared to H leads to an enhancement of the bond forces

103

for the Zn–O, shifting the vibration bands of APTES@ZnO to higher wavenumbers (Bini et al. 2012). The enhanced band between 2930.9 cm^{-1} and 2872.22 cm^{-1} is ascribed to the C–H bonds stretching vibration in the side chains derived from APTES conforming to the capping of APTES on ZnO QDs surface (Cheng et al. 2016). ZnO exhibits the vibration band at 3409.06 cm^{-1}, corresponding to the –OH group. These get broadened after capping with APTES and shifted to a lower wavenumber of 3311.59 cm^{-1} corresponds to the stretching vibration of N–H (Casa et al. 2016). Thus, when APTES is added to ZnO QDs solution, alkoxyl groups were partially hydrolyzed, and one group would react with the –OH group on the ZnO surface to form a capping layer, with the unreacted –NH$_2$ group protruding on the surface makes the surface stable (Barrak et al. 2016).

The EDX spectrum recorded in spot profile mode from densely populated ZnO manifested high peak intensity of Zn and oxygen at 1.1 KeV and 0.6 KeV, respectively, ensuring the oxide form of zinc (Fig. 4.47 a). Further, the bonding bridge between APTES and ZnO QDs is confirmed by SEM coupled EDX analysis. Fig. 4.47b displayed the elemental peak of O, Si, and Zn, which ensures the existence of ZnO and SiO$_2$. Thus, the EDX spectrum of nanostructures confirms the functionalization of ZnO QDs with APTES.
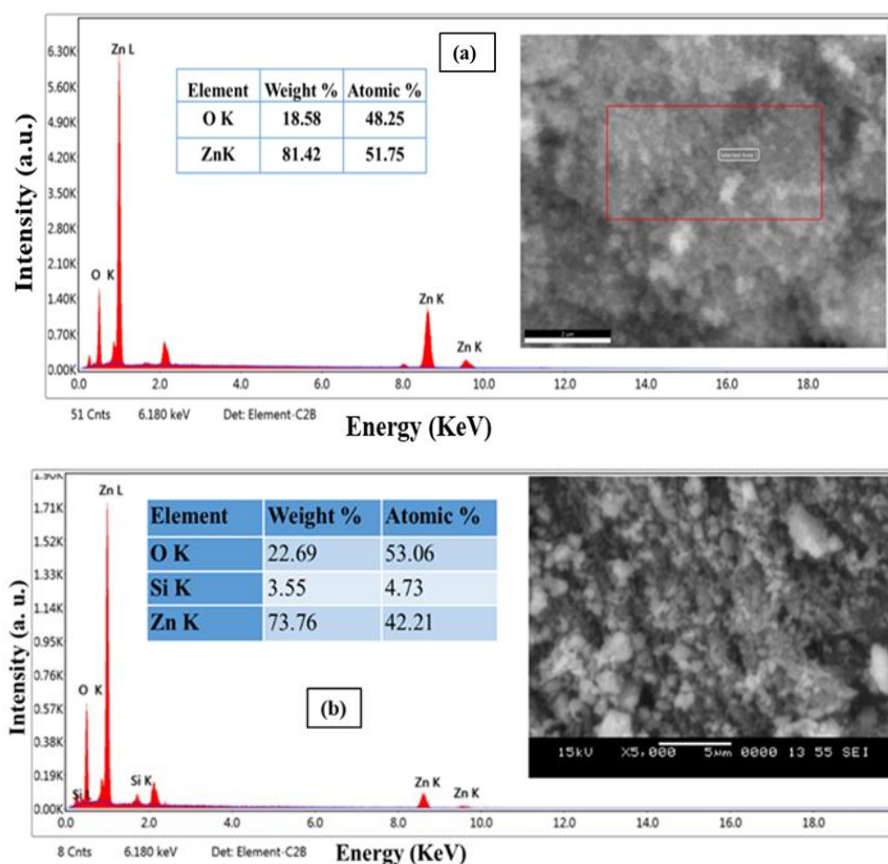
Fig. 4.47 EDX spectrum with elemental composition. Inset: SEM micrograph (a) ZnO and (b) APTES@ZnO

UV-vis spectrum of functionalized QDs exhibited a characteristic absorption shoulder at 335 nm based on surface plasmon resonance of ZnO nanoparticles (Fig. 4.48). 80 μM p-NP shows absorption peaks at 226, 318, and 397 nm, respectively. UV-vis spectrum of the APTES@ZnO QDs in the presence of p-NP exhibited the absorption peaks at 335 and 397 nm, respectively, showing the overlapping characteristics of APTES@ZnO QDs and p-NP. However, the absorbance of APTES@ZnO QDs and p-NP admixture increases with an increase in the p-NP concentration from 1-80 μm (Fig. 4.48). Thus, the above results reveal that the increased absorbance of APTES@ZnO in the presence of p-NP remarkably influenced nanocrystals' emission, further becoming the basis of p-NP detection using APTES@ZnO QDs.
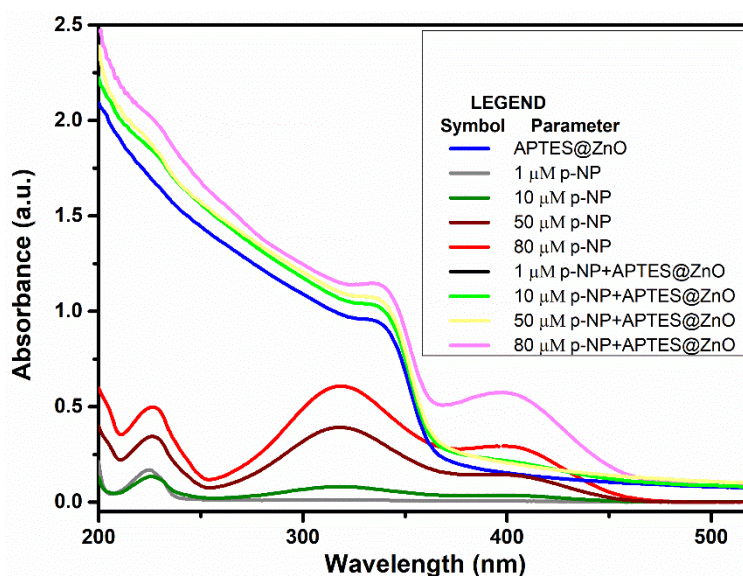
Fig. 4.48 UV-vis characteristic of p-NP, APTES@ZnO, the admixture of APTES@ZnO with p-NP

4.4.2 Fluorescence studies

ZnO QDs display the maximum fluorescence intensity at 572 nm in the absence of p-NP, as shown in Fig. 4.49a. Further, the addition of p-NP exhibits a quenching of fluorescence intensity at the same wavelength. The fluorescence intensity of QDs decreased to 27% in the presence of 80 μM p-NP. Similarly, the fluorescence intensity of APTES@ZnO QDs decreased to 59.95 % in the presence of 80 μM p-NP, indicating high quenching compared to the former (Fig. 4.49b). These results show that quenching efficiency was obviously enhanced after QDs being capped by APTES (Zhang et al. 2012).
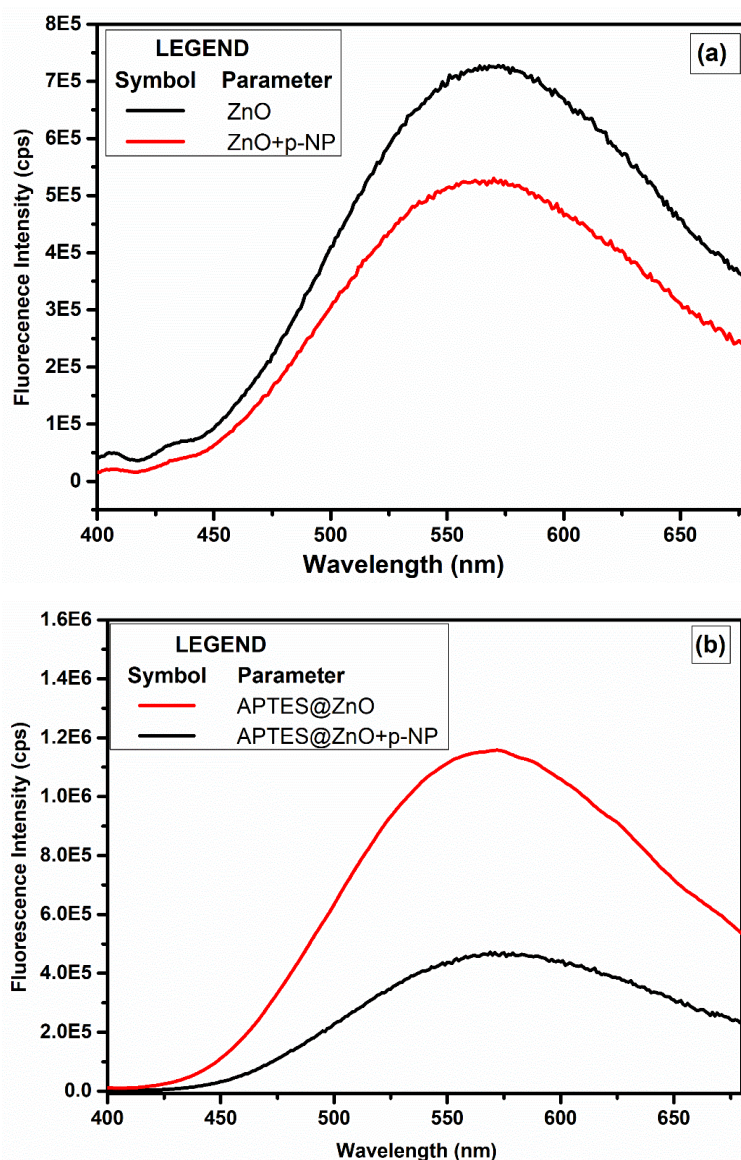
Fig. 4.49 Fluorescence spectra of (a) bare ZnO in the absence and presence of p-NP and (b) APTES@ZnO in the absence and presence of p-NP

A set of various analytical experiments were carried out to obtain the highest fluorescence quenching efficiency. The effect of several buffer solutions on the fluorescence intensity of APTES@ZnO QDs was investigated by measuring the fluorescence intensity of functionalized QDs in the presence and absence of p-NP (80 μM). As represented in Fig. 4.50a, the alteration in the magnitude of fluorescence intensity in different buffer solutions corresponding to the presence or absence of p-NP revealed that the fluorescence quenching efficiency is highest in the presence of ultrapure water as compared to other buffers. This is followed by tris base > phosphate buffer > phosphate buffer saline under the same reaction conditions. Furthermore, acetate buffer was found to

be non-conductive for detecting p-NP using functionalized QDs under the same reaction conditions due to decomposition of APTES@ZnO QDs (Liu et al. 2017a).
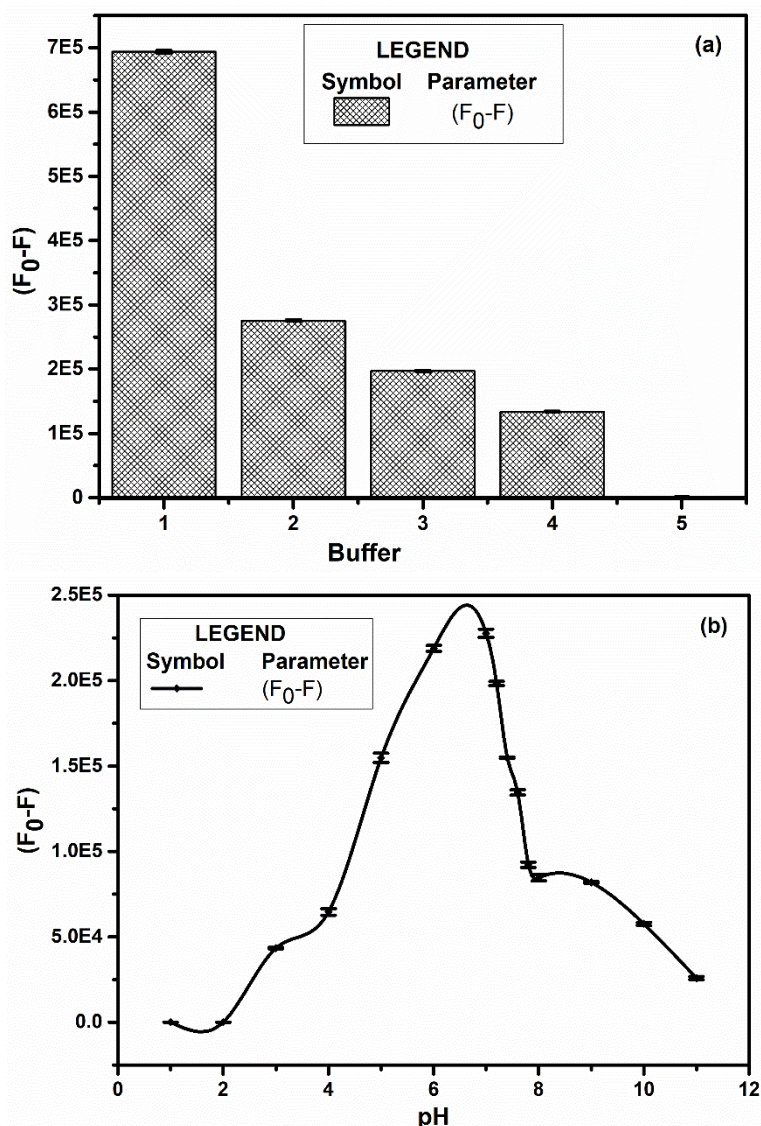
Fig. 4.50 (a) Response of the (F_0-F) in different buffers (1) ultrapure water, (2) tris base, (3) phosphate buffer, (4) phosphate buffer saline, (5) acetate buffer, and (b) effect of pH

The effect of pH was investigated to understand the response of APTES@ZnO QDs in the sensing of p-NP. For this purpose pH of ultrapure water was varied between 1 to 11 using HCL or NaOH. When the pH $\leq$ 4, dominating H^+ ions in the solution leads to partial dissolution of QDs (Bian et al. 2011), whereas high alkalinity results in competitive binding between hydroxyl ions and the ligands to the crystals, leads to increased surface defects of QDs (Zhang et al. 2008). Thus, fluorescence quenching efficiency was significantly affected under highly acidic and alkaline conditions, as shown in Fig. 4.50b. Therefore, the

pH in the range of 5-9 was tested prudently. The fluorescence intensity increases with an increase in pH from 6 to 7 and swiftly decreases in the range of 7 to 8 and continues to decline thereafter. The highest fluorescence quenching was observed in the ultrapure water at pH 7, making the sensor suitable for potential applications in real water samples as the pH values of environmental water samples are usually (near) neutral or slightly alkaline. Further, detection experiments were conducted using ultrapure water of optimized pH 7, and their quenching efficiency was determined.
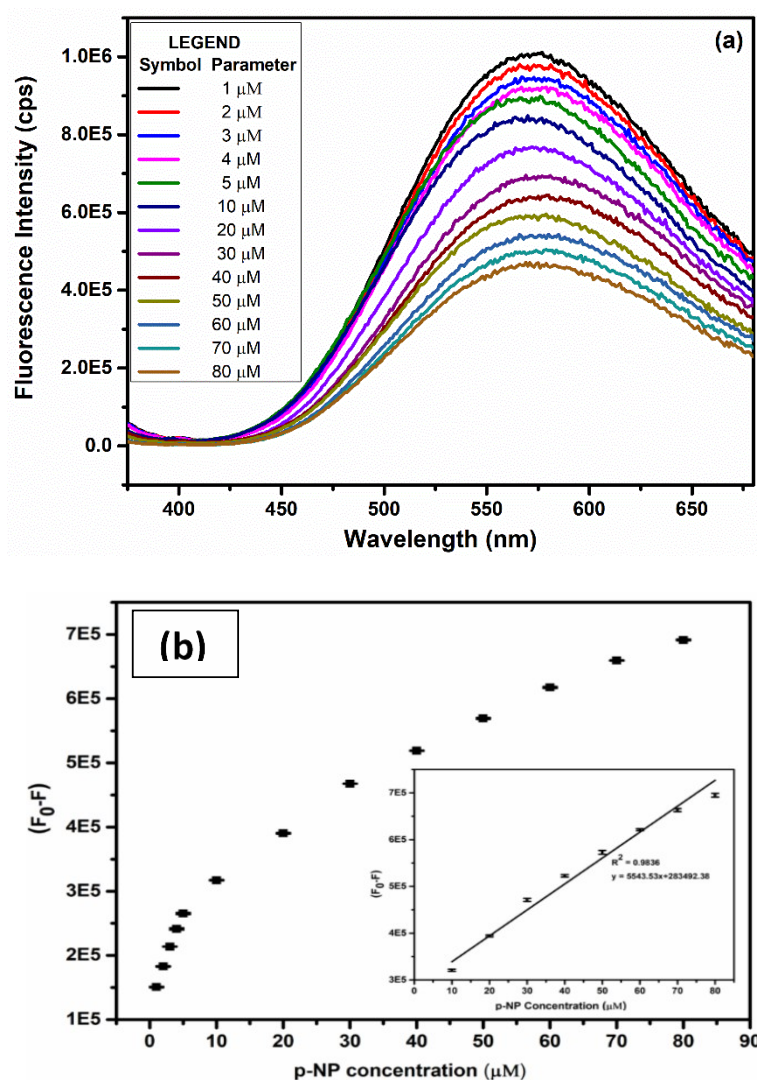
Fig. 4.51 (a) Effect of p-NP concentration on fluorescence intensity and (b) fluorescence quenching efficiency (F_0-F) Vs. p–NP concentration. Inset: Calibration curve of APTES@ZnO QDs for p-NP detection

Table 4.8 Comparison with analytical results from the literature

S. No.	Analytical method	Linear range (µM)	LOD (µM)	References
1	Polymer carbon dots	0.5-60	0.26	Han et al. 2019
2	B-CD-Au NC	1-50	0.21	Yang et al. 2018
3	Cu-CDs	0.5–50	0.08	Fang et al. 2019
4	Au NC	0.1-100	0.09	Li et al. 2020
5	APTES@ZnO QDs	1-80	0.089	Present study

APTES@ZnO QDs, as a sensing platform for p-NP, were studied under the optimum reaction conditions. Fluorescence intensity was found to be gradually decreased with an increase in p-NP concentration from 1-80 µM, as shown in Fig. 4.51a. Fluorescence quenching efficiency (F_0-F) is increased with the p-NP concentration from 1-80 µM, as shown in Fig. 4.51(b). The unknown concentration of p-NP in the sample was estimated by using the calibration curve as shown in Fig. 4.51(b) inset with a correlation coefficient of 0.98, and the LOD is found to be 0.089 µM. Moreover, Table 4.8 enlisted linear ranges and detection limits for p-NP using various fluorometric sensors and compared them with the present method. Cu-CDs exhibits low LOD over a narrow range of detection (Fang et al. 2019). The present method offers good sensitivity with a wide range of detection compared to other analytical procedures (Table 4.8). The obtained LOD for p-NP is much lower than the permissible limit of 0.43 µM provided by EPA (Wei et al. 2011). Thus, the developed sensor holds the potential to determine p-NP traces in water for pollution monitoring.

4.4.3 Hypothetical sensing mechanism

As displayed in Fig. 4.52a, the absorption spectrum (226 nm – 397 nm) of the analyte (80 µM p-NP) was observed to slightly overlap with the applied excitation wavelength (350 nm), indicating partly primary IFE. However, the analytes absorption spectrum (226, 318, and 397 nm) partially overlaps with the APTES@ZnO QDs emission spectrum (370 nm - 680 nm). Thus, it can be concluded that some extent of fluorescence quenching is observed due to primary and secondary IFE. According to a previous study (Geng et al. 2016), a significant overlap between the p-NP absorption spectrum and the excitation spectrum of β-CD@ZnO QDs may lead to quenching of fluorescence. Further, they reported that the considerable fluorescence quenching could be attributed to the

electron transfer mechanism when the host-guest inclusion complexes of the β-CD and p-NP are formed. Similarly, the sensing mechanism of p-NP using thiol-CD-Au NCs reported by Li et al. (2020) has primary IFE as UV-vis absorption spectrum of p-NP and Au NCs mixture found to overlap with the fluorescence excitation band (365 nm) of thiol-CD-Au NCs and led to fluorescence quenching of thiol-CD-Au NCs.
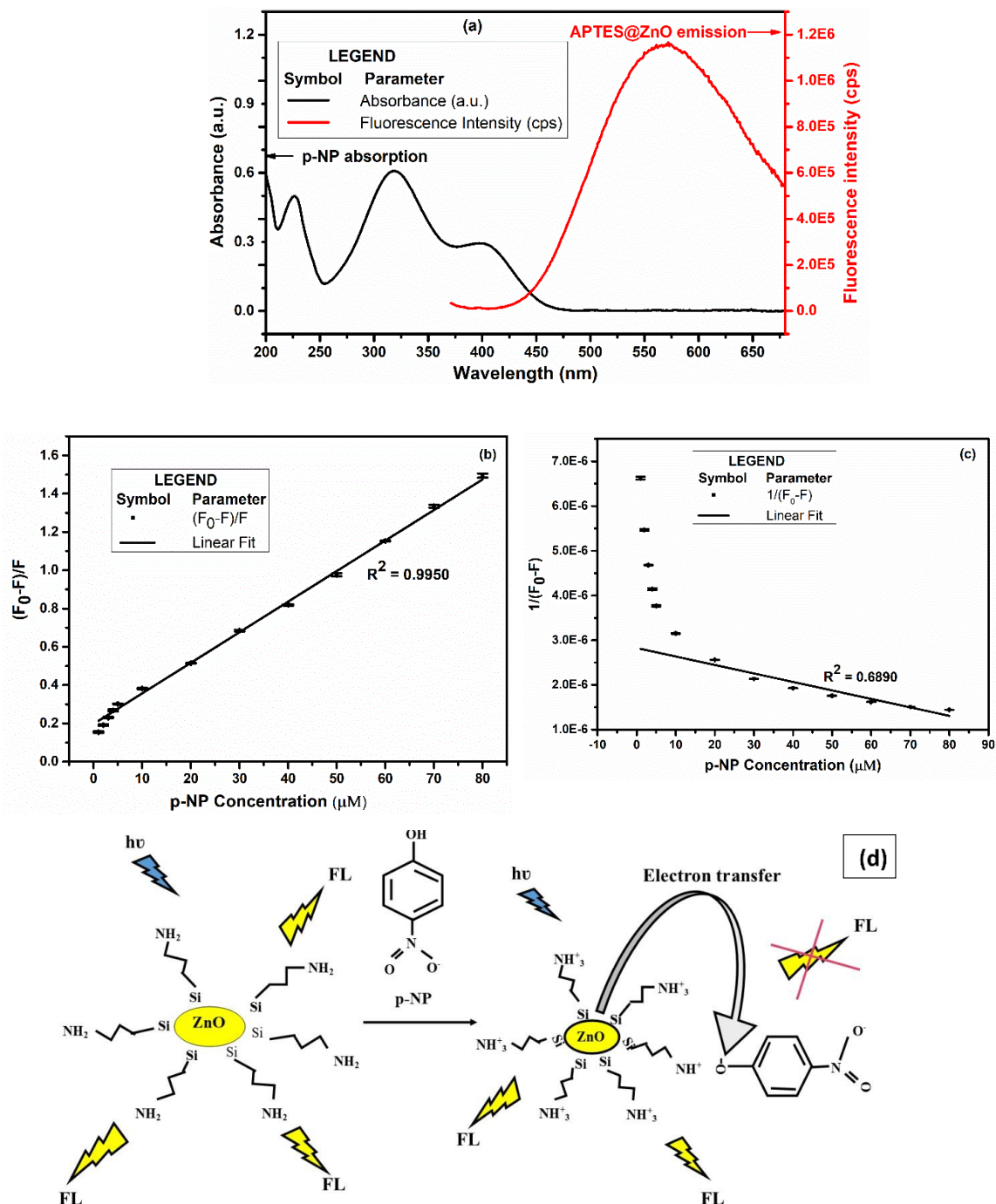
Fig. 4.52 (a) UV-vis absorption spectrum of p-NP and fluorescence emission spectrum of APTES@ZnO QDs (b) Stern-Volmer plot (c) Lineweaver-Burk plot and (d) fluorescence quenching mechanism

The FTIR spectrum of APTES@ZnO with p-NP exhibits the combined characteristics of p-NP and APTES@ZnO (Fig. 4.46). In the presence of p-NP, N-H stretching vibration of APTES@ZnO, 3311.59 cm^{-1} has moved to a higher wavenumber of 3457.55 cm^{-1}, and a vibration band at 1631.59 cm^{-1} gets enhanced (Xiong et al. 2019). Thus, with the addition of p-NP to APTES@ZnO QDs, the Zn-O stretching vibration region gets broadened, which expresses the interaction between p-NP with APTES@ZnO (Fig. 4.46). As shown in Fig. 4.48, the addition of p-NP to APTES@ZnO QDs leads to an increase in its absorbance value with an increased concentration of p-NP. Thus, the UV-vis spectra of APTES@ZnO QDs in the presence of p-NP indicate the formation of an excited-state complex between electron-deficient p-NP (Xiong et al. 2019) and electron-donor APTES (Xu et al. 2013). Subsequently, the p-NP accepts excited state electrons from APTES@ZnO QDs characterized by non-radiative recombination of the electron-hole pair resulting in quenching of APTES@ZnO fluorescence as shown in Fig. 4.52d. A similar observation was reported by Tong et al. (2019) while detecting chromium ions using urea-ZnO QDs. A linear relationship between the relative fluorescence efficiency and p-NP concentration that follows the Stern-Volmer plot and its non-compliance with the Lineweaver-Burk plot is presented in Fig. 4.52b and Fig. 4.52c.
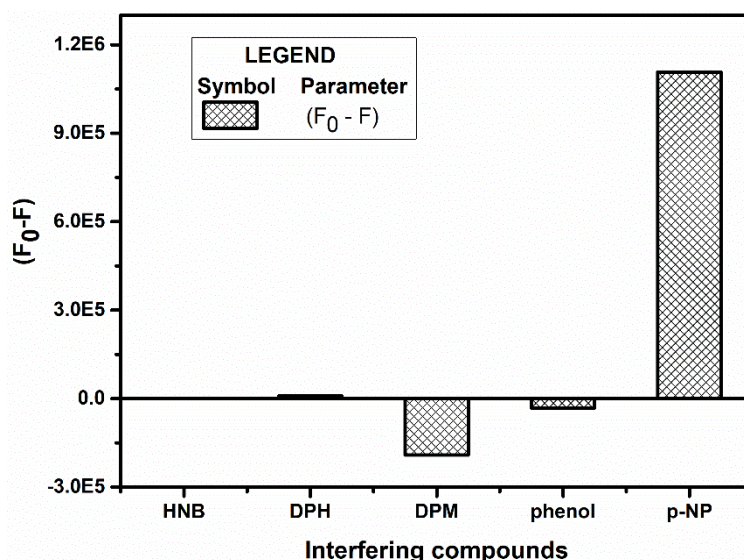
Fig. 4.53 Fluorescence quenching efficiency (F_0-F) of APTES@ZnO QDs in the presence of different interfering compounds

A comparative study was carried out by measuring the fluorescence of various aromatic compounds along with the p-NP. Fig. 4.53 exhibited the response of 20 µM

solutions of HNB, DPH, DPM, and phenol (Sigma-Aldrich, USA). Phenol and DPM lead to enhancement of fluorescence intensity. Except for p-NP, none of the above aromatic compounds can quench the fluorescence of APTES@ZnO QDs. Hence, APTES@Zno QDs have the potential for selective detection of p-NP.

4.5 Chemical synthesis and functionalization of ZnO for detection of BPA
4.5.1 Characterization of β-CD functionalized ZnO QDs

UV-vis spectra of ZnO and functionalized ZnO showed an absorption shoulder at 332 nm and 347 nm, respectively, in the ultra-violet region, as shown in Fig. 4.54. The absorption spectra are the characteristic of ZnO nanoparticles in the quantum size regime as the excitonic absorption is blue-shifted as compared to the bulk ZnO (Singh et al. 2014). Further, the comparatively sharp absorption shoulders indicate the narrow size distribution of the functionalized ZnO nanoparticles (Darroudi et al. 2014; Zhang et al. 2013a). The average size of ZnO nanoparticles was calculated from equation (3), which represents the effective mass approximation equation (Prabhu et al. 2013; Aboulaich et al. 2012), and the peak absorbance at 332 nm corresponds to the average particle size of 3.6 nm. UV-vis study on synthesized ZnO nanoparticles demonstrated that the particles are in a quantum size regime. Moreover, the average particle size of functionalized ZnO QDs corresponds to a characteristic wavelength of 347 nm that estimates to 3.89 nm size of the particles based on the effective mass approximation equation.
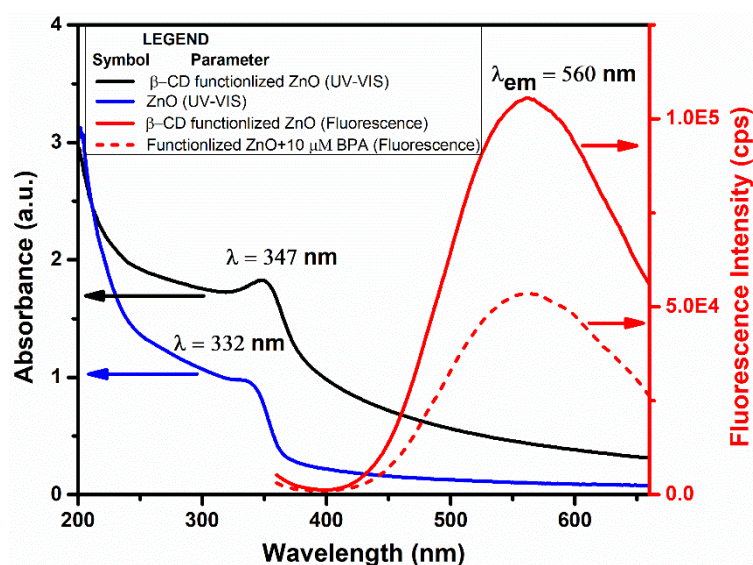
Fig. 4.54 UV-vis spectra and fluorescence emission spectra of synthesized ZnO and β-CD functionalized ZnO QDs

Fluorescence spectra of the functionalized QDs represented in Fig.4.54 exhibit an emission peak at 560 nm upon excitation with 340 nm. The yellow fluorescence emission spectra were observed due to the transition of an electron from a shallow donor to a deeply trapped hole (Suyver et al. 2001; Djurisic et al. 2006).
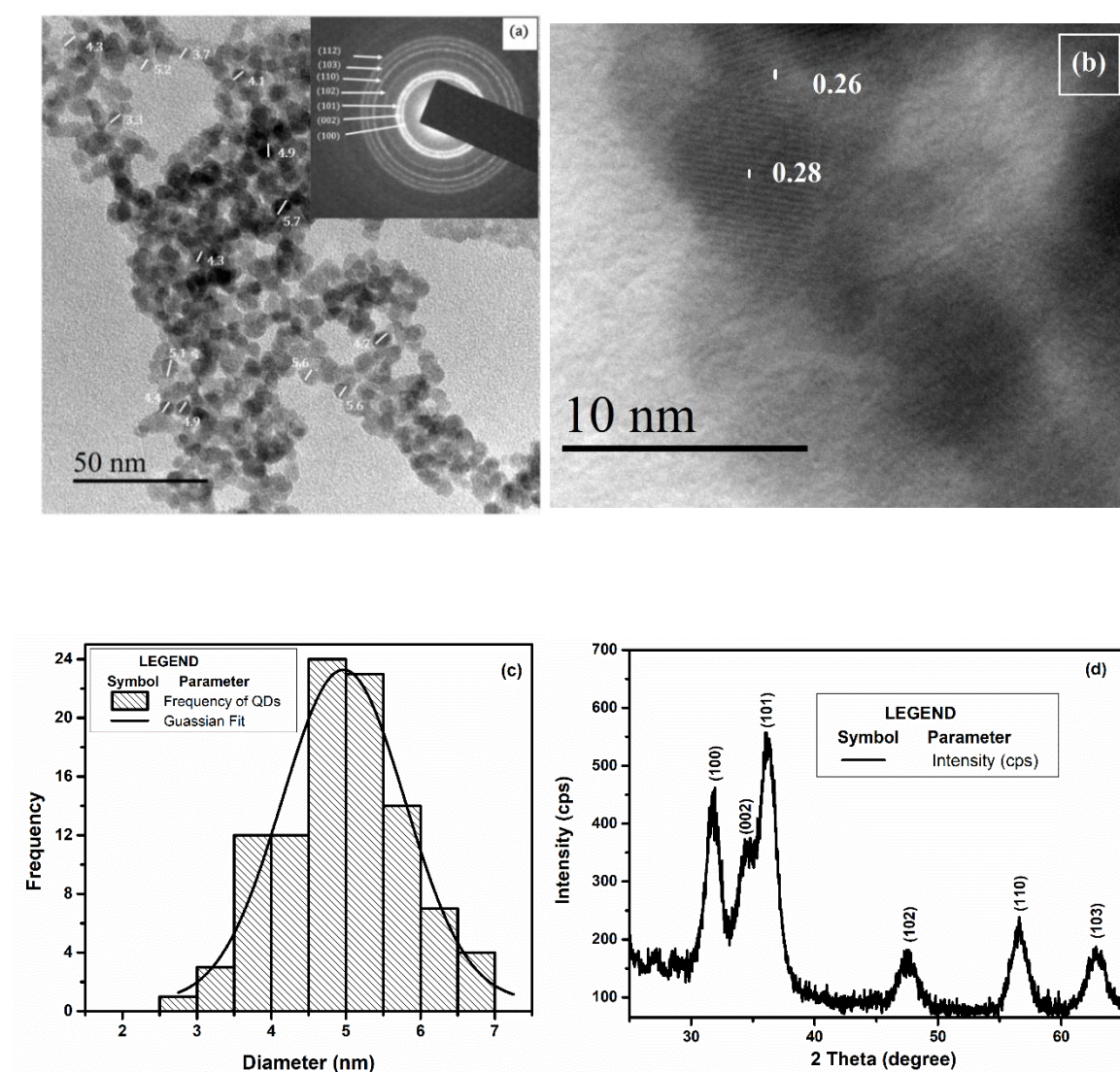
Fig. 4.55 (a) TEM image of β-CD functionalized ZnO QDs at a scale bar of 50 nm, Inset: SAED pattern. (b) High magnification TEM at 10 nm scale bar. (c) Particle size distribution analysis of functionalized QDs. (d) XRD pattern of functionalized ZnO QDs

Fig. 4.55a displays the TEM image and SAED pattern of functionalized QDs. As presented in Fig. 4.55c, a histogram of particle size distribution analysis depicted particle size in the range of 2.5 nm - 7 nm with an average size of 4.96 ± 0.97 nm having a

polydispersity index of 0.20. Moreover, the particle size of functionalized QDs obtained from TEM, was in good agreement with the calculated one using an effective mass approximation equation (3) based on UV-vis absorbance. The crystallinity of functionalized ZnO nanoparticles was confirmed using XRD analysis, as shown in Fig. 4.55d. The XRD pattern of functionalized QDs exhibited a peak at $2\theta = 31.77, 34.48, 36.13,$ 47.45, 56.61, and 62.91 correspondings to (100), (002), (101), (102), (110) and (103) planes of hexagonal wurtzite ZnO nanoparticles respectively which was well indexed with ICSD No. 65121. SAED pattern shown in Fig. 4.55a inset can be well index with (100), (002), (101), (102), (110), (103) and (112) reflection lines of ZnO with a hexagonal wurtzite structure which is consistent with XRD results. The high magnification TEM image displayed lattice fringes with a distance of 0.28 and 0.24 nm, as shown in Fig. 4.55b, which corresponds to an interplanar distance of (100) and (002) planes of wurtzite ZnO. Hence, the above results reveal that the synthesized ZnO nanoparticles fall under the QD regime with good crystallinity.
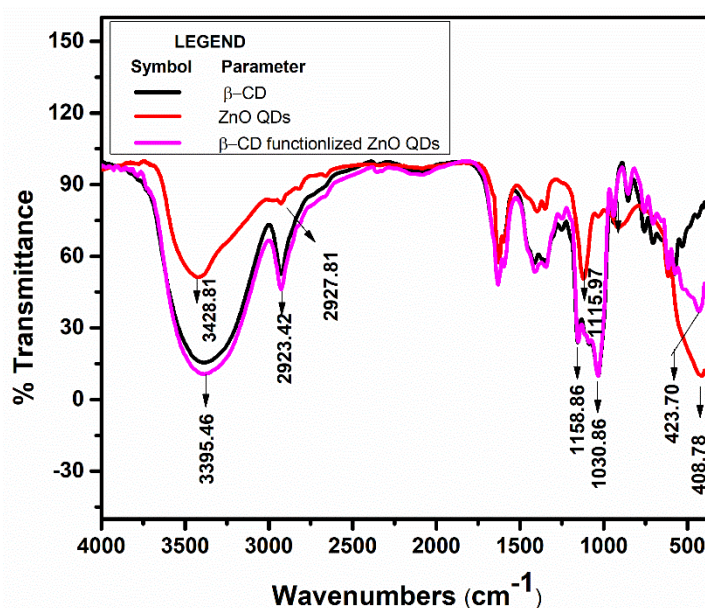
Fig. 4.56 FTIR spectra of ZnO QDs (red line), β-CD (black line) and β-CD functionalized ZnO QDs (pink line)

The conjugation between β-CD and ZnO QDs was evaluated using the FTIR spectra of β-CD, ZnO QDs, and β-CD functionalized ZnO QDs as represented in Fig. 4.56. The functionalized QDs showed a shift in peaks at 3387.57, 2923.42, 1151.94, 1033.90, and 430.78 cm⁻¹, which can be associated with β-CD and ZnO QDs. However, after the conjugation of β-CD with ZnO, as represented in Fig. 4.56, the spectrum of functionalized QDs expressed the combined characteristic peaks of β-CD and ZnO QDs. ZnO QDs and β-

CD exhibited a vibration band at 3428.81 and 3394.59 cm^{-1}, respectively. And a functionalized QDs displayed a shift in the peak position at 3387.57 cm^{-1} and further moved to a lower wavelength and became broader and stronger, representing the bond formation between β-CD and ZnO QDs (Zhao and Chen 2007; Cao et al. 2014). The functionalized QDs displayed β-CD absorption features on ZnO of the combined C-O-C stretching/OH bending vibration at 1151.94 cm^{-1} and combined C-O/C-C stretching vibration observed at 1033.90 cm^{-1} (Yang et al. 2015). Moreover, an absorption band at 430.78 cm^{-1} was ascribed to Zn-O stretching vibration (Singh et al. 2014), demonstrating that the β-CD successfully coated on the ZnO QDs surface. However, the spectral characteristic and shifts in significant peak positions indicate that β-CD was well chemically bound onto the surface of ZnO QDs (Zhao and Chen 2007; Geng et al. 2017).
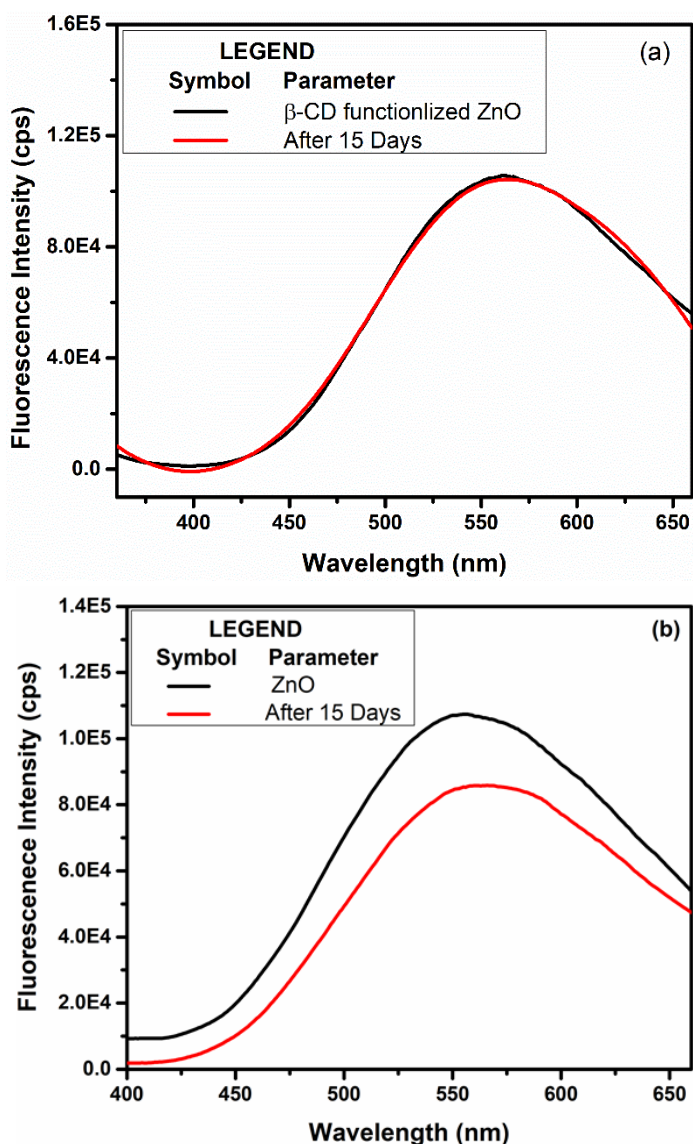
Fig. 4.57 Fluorescence spectra of (a) β-CD functionalized ZnO QDs (black) and after 15 days (red) and (b) ZnO QDs (black) and after 15 days (red)

The stability studies for ZnO QDs and β-CD functionalized ZnO QDs in an aqueous solution were carried out by recording fluorescence intensity after 15 days of storage. As exhibited in Fig. 4.57, a considerable decrease in fluorescence intensity of ZnO QDs (Fig. 4.57b) was observed as compared to that of functionalized QDs (Fig. 4.57a) in an aqueous solution. As depicted in Fig. 4.57a, it reveals that functionalized QDs remain stable even after 15 days in an aqueous solution. Further, showing that β-CD confers aqueous stability to ZnO QDs as bare inorganic semiconductor ZnO core is highly reactive (Jamieson et al. 2007; Geng et al. 2017).

4.5.2 Fluorescence quenching of β-CD functionalized ZnO QDs by BPA

As represented in Fig. 4.58, the addition of BPA led to substantial fluorescence quenching of functionalized QDs. The fluorescence intensity of functionalized QDs decreased to 52 % in the presence of 10 μM of BPA (dashed lines). Even though the emission spectra of the functionalized QDs were observed at the same wavelength (560 nm), the drop in the fluorescence intensity indicates the concentration of the BPA detected. The increase in the concentration of BPA decreases the fluorescence intensity of the QDs. Many analytical experiments were also carried out to investigate the effect of the buffers, pH, and reaction time, as shown in Fig. 4.58a and b.
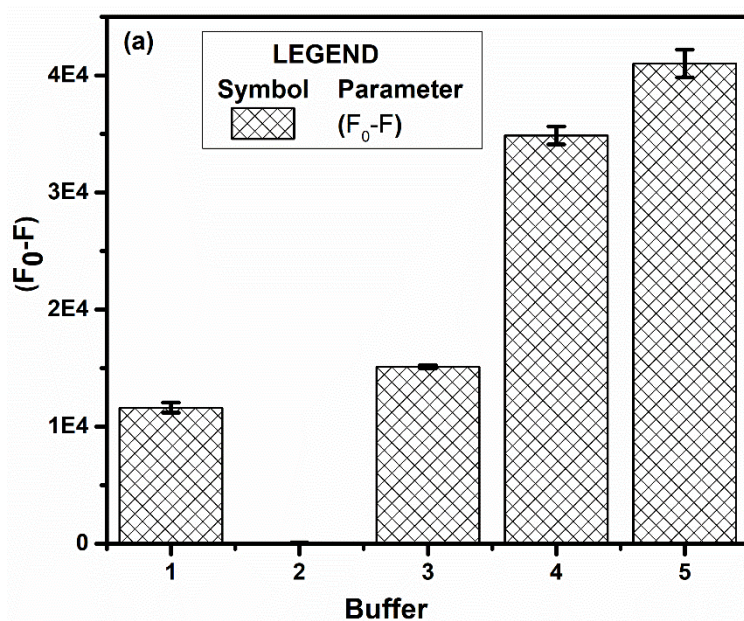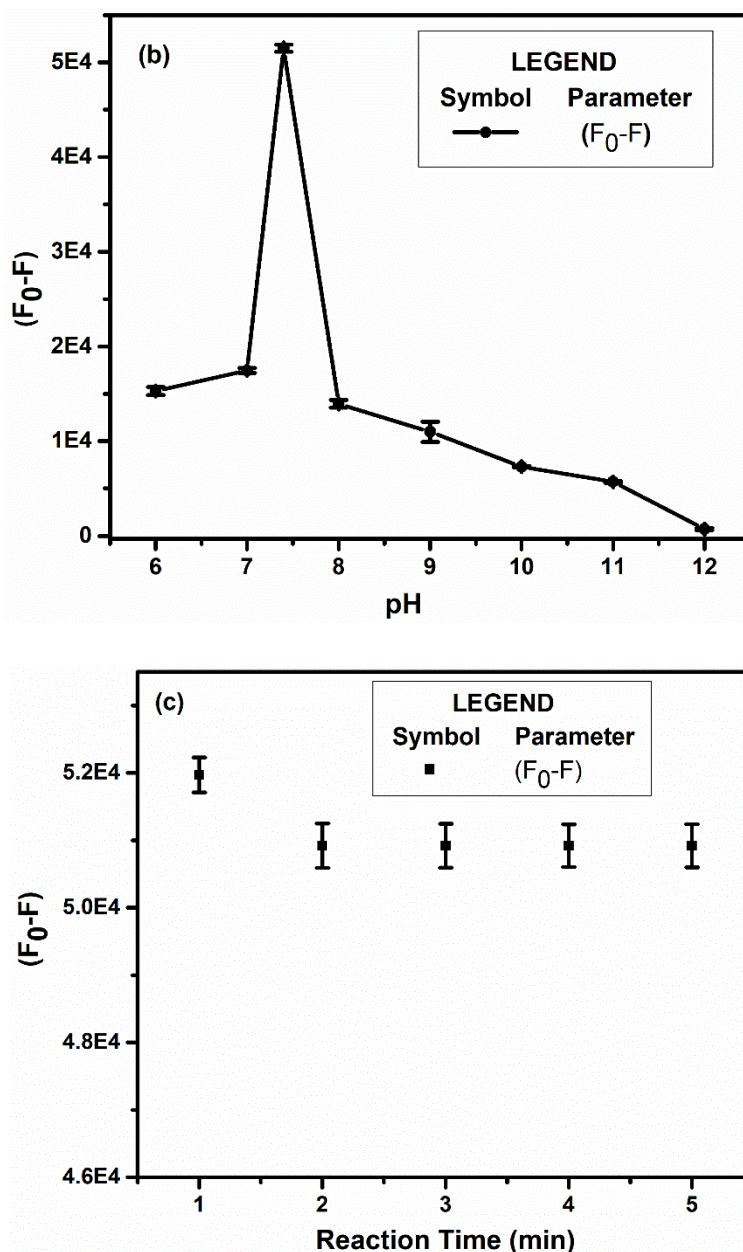
Fig. 4.58 (a) Effect of different buffer solutions on (F₀-F) (1) phosphate buffer, (2) acetate buffer, (3) tris buffer, (4) ultrapure water, and (5) phosphate buffer saline. (b) Effect of pH on (F₀-F). (c) Effect of reaction time on (F₀-F)

As represented in Fig. 4.58a, the fluorescence quenching efficiency of 10 μM BPA in PBS was significantly higher than other buffer solutions. Ultrapure water exhibits a moderate level of fluorescence quenching intensity whereas, basic buffers such as phosphate buffer and tris buffer showed a reduced level of fluorescence quenching intensity compared to that in phosphate buffer saline. Moreover, in acetate buffer, the fluorescence quenching of β-CD functionalized ZnO QDs was not observed (Fig. 4.58a). The absence

of the emission peak in the presence of acetate buffer reveals that the functionalized QDs have been decomposed (Bian et al. 2011). However, the fluorescence quenching efficiency of the functionalized QDs in the presence and absence of different buffers for the detection of 10 µM BPA revealed that the presence of buffer is conductive (Geng et al. 2016; Singh and Mehta 2016) for the detection of BPA.

The alteration in fluorescence intensity of the β-CD functionalized ZnO QDs with respect to pH was examined by varying the pH of PBS from 6.0 to 12.0. The effect of pH on fluorescence quenching efficiency was investigated by recording the fluorescence spectrum of functionalized QDs in the presence and absence of 10 µM BPA (Fig. 4.58b). The fluorescence of functionalized QDs was quenched well in the presence of 10 µM BPA at pH 6.0, which may be due to an increase in H^+ ions that can dissociate ZnO efficiently (Suyver et al. 2001; Bian et al. 2011). The functionalized QDs showed an increase in fluorescence intensity from pH 6.0 to 7.4, with a maximum of pH 7.4. The quenched fluorescence intensity is found to decrease when the pH is leveled off from 8.0 to 12.0. However, the reduction in fluorescence intensity of functionalized QDs was observed due to competitive binding between ligands and hydroxyl ions to the crystal and, thus, increases the surface defects of nanoparticles (Zhang et al. 2008). The fluorescence quenching efficiency was recorded in terms of (F_0-F), which indicates the optimum pH value of 7.4. Hence, pH 7.4 was used as an optimum reaction condition for further analytical experiments.

The fluorescence intensity of β-CD functionalized ZnO QDs was found to decrease rapidly with the addition of 10 µM BPA solution, which was maintained at pH 7.4 using PBS. The fluorescence quenching efficiency was found to attain a minimum value within 2 min (optimum time) and remained constant after that for the above condition (Fig. 4.58c). Similarly, the fluorescence quenching intensity of a reaction mixture of alkaline phosphatase detection was reported to decrease progressively with an increase in reaction time and attained a minimum value of 30 min (Hu et al. 2017).
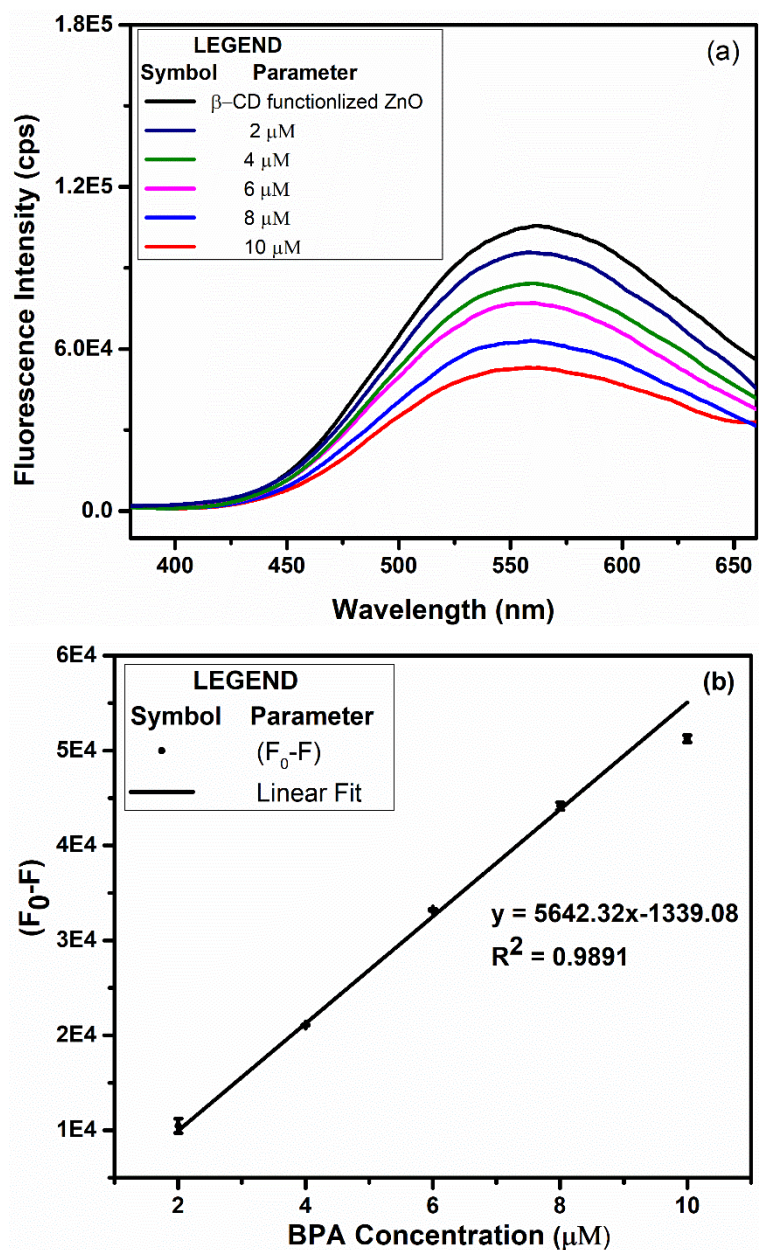
Fig. 4.59 (a) Effect of BPA concentration on fluorescence intensity of β-CD functionalized ZnO QDs. (b) A plot of fluorescence quenching efficiency (F_0-F) of functionalized QDs and BPA concentration

Under the optimum reaction conditions, the effect of BPA concentration on fluorescence intensity of β-CD functionalized QDs was investigated. As shown in Fig. 4.59a, the fluorescence intensity of functionalized QDs was reduced gradually with increasing concentration of BPA from 2 μM-10 μM, exhibiting linearity with a correlation coefficient of 0.9891 (Fig. 4.59b). The limit of detection (LOD) for BPA was found to be 0.19 μM. The performance of β-CD functionalized ZnO QDs as BPA detection method is compared with other fluorescence-based analytical methods reported in the literature and

represented in Table 4.9. Comparing with the previously reported fluorescence-based detection methods for BPA, a low detection limit signifies high sensitivity for the prepared β-CD functionalized ZnO QDs sensor.

Table 4.9 Comparison of the proposed method with other fluorescence mediated methods for detection of BPA

S. No.	Analytical method	LOD	Linearity range	Reference
1	β-CD	1 μM	6 μM- 1 mM	(Wang et al. 2006)
2	BPO	5 μM	5 - 100 μM	(Zhang et al. 2014)
3	HPTS	4.4 μM	0 - 88 μM	(Mccracken et al. 2017)
4	GMIN@NC	0.21 μM	50 - 1000 μg/L	(Uzek et al. 2019)
5	β-CD functionalized ZnO	0.19 μM	2 - 10 μM	Present work

4.5.3 Fluorescence quenching mechanism of β-CD functionalized ZnO QDs for detection of BPA

As shown in Fig. 4.60a, there is no overlap between the absorption spectrum of BPA and the emission spectrum of functionalized QDs, nullifying the FRET mechanism for sensing. A stern-Volmer equation (1) was used to get further insight into the quenching mechanism of β-CD functionalized ZnO QDs as a detection method for BPA (Singh and Mehta 2016).

120
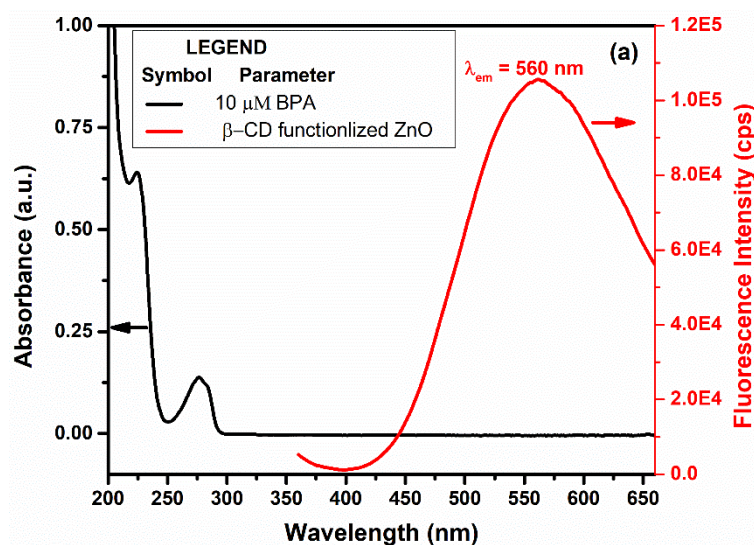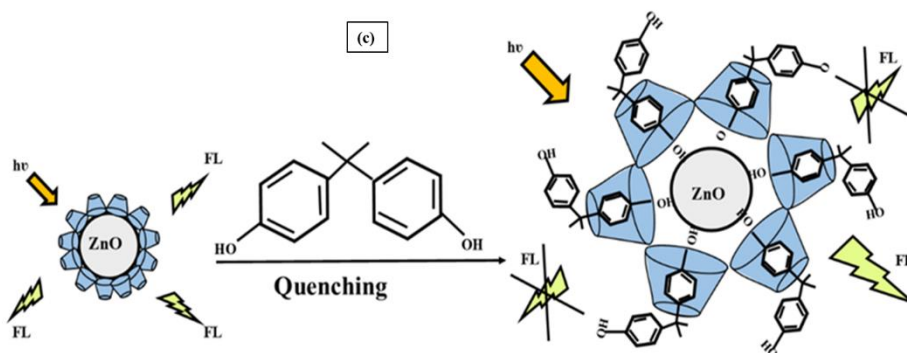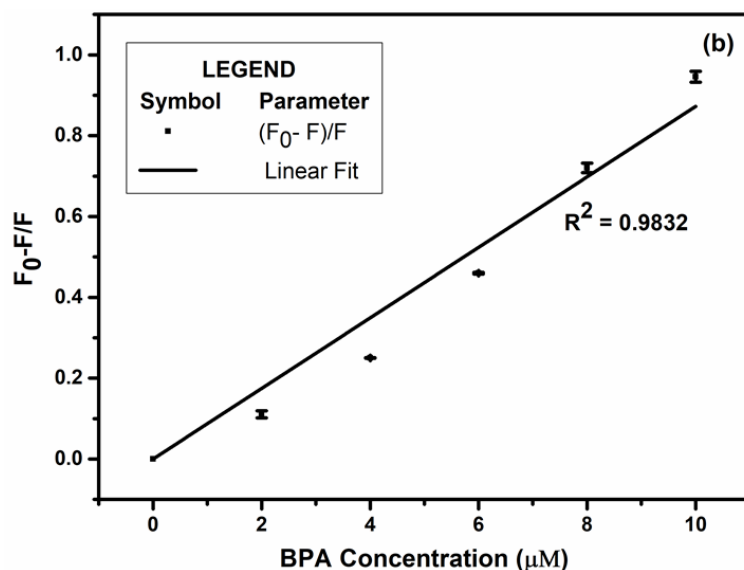
Fig. 4.60 (a) UV-vis spectra of 10 μM of BPA and fluorescence emission spectra of β-CD functionalized ZnO QDs (b) The stern-Volmer plot of BPA (c) Fluorescence quenching mechanism

The plot of $[\frac{F_0-F}{F}]$ at 560 nm against [BPA] exhibited a linear behavior with the regression coefficient of 0.9832 (Fig. 4.60b). From equation (1), the value of the Stern-Volmer constant K_{sv} was found to be 8725 M^{-1}, which indicates strong binding effects and higher quenching intensities due to complex formation between β-CD functionalized ZnO and BPA with an increase in concentrations of BPA. Kitano et al. (2003) reported that β-CD could form an inclusion complex with BPA (135 μM) having an association constant of 35000 M^{-1} (Kitano et al. 2003). BPA and β-CD can form a stoichiometric 1:1 inclusion complex with a high association constant (Olmo et al. 2006). As shown in Fig. 4.60b, a plot between relative fluorescence intensity and BPA concentration resulted in a linear relationship that follows the Stern-Volmer equation. Thus, the addition of BPA leads to the

deactivation of excited state β-CD functionalized ZnO QDs through the steric hindrance of BPA over the hydrophobic cavity of β-CD forming host-guest inclusion complexes via electron transfer quenching process (Fig. 4.60c).

4.5.4 Selectivity and interference study

The specificity of the functionalized ZnO QDs towards BPA detection was evaluated by analyzing the structural analogs of BPA and dyestuff. However, industrial and anthropogenic activity leads to the presence of some common metal ions and organic substances in water bodies. These common interfering compounds were chosen for the selectivity test in BPA detection (Table 4.10). The presence of foreign species leads to a change in fluorescence intensity below 5 %, which was considered as no interfering species in BPA detection (Wang et al. 2006). As represented in Table 4.10, metal ions, dyestuff, and BPA structural analogs exhibit very little interference in BPA detection.

Table 4.10 Selectivity and interference study for BPA detection

Species tested	Concentration	Change of Fluorescence (%)
Ba^{2+}	$10*10^{-5}$ mol/L	-4.3
Ca^{2+}	$10*10^{-5}$ mol/L	+0.9
Cd^{2+}	$10*10^{-5}$ mol/L	-1.4
Cr^{3+}	$10*10^{-5}$ mol/L	+1.8
Fe^{3+}	$10*10^{-5}$ mol/L	+3.7
Pb^{2+}	$10*10^{-5}$ mol/L	+1.6
Hg^{2+}	$10*10^{-5}$ mol/L	-2.2
K^+	$10*10^{-5}$ mol/L	+4.6
Mn^{2+}	$10*10^{-5}$ mol/L	+2.3
Mg^{2+}	$10*10^{-5}$ mol/L	-0.1
Na^+	$10*10^{-5}$ mol/L	+3.8
Zn^{2+}	$10*10^{-5}$ mol/L	+4.1
CO_3^{2-}	$10*10^{-5}$ mol/L	-3.2
So_4^{2-}	$10*10^{-5}$ mol/L	+4.7
Cl-	$10*10^{-5}$ mol/L	+1.9
Reactive blue	100 μM	-0.4
Methyl orange	100 μM	+0.1

4-Fluorophenol	100 µM	-6.7
2,4,6-Trichlorophenol	100 µM	+2.7
4-Aminophenol	100 µM	+2.5

4.5.5 Analysis of real water samples for analytical application of β-CD functionalized ZnO QDs

Different concentrations of 300 µl BPA (2, 8, and 10 µM) were spiked in two different water samples, viz. Tap-water (TW) and double distilled water (DDW) as given in Table 4.11. Further, 100 µl of functionalized QDs was added, and the reaction mixtures were diluted with 900 µl of PBS solution each. The samples were incubated for 2 min at room temperature, and the fluorescence intensities were measured at an excitation wavelength of 340 nm.

Table 4.11 Detection of BPA spiked in different water samples

Sample	Spiked with BPA (µM)	Observed (µM)[a]	Recovery (%)[b]	RSD (%)[c]
Tap water	0	ND	-	-
	2	2.16±0.24	102.30±1.40	1.42
	8	8.18±0.11	102.30±1.41	1.05
	10	9.41±0.069	94.13±0.69	0.72
Double distilled water	0	ND	-	-
	2	2.08±0.20	104.31±10.13	1.20
	8	8.15±0.088	101.84±1.10	0.82
	10	9.34±0.003	93.41±0.03	0.031

ND-Not detected

[a] concentration of BPA expressed as a mean of three consecutive measurements ± standard deviation (SD)

[b] Recovery was defined as (concentration recovered/initial concentration)* 100%

[c] Relative standard deviation (RSD) was defined as (standard deviation/average)* 100%

A spike is generated by adding a known amount of the analyte to a sample, testing the spiked sample, and determining if the added amount is recovered or not. And the

recovery is used for validating the spiking method. As per the USFDA standards for validating the spiking method, the relative recovery should be 80 % to 120 %, and the precision should be ≤ 20 % (USFDA 2019). Here, the recovery of the spiked BPA was found to be higher than 100% and higher than the nominal value of the spike. Hence the spiking method was adopted to validate the detection technique of BPA. The recoveries of spiked BPA in TW and DDW samples were found to be in the range of 94 – 102 % (TP) and 93 – 104 %, respectively, as given in Table 4.11. Even though the efficiencies of the β-CD functionalized ZnO QDs in detecting BPA in TW and DDW samples differ, the difference is still marginal, and it can be used for BPA detection in natural waters without having any other components of a hindrance.

CHAPTER 5

CONCLUSIONS

5.1 Summary and significant finding

The research work presented in this report emphasizes the utilization of ZnO nanoparticles to detect and degrade endocrine disruptors. The ZnO nanoparticles were synthesized using biological and chemical methods. For biological synthesis, a total of 6 morphologically distinct endophytic fungal species were isolated from the leaves of a medicinal plant, *Nothapodytes foetida*, collected from Agumbe forest, Karnataka, India. A zinc metal tolerant endophytic fungus was identified as *Cochliobolus geniculatus* among the six fungi based on the internal transcribed spacer (ITS) region of rDNA with NCBI accession number KF946042. Physicochemical parameters such as precursor salts concentrations, reaction time and pH for the biosynthesis of ZnO nanoparticles were optimized using one factor at a time method. The structural, optical and morphological properties were studied using UV-vis, FTIR, FESEM coupled EDX, HRTEM and fluorescence analysis. The mechanism for the synthesis of nanoparticles was studied based on the SDS-PAGE analysis. The discrete, polydisperse and quasi-spherical hexagonal wurtzite structured ZnO nanoparticles with an average size of 5.25 ± 1.43 nm were synthesized. The degradation potential of ZnO nanoparticles under UV irradiation was evaluated for p-NP and BPA. Studies on kinetics of degradation, degree of mineralization, reuse potential of catalyst and degradation pathway based on radical scavenging experiment were carried out. Moreover, the fluorescence property of ZnO nanoparticles was explored for the detection of p-NP and BPA. The influence of different excitation wavelengths, buffers and pH on fluorescence quenching efficiency of ZnO nanoparticles were studied. Further, the detection mechanism was studied and detection limits for p-NP and BPA were reported.

A yellow fluorescent β-CD and APTES capped ZnO nanoparticles were synthesized by the co-precipitation method for the detection of BPA and p-NP, respectively. The yellow fluorescence emission spectra were observed due to the transition of an electron from a shallow donor to a deeply trapped hole. The capping of β-CD and APTES on the surface of the nanoparticle was confirmed by FTIR, UV-vis, TEM, SEM coupled EDX, XRD and

fluorescence analysis. Further, the detection of endocrine disruptors such as BPA and p-NP was studied using fluorescence spectroscopy. The operational parameters such as the effect of different buffers and pH of reaction were studied to attain the highest fluorescence quenching efficiency. Lastly, the detection mechanism was discussed based on the Stern-Volmer and Lineweaver-Burk plot.

The significant findings of the present research work are summarized as below:

1. **Biosynthesized ZnO for detection and degradation of p-NP and BPA**

➢ In the present study, a total of 6 fungi were isolated from the healthy leaves of *Nothapodytes foetida* by repetitive subculturing based on discrete morphological characteristics. Fungal isolate exhibiting the highest zinc tolerance index was subjected to rDNA ITS sequencing and identified as *C. geniculatus*.

➢ The size-tunable blue shift in SPR of ZnO nanoparticles was observed at 30 mM of zinc acetate dihydrate as a precursor salt with 24 h of reaction time at pH 10 and is considered as optimum conditions for the synthesis of ZnO nanoparticles.

➢ The UV-vis spectra exhibit the spectroscopic signature peak based on the SPR of ZnO at 369 nm and the peak at 280 nm indicating the presence of protein capping on the nanoparticles surface and is confirmed by FTIR analysis.

➢ The bandgap of ZnO nanoparticles was estimated using a derivative of absorbance concerning photon energy and found to be 3.26 eV. The observed bandgap is lesser than its bulk counterpart (3.7 eV), which signifies the quantum confinement effects and the presence of intrinsic crystal defects.

➢ Denatured proteins with precursor salt exhibit the characteristic SPR peak of ZnO nanoparticles, which signifies that the reduction of metal resulted from the amino acid residues of the proteins rather than the enzymatic process.

➢ SDS-PAGE analysis exhibits protein with a molecular weight in the range of 97 kDa-36 kDa involved in the reduction of zinc acetate into ZnO nanoparticles. Consequently, 58 and 52 kDa proteins act as capping material in ZnO nanoparticle synthesis and impart stability to the nanomaterial.

➢ Under optimum reaction conditions, the photocatalytic degradation of p-NP and BPA follows first-order reaction kinetics and degradation efficiency of 78.57 % and 85.18 %, respectively, were obtained.

- COD and TOC analysis exhibit 60 % and 50.9 % of the mineralization degree for p-NP (25 mg/L) at the end of 300 min. At 220 min of UV irradiation, BPA (10 mg/L) exhibits 63.6 % and 63.6 % of COD and TOC removal, respectively.

- The degradation reaction of p-NP and BPA were found to be initiated and dominated by •OH and h^+ radicals. The intermediates and products of photocatalytic degradation of p-NP and BPA were identified through LC-MS analysis and the degradation pathway was proposed.

- A characteristic fluorescence emission peak was observed at 440 nm due to the blue emission of ZnO. The intrinsic defects such as oxygen and zinc interstitials are attributed to the blue emission band of biogenic ZnO nanoparticles.

- The Addition of BPA leads to a blue shift in ZnO emission wavelength, whereas p-NP leads to the redshift in ZnO emission wavelength. The fluorescence intensity was decreased to 92.8 % and 67.1 % in the presence 750 μM of p-NP and 400 μM of BPA, respectively.

- The limit of detection was found to be 17.9 μM and 0.35 μM for p-NP and BPA, respectively. The hypothetical sensing mechanism for BPA is ascribed to dynamic quenching and for p-NP, it follows static quenching.

2. APTES@ZnO for detection of p-NP

- The fluorescence intensity of ZnO and APTES@ZnO QDs decreased to 27% and 59.95 %, respectively, in the presence of 80 μM p-NP, indicating high quenching compared to the former.

- A particle size histogram obtained from TEM analysis displayed particles in the range of 2-6 nm with an average size of 3.7 ± 0.51 nm with a polydispersity index of 0.13.

- UV-vis spectrum of APTES@ZnO exhibited a characteristic absorption shoulder at 335 nm and p-NP shows absorption peaks at 226, 318, and 397 nm. Further, the UV-vis spectrum of the APTES@ZnO QDs in the presence of p-NP exhibited the absorption peaks at 335 and 397 nm, showing the overlapping characteristics of APTES@ZnO QDs and p-NP and is confirmed by FTIR, XRD and SEM coupled EDX analysis.

- A linear relationship was obtained between fluorescence quenching efficiency of APTES@ZnO QDs towards the 10-80 μM of p-NP with 0.089 μM as LOD. Further, the hypothetical sensing mechanism for fluorescence sensing was ascribed to the

partially inner filter effect of p-NP towards APTES@ZnO QDs, and the transfer of excited state electrons of the APTES@ZnO QDS to p-NP.

3. β-CD@ZnO QDs for detection of BPA

➢ A yellow fluorescent β-CD-functionalized water-stable ZnO QDs with a mean particle size of 4.96 ± 0.97 nm and a polydispersity index of 0.20 have been synthesized. And the conjugation of β-CD with ZnO was confirmed by the UV-vis, XRD and FTIR analysis.

➢ The fluorescence intensity of functionalized QDs decreased to 52 % in the presence of 10 μM of BPA. And a linear response was obtained between fluorescence-quenching intensity and BPA concentration ranges from 2 to 10 μM, having a lower detection limit of 0.19 μM.

➢ The Stern–Volmer plot revealed a quenching mechanism by electron transfer between β-CD-functionalized ZnO QDs and BPA due to inclusion complex formation.

In conclusion, the isolated endophytic fungus *C. geniculatus* can effectively synthesize ZnO nanoparticles by an eco-friendly, one-step synthesis method. The biosynthesized ZnO nanoparticles can be considered as an efficient photocatalyst for the degradation of endocrine disruptors by avoiding electron-hole recombination due to the presence of protein capping on nanoparticles surfaces. The recyclability of the nano-agent, which is significant to minimize waste and energy consumption, describes the effectiveness of the degradation process. Moreover, the fluorescence property of biogenic ZnO nanoparticles aids in the detection of endocrine disruptors. Thus, the presence of proteins on nanoparticles surface aids in the degradation and detection of two different endocrine disruptors. Further, the yellow fluorescent ZnO nanoparticles were synthesized by chemical method and different capping agents were used for the detection of two different endocrine disruptors. However, the obtained LOD is lower in the case of chemically synthesized ZnO nanoparticles.

5.2 Scope for Future Work

The biosynthesized nanoparticles from endophytic fungi *C. geniculatus* can be used as a potential photocatalyst in wastewater treatment for the degradation of various organic compounds and decontamination of water. Further, the remarkable fluorescence of ZnO nanoparticles can be utilized in the field of bio-imaging and drug delivery. Moreover, the

nano-engineered membrane systems impregnated with nanoparticles can be used as a fluorescence-based indicator for organic pollutants/bio-burden/heavy metal threshold. The synthesized nanoparticles can be modified by encapsulation in a silica shell and immobilized by a polymer matrix or hydrogel-based systems to remove pollutants from contaminated water effectively. Moreover, the composites of ZnO nanoparticles with rare earth metals/noble metals/other metalloid nanoparticles can be used as efficient entities for the degradation of various aromatic compounds. Further, the large-scale system can be designed based on experimental results of small-scale models.

Water stable, chemically functionalized ZnO QDs were employed for the fluorescent-mediated selective detection of BPA and p-NP. Further, similar kinds of functionalized ZnO QDs can be used for the ultrasensitive detection of nitroaromatics, pesticides, pharmaceutical compounds, and radioactive elements with rapid, simple, and portable monitoring systems. Moreover, the functionalized ZnO QDs have been found to be used as chlorine (Singh and Mehta 2016), cobalt ion sensors (Geng et al. 2017), gas sensors (Zhu and Zeng 2017), and also used as fluorescent labels for ultrasensitive detection and imaging (Zhang and Xiong 2015; Liu et al. 2017a). In this context, several strategies can be designed to effectively synthesize functionalized ZnO QDs, which can act as a multicomponent receptor system for the detection and or removal of pollutants for the environmental cleanup process. Thus, future studies explore the potential of ZnO nanoparticles as a novel catalyst and or sensor system in the field of material and environmental science.

REFERENCES

Aboulaich, A., Tilmaciu, C. M., Merlin, C., Mercier, C., Guilloteau, H., Medjahdi, G., Schneider, R. (2012). "Physicochemical properties and cellular toxicity of (poly) aminoalkoxysilanes-functionalized ZnO quantum dots." *Nanotechnology* 23:33.

Achour, A., Islam, M., Vizireanu, S., Ahmad, I., Akram, M. A., Saeed, K., Pireaux, J. J. (2019). Orange/red photoluminescence enhancement upon sf6 plasma treatment of vertically aligned ZnO nanorods. *Nanomaterials*, *9*(5), 794.

Ahamad, T., Naushad, M., Alzaharani, Y. and Alshehri, S. M. (2020). "Photocatalytic degradation of bisphenol-A with g-C_3N_4/MoS_2-PANI nanocomposite: kinetics, main active species, intermediates and pathways.'' *Journal of Molecular Liquids*, 311, p.113339.

Ahangaran, F., & Navarchian, A. H. (2020). Recent advances in chemical surface modification of metal oxide nanoparticles with silane coupling agents: A review. *Advances in Colloid and Interface Science*, 102298.

Ahmed, S. N. & Haider, W. (2018). "Heterogeneous photocatalysis and its potential applications in water and wastewater treatment: a review." *Nanotechnology*, *29* (34), 342001.

Ahmed, S., Rasul, M. G., Brown, R., Hashib, M. A. (2011). "Influence of parameters on the heterogeneous photocatalytic degradation of pesticides and phenolic contaminants in wastewater: a short review." *J Environ Manag*, 92, pp.311–330.

Agency for Toxic Substances and Disease Registry (ATSDR) (1992). "Toxicological Profile for Nitrophenols (Draft)." Public Health Service, U.S. Department of Health and Human Services, Atlanta, GA. 1990.

Afzal, S., Julkapli, N. M. and Mun, L. K. (2019). "Response surface approach for visible light assisted photocatalytic degradation of ortho nitrophenol by magnetically separable TiO_2/CS nanocomposite.'' *Materials Science in Semiconductor Processing*, 99, pp.34-43.

Anandan, S., Kumar, P. S., Pugazhenthiran, N. (2008). "Effect of loaded silver nanoparticles on TiO_2 for photocatalytic degradation of Acid Red 88." *Sol Energy Mater Sol Cells* 92:929–937.

Anucha, C. B., Altin, I., Bacaksız, E., Kucukomeroglu, T., Belay, M. H., & Stathopoulos, V. N. (2021). "Enhanced photocatalytic activity of CuWO₄ doped TiO₂ photocatalyst towards carbamazepine removal under UV irradiation." *Separations*, 8(3), 25.

Alexander, H.C., Dill, D.C., Smith, L.W., Guiney, P.D. and Dorn, P. (1988). "Bisphenol A: acute aquatic toxicity.'' *Environmental Toxicology and Chemistry: An International Journal*, *7*(1), pp.19-26.

Alias, S. S., Ismail, A. B., and Mohamad A. A. (2010). "Effect of pH on ZnO nanoparticle properties synthesized by sol–gel centrifugation." *Journal of Alloys and Compounds,* 499, 231-237.

Aljuboury, D. A. D. A., Palaniandy, P., Abdul Aziz, H. B., & Feroz, S. (2017). "Degradation of total organic carbon (TOC) and chemical oxygen demand (COD) in petroleum wastewater by solar photo-Fenton process." *Global NEST Journal*, 19(3), 430-438.

Alshehri, A. A., & Malik, M. A. (2019). "Biogenic fabrication of ZnO nanoparticles using Trigonella foenum-graecum (Fenugreek) for proficient photocatalytic degradation of methylene blue under UV irradiation." *Journal of Materials Science: Materials in Electronics*, *30*(17), 16156-16173.

Arora, P. K., Srivastava, A. & Singh, V. P. (2014). "Bacterial degradation of nitrophenols and their derivatives." *Journal of Hazardous Materials*, 266, 42-59.

Bakker, J., Biesenbeek, J. D., Boon, P., Bos, P., Broekhuizen, F. Van., Geertsma, R., Liesbeth, Mennes, W., Palmen, N., Piersma, A., Schuur, G., Sijm, D., Ven, L. van der, Verbist, K., Wouters, M., and Zeilmaker, M. (2014). "Bisphenol A part 1. Facts and figures on human and environmental health issues and regulatory perspectives." *RIVM Rep. 601351001/2014*, 78.

Balakumaran, M. D., Ramachandran, R., and Kalaichelvan, P. T. (2015). "Exploitation of endophytic fungus, Guignardia mangiferae for extracellular synthesis of silver nanoparticles and their in vitro biological activities." *Microbiological Research*, 178, 9–17.

Baskar, G., Chandhuru, J., Fahad, K. S., and Praveen, A. S. (2013). "Mycological Synthesis, Characterization and Antifungal Activity of Zinc Oxide Nanoparticles." *Asian Journal of Pharmacy and Technology*, 3(4), 142–146.

Barrak, H., Saied, T., Chevallier, P., Laroche, G., M'nif, A., Hamzaoui, A. H., 2016. "Synthesis, characterization, and functionalization of ZnO nanoparticles by N-(trimethoxysilylpropyl) ethylenediamine triacetic acid (TMSEDTA): investigation of the interactions between Phloroglucinol and ZnO@ TMSEDTA." *Arab. J. Chem.* 12 (8), 4340–4347.

Bazrafshan, E., Al-Musawi, T. J., Silva, M. F., Panahi, A. H., Havangi, M. and Mostafapur, F. K. (2019). "Photocatalytic degradation of catechol using ZnO nanoparticles as catalyst: Optimizing the experimental parameters using the Box-Behnken statistical methodology and kinetic studies.'' *Microchemical Journal*, 147, pp.643-653.

Bharathi, D., Siddlingeshwar, B., Krishna, R. H., Singh, V., Kottam, N., Divakar, D. D., & Alkheraif, A. A. (2018). "Green and cost effective synthesis of fluorescent carbon quantum dots for dopamine detection." *Journal of fluorescence*, 28(2), 573-579.

Bhatkhande, D. S., Pangarkar, V. G., Beenackers, A. A. C. M. (2002). "Photocatalytic degradation for environmental applications – a review.'' *J Chem Technol Biotechnol*, 77, pp.102–116.

Bini, R. A., Marques, R. F. C., Santos, F. J., Chaker, J. A., Jafelicci Jr. M., 2012. "Synthesis and functionalization of magnetite nanoparticles with different amino-functional alkoxysilanes." *J. Magn. Magn. Mater.* 324 (4), 534–539

Bechambi, O., Chalbi, M., Najjar, W., and Sayadi, S. (2015). "Photocatalytic activity of ZnO doped with Ag on the degradation of endocrine disrupting under UV irradiation and the investigation of its antibacterial activity." *Appl. Surf. Sci*., 347, 414–420.

Bechambi, O., Jlaiel, L., Najjar, W., Sayadi, S. (2016). ''Photocatalytic degradation of bisphenol A in the presence of Ce–ZnO: Evolution of kinetics, toxicity and photodegradation mechanism.'' *Mater. Chem. Phys*., 173, pp. 95-105.

Bergman, A., Heindel, J. J., Jobling, S., Kidd, K., Zoeller, T. R. & World Health Organization. (2013). State of the science of endocrine disrupting chemicals 2012. World Health Organization.

Bian, S. W., Mudunkotuwa, I. A., Rupasinghe, T., Grassian, V. H., 2011. "Aggregation and dissolution of 4 nm ZnO nanoparticles in aqueous environments: influence of pH, ionic strength, size, and adsorption of humic acid." *Langmuir* 27 (10), 6059–6068.

Birla, S. S., Gaikwad, S. C., Gade, A. K. and Rai, M. K. (2013). "Rapid Synthesis of Silver Nanoparticles from Fusarium oxysporum by Optimizing Physicocultural Conditions." *The Scientific World Journa„* 12.

Boehncke, A., Mangelsdorf, I., Wibbertmann, A. and World Health Organization (2000). ''Mononitrophenols.'' World health organization.

Bradley, R., Burt, A. J., & Read, D. J. (1982). "The biology of mycorrhiza in the Ericaceae: VIII. The role of mycorrhizal infection in heavy metal resistance." *New Phytologist*, *91*(2), 197-209.

Bruce, I. J., & Sen, T. (2005). Surface modification of magnetic nanoparticles with alkoxysilanes and their application in magnetic bioseparations. *Langmuir*, *21*(15), 7029-7035.

Cao, X., Shen, F., Zhang, M., Bie, J., Liu, X., Luo, Y., Guo, J., Sun, C. (2014). "Facile synthesis of chitosan-capped ZnS quantum dots as an eco-friendly fluorescence sensor for rapid determination of bisphenol A in water and plastic samples." *R Soc Chem* 4:16597–16606.

Casa, M., Sarno, M., Paciello, L., Beaumont, M.R., Ciambelli, P., 2016. "Synthesis and characterization of water stable ZnO quantum dots based-sensor for nitro-organic compounds." *Chem. Eng. Trans.* 47, 7–12.

Chai, W., Handa, Y., Suzuki, M., Saito, M., Kato, N. and Horiuchi, C. A., 2005. "Biodegradation of bisphenol A by fungi." *Appl. Biochem. Biotechnol.*, 120, pp. 175-182.

Chemingui, H., Missaoui, T., Mzali, J. C., Yildiz, T., Konyar, M., Smiri, M. & Yatmaz, H. C. (2019). "Facile green synthesis of zinc oxide nanoparticles (ZnO NPs): antibacterial and photocatalytic activities." *Materials Research Express*, *6*(10), 1050b4.

Central Pollution Control Board (CPCB) (2016), "Phenols & phenolic compounds." www.cpcb.nic.in

Chen, X., Wu, Z., Liu, D., & Gao, Z. (2017). "Preparation of ZnO photocatalyst for the efficient and rapid photocatalytic degradation of azo dyes." *Nanoscale research letters*, 12(1), 1-10.

Cheng, J., Tan, G., Li, W., Li, J., Wang, Z., Jin, Y. (2016). "Preparation, characterization and in vitro photodynamic therapy of a pyropheophorbide-a-conjugated Fe_3O_4 multifunctional magneto fluorescence photosensitizer." *RSC Adv.* 6 (44), 37610–37620.

Chen, X., Wang, Q., Wang, X. J., Li, J., & Xu, G. B. (2021). Synthesis and performance of ZnO quantum dots water-based fluorescent ink for anti-counterfeiting applications. *Scientific Reports*, *11*(1), 1-9.

Chiu, Y. H., Chang, T. F. M., Chen, C. Y., Sone, M., Hsu, Y. J. (2019). ''Mechanistic insights into photodegradation of organic dyes using heterostructure photocatalysts.'' *Catalysts*., 9, pp.430.

Chullasat, K., Nurerk, P., Kanatharana, P., Davis, F., Bunkoed, O. (2018). A facile optosensing protocol based on molecularly imprinted polymer coated on CdTe quantum dots for highly sensitive and selective amoxicillin detection. *Sensors and Actuators B: Chemical*, *254*, 255-263.

Cialla-May, D., Weber, K., & Popp, J. (2020). "Sensitive detection of organic pollutants by advanced nanostructures." *In Advanced Nanostructures for Environmental Health* (pp. 35-74). Elsevier.

Clarance, P., Luvankar, B., Sales, J., Khusro, A., Agastian, P., Tack, J. C. & Kim, H. J. (2020). "Green synthesis and characterization of gold nanoparticles using endophytic fungi Fusarium solani and its in-vitro anticancer and biomedical applications." *Saudi journal of biological sciences*, *27*(2), 706-712.

Corrales, J., Kristofco, L.A., Steele, W.B., Yates, B.S., Breed, C.S., Williams, E.S. and Brooks, B.W. (2015). "Global assessment of bisphenol A in the environment: review and analysis of its occurrence and bioaccumulation.'' *Dose-Response*, *13*(3), p.1559325815598308.

Costenaro, D., Carniato, F., Gatti, G., Marchese, L., & Bisio, C. (2013). "Preparation of luminescent ZnO nanoparticles modified with aminopropyltriethoxy silane for optoelectronic applications." *New Journal of Chemistry*, *37*(7), 2103-2109.

Cullity, B. D., Stock, S.R. "Elements of X-ray Diffraction". third ed., *Pearson Education*, 2001.

Danagoudar, A., Pratap, G. K., Shantaram, M., Ghosh, K., Kanade, S. R., & Joshi, C. G. (2020). "Characterization, cytotoxic and antioxidant potential of silver nanoparticles biosynthesised using endophytic fungus (Penicillium citrinum CGJ-C1)." *Materials Today Communications*, *25*, 101385.

Daneshvar, N., Salari, D., Khataee, A., R. (2004). "Photocatalytic degradation of azo dye acid red 14 in water on ZnO as an alternative catalyst to TiO_2''. *J Photochem Photobiol A Chem*, 162, pp.317–322.

Daniel, R. M., Danson, M. J., Eisenthal R., Lee, C. K., and Peterson, M. E. (2008). "The effect of temperature on enzyme activity: new insights and their implications." *Extremophiles*, 12, 51–59

Darroudi M, Sabouri Z, Kazemi R (2014) "Green chemistry approach for the synthesis of ZnO nanopowders and their cytotoxic effects." *Ceram Int*, 40:4827–4831.

Daskalaki, V.M., Frontistis, Z., Mantzavinos, D. and Katsaounis, A. (2011). ''Solar light-induced degradation of bisphenol-A with TiO_2 immobilized on Ti.'' *Catal. Today*, 161, pp. 110- 114.

Devi, L. S., and Joshi, S. R. (2015). "Ultrastructures of silver nanoparticles biosynthesized using endophytic fungi." *Journal of Microscopy and Ultrastructure*, 3(1), 29–37.

Di Paola, A., Augugliaro, V., Palmisano, L., Pantaleo, G., & Savinov, E. (2003). "Heterogeneous photocatalytic degradation of nitrophenols." *Journal of Photochemistry and Photobiology A: Chemistry*, *155*(1-3), 207-214.

Diamanti-Kandarakis, E., Bourguignon, J. P., Giudice, L. C., Hauser, R., Prins, G. S., Soto, A. M., & Gore, A. C. (2009). "Endocrine-disrupting chemicals: an Endocrine Society scientific statement." *Endocrine reviews*, *30*(4), 293-342.

Din MI, Khalid R, Hussain Z (2019). "Nanocatalytic assemblies for catalytic reduction of nitrophenols: a critical review." *Crit Rev Anal Chem* 50:1–17.

Ding, Y., Zhou, P., Tang, H. (2016). ''Visible-light photocatalytic degradation of bisphenol A on NaBiO$_3$ nanosheets in a wide pH range: a synergistic effect between photocatalytic oxidation and chemical oxidation.'' *Chem. Eng. J.*, 291, pp. 149-160.

Djurišić AB, Leung YH, Tam KH (2006). "Influence of excitation wavelength Green , yellow, and orange defect emission from ZnO nanostructures." *Appl Phys Lett* 103107:28–31.

Dodds, E.C. and Lawson, W. (1936). "Synthetic strogenic agents without the phenanthrene nucleus.'' *Nature*, *137*(3476), pp.996-996.

Dong, S., Lee, G.J., Zhou, R. and Wu, J.J. (2020). "Synthesis of g-C3N4/BiVO4 heterojunction composites for photocatalytic degradation of nonylphenol ethoxylate.'' *Separation and Purification Technology*, *250*, p.117202.

Eio, E.J., Kawai, M., Tsuchiya, K., Yamamoto, S. and Toda, T., 2014. "Biodegradation of bisphenol A by bacterial consortia." *Int. Biodeterior. Biodegr.*, 96, pp. 166-173.

Elbarbry, F., Wilby, K., Alcorn, J., 2006. "Validation of a HPLC method for the determination of p-nitrophenol hydroxylase activity in rat hepatic microsomes." J. Chromatogr. B 834 (1–2), 199–203.

Eltoukhy, A., Jia, Y., Nahurira, R., Abo-Kadoum, M. A., Khokhar, I., Wang, J., & Yan, Y., 2020. "Biodegradation of endocrine disruptor bisphenol A by *Pseudomonas putida* strain YC-AE1 isolated from polluted soil, Guangdong, China." BMC Microbiol., 20, pp. 1-14.

Environment Canada (2008). "Screening assessment for the challenge phenol, 4, 4′-(1-methylethylidene) bis-(Bisphenol A)." Chemical abstracts service registry number 80–05-7. Ministers of the Environment and of Health, ed.1:107

Espitia, P., J., P., de Fátima Ferreira Soares, N., dos Reis Coimbra, J., S. (2012). ''Zinc oxide nanoparticles: synthesis, antimicrobial activity and food packaging applications.'' *Food Bioprocess Techno,l* 5, pp.1447–1464.

Esposito RVVD, Cimmino FAI (2015) "Bisphenol A environmental exposure and the detrimental effects on human metabolic health: is it necessary to revise the risk assessment in vulnerable population." J Endocrinol Investig 39:1–5.

Fang, J., Zhuo, S., Zhu, C., 2019. "Fluorescent sensing platform for the detection of p-nitrophenol based on Cu-doped carbon dots." Opt. Mater. (Amst) 97, 109396.

Fabbri, F., Villani, M., Catellani, A., Calzolari, A., Cicero, G., Calestani, D., ... & Salviati, G. (2014). Zn vacancy induced green luminescence on non-polar surfaces in ZnO nanostructures. *Scientific reports*, *4*(1), 1-6.

Fisher, P. J., Petrini, O., Petrini, L. E., & Sutton, B. C. (1994). "Fungal endophytes from the leaves and twigs of *Quercus ilex L.* from England, Majorca and Switzerland." *New Phytologist*, 127(1), 133-137.

Flint, S., Markle, T., Thompson, S. and Wallace, E. (2012). ''Bisphenol A exposure, effects, and policy: a wildlife perspective.'' *Journal of environmental management*, *104*, pp.19-34.

Fujishima, A., & Honda, K. (1972). "Electrochemical photolysis of water at a semiconductor electrode." *Nature*, *238*(5358), 37-38.

Galdámez-Martinez, A., Santana, G., Güell, F., Martínez-Alanis, P. R., & Dutt, A. (2020). "Photoluminescence of ZnO nanowires: a review." *Nanomaterials*, *10*(5), 857.

Garg, R., Gupta, R. and Bansal, A. (2021). "Synthesis of g-C3N$_4$/ZnO nanocomposite for photocatalytic degradation of a refractory organic endocrine disrupter.'' *Materials Today: Proceedings*, *44*, pp.855-859.

Gaviria-Arroyave, M. I., Cano, J. B., & Peñuela, G. A. (2020). "Nanomaterial-based fluorescent biosensors for monitoring environmental pollutants: a critical review." *Talanta Open*, 100006.

Gautam, S., Agrawal, H., Thakur, M., Akbari, A., Sharda, H., Kaur, R., & Amini, M. (2020). "Metal oxides and metal organic frameworks for the photocatalytic degradation: A review." *Journal of Environmental Chemical Engineering*, *8*(3), 103726.

Geng, S., Lin, S.M., Liu, S.G., Li, N.B., Luo, H.Q., 2016. "A new fluorescent sensor for detecting p-nitrophenol based on β-cyclodextrin-capped ZnO quantum dots." *RSC Adv*. 6 (89), 86061–86067.

Geng S, Lin SM, Shi Y, Li NB, Luo HQ (2017). "Determination of cobalt (II) using β-cyclodextrin-capped ZnO quantum dots as a fluorescent probe." *Microchim Acta* 184:2533–2539.

Gmurek, M., Olak-Kucharczyk, M., Ledakowicz, S. (2017). ''Photochemical decomposition of endocrine-disrupting compounds–a review.'' *Chem Eng J*, 310, pp.437–456.

Gole, A., Dash, C., Ramakrishnan, V., Sainkar, S. R., Mandale, A. B., Rao, M., and Sastry, M. (2001). "Pepsin - Gold Colloid Conjugates : Preparation , Characterization, and Enzymatic Activity." *Langmuir*, 16(5), 1674–1679.

Golmohammadi, M., Honarmand, M. and Ghanbari, S., 2020. "A green approach to synthesis of ZnO nanoparticles using jujube fruit extract and their application in photocatalytic degradation of organic dyes." *Spectrochimica Acta Part A: Molecular and Biomolecular Spectroscopy*, 229, p.117961.

Gomes SAO, Vieira CS, Almeida DB (2011). "CdTe and CdSe quantum dots cytotoxicity: a comparative study on microorganisms." *Sensors* 11:11664–11678.

Govindappa, M., Farheen, H., Chandrappa, C. P., Rai, R. V., & Raghavendra, V. B. (2016). "Mycosynthesis of silver nanoparticles using extract of endophytic fungi, Penicillium species of Glycosmis mauritiana, and its antioxidant, antimicrobial, anti-inflammatory and tyrokinase inhibitory activity." *Advances in Natural Sciences: Nanoscience and Nanotechnology*, 7(3), 035014.

Goudar, C. T., Ganji, S. H., Pujar, B. G., & Strevett, K. A. (2000). "Substrate inhibition kinetics of phenol biodegradation." *Water environment research*, 72(1), 50-55.

Güell, F., & Martínez-Alanis, P. R. (2019). "Tailoring the Green, Yellow and Red defect emission bands in ZnO nanowires via the growth parameters." *Journal of Luminescence*, 210, 128-134.

Han, L., Liu, S.G., Liang, J.Y., Ju, Y.J., Li, N.B., Luo, H.Q., 2019. "pH-mediated reversible fluorescence nanoswitch based on inner filter effect induced fluorescence quenching for selective and visual detection of 4-nitrophenol." *J. Hazard. Mater*. 362, 45–52.

Han, Q., Wang, H., Dong, W., Liu, T., Yin, Y., Fan, H. (2015). ''Degradation of bisphenol A by ferrate (VI) oxidation: Kinetics, products and toxicity assessment.'' *Chem. Eng. J*., 262, pp.34-40.

Han, S., Yang, L., Wen, Z., Chu, S., Wang, M., Wang, Z., & Jiang, C. (2020). "A dual-response ratiometric fluorescent sensor by europium-doped CdTe quantum dots for visual and colorimetric detection of tetracycline." *Journal of hazardous materials*, *398*, 122894.

Hassan, S. S., El Azab, W. I., Ali, H. R., & Mansour, M. S. (2015). "Green synthesis and characterization of ZnO nanoparticles for photocatalytic degradation of anthracene." *Advances in Natural Sciences: Nanoscience and Nanotechnology*, *6*(4), 045012.

He, J., Zhang, Y., Guo, Y., Rhodes, G., Yeom, J., Li, H. and Zhang, W. (2019). "Photocatalytic degradation of cephalexin by ZnO nanowires under simulated sunlight: Kinetics, influencing factors, and mechanisms.'' *Environment international*, *132*, p.105105.

Herrmann, J. M., Guillard, C., Arguello, M., Agüera, A., Tejedor, A., Piedra, L., & Fernandez-Alba, A. (1999). "Photocatalytic degradation of pesticide pirimiphos-methyl: Determination of the reaction pathway and identification of intermediate products by various analytical methods." *Catalysis Today*, *54*(2-3), 353-367.

Hitkari, G., Singh, S., and Pandey, P. (2017). "Structural, optical and photocatalytic study of ZnO and ZnO–ZnS synthesized by chemical method." *Nano-Structures & Nano-Objects*, 12, 1–9.

Hoffmann, M., R., Martin, S., T., Choi, W., Bahnemannt, D., W. (1995). "Environmental applications of semiconductor photocatalysis.'' *Chem Rev*, 95(1), pp.69–96.

Hou, C., Hu, B., & Zhu, J. (2018). "Photocatalytic degradation of methylene blue over TiO2 pretreated with varying concentrations of NaOH." *Catalysts*, *8*(12), 575.

Hu Y, Geng X, Zhang L (2017) . "Nitrogen-doped carbon dots mediated fluorescent on-off assay for rapid and highly sensitive pyrophosphate and alkaline phosphatase detection." *Sci Rep*:1–9.

Huang, S., Chen, C., Tsai, H., Shaya, J. and Lu, C. (2018). "Photocatalytic degradation of thiobencarb by a visible light-driven MoS_2 photocatalyst.'' *Separation and Purification Technology*, *197*, pp.147-155.

Jaffri, S. B., & Ahmad, K. S. (2018). "Prunus cerasifera Ehrh. fabricated ZnO nano falcates and its photocatalytic and dose dependent in vitro bio-activity." *Open Chemistry*, *16*(1), 141-154.

Jain, N., Bhargava, A., and Panwar, J. (2014). "Enhanced photocatalytic degradation of methylene blue using biologically synthesized 'protein-capped' ZnO nanoparticles." *Chemical Engineering Journal*, 243, 549–555.

Jain, N., Bhargava, A., Tarafdar, J. C., Singh, S. K., and Panwar, J. (2013). "A biomimetic approach towards synthesis of zinc oxide nanoparticles." *Applied Microbiology and Biotechnology*, 97(2), 859–869.

Jain, D., Bhojiya, A.A., Singh, H., Daima, H.K., Singh, M., Mohanty, S.R., Stephen, B.J. and Singh, A. (2020). "Microbial fabrication of zinc oxide nanoparticles and evaluation of their antimicrobial and photocatalytic properties." *Frontiers in chemistry*, *8*, p.778.

Jamieson T, Bakhshi R, Petrova D (2007). "Biological applications of quantum dots. Biomaterials." 28:4717–4732.

Jana, J., Chung, J. S., & Hur, S. H. (2019). "ZnO-associated carbon dot-based fluorescent assay for sensitive and selective dopamine detection." *ACS omega*, *4*(16), 17031-17038.

Jayaseelan, C., Rahuman, A. A., Kirthi, A. V., Marimuthu, S., Santhoshkumar, T., Bagavan, A., Gaurav, K., Karthik, L., and Rao, K. V. B. (2012). "Novel microbial route to synthesize ZnO nanoparticles using Aeromonas hydrophila and their activity against pathogenic bacteria and fungi." *Spectrochimica Acta - Part A: Molecular and Biomolecular Spectroscopy*, 90, 78–84.

Joshi, C. G., Danagoudar, A., Poyya, J., Kudva, A. K., & Dhananjaya, B. L. (2017). "Biogenic synthesis of gold nanoparticles by marine endophytic fungus-Cladosporium

cladosporioides isolated from seaweed and evaluation of their antioxidant and antimicrobial properties." *Process Biochemistry*, *63*, 137-144.

Kahsay, M. H., Tadesse, A., Rama Devi, D., Belachew, N., Basavaiah, K. (2019). "Green synthesis of zinc oxide nanostructures and investigation of their photocatalytic and bactericidal applications." *RSC Advances*, 9(63), pp.36967-36981

Kang, J. H., Kondo, F. and Katayama, Y. (2006). "Human exposure to bisphenol A.'' *Toxicology*, *226*(2-3), pp.79-89.

Kamaraj, M., Ranjith, K.S., Sivaraj, R., RT, R.K. and Salam, H.A. (2014a). "Photocatalytic degradation of endocrine disruptor Bisphenol-A in the presence of prepared $C_{ex}Zn_{1-x}O$ nanocomposites under irradiation of sunlight.'' *Journal of Environmental Sciences*, *26*(11), pp.2362-2368.

Kamaraj, M., Sivaraj, R. and Venckatesh, R., 2014b. "Biodegradation of bisphenol A by the tolerant bacterial species isolated from coastal regions of Chennai, Tamil Nadu, India." *Int. Biodeterior. Biodegr.,* 93, pp. 216-222.

Khalafi, T., Buazar, F. and Ghanemi, K., 2019. "Phycosynthesis and enhanced photocatalytic activity of zinc oxide nanoparticles toward organosulfur pollutants." *Scientific reports*, *9*(1), pp.1-10.

Khalil, A. T., Ovais, M., Ullah, I., Ali, M., Shinwari, Z. K., Khamlich, S., and Maaza, M. (2017). "Sageretia thea (Osbeck.) mediated synthesis of zinc oxide nanoparticles and its biological applications." *Nanomedicine*, 12 (15),1767-1789.

Khan, S. A., Shahid, S., Shahid, B., Fatima, U., & Abbasi, S. A. (2020). "Green synthesis of MnO nanoparticles using abutilon indicum leaf extract for biological, photocatalytic, and adsorption activities." *Biomolecules*, *10*(5), 785.

Khan, T., Bhagabani, K., Kumari, P., Datta, A. (2018). "Accounting for secondary inner filter effect in fluorescence spectra from solid samples." Curr. Sci. 114, 2353–2355.

Khan, Z. U. H., Sadiq, H. M., Shah, N. S., Khan, A. U., Muhammad, N., Hassan, S. U., Zakir, A. (2019). "Greener synthesis of zinc oxide nanoparticles using Trianthema portulacastrum extract and evaluation of its photocatalytic and biological applications." *Journal of Photochemistry and Photobiology B: Biology*, *192*, 147-157.

Khavar, A. H. C., Moussavi, G., Mahjoub, A. R., Luque, R., Rodríguez-Padrón, D., Sattari, M. (2019). "Enhanced visible light photocatalytic degradation of acetaminophen with Ag2S-ZnO@ rGO core-shell microsphere as a novel catalyst: Catalyst preparation and characterization and mechanistic catalytic experiments." *Separation and Purification Technology*, *229*, 115803.

Kitano H, Endo H, Gemmei-ide M, Kyogoku M (2003). "Inclusion of bisphenols by cyclodextrin derivatives." *J Incl Phenom. Macrocycl Chem* 47:83–90.

Kolev, S. K., Petkov, P. S., Rangelov, M. A., & Vayssilov, G. N. (2011). Density functional study of hydrogen bond formation between methanol and organic molecules containing Cl, F, NH_2, OH, and COOH functional groups. *The Journal of Physical Chemistry A*, *115*(48), 14054-14068.

Kołodziejczak-Radzimska, A. and Jesionowski, T. (2014). "Zinc oxide—from synthesis to application: a review.'' *Materials*, *7*(4), pp.2833-2881.

Kuang, R., Kuang, X., Pan, S., Zheng, X., Duan, J., & Duan, Y. (2010). "Synthesis of cysteamine-coated CdTe quantum dots for the detection of bisphenol A." *Microchimica Acta*, *169*(1-2), 109-115.

Kundu, D., Hazra, C., Chatterjee, A., Chaudhari, A., and Mishra, S. (2014). "Extracellular biosynthesis of zinc oxide nanoparticles using Rhodococcus pyridinivorans NT2: Multifunctional textile finishing, biosafety evaluation and in vitro drug delivery in colon carcinoma." *Journal of Photochemistry and Photobiology B: Biology*, 140, 194–204.

Laemmli U.K. (1970). "Clevage of structural proteins during the assembly of the head of the bacteriophage T4." *Nature*, 227, 680-685

Lakowicz, J. R. (1999). "Introduction to fluorescence." *Principles of fluorescence spectroscopy* (pp. 1-23). Springer, Boston, MA.

Lalwani, D., Ruan, Y., Taniyasu, S., Yamazaki, E., Kumar, N.J., Lam, P.K., Wang, X. and Yamashita, N. (2020). "Nationwide distribution and potential risk of bisphenol analogues in Indian waters." *Ecotoxicology and Environmental Safety*, *200*, p.110718.

Lee, K.M., Lai, C.W., Ngai, K.S. and Juan, J.C. (2016). "Recent developments of zinc oxide based photocatalyst in water treatment technology: a review." Water Res., 88, pp. 428-448.

Lee, G. J., Lee, X. Y., Lyu, C., Liu, N., Andandan, S., & Wu, J. J. (2020). "Sonochemical synthesis of copper-doped $BiVO_4$/g-C_3N_4 nanocomposite materials for photocatalytic degradation of bisphenol A under simulated sunlight irradiation." *Nanomaterials*, *10*(3), 498.

Leung, Y. H., Chen, X. Y., Ng, A., Guo, M. Y., Liu, F. Z., Djurišić, A. B. & Van Hove, M. A. (2013). "Green emission in ZnO nanostructures—Examination of the roles of oxygen and zinc vacancies." *Applied Surface Science*, *271*, 202-209.

Li, B., Wang, Y. (2010a). "Facile synthesis and enhanced photocatalytic performance of flower-like ZnO hierarchical microstructures.'' *J Phys Chem C*, 114, pp.890–896.

Li, J., Fan, H. and Jia, X. (2010b). "Multilayered ZnO nanosheets with 3D porous architectures: synthesis and gas sensing application." *J. Phys. Chem. C.*, 114, pp. 14684-14691.

Li, J. F., Rupa, E. J., Hurh, J., Huo, Y., Chen, L., Han, Y., chan Ahn, J., Park, J. K., Lee, H. A., Mathiyalagan, R. and Yang, D. C. (2019). "*Cordyceps militaris* fungus mediated Zinc Oxide nanoparticles for the photocatalytic degradation of Methylene blue dye." *Optik*, 183, pp.691-697.

Li, Y., Sun, S., Ma, M., Ouyang, Y., Yan, W. (2008). "Kinetic study and model of the photocatalytic degradation of rhodamine B (RhB) by a TiO_2-coated activated carbon catalyst: effects of initial RhB content, light intensity and TiO_2 content in the catalyst." *Chem Eng J* 142(2):147–155.

Li, Y., Wen, Q. L., Liu, A. Y., Long, Y., Liu, P., Ling, J., Ding, Z. T., Cao, Q. E. (2020). "One-pot synthesis of green-emitting gold nanoclusters as a fluorescent probe for determination of 4-nitrophenol." *Microchim. Ichnoanal. Acta* 187 (2), 1–9.

Lin, J., Hu, Y., Wang, L., Liang, D., Ruan, X. and Shao, S. (2020a). "M88/PS/Vis system for degradation of bisphenol A: Environmental factors, degradation pathways, and toxicity evaluation.'' *Chemical Engineering Journal*, *382*, p.122931.

Lin, L., Xie, Q., Zhang, M., Liu, C., Zhang, Y., Wang, G. & Zhao, M. (2020b). "Construction of Z-scheme Ag-AgBr/BiVO4/graphene aerogel with enhanced photocatalytic degradation and antibacterial activities." *Colloids and Surfaces A: Physicochemical and Engineering Aspects*, *601*, 124978.

Lin, X., Wu, Y., Hao, Y., Sun, Q., Yan, Y., & Li, C. (2018). "Sensitive and selective determination of 2, 4, 6-trichlorophenol using a molecularly imprinted polymer based on zinc oxide quantum dots." *Analytical Letters*, *51*(10), 1578-1591.

Liqiang, J., Yichun, Q., Baiqi, W., Shudan, L., Baojiang, J., Libin, Y., Wei, F., Honggang, F., and Jiazhong, S. (2006). "Review of photoluminescence performance of nano-sized semiconductor materials and its relationships with photocatalytic activity." *Solar Energy Materials and Solar Cells*, 90(12), 1773–1787.

Liu, G., Chen, Z., Jiang, X., Feng, D. Q., Zhao, J., Fan, D., & Wang, W. (2016). "In-situ hydrothermal synthesis of molecularly imprinted polymers coated carbon dots for fluorescent detection of bisphenol A." *Sensors and Actuators B: Chemical*, *228*, 302-307.

Liu, K. K., Shan, C. X., He, G. H., Wang, R. Q., Sun, Z. P., Liu, Q., Dong, L., Shen, D. Z. (2017a). "Advanced encryption based on fluorescence quenching of ZnO nanoparticles." *J. Mater. Chem.* C 5 (29), 7167–7173.

Liu, Y., Sun, N., Hu, J., Li, S. and Qin, G. (2018). "Photocatalytic degradation properties of α-Fe$_2$O$_3$ nanoparticles for dibutyl phthalate in aqueous solution system.'' *Royal Society open science*, *5*(4), p.172196.

Liu, T., Wang, L., Lu, X., Fan, J., Cai, X., Gao, B., Lv, Y. (2017b). "Comparative study of the photocatalytic performance for the degradation of different dyes by ZnIn 2 S 4: adsorption, active species, and pathways." *RSC advances*, *7*(20), 12292-12300.

Liu, Y., Su, G., Zhang, B., Jiang, G., & Yan, B. (2011). Nanoparticle-based strategies for detection and remediation of environmental pollutants. *Analyst*, *136*(5), 872-877.

Lowry O.H., Rosebrough N.J., Farr A.L., Randall R.J. (1951). "Protein measurement with the folin phenol reagent." *Journal of Biological Chemistry*, 193, 265–275.

Makhal, A., Sarkar, S., & Pal, S. K. (2012). "Protein-mediated synthesis of nanosized Mn-

doped ZnS: a multifunctional, UV-durable bio-nanocomposite." *Inorganic chemistry*, 51(19), 10203-10210.

Maliszewska, I., Juraszek, A., and Bielska, K. (2014). "Green Synthesis and Characterization of Silver Nanoparticles Using Ascomycota Fungi *Penicillium nalgiovense* AJ12."*Journal of Cluster Science*, 25, 989–1004.

Mao, M., Deng, C., He, Y., Ge, Y., Song, G. (2017). "Fluorescence detection of p-nitrophenol in water using bovine serum albumin capped ag nanoclusters." *J. Fluoresc.* 27 (4), 1421–1426.

Mccracken KE, Tat T, Yoon J (2017). "Smartphone-based fluorescence detection of bisphenol A from water samples." *R Soc Chem Adv* 7: 9237–9243.

Messaoudi, O., & Bendahou, M. (2020). "Biological synthesis of nanoparticles using endophytic microorganisms: Current development." *Nanotechnology and the Environment*.

Mehrzad-Samarin, M., Faridbod, F., Ganjali, M. R. (2019). "A luminescence nanosensor for Ornidazole detection using graphene quantum dots entrapped in silica molecular imprinted polymer." *Spectrochimica Acta Part A: Molecular and Biomolecular Spectroscopy*, *206*, 430-436.

Mirzaei, A., Chen, Z., Haghighat, F., Yerushalmi, L. (2016). "Removal of pharmaceuticals and endocrine disrupting compounds from water by zinc oxide-based photocatalytic degradation : a review." *Sustain Cities Soc*, 27, pp.407–418.

Mondal, K., Sharma, A. (2014). "Photocatalytic oxidation of pollutant dyes in wastewater by TiO$_2$ and ZnO nano-materials – a mini-review."

Mohamed, M. A. (2015). "One-step functionalization of silver nanoparticles using the orsellinic acid compound isolated from the endophytic fungus *Epicoccum Nigrum* : Characterization and antifungal activity." *International Journal of Nanomaterials and Chemistry*, 110(3), 103–110.

Moliner-Martínez, Y., Argente-García, A., Herráez-Hernández, R.,Verdú-Andrés, J., Molins-Legua, C. and Campíns Falcó, P. (2015). "Environmental Applications of Instrumental Chemical Analysis" *Apple Academic Press, Inc.*

Moriyama, K., Tagami, T., Akamizu, T., Usui, T., Saijo, M., Kanamoto, N., Hataya, Y., Shimatsu, A., Kuzuya, H. and Nakao, K. (2002). "Thyroid hormone action is disrupted by bisphenol A as an antagonist." *The Journal of Clinical Endocrinology & Metabolism*, *87*(11), pp.5185-5190.

Morkoc, H., and Ozgur, U. (2009). "General Properties of ZnO. Zinc Oxide: Fundamentals, Materials and Device Technology." *John Wiley and Sons.*

Mukherjee, I., Mishrra, A., Saha, R. and Chatterjee, S. (2017). "Efficient degradation of endocrine disruptors using 1D and 3D copper (I) oxide nanostructures.'' *ChemistrySelect*, *2*(22), pp.6388-6398.

Munawer, U., Raghavendra, V. B., Ningaraju, S., Krishna, K. L., Ghosh, A. R., Melappa, G., & Pugazhendhi, A. (2020). "Biofabrication of gold nanoparticles mediated by the endophytic *Cladosporium species*: Photodegradation, in vitro anticancer activity and in vivo antitumor studies." *International Journal of Pharmaceutics*, *588*, 119729.

National Toxicology Programme (1993) (NT. "Toxicology and carcinogenesis studies of p-nitrophenol (CAS No. 100–02-7) in Swiss Webster Mice (Dermal Studies) US Department of Health and Human Services." *Public Health Service. National Institute of Health.*

Nagajyothi, P. C., Sreekanth, T. V. M., Tettey, C. O., In, Y., and Heung, S. (2014). "Bioorganic & Medicinal Chemistry Letters of ZnO nanoparticles using Coptidis Rhizoma." *Bioorganic & medicinal chemistry letters*, 1, 2–7.

Neppolian, B., Choi, H. C., Sakthivel, S. (2002). "Solar/UV-induced photocatalytic degradation of three commercial textile dyes." *J Hazard Mater* 89:303–317.

Netala, V. R., Bethu, M. S., Pushpalatha, B., Baki, V. B., Aishwarya, S., Rao, J. V., & Tartte, V. (2016). "Biogenesis of silver nanoparticles using endophytic fungus *Pestalotiopsis microspora* and evaluation of their antioxidant and anticancer activities." *International journal of nanomedicine*, 11, 5683.

Olmo MD, Zafra A, Gonzalez-casado A, Jose L (2006). "The use of β- cyclodextrin inclusion complexes for the analysis of bisphenol a residues in water by spectrofluorimetry." *Int J Environ Anal Chem* 69:99–110.

Olujimi, O.O., Fatoki, O.S., Odendaal, J.P. and Okonkwo, J.O. (2010). "Endocrine disrupting chemicals (phenol and phthalates) in the South African environment: a need for more monitoring." *Water Sa*, 36(5).

Onkani, S.P., Diagboya, P.N., Mtunzi, F.M., Klink, M.J., Olu-Owolabi, B.I. and Pakade, V. (2020). "Comparative study of the photocatalytic degradation of 2–chlorophenol under UV irradiation using pristine and Ag-doped species of TiO_2, ZnO and ZnS photocatalysts." *Journal of environmental management*, 260, p.110145.

Oubina, A., Ballesteros, B., Galve, R., Barcelo, D., & Marco, M. P. (1999). "Development and optimization of an indirect enzyme-linked immunosorbent assay for 4-nitrophenol. Application to the analysis of certified water samples." *Analytica chimica acta*, *387*(3), 255-266.

Osuntokun, J., Onwudiwe, D. C., & Ebenso, E. E. (2019). "Green synthesis of ZnO nanoparticles using aqueous Brassica oleracea L. var. italica and the photocatalytic activity." *Green chemistry letters and reviews*, *12*(4), 444-457.

Palominos, R. A., Mondaca, M. A., Giraldo, A., Peñuela, G., Pérez-Moya, M., & Mansilla, H. D. (2009). "Photocatalytic oxidation of the antibiotic tetracycline on TiO2 and ZnO suspensions." *Catalysis Today*, *144*(1-2), 100-105.

Pare, B., Jonnalagadda, S. B., Tomar, H., Singh, P., Bhagwat, V. W. (2008). "ZnO assisted photocatalytic degradation of acridine orange in aqueous solution using visible irradiation." *Desalination*. 232(1–3):80–90.

Pham, T. A. T., Tran, V. A., Le, V. D., Nguyen, M. V., Truong, D. D., Do, X. T. and Vu, A. T. (2020). "Facile Preparation of ZnO nanoparticles and Ag/ZnO nanocomposite and their photocatalytic activities under visible light." *Int. J. Photoenergy*., 14.

Prabhu, Y. T., Rao, K. V., Sesha, V. (2013). "Synthesis of ZnO nanoparticles by a novel surfactant assisted amine combustion method." *Adv Nanopart:* 45–50.

Prosser, J. I. (1995). "Mathematical modelling of fungal growth." *The Growing Fungus*, Springer, Dordrecht, 319-335.

Pudukudy, M., and Yaakob, Z. (2015). "Facile Synthesis of Quasi Spherical ZnO Nanoparticles with Excellent Photocatalytic Activity." *Journal of Cluster Science*, 26(4), 1187–1201.

Qian, J., Hua, M., Wang, C., Wang, K., Liu, Q., Hao, N., & Wang, K. (2016). "Fabrication of l-cysteine-capped CdTe quantum dots based ratiometric fluorescence nanosensor for onsite visual determination of trace TNT explosive." *Analytica chimica acta*, *946*, 80-87.

Qian, Y., Yu, H., He, D., Yang, H., Wang, W., Wan, X., Wang, L. (2013). "Biosynthesis of silver nanoparticles by the endophytic fungus Epicoccum nigrum and their activity against pathogenic fungi." *Bioprocess and Biosystems Engineering*, 36(11), 1613–1619.

Qingshan, Y., Yongjin, L., Lingling, M. (2012). "Kinetics of photocatalytic degradation of gaseous organic compounds on modified TiO_2/AC composite photocatalyst." *Chin J Chem Eng* 20(3):572–576.

Raevskaya, A. E., Panasiuk, Y. V., Stroyuk, O. L., Kuchmiy, S. Y., Dzhagan, V. M., Milekhin, A. G., Yeryukov, N. A., Sveshnikova, L. A., Rodyakina, E. E., Plyusnin, V. F., Zahn, D. R. T., (2014). "Spectral and luminescent properties of $ZnO–SiO_2$ core–shell nanoparticles with size-selected ZnO cores." *RSC Adv*. 4 (108), 63393–63401.

Raheman, F., Deshmukh, S., Ingle, A., Gade, A., and Rai, M. (2011). "Silver Nanoparticles: Novel Antimicrobial Agent Synthesized from an Endophytic Fungus Pestalotia sp. Isolated from Leaves of Syzygium cumini (L)." *Nano Biomedicine and Engineering*, 3(3).

Rajamanickam, D. and Shanthi, M., (2012). "Photocatalytic degradation of an organic pollutant, 4-nitrophenol by zinc oxide-UV process." *Res. J. Chem. Environ.*, 9, pp. 1858 - 1868

Rajan, A., Cherian, E., & Baskar, G. (2016). "Biosynthesis of zinc oxide nanoparticles using Aspergillus fumigatus JCF and its antibacterial activity." *International Journal of Modern Science and Technology*, 1(2), 52-57.

Raji, R., & Gopchandran, K. G. (2017). "ZnO nanostructures with tunable visible luminescence: Effects of kinetics of chemical reduction and annealing." *Journal of Science: Advanced Materials and Devices*, *2*(1), 51-58.

Raliya, R., and Tarafdar, J. C. (2013). "ZnO Nanoparticle Biosynthesis and Its Effect on Phosphorous-Mobilizing Enzyme Secretion and Gum Contents in Clusterbean (Cyamopsis tetragonoloba L.)." *Agricultural Research*, 2(1), 48–57.

Rani, M., and Shanker, U. (2018). "Insight in to the degradation of bisphenol A by doped ZnO@ZnHCF nanocubes: High photocatalytic performance.'' *J. Colloid Interface Sci.*, 530, pp. 16-28.

Rani, M., Yadav, J. and Shanker, U. (2020). "Efficient degradation of nonylphenol and 2, 4-dinitrophenol by sunlight responsive hexacyanocobaltates nanostructures.'' *Environmental Nanotechnology, Monitoring & Management*, *14*, p.100325.

Ravichandran, L., Selvam, K., & Swaminathan, M. (2007). "Photoassisted catalytic cleavage of the C–F bond in pentafluorophenol with ZnO and the effect of operational parameters." *Australian Journal of Chemistry*, *60*(12), 951-956.

Raviraja, N. S. (2005). "Fungal endophytes in five medicinal plant species from Kudremukh Range, Western Ghats of India." *Journal of Basic Microbiology: An International Journal on Biochemistry, Physiology, Genetics, Morphology, and Ecology of Microorganisms*, *45*(3), 230-235.

Rehman, S., Shawl, A. S., Kour, A., Andrabi, R., Sudan, P., Sultan, P., Qazi, G. N. (2008). "An endophytic *Neurospora sp.* from *Nothapodytes foetida* producing camptothecin." *Applied biochemistry and microbiology*, *44*(2), 203-209.

Rochester, J.R., (2013). "Bisphenol A and human health: A review of the literature. Reprod. Toxicol., 42, pp. 132–155.

Rodriguez, R., Castillo, E., & Sinuco, D. (2019). "Validation of an HPLC method for determination of bisphenol-A migration from baby feeding bottles." *Journal of analytical methods in chemistry*.

Saha, D., & Negi, D. P. (2018). "Spectroscopic investigations on the interaction of thioacetamide with ZnO quantum dots and application for its fluorescence sensing." *Spectrochimica Acta Part A: Molecular and Biomolecular Spectroscopy*, *189*, 516-521.

Sakthivel, S., Neppolian, B., Shankar, M.V., Arabindoo, B., Palanichamy, M. and Murugesan, V. (2003). "Solar photocatalytic degradation of azo dye: comparison of photocatalytic efficiency of ZnO and TiO$_2$.'' *Solar energy materials and solar cells*, *77*(1), pp.65-82.

Salehi, Z., Rasouli, A. and Doosthosseini, H. (2019). "p-nitrophenol Degradation Kinetics and Mass Transfer Study by *Ralstonia eutropha* as a Whole Cell Biocatalyst." *Polycyclic Aromatic Compounds*.

Samuel, M. S., Jose, S., Selvarajan, E., Mathimani, T. and Pugazhendhi, A. (2020). "Biosynthesized silver nanoparticles using *Bacillus amyloliquefaciens*; Application for cytotoxicity effect on A549 cell line and photocatalytic degradation of p-nitrophenol.'' *Journal of Photochemistry and Photobiology B: Biology*, *202*, p.111642.

Saravanan, A., Kumar, P. S., Vo, D. V. N., Yaashikaa, P. R., Karishma, S., Jeevanantham, S. & Bharathi, V. D. (2021). "Photocatalysis for removal of environmental pollutants and fuel production: a review." *Environmental Chemistry Letters*, *19*(1), 441-463.

Sarkar, P. & Dey, A. (2020). "4-Nitrophenol biodegradation by an isolated and characterized microbial consortium and statistical optimization of physicochemical parameters by Taguchi Methodology." *Journal of Environmental Chemical Engineering*, *8*(5), 104347.

Sarkar, J., Ghosh, M., Mukherjee, A., Chattopadhyay, D., Acharya, K. (2014). "Biosynthesis and safety evaluation of ZnO nanoparticles." *Bioprocess and Biosystems Engineering*, 37(2), 165–171.

Saraswathi, V. S., Tatsugi, J., Shin, P. K., & Santhakumar, K. (2017). "Facile biosynthesis, characterization, and solar assisted photocatalytic effect of ZnO nanoparticles mediated by leaves of *L. speciosa*." *Journal of photochemistry and photobiology B: Biology*, *167*, 89-98.

Sastry, M., Ahmad, A., Islam Khan, M., and Kumar, R. (2003). "Biosynthesis of metal nanoparticles using fungi and actinomycete." *Current Science*, 85(2), 162–170.

Seachrist, D.D., Bonk, K.W., Ho, S.M., Prins, G.S., Soto, A.M. and Keri, R.A. (2016). "A review of the carcinogenic potential of bisphenol A.'' *Reproductive Toxicology*, *59*, pp.167-182.

Selvam, N.C.S., Vijaya, J.J. and Kennedy, L.J., 2013. "Comparative studies on influence of morphology and La doping on structural, optical, and photocatalytic properties of zinc oxide nanostructures." *Journal of colloid and interface science*, *407*, pp.215-224.

Selvarajan, E., and Mohanasrinivasan, V. (2013). "Biosynthesis and characterization of ZnO nanoparticles using *Lactobacillus plantarum* VITES07." *Materials Letters*, 112, 180–182.

Shafaei A, Nikazar M, Arami M (2010). "Photocatalytic degradation of terephthalic acid using titania and zinc oxide photocatalysts: comparative study." *Desalination* 252(1–3):8–16.

Shafei, A., Ramzy, M.M., Hegazy, A.I., Husseny, A.K., El-Hadary, U.G., Taha, M.M. and Mosa, A.A. (2018). "The molecular mechanisms of action of the endocrine disrupting chemical bisphenol A in the development of cancer." *Gene*, *647*, pp.235-243.

Shamsuzamman, Ali, A., Asif, M., Mashrai, A., and Khanam, H. (2014). "Green synthesis of ZnO nanoparticles using Bacillus subtilis and their catalytic performance in the one-pot synthesis of steroidal thiophenes." *European Chemical Bulletin*, 3 (9)(9), 939–945.

Shankar, S. S., Ahmad, A., Pasricha, R., and Sastry, M. (2003). "Bioreduction of chloroaurate ions by geranium leaves and its endophytic fungus yields gold nanoparticles of different shapes." *Journal of Materials Chemistry*, 13(7), 1822.

Singh, J., Kaur, S., Kaur, G., Basu, S., & Rawat, M. (2019). "Biogenic ZnO nanoparticles: a study of blueshift of optical band gap and photocatalytic degradation of reactive yellow 186 dye under direct sunlight." *Green Processing and Synthesis*, *8*(1), 272-280.

Singh K, Chaudhary GR, Singh S, Mehta SK (2014). "Synthesis of highly luminescent water stable ZnO quantum dots as photoluminescent sensor for picric acid." *J Lumin* 154:148–154.

Singh, K., & Mehta, S. K. (2016). "Luminescent ZnO quantum dots as an efficient sensor for free chlorine detection in water." *Analyst*, *141*(8), 2487-2492.

Singh, S., D'Britto, V., Bharde, A., Sastry, M., Dhawan, A., & Prasad, B. L. V. (2010). "Bacterial synthesis of photocatalytically active and biocompatible TiO_2 and ZnO nanoparticles." *International Journal of Green Nanotechnology: Physics and Chemistry*, *2*(2), P80-P99.

Singh, T., Jyoti, K., Patnaik, A., Singh, A., Chauhan, R., and Chandel, S. S. (2017). "Biosynthesis, characterization and antibacterial activity of silver nanoparticles using an

endophytic fungal supernatant of *Raphanus sativus*." *Journal of Genetic Engineering and Biotechnology*, 15(1), 31–39.

Soori, F., & Nezamzadeh-Ejhieh, A. (2018). "Synergistic effects of copper oxide-zeolite nanoparticles composite on photocatalytic degradation of 2, 6-dimethylphenol aqueous solution." *Journal of molecular liquids*, *255*, 250-256.

Spain, J.C. (1995). "Biodegradation of nitroaromatic compounds." *Annual review of microbiology*, *49*(1), pp.523-555.

Staples, C.A., Dome, P.B., Klecka, G.M., Oblock, S.T. and Harris, L.R. (1998). "A review of the environmental fate, effects, and exposures of bisphenol A." *Chemosphere*, *36*(10), pp.2149-2173.

Stylidi, M., Kondarides, D. I., & Verykios, X. E. (2004). "Visible light-induced photocatalytic degradation of Acid Orange 7 in aqueous TiO2 suspensions." *Applied Catalysis B: Environmental*, *47*(3), 189-201.

Su, F., Li, P., Huang, J., Gu, M., Liu, Z., & Xu, Y. (2021). "Photocatalytic degradation of organic dye and tetracycline by ternary $Ag_2O/AgBr–CeO_2$ photocatalyst under visible-light irradiation." *Scientific Reports*, *11*(1), 1-13.

Suyver, J. F., Wuister, S. F., Kelly, J. J., Meijerink, A. (2001). "Synthesis and photoluminescence of nanocrystalline ZnS : Mn^{2+}." *Nano Lett* 1: 429–433.

Tajik, S., Beitollahi, H., Nejad, F. G., Zhang, K., Le, Q. V., Jang, H. W. & Shokouhimehr, M. (2020). "Recent advances in electrochemical sensors and biosensors for detecting bisphenol A." *Sensors*, *20*(12), 3364.

Tang, B., Cao, L., Xu, K. (2008). "A new nanobiosensor for glucose with high sensitivity and selectivity in serum based on fluorescence resonance energy transfer (FRET) between CdTe quantum dots and Au nanoparticles." *Chemistry*:3637–3644.

Tao, Y., Cheng, Z. L., Ting, K. E., & Yin, X. J. (2012). "Photocatalytic degradation of phenol using a nanocatalyst: the mechanism and kinetics." *Journal of Catalysts*, *2013*.

Tchieno, F. M. M., & Tonle, I. K. (2018). "p-Nitrophenol determination and remediation: an overview." *Reviews in Analytical Chemistry*, *37*(2).

Tong, Z., Xing, X., Yang, Y., Hong, P., Wang, Z., Zhao, R., Zhang, X., Peng, S., Wang, Y., (2019). "Fluorescent ZnO quantum dots synthesized with urea for the selective detection of Cr6$^+$ ion in water with a wide range of concentrations." *Methods Appl. Fluoresc*. 7 (3), 035007.

Truc, N. T. T., Duc, D. S., Van Thuan, D., Al Tahtamouni, T., Pham, T. D., Hanh, N. T. & Le Chi, N. T. P. (2019). "The advanced photocatalytic degradation of atrazine by direct Z-scheme Cu doped ZnO/g-C$_3$N$_4$." *Applied Surface Science*, *489*, 875-882.

Vahid, B. (2017). "Specific fluorescence probe for direct recognition of dimethoate using molecularly imprinting polymer on ZnO quantum dots." *Journal of fluorescence*, *27*(4), 1339-1347.

Valix, M., and Loon, L. O. (2003). "Adaptive tolerance behaviour of fungi in heavy metals." *Minerals Engineering*, 16, 193–198.

Vandenberg, L. N., Hauser, R., Marcus, M., Olea, N. and Welshons, W. V. (2007). ''Human exposure to bisphenol A (BPA).'' *Reproductive toxicology*, *24*(2), pp.139-177.

Velmurugan, K., Prabhu, J., Kannan, V. R., & Nandhakumar, R. (2014). "Antimicrobial activity of different solvent extracts of the leaves and stem of *Mappia foetida*."

Verma, V. C., Kharwar, R. N., and Gange, A. C. (2010). "Biosynthesis of antimicrobial silver nanoparticles by the endophytic fungus *Aspergillus clavatus*." *Nanomedicine (London, England)*, 5(1), 33–40.

Vijayanandan, A. S., Balakrishnan, R. M. (2018). "Biosynthesis of cobalt oxide nanoparticles using endophytic fungus *Aspergillus nidulans*." *Journal of environmental management*, *218*, 442-450.

Vidya, C., Prabha, M. C., Raj, M. A. (2016). "Green mediated synthesis of zinc oxide nanoparticles for the photocatalytic degradation of Rose Bengal dye." *Environmental Nanotechnology, Monitoring & Management,* 6, pp.134-138.

Vrabl, P., Schinagl, C. W., Artmann, D. J., Heiss, B., Burgstaller, W. (2019). "Fungal growth in batch culture–what we could benefit if we start looking closer." *Frontiers in microbiology*, 10, 2391.

USEPA (2012). IRIS (Integrated Risk Information System). US Environmental Protection Agency, Washington, DC. <http://www.epa.gov/iris/index.html>.

U.S. Food and Drug Administration (2019). "Guidelines for the Validation of Chemical Methods in Food, Feed, Cosmetics, and Veterinary Products, 3rd edn, pp 1–39.

Üzek R, Sari E, Serap Ş (2019). "A nitrocellulose paper strip for fluorometric determination of bisphenol A using molecularly imprinted nanoparticles." *Microchim Acta* 186:218–210.

Wang, X., Zeng, H.,Wei, Y., Lin, J. M. (2006). "A reversible fluorescence sensor based on insoluble β-cyclodextrin polymer for direct determination of bisphenol a (BPA)." *Sensors Actuators B Chem* 114:565–572.

Wang, C., Zhang, H., Li, F. and Zhu, L. (2010). "Degradation and mineralization of bisphenol A by mesoporous Bi_2WO_6 under simulated solar light irradiation." *Environ. Sci. Technol.*, 44, pp. 6843-6848

Wang, X., Liu, Y., Wang, Q., Bu, T., Sun, X., Jia, P., & Wang, L. (2021). Nitrogen, silicon co-doped carbon dots as the fluorescence nanoprobe for trace p-nitrophenol detection based on inner filter effect. *Spectrochimica Acta Part A: Molecular and Biomolecular Spectroscopy*, *244*, 118876.

Wang, Y., Chang, X., Jing, N., Zhang, Y. (2018). "Hydrothermal synthesis of carbon quantum dots as fluorescent probes for the sensitive and rapid detection of picric acid." *Analytical Methods*, 10(23), 2775-2784.

West, A. (2018). "Experimental methods to investigate self-assembly at interfaces." *Interface Science and Technology* 21, 131–241.

Wei, Y., Kong, L.T., Yang, R., Wang, L., Liu, J.H. and Huang, X.J. (2011). "Single-walled carbon nanotube/pyrenecyclodextrin nanohybrids for ultrahighly sensitive and selective detection of p-nitrophenol.'' *Langmuir*, *27*(16), pp.10295-10301.

Wu, X., Zhang, Z., Li, J., You, H., Li, Y., & Chen, L. (2015). "Molecularly imprinted polymers-coated gold nanoclusters for fluorescent detection of bisphenol A." *Sensors and Actuators B: Chemical*, *211*, 507-514.

Xie, J., Lee, Y. J., I. C, Daniel, Wang, and Ting, Y. P. (2007). "Silver Nanoplates: From Biological to Biomimetic Synthesis." *American Chemical Society Nano*, 1(5), 429-439.

Xie, Y., Li, P., Zeng, Y., Li, X., Xiao, Y., Wang, Y., Zhang, Y. (2018). "Thermally treated

fungal manganese oxides for bisphenol A degradation using sulfate radicals." *Chem. Eng. J.*, 335, pp. 728-736.

Xiong, S., Marin, L., Duan, L., Cheng, X. (2019). "Fluorescent chitosan hydrogel for highly and selectively sensing of p-nitrophenol and 2, 4, 6-trinitrophenol." *Carbohydr. Polym.* 225, 115253.

Xu, S., Lu, H., Li, J., Song, X., Wang, A., Chen, L., Han, S. (2013). "Dummy molecularly imprinted polymers-capped CdTe quantum dots for the fluorescent sensing of 2, 4, 6-trinitrotoluene." *ACS Appl. Mater. Interfaces* 5 (16), 8146–8154.

Yang, H., Lu, F., Sun, Y., Yuan, Z., Lu, C. (2018). "Fluorescent gold nanocluster-based sensor array for nitrophenol isomer discrimination via an integration of host–guest interaction and inner filter effect." *Anal. Chem.* 90 (21), 12846–12853.

Yang, T. Q., Peng, B., Shan, B. Q., Zong, Y. X., Jiang, J. G., Wu, P., Zhang, K. (2020). "Origin of the photoluminescence of metal nanoclusters: from metal-centered emission to ligand-centered emission." *Nanomaterials* 10 (2), 261.

Yang, Y., Guo, H., Zhang, Y., Deng, Q. and Zhang, J. (2016). "Degradation of bisphenol A using ozone/persulfate process: kinetics and mechanism." *Water Air Soil Pollut.*, 227(2), p.53.

Yang L, Zhao H, Li Y, Li C (2015). "Electrochemical simultaneous determination of hydroquinone and p-nitrophenol based on host – guest molecular recognition capability of dual β-cyclodextrin functionalized Au @ graphene nanohybrids." *Sensors Actuators B Chem* 207: 1–8.

Yoshida, K., Shigeoka, T. and Yamauchi, F. (1983). "Non-steady-state equilibrium model for the preliminary prediction of the fate of chemicals in the environment." *Ecotoxicology and environmental safety*, 7(2), pp.179-190.

Zhang, J., Zhao, S., Zhang, K., Zhou, J. (2013a). "Cd-doped ZnO quantum dots based immunoassay for the quantitative determination of bisphenol A." *Chemosphere* 95:105–110.

Zhang, Y., Mi, L., Wang, P. N., Ma, J., Chen, J. Y., (2008). "pH-dependent aggregation and photoluminescence behavior of thiol-capped CdTe quantum dots in aqueous solutions." *J. Lumin.* 128 (12), 1948–1951.

Zhang, Y., Piao, Y., Li, Y., Song, M., Tang, P. and Li, C. (2013b). "4-Nitrophenol induces Leydig cells hyperplasia, which may contribute to the differential modulation of the androgen receptor and estrogen receptor-α and-β expression in male rat testes." *Toxicology letters*, *223*(2), pp.228-235.

Zhang, Z., Zhou, J., Liu, Y., Tang, J., & Tang, W. (2015a). "Cyclodextrin capped CdTe quantum dots as versatile fluorescence sensors for nitrophenol isomers." *Nanoscale*, *7*(46), 19540-19546.

Zhang, X., Yang, S., Zhao, W., Liu, B., Sun, L., & Luo, A. (2015b). "Surface molecular imprinting on manganese-doped zinc sulfide quantum dots for fluorescence detection of bisphenol A in water." *Analytical Letters*, *48*(13), 2075-2089.

Zhang, J., Zhang, R., Zhao, L. H., Sun, S. Q. (2012). "Synthesis of water-soluble γ-aminopropyltriethoxysilane-capped ZnO: MgO nanocrystals with biocompatibility." *Cryst Eng Comm* 14 (2), 613–619.

Zhang, L., Cheng, J., Xu, W. (2014). "Orange alert: a fluorescent detector for bisphenol A in water environments." *Anal Chim Acta* 815:51–56.

Zhang, Z. Y., Xiong, H. M. (2015). "Photoluminescent ZnO nanoparticles and their biological applications." *Materials* 8:3101–3127.

Zhao, B., Chen, H. (2007). "Synthesis novel multi-petals ZnO nano-structure by a cyclodextrin assisted solution route." *Mater Lett* 61:4890–4893.

Zhao, D., Wan, X., Song, H., Hao, L., Su, Y., & Lv, Y. (2014). "Metal–organic frameworks (MOFs) combined with ZnO quantum dots as a fluorescent sensing platform for phosphate." *Sensors and Actuators B: Chemical*, *197*, 50-57.

Zhao, L. H., Zhang, R., Zhang, J., & Sun, S. Q. (2012). "Synthesis and characterization of biocompatible ZnO nanoparticles." *Cryst Eng Comm*, 14(3), 945-950.

Zeng, H., Duan, G., Li, Y., Yang, S., Xu, X., & Cai, W. (2010). "Blue Luminescence of ZnO nanoparticles based on non-equilibrium processes: defect origins and emission controls." *Advanced Functional Materials*, *20*(4), 561-572.

Zheng, J., Zhao, S. Q., Xu, X. T., & Zhang, K. (2011). "Detection of bisphenol A in water samples using ELISA determination method." *Water Science and Technology: Water Supply*, *11*(1), 55-60.

Zhou, Y., Zhao, J., Li, S., Guo, M., Fan, Z., (2019). "An electrochemical sensor for the detection of p-nitrophenol based on a cyclodextrin-decorated gold nanoparticle–mesoporous carbon hybrid." *Analyst* 144 (14), 4400–4406.

Zhu, H., Li, Z., Yang, J. (2018). "A novel composite hydrogel for adsorption and photocatalytic degradation of bisphenol A by visible light irradiation." *Chemical Engineering Journal*, *334*, pp.1679-1690.

Zou, T., Xing, X., Yang, Y., Wang, Z., Wang, Z., Zhao, R., Zhang, X., Wang, Y., (2020). "Water-soluble ZnO quantum dots modified by (3-aminopropyl) triethoxysilane: the promising fluorescent probe for the selective detection of Cu^{2+}ion in drinking water." *J. Alloys. Compd.* 825, 153904.

LIST OF PUBLICATIONS

1. Kadam, V.V., Ettiyappan, J.P., Balakrishnan, R.M., 2019. Mechanistic insight into the endophytic fungus mediated synthesis of protein capped ZnO nanoparticles. Material Science and Engineering: B, 243, pp.214–221. https://doi.org/10.1016/j.mseb.2019.04.017

2. Kadam, V.V., Balakrishnan, R.M., Ettiyappan, J.P., 2020. Fluorometric detection of bisphenol A using β-cyclodextrin-functionalized ZnO QDs. Environmental Science and Pollution Research, Int. 1–11. https://doi.org/10.1007/s11356-020-07797-2.

3. Kadam, V.V., Shanmugam, S.D., Ettiyappan, J.P. and Balakrishnan, R.M., 2021. Photocatalytic degradation of p-nitrophenol using biologically synthesized ZnO nanoparticles. Environmental Science and Pollution Research, 28(10), pp.12119-12130. https://doi.org/10.1007/s11356-020-10833-w

4. Kadam, V.V., Balakrishnan, R.M., Ettiyappan, J.P., Thomas, N.S., Souza, S.A.D. and Parappan, S., 2021. Sensing of p-nitrophenol in aqueous solution using zinc oxide quantum dots coated with APTES. Environmental Nanotechnology, Monitoring & Management, 16, p.100474. https://doi.org/10.1016/j.enmm.2021.100474

5. Kadam, V.V., Balakrishnan, R.M., Ettiyappan, J.P. Photocatalytic degradation of bisphenol A using biosynthesized zinc oxide nanoparticles: kinetic studies, degradation pathways and toxicity assessments. Environmental Technology and Innovation (**Under review**).

Vrushali V. Kadam

Mobile: +91-7709710093   A606, Venkatesh Graffiti, Mundhwa, Pune

Email: vrushalikadam999@gmail.com   Maharashtra – 411036

<hr>

PhD area of research

"Detection and degradation of endocrine disruptors using ZnO nanoparticles"

Academic qualification

- Ph. D. from National Institute of Technology Karnataka, Surathkal, India from 2016 to 2021 in the Department of Chemical Engineering
- Master's from Kolhapur Institute of Technology, College of Engineering Kolhapur, Shivaji University, Kolhapur, Maharashtra, India from 2013-2016 in the Department of Biochemical Engineering and Biotechnology with an aggregate of 77.25 %.
- Bachelor's from Tatyasaheb Kore Institute of Engineering and Technology, Shivaji University, Kolhapur, Maharashtra, India from 2008-2012 in the Department of Biotechnology with an aggregate of 74.25 %.

Book Chapter

- Raj Mohan Balakrishnan and Vrushali Vinayak Kadam (2021). "Biological synthesis of metal selenide nanoparticles and their applications." Environmental Technologies to Treat Selenium Pollution: Principles and Engineering, IWA Publishing.

Publication

- Vrushali Vinayak Kadam, Raj Mohan Balakrishnan, Jagadeeshbabu Ponnan Ettiyappan, Nithya Sarah Thomas, Shaun Aaron D Souza, Subin Parappan (2021). "Sensing of p-nitrophenol in aqueous solution using zinc oxide quantum dots coated with APTES." Environmental Nanotechnology, Monitoring & Management 16 pp. 100474.

- <u>Vrushali Vinayak Kadam</u>, Soundharya Dharshini Shanmugam, Jagadeeshbabu Ponnan Ettiyappan, Raj Mohan Balakrishnan (2020). "Photocatalytic degradation of p-nitrophenol using biologically synthesized ZnO nanoparticles." Environmental Science and Pollution Research 28(10), pp.12119-12130.

- <u>Vrushali Vinayak Kadam</u>, Raj Mohan Balakrishnan Jagadeeshbabu Ponnan Ettiyappan (2020). "Fluorometric detection of bisphenol A using β-cyclodextrin-functionalized ZnO QDs." Environmental Science and Pollution Research, 28(10), pp.11882-11892.

- <u>Vrushali Vinayak Kadam</u>, Jagadeeshbabu Ponnan Ettiyappan, Raj Mohan Balakrishnan (2019). "Mechanistic insight into the endophytic fungus mediated synthesis of protein capped ZnO nanoparticles." Materials Science & Engineering:B 243:214–221.

- Jameer D. Bagwan, Supriya J. Patil, Amruta S. Mane, Sayali Vichare, <u>Vrushali Vinayak Kadam</u> (2010). "Genetically modified crops: food of the future (review)". International Journal of Advanced Biotechnology and Research. 1(1)- 21-30.

Conference/Symposium

- Presented technical paper on "**Photocatalytic degradation of p nitrophenol using biologically synthesized ZnO nanoparticles**." in Environmental Pollution Prevention and Control: Future Perspectives (EPPCFP-2019) held on 23-25 August 2019 organized by NITK, Surathkal.

- Presented poster on "**Ultrasound assisted mechanistic insight into sonochemical degradation of toxic organic pollutants from waste water**" in 5th International Conference on Research Frontiers in Chalcogen Cycle Science and Technology held on 19-21st December, 2016 organized by UNESCO-IHE and NITK, Surathkal.

- Presented technical paper on "**Ultrasonic assisted investigation of biodiesel synthesis" in the International event**, "OYCE 2015" held on 13th-14th March, 2015 at D. J. Sanghvi College of Engineering, Mumbai, Maharashtra.

Technical skills

- Hands on experience in the synthesis of nanoparticles using different methods.

- Proficient in basic and traditional microbiology techniques like cultivation, enumeration, isolation and preservation of microbes.
- Proficient in handling equipment's and instruments like High speed Centrifuges, UV-vis spectrophotometer, Fluorescence spectroscopy, Lyophilizer, Compound Microscope, Sonicator and conventional instruments used in microbiological studies like autoclave, laminar airflow, pH meter, incubated shakers and incubators, weighing balance.
- Proficient in handling instruments such as Total organic carbon analyzer, Scanning electron microscope, Particle size and Zeta potential analyzer, High-performance liquid chromatography, Liquid chromatography-mass spectroscopy, Affinity Chromatography, Gas Chromatography.
- Familiar with basic and conventional techniques in molecular biology, bio nanotechnology, Downstream process, Bioorganic chemistry, enzyme technology and concepts of chemical engineering.

Declaration

I hereby declare that all the above-given information is true and correct to the best of my knowledgeand belief.

Date: 24/02/2022   Vrushali Vinayak Kadam

Place: Pune, India.